UNIVERSITY OF SOUTHAMPTON

FACULTY OF ENGINEERING, SCIENCE & MATHEMATICS

School of Engineering Sciences

Materials Research Group

Strength Modelling of Al-Cu-Mg Type Alloys

By

Jialin Yan

Thesis for the degree of Doctor of Philosophy

March 2006

UNIVERSITY OF SOUTHAMPTON

ABSTRACT

FACULTY OF ENGINEERING, SCIENCE AND MATHEMATICS
SCHOOL OF ENGINEERING SCIENCES
MATERIALS RESEARCH GROUP

Doctor of Philosophy

STRENGTH MODELLING OF Al-Cu-Mg TYPE ALLOYS

By Jialin Yan

Age hardening of Al-Cu-Mg type alloys occurs in two stages separated by a constant hardness plateau when the alloys are aged at 110°C to 240°C after solution treatment and quenching. This work aims to develop a physically based two-stage hardening model to predict the yield strength of Al-Cu-Mg alloys with compositions in the (α+S) phase region. Experiments by means of hardness and tensile tests, differential scanning calorimetry and transmission electron microscopy (TEM) have been carried out to provide the relevant information for the calibration and validation of the model.

The model considers a simplified precipitation sequence which involves a pre-precipitate structure followed by S phase. This pre-precipitate structure is referred to as Cu-Mg co-clusters instead of GPB zones based on atom probe and TEM studies from collaborators and a review of the literature. The competition between the Cu-Mg co-clusters and the S phase is modelled by assuming S phase forms at the expense of Cu-Mg co-clusters. In the model, the solvi of the Cu-Mg co-clusters and the S phase are calculated, the evolution of precipitates in terms of volume fraction, average size and the solute concentration in the matrix are described and the superposition of various contributions from precipitation strengthening, solution strengthening and dislocation strengthening are modelled. Strengthening by Cu-Mg co-clusters and S phase is described by the modulus strengthening mechanism and the Orowan bypassing mechanism, respectively. The predicted contributions to the critical resolved shear stress show that strengthening in the alloys is mainly due to the Cu-Mg co-clusters in the first stage of hardening and due to the S phase in the second stage of hardening. The model takes account of the composition dependency of precipitation rate for Cu-Mg co-clusters formation as well as the amount of Cu and Mg present in undissolved intermetallic phases.

With a training root mean square error of 12MPa on an artificially aged 2024 alloy, the modelling accuracy on unseen yield strength data of two other alloys is 16MPa. Using a single set of parameters, the model has been applied to predict the hardness of a 2024-T351 alloy artificially aged at low temperature followed by short term underageing at higher temperature and then room temperature ageing. Good agreement between the predictions and the experiments indicates that the hardness changes during these multi-stage heat treatments can be well interpreted by considering Cu-Mg co-cluster dissolution, S precipitation and Cu-Mg co-cluster re-formation. Application to Al-xCu-1.7Mg alloys (x=0.2, 0.5, 0.8 and 1.1at.%) has shown good predictive capabilities of the model for the first stage of hardening. It is also shown that the model is applicable to Al-Cu-Mg alloys with Si contents at levels of 0.1-0.2wt.%. Modelling results of various Al-Cu-Mg alloys during natural ageing, artificial ageing and multi-stage heat treatments indicate that the model is capable of predicting the evolution of microstructure and the yield strength as a function of composition and heat treatments, and can provide a predictive tool for predicting the strength of Al-Cu-Mg based welds.

CONTENTS

PREFACE

This thesis is submitted for the degree of Doctor of Philosophy at the University of Southampton. The research work described herein was carried out wholly by the author under the supervision of Professor M.J. Starink in the Materials Research Group, School of Engineering Sciences, University of Southampton, during the period of October 2001 to January 2006.

This work is to the best of my knowledge original and this thesis is entirely my own work, except where acknowledgements and reference are made to other published work or work done by collaborators. No part of this thesis has been submitted for any other degree at any other university. This thesis does not exceed 75,000 words.

Parts of this work have been presented in the following publications:

[1] M. J. Starink, A. Cerezo, J. Yan, and N. Gao, 'Reply to the Comments on "Room-temperature precipitation in quenched Al-Cu-Mg alloys: a model for the reaction kinetics and yield-strength development."', accepted for *Philos. Mag. Lett.*, 2006.

[2] M. J. Starink and J. L. Yan, 'Precipitation hardening in Al-Cu-Mg alloys: analysis of precipitates, modelling of kinetics, strength predictions', accepted for *Proc. 10th International Conference on Aluminium Alloys (ICAA10), 2006*.

[3] M. J. Starink, N. Gao, L. Davin, J. Yan and A. Cerezo, 'Room temperature precipitation in quenched Al–Cu–Mg alloys: a model for the reaction kinetics and yield strength development', *Philos. Mag.*, 2005, **85**, 1395-1417.
- I co-wrote the sections on kinetics and strength modelling with my supervisor.

[4] J. Yan, M. J. Starink, and N. Gao, 'Modelling of Precipitation Hardening of Al-Cu-Mg Alloys', in: J.F.Nie, A.J.Morton, and B.C.Muddle (Eds.), *Proc. 9th International Conference on Aluminium Alloys (ICAA9)*, Institute of Materials Engineering Australasia Ltd., Brisbane, Australia, 2-5 August, 2004, p.926-932.

[5] M. J. Starink, N. Gao, and J. L. Yan, 'The origins of room temperature hardening of Al-Cu-Mg alloys', *Mater. Sci. Eng. A*, 2004, **387-389**, 222-226.
- I contributed to the analysis of cluster hardening mechanisms.

[6] M. J. Starink and J. Yan, 'A model for strengthening of Al-Cu-Mg alloys by S phase', in: M. Tiryakioglu and L. A. Lalli (Eds.), *1st International Symposium on Metallurgical Modeling for Aluminum Alloys, ASM Materials Solution 2003*, Pittsburgh, PA, October 12-15, 2003, p.119-126.
- Most of the text was written by my supervisor. I wrote the modelling programme, did the tensile tests and DSC experiments, analysed TEM data.

Jialin Yan
January 2006

ACKNOWLEDGEMENTS

I would like to express my sincere thanks to my supervisor Professor Marco J. Starink for his guidance, inspiration and patience. I am indebted to the School of Engineering Sciences, University of Southampton for financial support.

I would like to acknowledge and thank Dr. Philippa Reed for her support in my application for conference attendance fund, and to Dr. Ian Sinclair for his helpful suggestions and important comments on my work. My appreciation is also extended to Dr. Krishnamurthy Raviprasad of Nanotechnology Victoria, Australia and Dr. Nong Gao for the supply of unpublished experimental data, and to Dr. Shuncai Wang for his assistance with TEM.

I take this opportunity to thank all the members of the Materials Research Group for their kind help. In particular thanks go to Professors P.J. Gregson and A. Willoughby, Mr. D. Beckett, Mr. E. Bonner, Mr. E. Roszkowiak, Mrs. S. Walker, Mrs. G. Skiller, Dr. X.M. Li, Dr. J.Y Chen, Dr. N. Kamp, Dr. P. Rometsch, Dr. M. Joyce, Dr. L. Wang, Dr. Y.M. Xu, Dr. A.H. Wu, Dr. J. Liu, Dr. K.H. Khor, Dr. H.T. Pang, Dr. F. Lefebvre, Mr. M. Miller, Mr. J. Sun, Ms.Z.Z. Hua, Ms. L. Venning, Ms. P. Kittidachachan, Mr. I. Khan and Mr. M. Ali. Thanks also to my other friends in Southampton who have made my time here much easier and happier.

Finally I wish to express my gratitude to my family members for their understanding, encouragement and support. Special thanks to my husband and my son for everything.

NOMENCLATURE

a	lattice parameter of precipitate (m)
A_a	a constant
A_e	total area of the exothermic/endothermic heat effect
b	magnitude of the Burgers vector (m)
c_1, c_2	pre-exponential factors
c	solute concentration in the matrix (at%)
c_g	gross solute concentration in the matrix (at%)
c_0	initial solute concentration in the matrix (at%)
c_e	equilibrium solute concentration (at%)
c_{eff}	effective solute concentration in the matrix (at%)
c_r	solute concentration at the particle/matrix interface (at%)
c_p	equilibrium solute concentration of precipitate (at%)
c_{cl}^{Cu}	atomic fraction of Cu in the Cu-Mg co-clusters (at%)
c_{cl}^{Mg}	atomic fraction of Mg in the Cu-Mg co-clusters (at%)
d	diameter of the cross-section of the particles (m)
d_{GB}	average grain size (m)
D	diffusion coefficient of the solute in the matrix (m^2/s)
D_0	pre-exponential factor
D_r	diameter of the rod-shaped precipitates (m)
E_a	activation energy for reaction (J/mol)
$E_{a,c}$	activation energy for coarsening (J/mol)
E_{eff}	effective activation energy for nucleation and growth (J/mol)
E_G	activation energy for growth (J/mol)
E_N	activation energy for nucleation (J/mol)
f	volume fraction of precipitates
F_m	obstacle strength (N)
ΔF_v	driving force per unit volume for precipitation (J/m^3)
G	growth rate (m/s)
G_0	pre-exponential factor (m/s)
ΔG^o	standard Gibbs free energy of reaction (J/mol)

ΔG^*	activation energy barrier for nucleation of precipitates (J/mol)
ΔH^0	standard enthalpy of reaction (J/mol)
ΔH	formation enthalpy (J/mol)
I	nucleation rate (/m^{3}s)
I_0	pre-exponential factor (/m^{3}s)
k	rate constant for precipitation (/s)
k_B	Boltzman constant
k_c	rate constant for coarsening (nm^3/s)
k_0	pre-exponential constant for precipitation (/s)
$k_{o,c}$	pre-exponential constant for coarsening (nm^3/s)
k_{Cu}	strengthening coefficient of Cu atoms (MPa/at.%Cu)
k_{Mg}	strengthening coefficient of Mg atoms (MPa/at.%Mg)
k_{HP}	Hall-Petch coefficient (MPa$\sqrt{m}$)
k_n	a constant
K	equilibrium constant
K_A	strain hardening factor (MPa)
L	effective obstacle spacing in the slip plane (m)
$\bar{l}(t)$	average precipitate size (m)
$\bar{l}_0$	average size of precipitates at the start of coarsening (m)
$\bar{l}_c$	average size of precipitates in the coarsening stage (m)
$\bar{l}_g$	average size of precipitates in the nucleation and growth stages (m)
l_r	length of the rod-shaped precipitates
L_s	average planar spacing of particles in the slip plane
m	a constant
M	Taylor factor
n	reaction exponent or strain-hardening exponent
N	precipitate number density (/m^3)
N_0	number of atoms per unit volume (/m^3)
q	superposition exponent
Q_d	activation energy for diffusion of the solutes in the matrix (J/mol)
ΔQ	heat evolved due to the formation or dissolution of the precipitates (J/g)
ΔQ_{AQ}	heat evolved of the cluster formation effect in as-quenched condition (J/g)

ΔQ_{AR}	heat evolved of the S formation effect in as-received condition (J/g)
ΔQ_t	heat evolved of the exothermic effect for sample aged for time t (J/g)
ΔQ_{Tp}	heat evolved at peak temperature (J/g)
ΔQ_∞	heat evolved of the exothermic effect for sample aged for very long time (J/g)
r	radius of spherical precipitates (m)
r_e	effective particle radius (m)
r_0	dislocation inner cut-off radius (m)
$\bar{r}$	average radius of precipitates (m)
$\overline{r_o}$	initial average radius of precipitates (m)
r^*	critical radius for nucleation (m)
R	universal gas constant (8.314 J/Kmol)
s	reaction exponent
ΔS^0	standard entropy of reaction
t	ageing time (s)
t_e	time when the heat flow is 0.5% of the maximum heat flow
t_f	time needed for a fixed fraction transformed (s)
t_p	time to peak heat flow (s)
t_{eq}	equivalent time (s)
T	absolute temperature (K)
T_{av}	average temperature of a temperature range (K)
T_p	peak temperature (K)
T_s	solvus temperature (K)
V_{at}	atomic volume of precipitate (m^3)
V_m	molar volume of precipitates (m^3/mol)
V_t	actual transformed volume
V_e	extended volume
x	amounts (the number of moles) of precipitates (at%)
z	time at which the nucleus is formed (s)
Z	Zeldovich factor
α	fraction transformed
α_{ext}	extended fraction
β	heating rate (K/s)

β^*	frequency factor or rate of impingement (/s)
γ	particle/matrix interfacial energy (J/m^2)
Γ	dislocation line tension
$\Delta\mu$	difference in shear modulus between matrix and Cu-Mg co-clusters (GPa)
$\Delta\sigma_{GB}$	strengthening increment due to grain boundaries (MPa)
$\Delta\sigma_{ss}$	increment in yield strength due to solid solution strengthening (MPa)
$\Delta\tau$	critical resolved shear stress (CRSS) (MPa)
$\Delta\tau_{cl}$	CRSS contribution from modulus strengthening (MPa)
$\Delta\tau_{ch}$	CRSS contribution from chemical hardening (MPa)
$\Delta\tau_{d}$	CRSS contribution from discolation strengthening (MPa)
$\Delta\tau_{S}$	CRSS contribution from S strengthening (MPa)
$\Delta\tau_{\Sigma}$	CRSS contribution from discolation strengthening and S strengthening (MPa)
$\Delta\tau_{ppt}$	CRSS contribution from $\Delta\tau_{\Sigma}$ and cluster strengthening $\Delta\tau_{cl}$ (MPa)
ε	true strain
η_i	impingement exponent
λ_i	impingement parameter
λ_1, λ_2	proportionality constants
μ_{Cu}	shear modulus of copper (48.3GPa)
μ_{Mg}	shear modulus of magnesium (17.3GPa)
μ_{Al}	shear modulus of aluminium (26.2GPa)
μ_{cl}	shear modulus of Cu-Mg co-clusters (GPa)
ν	Poisson's ratio for Al
$\overline{v_N}$	average volume of a single nucleus (m^3)
ρ_N	number density of growing nuclei (/m^3)
σ	true stress
σ_i	intrinsic strength of Al matrix (MPa)
σ_y	conventional yield strength (MPa)
ψ_c	breaking angle for a gliding dislocation to overcome the obstacles

LIST OF ABBREVIATIONS

1DAP	one dimensional atom probe
3DAP	three dimensional atom probe
APFIM	atom probe field ion microscopy
BF	bright field
CDB	Coincidence Doppler Broadening
CRSS	critical resolved shear stress
DIC	differential isothermal calorimetry
DSC	differential scanning calorimetry
EBSD	electron backscatter diffraction
EDS	energy dispersive spectroscopy
GP zones	Guinier-Preston zones
GPB zones	Guinier-Preston-Bagaratsky zones
HF	heat flow
HREM	high resolution electron microscopy
Hv	Vickers hardness
ODF	orientation distribution function
RMSE	root mean square error
SAD	selected area diffraction
SAXS	small angle X-ray scattering
SEM	scanning electron microscopy
STD	standard deviation
TEM	transmission electron microscopy
UTS	ultimate tensile strength
XRD	X-ray diffraction
YS	yield strength

Chapter 1 Introduction

2xxx series Al-Cu-Mg aluminium alloys are precipitation hardenable alloys that rely on the precipitation of fine (metastable) precipitates for strengthening. Among the 2xxx alloys, the 2024-T3 alloy (which is solution treated, cold worked and naturally aged) is widely used in the civil aerospace industry due to its good combination of specific strength and damage tolerance. Traditionally the requirements for high specific strength, high fracture toughness and good fatigue crack growth resistance are mostly fulfilled via the appropriate alloy chemistry and thermo-mechanical treatment by trial and error based on metallurgical experience. This can be costly and slow. Therefore as a cost effective approach to improve the properties of existing materials and to develop new materials, development of models to relate the process parameters (alloy composition, heat treatment temperature and time) to the mechanical properties such as yield strength via microstructure evolution is highly desirable. Over the last fifteen years, the increasing demand for materials optimization has led to the development of physically based models with varying approaches and complexity for microstructure evolution and precipitation hardening in 2xxx series [1-4], 6xxx series [5, 6], 7xxx series [7-10] and 8xxx series [11] aluminium alloys. The published age hardening models for Al-Cu alloys developed by Shercliff and Ashby [1] and by Liu *et al.* [2] both consider a single precipitate throughout the ageing process; thus these models are applicable only for the ageing curves with a single peak. Models for Al-Cu-Mg alloys developed by Gomiero *et al.* [3] and by Genevois *et al.* [4] consider various precipitates, but using measured microstructural parameters for the prediction of the yield strength. It would thus be beneficial to be able to predict the evolution of microstructural parameters based on alloy composition and thermal history.

Age hardening of Al-Cu-Mg type alloys with composition in the (α+S) phase field occurs in two distinct stages separated by a constant hardness plateau when the alloys are aged at 110°C to 240°C after solution treatment and quenching [12]. The aim of this work is to develop a physically based two-stage age hardening model to predict the yield strength of Al-Cu-Mg type alloys as a function of composition and heat treatments. The model would consider two types of precipitates; describe the thermodynamics and kinetics of microstructure evolution and the yield strength evolution. The model will be designed such that it can describe precipitation kinetics and precipitation hardening by an analytical method, with a minimum of computational effort while showing good accuracy of predictive power.

This work involves extensive analysis of theory and models, with experimental work especially aimed at providing key information that is directly relevant to evaluate the validity of the model. Experimental data for the calibration and validation of the model are from three sources: from experiments performed for this work on four Al-Cu-Mg alloys as presented in this thesis, from experiments performed for other projects at the University of Southampton and from the literature. In this work, the mechanical properties have been investigated by Vickers hardness and tensile tests. The precipitation kinetics has been studied using differential scanning calorimetry (DSC) and isothermal calorimetry. Microstructure characterization has been carried out using transmission electron microscopy (TEM).

The structure of this thesis is as follows: firstly a literature review in Chapter 2 covers published experimental studies of the age hardening behaviour in Al-Cu-Mg based alloys, the approaches of modelling of microstructure evolution and of the yield strength, and the existing strengthening models for aluminium alloys. Chapter 3 describes the experimental techniques used in the present study. Then the results and analysis of the kinetic study, mechanical tests and TEM analysis are presented in Chapter 4. Also presented is a new method for conversion of Vickers hardness to yield strength. The model, which consists of a thermodynamic model, a kinetic model and a strength model, is described in Chapter 5. The model predictions and discussion are given in Chapter 6. Finally, summary and conclusions are outlined in Chapter 7.

References

[1] H. R. Shercliff and M. F. Ashby, 'A Process Model for Age Hardening of Aluminum-Alloys .1. The Model', *Acta Metall. Mater.*, 1990, **38**, 1789-1802.

[2] G. Liu, G. J. Zhang, X. D. Ding, J. Sun, and K. H. Chen, 'Modeling the strengthening response to aging process of heat- treatable aluminum alloys containing plate/disc- or rod/needle- shaped precipitates', *Mater. Sci. Eng.*, 2003, **344**, 113-124.

[3] P. Gomiero, Y. Brechet, F. Louchet, A. Tourabi, and B. Wack, 'Microstructure and Mechanical-Properties of a 2091 Al-Li Alloy .2. Mechanical-Properties - Yield Stress and Work-Hardening', *Acta Metall. Mater.*, 1992, **40**, 857-861.

[4] C. Genevois, A. Deschamps, A. Denquin, and B. Doisneau-cottignies, 'Quantitative investigation of precipitation and mechanical behaviour for AA2024 friction stir welds', *Acta Mater.*, 2005, **53**, 2447-2458.

[5] O. R. Myhr, O. Grong, and S. J. Andersen, 'Modelling of the age hardening behaviour of Al-Mg-Si alloys', *Acta Mater.*, 2001, **49**, 65-75.

[6] S. Esmaeili, D. J. Lloyd, and W. J. Poole, 'A yield strength model for the Al-Mg-Si-Cu alloy AA6111', *Acta Mater.*, 2003, **51**, 2243-2257.

[7] A. Deschamps and Y. Brechet, 'Influence of predeformation and ageing of an Al-Zn-Mg alloy - II. Modeling of precipitation kinetics and yield stress', *Acta Mater.*, 1999, **47**, 293-305.

[8] M. J. Starink and S. C. Wang, 'A model for the yield strength of overaged Al-Zn-Mg-Cu alloys', *Acta Mater.*, 2003, **51**, 5131-5150.

[9] W. J. Poole, H. R. Shercliff, and T. Castillo, 'Process model for two step age hardening of 7475 aluminium alloy', *Mater. Sci. Technol.*, 1997, **13**, 897-904.

[10] W. J. Poole, J. A. Saeter, S. Skjervold, and G. Waterloo, 'A model for predicting the effect of deformation after solution treatment on the subsequent artificial aging behavior of AA7030 and AA7108 alloys', *Metall. Mater. Trans. A*, 2000, **31**, 2327-2338.

[11] M. J. Starink, P. Wang, I. Sinclair, and P. J. Gregson, 'Microstrucure and strengthening of Al-Li-Cu-Mg alloys and MMCs: II. Modelling of yield strength', *Acta Mater.*, 1999, **47**, 3855-3868.

[12] H. K. Hardy, 'The ageing characteristics of some ternary aluminium-copper-magnesium alloys with copper : magnesium weight ratios of 7:1 and 2.2:1', *J. Inst. Metals*, 1954-55, **83**, 17-34.

Chapter 2 Literature Review

With increased knowledge on the microstructure evolution and its corresponding relationship to the properties in aluminium alloys, there has been an increasing interest in modelling of microstructure evolution and the yield strength over the past fifteen years. It is well known that the strength of heat treatable aluminium alloys is derived mainly from the fine precipitates which form during precipitation hardening. For instance, the microstructures of high strength 2xxx alloys often consist of precipitates such as clusters and/or GP(B) zones, θ phase and its precursors, and/or S phase and its precursors. Current understanding of the precipitation in aluminium alloys is based on theories for thermodynamic stability of precipitates and models for their kinetics of nucleation, growth and coarsening. Analytical equations derived to relate the precipitation to strength usually include microstructural parameters such as precipitate size and volume fraction. Therefore modelling of strength development during the complete ageing process will require knowledge of strengthening mechanisms as well as a combination of knowledge of precipitation thermodynamics and kinetics to obtain relevant microstructural parameters.

In this chapter, firstly the physical metallurgy of 2xxx alloys is reviewed, with an emphasis on the precipitation hardening (Sections 2.1 and 2.2). Then modelling methods for microstructure evolution, both analytical and numerical, are presented (Section 2.3). Subsequently various strengthening mechanisms, the principle for theoretical derivation of mathematical equations which relate the microstructure to the yield strength and the superposition of the strengthening components to the yield strength are introduced (Section 2.4). Finally the existing models for the yield strength are summarised (Section 2.5).

2.1 Introduction to aluminium alloys

2.1.1 Aluminium alloy and temper designations

Wrought aluminium alloys are commonly classified into heat-treatable and non-heat-treatable alloys. Heat-treatable alloys respond to heat treatment and develop high strength via precipitation hardening. Examples are Al-Cu(-Mg), Al-Mg-Si, Al-Zn-Mg and Al-Li based alloys. Non-heat-treatable alloys rely mainly on work hardening for property development. Examples are Al-Mn and Al-Mg based alloys [1]. To identify wrought aluminium and aluminium alloys, the international alloy designation system (IADS), i.e. four-digit numerical designation system, has been adopted. The first digit indicates the major alloying elements; the last two of the four digits have no special significance but serve only to identify the different aluminium alloys in a group. The second digit indicates modification of base alloy. If the second digit is zero, it indicates the original alloy. The main alloying elements in 2xxx series alloys are copper and magnesium. **Fig. 2.1** shows the alloy and temper designations used for wrought heat-treatable alloys [2]. The mechanical properties of heat-treatable alloys depend on the heat treatment tempers, so specific tempers are selected for the alloys to provide the best compromise between mechanical properties. For example, many 2xxx alloys demonstrate a significant strengthening response at room temperature and also have a strong response to artificial ageing at elevated temperature. Generally, the fracture toughness of the age-hardened alloys decreases with increasing strength. For a specific yield strength, 2xxx alloys exhibit higher toughness in the underaged condition than in the overaged condition [3], so 2xxx alloys are generally used in naturally aged tempers such as T3 or T4 for a good combination of specific strength and damage tolerance.

Table 2.1 gives the composition ranges of some 2xxx aerospace alloys [4]. The 2014 Al-Cu-Mg-Si and 2024 Al-Cu-Mg-Mn alloys were developed as high strength alloys. The 2024 alloys are technically important structural materials due to their low density, high strength, good fatigue crack growth resistance and good fracture toughness, and are extensively used for aerospace applications as the fuselage skin and the lower wing skins. The 2618 Al-Cu-Mg-Fe-Ni alloy was developed for applications at

elevated temperatures due to its good creep resistance. The typical tensile properties of commercial 2014, 2024 and 2618 alloys are given in **Table 2.2** [2, 4].

2.1.2 General metallurgical features

Over 90% of the aluminium alloys for aerospace applications are fabricated via the ingot-casting route, and the semi-continuous direct chill casting process is the dominant method for the manufacture of rectangular or round section billets. The ingot is subsequently homogenised at a high temperature (~450-500°C) to reduce the compositional variation and remove soluble eutectic phases, and allow precipitation of submicron intermetallic particles (termed dispersoids) for grain size control. The billet may then be hot rolled to plate and subsequently cold rolled to sheet, forged close to shape or extruded to the required section with grain structure and texture being controlled by processing parameters and intermetallic particles. For wrought heat-treatable alloys, subsequent solution heat treatment, quenching, natural or artificial ageing are required for the development of high strength [1]. For 2xxx series alloys, cold work after quenching from the solution heat treatment increases strength in natural aged alloys by increasing dislocation density (e.g. the yield strength is increased by at least 30MPa in 2024-T3 alloys compared with that of 2024-T4 alloys [5]), and greatly enhances the alloys' response to subsequent artificial ageing [6-9].

During processing and ageing, three types of dispersed particles are generally present in commercial heat-treatable aluminium alloys as follows [1, 5, 10]:

(1) Intermetallic constituent particles. These particles form during ingot solidification, with size ranging from one to several tens of microns. These particles are either soluble, such as Al_2Cu, Mg_2Si and Al_2CuMg, that may dissolve during subsequent thermal treatments, or insoluble, such as Al_7Cu_2Fe, $Al_{12}Fe_3Si$ and $Al_6(Fe,Cu)$. The size and spacing of these particles are too coarse to impede the motion of dislocations, so they have relatively little effect on strength. However, the presence of these brittle particles causes a marked loss of ductility and fracture toughness. As the insoluble particles usually contain impurity elements specifically iron and silicon, the iron and silicon contents are kept to a minimum in commercial aluminium alloys.

(2) Dispersoids. These particles form during ingot homogenisation, with size in the range of about 0.05 to 0.5μm. Dispersoids are usually Mn, Zr or Cr containing particles such as $Al_{20}Cu_2Mn_3$, Al_3Zr and $Al_{12}Mg2Cr$. They are allowed to form to retard recrystallization and grain growth for grain control. Due to their large sizes, dispersoid particles contribute only slightly to strength, but they influence the strength indirectly by refining grain size.

(3) Precipitates. These particles form during ageing, with size up to 0.1μm. Examples are GP(B) zones, θ′ and S phases in 2xxx alloys. They provide most of the strengthening in heat treatable aluminium alloys. Detail of the principles associated with precipitation hardening will be given in the next section.

2.1.3 Basics of precipitation hardening

The phenomenon of precipitation hardening in aluminium alloys (otherwise known as age hardening) was discovered about 100 years ago when it was found that certain aluminium alloys changed in hardness on storage at room temperature. Along with the extensive experimental studies, the fundamental theories of precipitation hardening have been developed [1, 11-14].

The general requirements for precipitation strengthening include:

(1) The alloying elements have significant solid solubility in aluminium and the solubility decreases markedly with decreasing temperature;

(2) The formation of supersaturated solid solution (α_{SS}) after quenching;

(3) The formation of uniform, finely dispersed precipitates during ageing heat treatment.

To satisfy the above requirements, heat treatment to increase the strength of Al alloys is normally a three-step process:

(1) Solution heat treatment at a high temperature to maximize the solid solubility of the alloying elements within the single-phase region;

(2) Rapid cooling or quenching to a low temperature (below the solvus) to produce solid solution supersaturated with both solute elements and vacancies;

(3) Ageing at either room temperature (natural ageing) or some intermediate temperature (artificial ageing) for controlled decomposition of the α_{SS} to obtain the precipitates which contribute to strengthening.

In most precipitation-hardened systems, the decomposition of the supersaturated solid solution occurs by the following sequence:

$\alpha_{SS} \rightarrow$clusters and/or GP zones $\rightarrow$intermediate precipitates $\rightarrow$equilibrium precipitate

The precipitation path can be rather complex, sometimes involving the formation of several intermediate precipitates prior to reaching the equilibrium precipitate. During the initial stage of ageing, solute atoms collect within the solid solution lattice to form the clusters and/or Guinier-Preston (GP) zones. The clusters or GP zones retain the structure of the matrix and are coherent with it; they are metastable and thus either dissolve or convert into the intermediate precipitates as ageing time or temperature is increased. The metastable intermediate precipitate has a definite composition and a crystal structure that is distinct from that of the matrix and also different from that of the equilibrium precipitate; it is typically semicoherent with the matrix and has specific crystallographic orientation relationships with the matrix. It is often the presence of the clusters, GP zones and/or metastable intermediate precipitates that lead to age hardening. The incoherent equilibrium precipitate is generally larger than the intermediate precipitates, and strength progressively decreases with the coarsening of the equilibrium precipitate. Recommended commercial heat treatments are often compromises between the time/cost factors and the desire to obtain the optimum microstructure.

2.2 Precipitation in Al-Cu-Mg based alloys

2.2.1 Phase diagram

Alloy phase diagrams are useful guides in the development of new materials, as well as in the improvement of the performance of existing materials. The Al-Cu binary phase diagram has been well investigated [15]. For the study of age hardening in Al-

Cu based alloys, metastable solvus curves are of great importance for practical applications. The most widely quoted solvi of the GPI and GPII zones have been determined by the hardness reversion experiments of Beton and Rollason [16]. The solvus of θ′ has been assessed by Hornbogen [17]. **Fig. 2.2** shows the solubility curves of equilibrium phase θ as well as the intermediate precipitates GPI zone (i.e. GP), GPII zone (i.e. θ″) and θ′ phase [18].

Phase equilibria in the Al-rich corner of Al-Cu-Mg system are well known [19-23]. The isothermal section at 190°C of the Al-Cu-Mg equilibrium phase diagram is shown in **Fig. 2.3**. Three phases of interest in the Al-rich corner are θ (Al_2Cu) phase, S phase ($CuMgAl_2$) and T (Al_6CuMg_4) phase (some authors designated Al_6CuMg_4 phase as $(AlCu)_{49}Mg_{32}$ phase). T phase has a cubic structure, space group Im3, with a=1.428nm [24]. The characteristics of θ and S phases will be reviewed in Section 2.2.2.

Little *et al.* [19] investigated the 460°C isothermal section of the Al-Cu-Mg system by metallographic examinations and X-ray diffraction (XRD) studies. The α solid solubility curves at 460°C and at 375°C were determined carefully, as shown in **Fig. 2.4** and **Fig. 2.5**. Little *et al.* [19] found that the α/α+S solid solubility data could be represented by:

$$\log_{10}[Cu][Mg] = 5.576 - \frac{4082}{T} \qquad (2.1)$$

where [Cu] and [Mg] are the atomic percentages and *T* is the absolute temperature. This equation may be used to calculate the α/α+S phase boundary.

Little information is found for the metastable equilibrium phase diagram of the Al-Cu-Mg system. Beton and Rollason [16] tried to obtain the solubility curve of the zone which they called the "[Cu, Mg] complex zone" in Al-Cu-Mg alloys with Cu:Mg weight ratios of 2.2:1 and 7:1 by hardness reversion. They considered that the [Cu, Mg] complex zone should be a zone between the GP zone formed in Al-Cu alloy and the GP zone formed in pseudo-binary Al-Cu-Mg alloy with equi-atomic Cu:Mg ratio,

and proposed the possible α/α+GP[Cu, Mg] zone metastable phase boundaries as shown in **Fig. 2.6**.

The experimental determination of phase diagram is strenuous, and usually the phase boundaries at desired temperatures are not available experimentally, and therefore there is a demand for the thermodynamically calculated phase diagrams. Modelling of phase diagram will be reviewed in Section 2.3.1.

2.2.2 Microstructural development

2.2.2.1 Al-Cu based alloys

Although there are few commercial alloys based on Al-Cu alloys, this system has been studied in great detail as a model alloy for the 2xxx series of age-hardening Al alloys, especially relating to the formation of GP zones [11, 12, 25, 26].

The precipitation sequence is complex, depending on the degree of supersaturation and the ageing temperature, and usually follows [27]:

$$\alpha_{SS} \rightarrow \text{GPI} \rightarrow \text{GPII} / \theta'' \rightarrow \theta' \rightarrow \theta\ (Al_2Cu)$$

where the GPI zones are monolayers of Cu atoms on a {001} Al matrix plane, while GPII zones are two or more layers of Cu atoms separated by layers of Al atoms [28, 29]. Some authors used the term θ″ phase instead of GPII considering that it is a coherent intermediate precipitate rather than a zone [30]. Both GPI and GPII zones have disc or plate-like morphology with typical size in the order of tens of nanometers. θ′ phase is a semicoherent intermediate precipitate, and occurs as platelets oriented at $(001)_\alpha // (001)_{\theta'}$ and $[010]_\alpha // [010]_{\theta'}$ [27]. Further ageing produces the formation of the equilibrium θ phase.

2.2.2.2 Al-Cu-Mg based alloys

The precipitation hardening in Al-Cu-Mg alloys has been extensively studied because this system is the basis of the 2xxx series of commercial aluminium alloys. Generally

there are two precipitation sequences depending on the composition and Cu/Mg ratio in the alloys [2, 26, 31]. For alloys in the (α+θ) phase region, i.e. high Cu/Mg ratio alloys, the precipitation sequence identical to that in Al-Cu alloys occurs:

$$\alpha_{SS} \rightarrow \text{GPI} \rightarrow \text{GPII} / \theta'' \rightarrow \theta' \rightarrow \theta\ (Al_2Cu)$$

For alloys in the (α+S) phase region, i.e. medium to low Cu/Mg ratio alloys, the precipitation process has been described as:

$$\alpha_{SS} \rightarrow \text{GPB zones} \rightarrow (S'') \rightarrow S' \rightarrow S\ (Al_2CuMg)$$

where GPB (Guinier-Preston-Bagaratsky) zones are the Cu and Mg rich zones which were designated as GPB zones by Silcock [32]. S is the equilibrium phase Al_2CuMg, S″ and S′ are metastable precursors of S phase. For alloys in the (α+θ+S) phase region, both sequences may occur. Characteristics of these precipitates are summarized in **Table 2.3**.

Despite the extensive studies on Al-Cu-Mg alloys, details of the decomposition of the supersaturated solid solution and the precipitation mechanisms are still highly controversial, especially in the initial stage of ageing [18, 33-42]. The debate in the literature has focused on the GPB zones and the intermediate S″ phase. These will be presented in detail below.

Clusters and GPB zones

According to XRD studies by Bagaryatsky on an Al-3Cu-1.15Mg (wt.%) alloy [43] and by Silcock [32] on an Al-3.15Cu-1.52Mg (wt.%) alloy, the GPB zones first precipitate out from a supersaturated solid solution at the early stage of ageing. Bagaryatsky [43] considered the diffuse streaking along the $<100>_\alpha$ directions detected in aged Al-Cu-Mg alloys to be associated with short-range ordering along the $\{100\}_\alpha$ planes. Silcock [32] proposed that the GPB zones formed along the $<100>_\alpha$ directions as small cylinders with a diameter of 1-2nm and a length of about 4-8nm depending on the quenching rates. In later studies of precipitation in the Al-Cu-Mg

alloys, conventional TEM or high resolution electron microscopy (HREM) was used to investigate the existence of the GPB zones. However, limited contrast and small size of the GPB zones make the GPB zones difficult to observe even by HREM. No contrast effects or characteristic streaks indicating the presence of the GPB zones was found in an Al-0.6Cu-4.2Mg (wt.%) alloy in the course of ageing at 180°C (from as-quenched stage to ageing time up to 34h) using HREM, TEM and selected area diffraction (SAD) by Ratchev *et al.*[40]. Also microstructural studies of 2024 alloys aged at 150°C to 240°C by Shih *et al.* [44] and Gao *et al.* [45, 46] using TEM/SAD failed to reveal any features attributed to GPB zones. Some evidence for GPB zones was detected by TEM/SAD and HREM only after 100h aged at 150°C for an Al-1.1Cu-1.7Mg (at.%) alloy studied by Ringer *et al.* [36]. The GPB zones were observed as fine rods less than 1 nm in diameter causing diffuse streaking along the $<100>_\alpha$ directions and through the $\{010\}_\alpha$ positions in the SAD patterns. The GPB zones appear to lack internal order, but develop facets parallel to $\{102\}_\alpha$ and $\{011\}_\alpha$ planes [36]. However, in a recent paper, Wang *et al.* [47] questioned the evidence for the presence of GPB zones shown by Ringer *et al.* in [36], and pointed out that the small precipitates observed in HREM images (Fig.7a in [36]) could well be S phase. Charai *et al.* [38] studied the microstructure of an Al-0.9Cu-1.4Mg (at.%) alloy aged 4h at 200°C by HREM, and interpreted data as showing the coexistence of partially ordered Mg-rich clusters and ordered Cu-rich platelets which were termed GPB zones. The Mg-rich clusters are ellipsoidal with a diameter of about 1nm and show ordering parallel to $\{011\}_\alpha$ planes. The GPB zones are ordered on $\{001\}_\alpha$ planes with a width of about 4nm and a thickness of about 0.2nm. Zahra *et al.* [42] were unable to identify the GPB zones in an Al-0.9Cu-1.4Mg (at.%) alloy by HREM after room temperature ageing, whereas Abis *et al.* [41] reported streaks along $[100]_\alpha$ directions around $½(220)_\alpha$ in the SAD patterns of an Al-4.4Cu-1.7Mg (wt.%) alloy aged at room temperature for 15min and 48h, and attributed these diffraction effects to the presence of the GPB zones. It is seen that confusion exists in the literature concerning the nature of the GPB zones. It is worth noting that the Mg-rich clusters designated by Charai *et al.* [38] were once taken as GPB zones by researchers from the same group [42] on the basis of size and morphology. The Mg-rich clusters in [38] are very similar to the Cu and Mg rich clusters observed by Radmilovic *et al.* [48] using HREM in the study of an Al-2.0Cu-1.1Mg-0.14Zr (wt.%) alloy aged 72h at 190°C. It

was suggested [38, 48] that these clusters may be the nuclei for homogeneous S formation. When comparing the clusters described by Charai *et al.* [38] and by Radmilovic *et al.* [48] with the GPB zones in an Al-1.1Cu-1.7Mg (at.%) alloy aged 500h at 150°C described by Ringer *et al.* [36], it is further noted that the so-called clusters and the so-called GPB zones which these groups observed by HREM are actually very similar in terms of size (about 1nm), shape (spherical, cylindrical or ellipsoidal), composition (Cu and Mg rich), degree of order (partially ordered) and orientation (ordering parallel to $\{011\}_\alpha$ planes). This implies that the notations used in these papers [36, 38, 48] for clusters and GPB zones are not clearly defined.

Recently, studies of the initial stages of the decomposition of a supersaturated solid solution in aluminium alloys using atom probe field ion microscopy (APFIM), one dimensional atom probe (1DAP) and three dimensional atom probe (3DAP) techniques suggest that the evolution of microstructure involves clustering of solute atoms prior to formation of precipitates such as GP/GPB zones, θ or S phase [18, 34, 36, 37, 39, 45, 49]. From the study of an Al-1.1Cu-1.7Mg (at.%) alloy by means of APFIM and 1DAP, Ringer *et al.* [36] reported the presence of Cu-Cu and Mg-Mg clusters in the as-quenched condition and the presence of Cu-Mg co-clusters after 5min at 150°C. However, in accordance with a 3DAP study in [37], Ringer and co-workers [18, 39] concluded that the 3DAP's improved statistical accuracy showed little or no Cu-Mg co-clusters are present after 5 min ageing at 150°C. At these stages, the solute clusters detected by atom probe are not resolved by TEM or HREM. After 100h ageing at 150°C, precipitation of GPB zones was observed by TEM/SAD, and 1DAP analysis showed strong evidence for co-clustering of Cu and Mg atoms at the sites of the GPB zones and suggested that the zones contain approximately equal numbers of Cu and Mg atoms [18, 36]. Ringer *et al.* [36] therefore proposed that it was likely that the GPB zones nucleate at the sites of the Cu-Mg co-clusters. Reich *et al.* [37] conducted a detailed study of an Al-1.1Cu-1.7Mg (at.%) alloy aged at 200°C for 1min, 1h and 8h by means of 3DAP, TEM/SAD and HREM. To check whether the distribution of solute atoms is random or not, a statistical analysis was performed by the contingency table method. The 3DAP results showed that no Cu-Mg co-clusters form until after ageing for 1h. After 8h ageing rod-shaped Cu and Mg riched zones elongated along the $[100]_\alpha$ direction were observed in the 3DAP elemental map

and they were identified as GPB zones according to the above mentioned features and an interpretation on TEM images and SAD patterns. Reich *et al.* [37] thus suggested that the Cu-Mg co-clusters evolve into GPB zones through a continuous growth process with increasing size and ordering. TEM/SAD and HREM results indicated the heterogereous nucleation of S precipitates along dislocations after 1min at 200°C. No evidence for GPB zone formation was found until ageing for 8h at 200°C. However, Davin [49] pointed out that the contingency table method is inappropriate to prove the non-existence of clusters in the early stages of ageing, and stated that frequency distribution method [50] would be the correct tool for a statistical analysis of 3DAP data in detecting the clustering of one or several solute atoms.

Davin [49] and Gao and co-workers [45, 46] reported that small Cu-Mg co-clusters without any characteristic shape and a few (2 to 5) large precipitates with definite shapes have been found in 3DAP samples of a stretched Al-1.2Cu-1.2Mg (at.%) alloy (i.e. alloy D in this thesis) and a stretched Al-1.9Cu-1.6Mg (at.%) alloy (i.e. alloy B in this thesis) aged 12h at 150°C. At this stage TEM revealed only dislocation lines and loops. Clustering of Cu and Mg atoms was detected by the frequency distribution method, and Cu-Mg co-clusters, which cannot be observed directly in the atom map, were identified using the maximum separation method. The size of the Cu-Mg co-clusters was estimated from the radius of gyration as about 0.7nm to 0.8nm, and the average measured atomic concentration of Cu, Mg and Al in the Cu-Mg co-clusters is about 30%, 30% and 40%, respectively in these two alloys. The large precipitates in these two alloys have platelet or lath shapes with a thickness of about 2-3nm. It was speculated that the precipitates could be referred to as GPB zones in case of rod-like morphologies or fine S phase for platelet/lath-like morphologies. Cu-Mg co-clusters were also found in these two alloys aged at room temperature after solution treatment and quenching for ageing times from 1h or 2h up to 6 months for alloy B and alloy D, respectively [49, 51]. The average radius of the Cu-Mg co-clusters during this period is about 0.5nm to 0.7nm. The average measured composition of the Cu-Mg co-clusters varies with the ageing time. **Fig. 2.7** exhibits the average measured concentration of Mg, Cu and Al in the Cu-Mg co-clusters in alloy B as a function of the natural ageing time [49]. As the ageing proceeds, the Cu: Mg ratios in the Cu-Mg co-clusters approach unity. The Al content in the Cu-Mg co-clusters may vary between 30at.% to 90at.%. The high Al content in the early stages of ageing is

considered to be probably overestimated due to a local magnification effect and a trajectory aberration artefact. No precipitates were observed for ageing time up to 6 months during natural ageing.

The difference between Cu-Mg co-clusters and GPB zones is difficult to define. They are both aggregates of Cu and Mg atoms and are fully coherent with aluminium matrix. They do not have their own unique structure and composition. The difficulty may also partly arise from the use of different experimental techniques for their definitions and detections. It is possible to distinguish small clusters and large clusters, and the latter may be termed GBP zones. But it should be noted that a structure cannot be identified merely by the size, morphology and/or composition using 3DAP without the complementary investigations using other experimental techniques such as TEM/SAD and HREM. In addition, the GPB zones have proved difficult to be imaged and detected by TEM/SAD and HREM, and the identification of the precipitates, which were observed in the atom probe maps, as GPB zones using TEM/SAD or HREM is further complicated by the simultaneous presence of S phase. Although Ringer *et al.* [36] suggested the distinction between Cu-Mg co-clusters and GPB zones can be made on the basis of size, shape, composition, degree of order, orientation and structure, in practice such a criterion cannot provide useful information. It seems more useful and a better reflection of experimental data to consider that all the nano-sized Cu and Mg containing aggregates are similar and continuous forms. The terms used to describe them, Cu-Mg co-clusters or GPB zones, seem largely irrelevant, as are size or shape based criteria suggested to define one or the other. In this thesis, based on 3DAP and TEM/SAD results mentioned above on alloys B and D [45, 46, 49], the nomenclature of Cu-Mg co-clusters instead of GPB zones is used for the pre-precipitate structure. Throughout the thesis, the doubts about the definition of GPB zones are taken into account. In many cases, especially pre-1990 work, the term GPB zones may have been used without sufficient evidence of the actual nature of the structure present.

S″, S′ and S phases

The existence and characteristics of the S″ phase are controversial. Bagaryatsky [52] first proposed a coherent intermediate phase termed S″ phase between GPB zones and S′ phase. Silcock [32] did not observe any structure resembling the S″ phase reported by Bagaryatsky, instead she proposed the formation of GPB2 zones during ageing above 200°C. Later, studies by Cuisiat *et al.* [53], Zahra *et al.* (Al-2.0Cu-1.3Mg (wt.%) alloy) [42], Charai *et al.* (Al-2.0Cu-1.3Mg (wt.%) alloy) [38], Shih *et al.* (Al-3.98Cu-1.38Mg (wt.%) alloy and Al-2.62Cu-1.35Mg (wt.%) alloy) [44], Ratchev *et al.* (Al-0.6Cu-4.2Mg (wt.%) alloy) [40] and Kovarik *et al.* (Al-0.4Cu-3Mg-0.12Si (wt.%) alloy) [54] reported evidence of the existence of S″ phase or GPB2 zones using TEM/SAD or HREM, although different structure models were proposed to interpret the different observed diffraction patterns. On the other hand, Wilson and Partridge (Al-2.5Cu-1.2Mg (wt.%) alloy) [55] and Ringer *et al.* (Al-2.5Cu-1.5Mg (wt.%) alloy) [36, 39] did not observe the presence of the S″ phase. Ringer *et al.* [39] suggested that the diffraction spots assigned to the S″ phase by Zahra *et al.*[42] and Charai *et al.* [38] can actually be interpreted in terms of variants of the S phase. Furthermore Ringer *et al.* [18] pointed out that sample surface contamination by an oxide layer may also lead to the same diffraction spots. However, using ion milling in the final sample preparation step, Kovarik *et al.* [54, 56] showed diffraction data consistent with that of Charai *et al.* [38], and termed the precipitates that give rise to the diffraction spots GPB2. Recently Wang and Starink [57, 58] re-analysed the HREM images and diffraction patterns obtained by Charai *et al.* [38], Ratchev *et al.* [40] and Kovarik *et al.* [54] which were originally attributed to the S″ phase or GPB2. Wang and Starink [57, 58] suggested that the precipitates observed by the above three research groups are the same structure, termed GPB2/S″, and proposed a structure model, which is different from those proposed by Charai *et al.* [38], Ratchev *et al.* [40] and Kovarik *et al.* [54].

It has been generally accepted that the metastable S′ phase and the equilibrium S phase actually are very similar in chemical composition, crystal structure [55] and formation enthalpy [59, 60] and differ only slightly in lattice parameters [61]. Some authors suggest it is unnecessary to make any distinction between these two phases

[33, 61, 62]. Thus in this thesis, they are simply referred to as S phase. The S phase forms as laths along $\langle 100 \rangle_\alpha$ directions on $\{021\}_\alpha$ habit planes. The S phase has the following crystallographic orientation relationship with the matrix [32]:

$[100]_S \,//[100]_\alpha ; [010]_S \,//[021]_\alpha ; [001]_S \,//[01\bar{2}]_\alpha$

The S precipitates generally nucleate heterogeneously on quenched-in dislocation loops and helices [55]. Grain/subgrain boundaries and solute clusters may also constitute nuclei for S formation [38, 48]. Several models [26, 63-65] have been proposed for the crystal structure of S (Al_2CuMg). The unit cell of the Perlitz and Westgren model (PW model) [63] is orthorhombic with space group *Cmcm*, lattice parameters a=0.400 nm, b=0.923nm and c=0.714nm. Mondolfo [26] suggested a modified PW model with slightly different lattice parameters. Jin *et al.* [64] proposed an orthorhombic structure with space group *Pmm2*, lattice parameters *a*=0.4nm, *b*=0.461nm, *c*=0.718nm. Recently, Radmilovic *et al.* [65] and Kilaas *et al.* [66] have re-evaluated the above three models [26, 63, 64] using quantitative HREM and proposed a new model (RKDS model) which is identical to the PW model, but with an exchange of Cu and Mg. Wolverton [67] calculated the formation enthalpy of Al_2CuMg using both the PW and RKDS models. The results support the validity of the XRD-derived PW model.

2.2.3 Age hardening in Al-Cu-Mg based alloys

2.2.3.1 Al-Cu based alloys

Hardy [68, 69] studied systematically the hardness ageing curves of Al-Cu alloys containing 2.0 to 4.5wt.% Cu at ageing temperatures between 30°C and 240°C. **Fig. 2.8** shows the ageing curves for Al-Cu alloys aged at 110°C. It is seen that all alloys except 2.0 wt.% Cu alloy give two-stage age hardening curves separated by a flat hardness plateau. Silcock *et al.* [27] studied the structural changes of precipitates in Al-Cu alloys during the ageing by XRD and correlated these changes with the hardness ageing curves. It was found that the initial rise in hardness is attributed to the formation of GPI zones, and the second rise is mainly due to the precipitation of GPII/θ″ together with a small amount of θ′. The θ′ phase becomes the dominant structure at longer ageing times. The peak hardness in single-stage ageing curves are

attributed either to both GPII/θ″ and θ′ or to the θ′ phase only [27]. At a given stage of the ageing process, two structures can coexist and contribute to the hardening.

2.2.3.2 Al-Cu-Mg based alloys

Age hardening of Al-Cu-Mg alloys within the (α+S) phase field also occurs in two stages, separated by a hardness plateau over a range of ageing temperatures from 110°C to 240°C [7, 9]. As seen in **Fig. 2.9**, the first stage of hardening is a rapid hardness increase which occurs within about 1 min of ageing at 150°C. The rapid hardness increase accounts for approximately 50-70% of the total hardness increase. After this rapid rise, the hardness curve exhibits a long plateau during which the hardness remains constant for several hours until a second stage of hardening towards the peak hardness [33, 36]. Natural ageing of Al-Cu-Mg alloys causes an increase in hardness from the as-quenched value to a plateau value. The rate and extent of the hardening depend on alloy composition [9, 41, 70]. It is thought that the natural hardening and the first stage of hardening in artificial ageing curves are due to the same mechanism [39].

The origin of the age-hardening behaviour in Al–Cu–Mg alloys has been extensively studied. It has been generally accepted that the first stage of hardening and the plateau is attributed to the formation of GPB zones, while the second stage of hardening is mainly attributed to the precipitation of the S phase [7, 32]. Recently, since work on the age hardening of an Al-1.1Cu-1.7Mg (at.%) alloy by means of APFIM, TEM/SAD and HREM failed to reveal the GPB zones until near the end of the hardness plateau, Ringer *et al.*[36] proposed a ‘cluster hardening’ mechanism, related the initial rapid hardening to Cu-Mg co-clusters, and the second hardening to GPB zones. Later, 3DAP data of the same alloy were interpreted to indicate that little or no Cu-Mg co-clusters were present immediately after the first rapid hardening reaction [37, 39]. Based on the observation of additional rapid hardening in the specimen that was first aged for 1min at 150°C to reach the plateau then deformed and re-aged at 150°C, Reich *et al*. [37] suggested that the rapid hardening is caused by a dislocation–solute interaction, i.e. the locking of existing dislocations due to solute atoms segregated to the dislocations. Nagai *et al*. [71] employed Coincidence Doppler

Broadening of positron annihilation radiation (CDB) and positron lifetime spectroscopy techniques to study the vacancies and to identify the solute atoms that are associated with vacancies, i.e. to identify the vacancy-solute complexes in an Al-1.7Cu-1.3Mg (at.%) alloy. They suggested that vacancy–Mg complexes, which formed after quenching, rapidly migrate to vacancy sinks and vacancy–Mg–Cu complexes form along dislocations during the first 1 min ageing at 150°C. As this interpretation of the formation of vacancy–Mg–Cu complexes is difficult to reconcile with the interpretation of 3DAP data given by Reich *et al*. [37] and Ringer *et al*. [18], which reported that little or no Cu-Mg co-clusters form in this early stage, Nagai *et al*. [71] considered that their results support the suggestion proposed by Reich *et al*. [37]. Although the formation of vacancy–Mg–Cu complexes are considered as nucleation sites for coherent clusters and GP zones [72, 73], Ferragut *et al.* [74] pointed out that CDB and positron lifetime spectroscopy results cannot be used to indicate the origin of the rapid early hardening in Al-Cu-Mg alloys because these results only give information on the local chemistry near the positron annihilation sites such as vacancy-containing solute aggregates. Raviprasad *et al.* [75] reported the formation of complex multi-component clusters, enriched in Cu and Mg but also containing Si and Ag, in an Al-2.5Cu-1.5Mg-0.4Ag-0.25Si (wt%) alloy aged at 150°C for 5min by 1DAP analysis. They proposed that clustering of Mg-Cu-(Ag-Si) precedes the formation of the GPB zones and contributes to the initial rapid hardening. Ratchev *et al*. [40] studied the age hardening of an Al-0.6Cu-4.2Mg (wt.%) alloy by HREM and TEM/SAD, and suggested that the initial rapid hardening is caused by both the Cu-Mg co-clusters and the heterogeneous formation of S″ on dislocations. However, HREM results of an Al-1.1Cu-1.7Mg (at.%) alloy aged 5min at 150°C obtained by Reich *et al*. [37] and of an Al-1.7Cu-1.3Mg (at.%) alloy aged 1min at 150°C obtained by Nagai *et al*. [71] have shown that no precipitates are present either in the matrix or along dislocations, indicating that the rapid hardening cannot be caused by heterogeneous precipitation of the S″ phase. Using thermal analysis, Zahra *et al*. [42] insisted that the rapid hardening is due to precipitation of GPB zones, though no direct microstructural evidence for the presence of GPB zones in this stage was reported. Abis *et al*. [41] studied the early stages of precipitation in an Al-4.4Cu-1.7Mg (wt.%) alloy during natural ageing by hardness, DSC and TEM/SAD. Their results showed the presence of the GPB and GP zones with the GPB zones being the

dominating structure. Therefore it was suggested [41] that the classic mechanism [7, 32] should still be accepted, i.e. the initial hardness increase is associated with the formation of GPB zones. More recently, hardness and tensile tests for ageing-deformation-ageing cycles at room temperature have been performed on an Al-1.9Cu-1.6Mg (at.%) alloy [76]. The results indicated that no additional age hardening occurs after deformation. In addition, comparison of DSC curves for freshly solution treated samples aged at room temperature for 5min to one week and hardness ageing curves at room temperature showed that a substantial heat release coincides with the natural hardening. This suggests that the increase in hardness is due to the formation of a pre-precipitate, and a dislocation–solute interaction mechanism appears unlikely. Using 3DAP, Cu-Mg co-clusters were detected in an Al-1.2Cu-1.2Mg (at.%) alloy and an Al-1.9Cu-1.6Mg (at.%) alloy during natural ageing, while no structure that could be assigned to the GPB zones or S phase is detected [49, 51]. The estimated number density of the Cu-Mg co-clusters showed an increase up to about 4-5h at room temperature. This indicates that the natural hardening is due to the formation of Cu-Mg co-clusters.

In summary, the plausible origin of the rapid hardening seems to be a pre-precipitate alternately called GPB zones or Cu-Mg co-clusters. As discussed in Section 2.2.2.2, the distinction between the GPB zones and Cu-Mg co-clusters is not well defined. Following the use of the nomenclature of Cu-Mg co-clusters in Section 2.2.2.2, it is proposed that the rapid hardening is best attributed to Cu-Mg co-clusters.

As for the origin of the second stage of hardening, combined experiments of TEM/SAD, DSC and tensile/hardness tests have been carried out on alloys B and D [46, 47, 77]. The results showed that for samples aged at 190°C for 6h and 12h, which correspond to the peak and slightly overaged stages, a dense dispersion of rod or needle shaped precipitates was observed and these precipitates were identified by SAD as being variants of the S phase (**Fig. 2.10**). For samples aged 12h at 150°C, which corresponds to the onset of the second stage of hardening, TEM revealed only dislocation lines and loops. For samples aged at 150°C for 24h, 48h and 72h, i.e. at the rise to peak strength, faint reflections in the SAD patterns initially indicate the early stages of precipitation of the S phase (150°C/24h); then as the ageing proceeds,

more S precipitates form and a high density of S precipitates is observed. Consistent with the TEM observations, the S phase precipitation effects in DSC curves decrease with ageing time at 150°C, indicating the formation of S phase prior to DSC runs. This experimental evidence clearly supports the generally accepted view that the second stage of hardening is due to precipitation of the S phase. But Ringer *et al.* [36] suggested that it is due to the formation of GPB zones. Further discussion by Wang *et al*. [47] questioned this interpretation and indicated that the peak strengthening is related to the precipitation of S phase regardless of the samples being stretched or not.

It is thought that controversies regarding the origin of the hardening in the literature may partly arise from the use of experimental techniques with different resolutions or different techniques focused on the study of different aspects, and may arise from the investigation of different compositions or from the different interpretations of weak diffraction spots.

2.2.4 Effect of Si on age hardening of Al-Cu-Mg alloys

Trace additions of some alloying elements, such as cadmium, indium, tin, silver and silicon, have a marked effect on the age hardening of aluminium alloys, and therefore are of great importance to improve mechanical properties [7, 18, 78, 79]. Many commercial 2xxx aluminium alloys contain Si and Fe either as impurities or as controlled additions. As the presence of Si and Fe cause the formation of coarse intermetallic compounds (e.g. Mg_2Si, Al_7Cu_2Fe and $Al_{12}Fe_3Si$) which are detrimental to fracture toughness, Si and Fe contents are normally kept to a minimum in commercial aluminium alloys. However, several studies have shown that small additions of Si (at levels of 0.1-0.5 wt%) considerably increase the response to age hardening of Al-Cu-Mg alloys at elevated temperature [7, 9, 79, 80], and the 2618 alloy (Al-2.3Cu-1.5Mg-0.2Si-1.1Fe-1.1Ni (wt.%) alloy) was developed for use at elevated temperature based on this effect. It is reported that the presence of Si raises the ageing curves over the entire time scale, particularly with a noticeable increase in plateau hardness [79, 80]. Microstructural examination using TEM by Wilson *et al*. [55, 79, 81] and by Hutchinson and Ringer [80] revealed that additions of Si suppress the formation of dislocation loops upon quenching and produce a refined dispersion of

S precipitates. TEM images of a Si-free Al-2.62Cu-1.35Mg (wt.%) alloy and a Si-containing Al-3.98Cu-1.38Mg-0.1Si (wt.%) alloy [44] showed that the sizes of the S precipitates are smaller in the Si-containing alloy under the same ageing condition, and this was attributed to the presence of Si. Wilson *et al*. [79] reported long sharp streaks in $<001>_{\alpha}$ directions in the SAD patterns of the Si-containing alloys, whereas these streaks were shorter and more diffuse in the Si-free alloys, and suggested that the GPB zones are more stable in the Si-containing alloys. It is however known that streaks are also determined by the precipitate size. Long sharp streaks may indicate more or larger GPB zones in Si-containing alloys. That implies that GPB zones form earlier and grow larger in Si-containing alloys than those in Si-free alloys. TEM/SAD studies of an Al-2.5Cu-1.5Mg (wt%) alloy show no sign of GPB zones after 1h ageing at 200°C [37], while studies of Al-2.5Cu-1.5Mg-xSi (x=0.1-0.5) (wt%) alloys exhibit characteristic diffraction effects attributed to GPB zones after 5min aged at 200°C [80]. Comparison of these results suggests that the addition of Si accelerates the formation of GPB zones. This is further confirmed by Hirosawa *et al.* [82] on TEM/SAD studies of an Al-1.9Cu-1.7Mg (at%) alloy with and without 0.2Si addition. Contrary to the artificial ageing, the room temperature ageing of Si-containing alloys exhibits a delayed hardening response [79, 80]. The suppressed natural ageing response is understood to be due to the strong binding of the vacancy to the Si atom reducing the free vacancy concentration [79, 80], therefore reducing the rate of the GPB zone formation [79] or the rate of solute diffusion [80].

For enhanced artificial hardening, while attributing the plateau hardness to the GPB zones and the peak hardness to the S phase, Wilson *et al*. [79] suggested that much of the hardness increase results from the improved strength of the GPB zones, although the refinement of the S distribution also strengthens the alloy. Wilson *et al*. [79] further suggested that Si may enter into the structure of the GPB zones, and increases the strains associated with the formation of the GPB zones and also their perfection. Recently, using TEM/SAD, HREM and energy dispersive x-ray spectroscopy, Hutchinson and Ringer [80] showed that the peak hardness is dominated by a very fine and uniform distribution of so-called ‘Si-modified GPB zones’, which is rich in Cu and Mg, and containing a trace of Si. Heterogeneous precipitation of the S phase on dislocation helices was also observed. A refined distribution of S phase, which is

developed at the expense of the GPB zones or nucleated on the GPB zones, was only observed in the overaged Si containing alloys. Hence, Hutchinson and Ringer [80] attributed the enhanced peak hardness to the Si-modified GPB zones, as proposed in [36] for the base ternary Al-2.5Cu-1.5Mg (wt%) alloy. The authors also noted that despite the absence of quenched-in dislocation loops in Si containing alloys, a high density of the quenched-in defects such as dislocation helices remain after 5min at 200°C. They suggested that these defects are available to interact with vacancies and solute atoms, and that this interaction results in the rapid hardening [80]. Also by 1DAP analysis, clustering of Mg-Cu-(Ag-Si) was found in an Al-2.5Cu-1.5Mg-0.4Ag-0.25Si (wt%) alloy aged 5min at 150°C [75, 83], and the presence of Si and Ag within the GPB zones found after ageing for 20h at 200°C in the same alloy has been reported [75]. Based on the recent findings in the literature that the microstructure during the early stages of ageing is associated with co-clustering of solute atoms [18, 37, 45, 49, 84], the accelerated formation of GPB zones may be interpreted in terms of co-clusters of Cu, Mg and Si atoms. It is likely that at elevated temperature Si facilitates formation of GPB zones by forming the Cu-Mg-Si(-vacancy) clusters which either provide nucleation sites for GPB zones or evolve into GPB zones.

Si additions have been shown to stimulate formation of σ phase ($Al_5Cu_6Mg_2$, cubic P3m, a=0.831nm [85]) on overageing in Al-Cu-Mg alloys [75, 79, 80, 86-88]. The σ phase is known to exhibit a low rate of coarsening and have good potential for precipitation strengthening [86, 87, 89]. Stretching between quenching and ageing has been shown to substantially increase the volume fraction of S phase at the expense of σ phase [86, 87]. For example, σ precipitates are observed to form in a non-stretched Al-4.2Cu-1.6Mg-0.2Si (wt%) alloy on overageing, but are absent in the same alloy with a 5% cold stretch prior to ageing [86]. Barlow *et al.* [87] found that σ formation is sensitive to the total solute content of the alloy and to the Cu:Mg ratios. In most alloys where σ phase has been observed, the Si contents are about 0.2-0.5 wt.%, and the Cu:Mg weight ratios are in the range of 1.9 to 2.2. No σ phase was detected in an Al-4.0Cu-0.3Mg (wt%) alloy with Si levels of 0.1 to 1.1 wt.% [90]. However, Gable *et al.* [88] reported the precipitation of σ phase in Al-4.0Cu-0.4Mg (wt%) alloys (Cu:Mg ratio equals 10) with Si content as low as 0.1wt.% when aged at 250°C for 30 min and 2h. Mukhopadhyay [91] reported the precipitation of σ phase in the matrix

and on the Mn-containing dispersoids in two non-stretched 2024 type alloys with added Ag and Si: Al-5.0Cu-1.5Mg-0.7Mn-0.4Ag-0.7Si-0.13Fe (wt.%) alloy and Al-4.2Cu-1.5Mg-0.7Mn-0.4Ag-0.07Si-0.13Fe(wt.%) alloy. σ precipitation is very limited in the latter low-Si alloy and occurs on dispersoids only. Mukhopadhyay [91] concluded that nucleation of σ phase requires a critical minimum supersaturation of Si in the solid solution, and pointed out that several constituent phases and dispersoids dissolve Si thereby considerably reducing the Si supersaturation. However this cannot explain the presence of σ phase in the low-Si alloy. It is suggested that Ag may have a similar effect as Si on the precipitation of σ phase since σ phase was observed in an Al-4.0Cu-0.45Mg-0.4Ag (wt.%) alloy aged at 200°C [92].

2.3 Modelling of microstructure evolution

This work focuses on the modelling of the yield strength in Al-Cu-Mg based alloys based on microstructure evolution using a physically based approach. Physically based models quantitatively describe the nature of a process by mathematical constitutive equations based on a sound physical understanding of the underlying mechanisms [93, 94]. A complete physically based model without any adjustable parameter is only possible if a detailed understanding of the underlying mechanisms is established and if model parameters are accurately known. Obviously this only applies to idealised conditions. Realistic materials problems are complex and many models have an empirical component within a physical framework [93, 94]. For example, the modelling of phase transformation kinetics using the JMAK equation or Starink-Zahra equation (see Section 2.3.2.3 and 2.3.2.4 below) has its basis in statistical theory. The activation energy can sometimes be predicted from molecular models with useful accuracy, but the value of the pre-exponential factor must be inserted empirically [93]. Therefore, before it can be applied to make predictions, the model needs to be calibrated against a subset of experimental data to determine the unknown physical parameters, and then validated by comparing the predictions with experimental data to check the predictive power of the model. Here of particular importance is the accuracy of the data used to calibrate or validate a model.

To derive the equations which relate the microstructure to strength, a basic understanding of how microstructure develops, and how the microstructural features influence the motion of dislocations and affect the strength is required. Thus the model basically consists of two components: a microstructure model and a structural hardening model. Models for microstructure evolution usually consist of a thermodynamic model for prediction of stable or metastable solvus and a kinetic model for prediction of the fraction transformed as a function of time and temperature. The latter two types of models will be discussed in the following two sections.

2.3.1 Modelling of precipitation thermodynamics

Obtaining reliable phase diagram data is a prerequisite for kinetic and property modelling [95]. The stability of the precipitate is represented by its solvus, or solubility curve. As mentioned in Section 2.2.1, the equilibrium solvi of stable phases at desired temperatures and the solvi of metastable phases are not always available. The CALPHAD (**Cal**culation of **Pha**se **D**iagrams) technique was developed to meet such requirements, using the Gibbs free energy minimization method to calculate the thermodynamic phase diagram [96, 97]. For example, thermodynamic assessment of the Al-Cu-Mg ternary system has been made [98, 99]. However, success of thermodynamic modelling relies on the availability of the relevant high quality thermodynamic databases, and such databases are often expensive and proprietary. Also application requires a substantial programming effort. This is not within the aims of the present study.

Most industrial Al-Cu-Mg alloys are sufficiently dilute to allow a regular solution model to be applied to calculate the solubility of precipitates in the Al-rich corner of the phase diagram [60, 100, 101]. The regular solution model can be described as follows.

For a precipitate phase with a fixed stoichiometry of $M_m A_x B_y$ where M is the main constituent of the alloy, A and B are the alloying elements, a precipitation/dissolution reaction at a given temperature can be represented by:

$$M_m A_x B_y \Leftrightarrow mM + xA + yB$$

At equilibrium, the equilibrium constant K (also called the solubility product for a reaction at equilibrium between a solid solution and a compound), is given by the following expression:

$$K = (a^A)^x (a^B)^y \tag{2.2}$$

Where a^A and a^B are the activities of elements A and B. For an ideal solution or a sufficiently dilute regular solid solution, the activities can be replaced by the molar equilibrium concentrations c_e^A and c_e^B, i.e. the solubility limits of the elements in the solid solution. It is noted that pure solids (e.g. the compounds) and the matrix are not included in the solubility product equation because their activities or concentrations all equal to one.

From a relationship between the standard Gibbs free energy of reaction ΔG^o and the solubility product K:

$$\Delta G^0 = \Delta H^0 - T\Delta S^0 = -RT \ln K \tag{2.3}$$

It follows:

$$\ln(a^A)^x (a^B)^y \cong \ln(c_e^A)^x (c_e^B)^y = -\frac{\Delta H^0}{RT} + \frac{\Delta S^0}{R} \tag{2.4}$$

Where ΔH^0 is the standard enthalpy of reaction and ΔS^0 is standard entropy of reaction. R is the universal gas constant and T is the absolute temperature. This equation shows that a plot of the logarithm of the solubility product versus (1/T)

should result in a straight line. This is observed for aluminium alloys, e.g. Eq.(2.1) [19, 101]. By rearranging the above equation, the following equation used for the calculation of the solvus of $M_m A_x B_y$ is obtained:

$$(c_e^A)^x (c_e^B)^y = c_1 \exp(\frac{-\Delta H}{RT}) \tag{2.5}$$

where the symbol ΔH is used to replace the symbol ΔH^0 for simplicity and c_1 is a constant accounting for the entropy term. If appropriate values for ΔH or c_1 can be derived from available solubility data [60, 102], the solvus of the precipitate phase as a function of temperature can be estimated. Meanwhile the following relationship exists between the stoichiometry of the phase of the type $M_m A_x B_y$ and the compositions and the solubility limits of the phase:

$$c_e^A = c_0^A - \frac{x}{y}(c_0^B - c_e^B) \tag{2.6}$$

where c_0^A and c_0^B are the initial concentration of the alloying elements dissolved in the matrix. Combining Eq.(2.5) and (2.6), the stable and metastable equilibrium solute concentration in the matrix c_e^A and c_e^B can therefore be determined by the point of intersection of the solvus line and the line described by the latter equation.

2.3.2 Modelling of precipitation kinetics

Precipitation from a supersaturated solid solution is a diffusion controlled reaction, which usually involves three processes: nucleation, growth and coarsening. Phase transformation via nucleation and growth is driven by the reduction in free energy, while the coarsening of precipitates is driven by the reduction in the total interfacial energies between the particles and the matrix [103-105]. Since many of the technologically important properties, such as the strength, toughness, fatigue, creep, *etc.* are essentially controlled by the presence of precipitate particles, which result from the precipitation from a supersaturated solid solution, modelling of precipitation

kinetics has always been the subject of intensive research in physical metallurgy. Combined with the thermodynamic model for the solvus, the kinetic model can provide the information about the variation of microstructure parameters (such as volume fractions and sizes of the precipitates, remaining solute concentration in solid solution) with ageing time and temperature. A number of theoretical models for precipitation kinetics have been developed since the 1930s [103-111]. In this section, the classical models for three separate regimes: the nucleation regime, the growth regime and the coarsening regime are introduced, and subsequently the published integrated, multi-regime kinetic models are reviewed. In terms of solving approaches, these integrated models are classified into two kinds: one is models with numerical solutions; the other is models with analytical solutions.

2.3.2.1 Classical models for the nucleation regime, growth regime and coarsening regime

The classical precipitation kinetic theories treat the course of precipitation as consecutive processes by splitting it into a nucleation regime, a growth regime and a coarsening regime. The well-known modelling of homogeneous precipitation by a classical nucleation and growth mechanism is shown in the following sections.

The nucleation regime

In the nucleation stage, nuclei of the precipitates form as a result of localised compositional fluctuations that occur statistically within the supersaturated matrix. The steady state nucleation rate is expressed as [106]:

$$\frac{dN}{dt} = N_0 Z\beta^* \exp\left(-\frac{\Delta G^*}{RT}\right) \tag{2.7}$$

where N is the precipitate density, N_0 is the number of atomic nucleation sites per unit volume ($\cong 1/V_{at}$) and ΔG^* is the activation energy barrier for homogeneous nucleation. Z is the Zeldovich non-equilibrium factor (in the order of 1/20 to 1/40) to take account of the probability of dissolution of supercritical nuclei. β^* is the frequency factor, i.e.

the rate at which solute atoms impinge upon the critical nuclei. For spherical particles, the expressions for ΔG^*, Z and β^* have been provided as follows [112]:

$$\Delta G^* = \frac{16\pi\gamma^3}{3\Delta F_v^2} = \frac{4}{3}\pi r^{*2}\gamma \tag{2.8}$$

$$Z = \sqrt{\frac{\Delta G^*}{3\pi k_B T}} \frac{V_{at}}{\frac{4}{3}\pi r^{*3}} \tag{2.9}$$

$$\beta^* = \frac{4\pi r^{*2} Dc}{a^4} \tag{2.10}$$

where γ is the interfacial energy, ΔF_v is the driving force per unit volume for precipitation, k_B is the Boltzman constant, V_{at} is the atomic volume, r^* is the critical radius for nucleation, c is the atomic concentration of solute in the matrix and a is the lattice parameter of the precipitate. D is the diffusion coefficient of solute atoms in the matrix, which can be expressed by an Arrhenius relation:

$$D(T) = D_0 \exp(-\frac{Q_d}{RT}) \tag{2.11}$$

Where Q_d is the activation energy for diffusion and D_0 is the pre-exponential factor.

The growth regime

For diffusion-controlled growth of nuclei, in the case of plate-like or spherical precipitates, a flux balance at the particle/matrix interface gives the following equation for the growth/dissolution rate [106]:

$$\frac{dr}{dt} = \frac{c - c_r}{c_p - c_r}\frac{D}{r} \tag{2.12}$$

where r is the radius of a spherical precipitate, c is the instantaneous solute concentration in the matrix, c_r is solute concentration at the particle/matrix interface, c_p is equilibrium solute concentration of precipitate.

For dilute solid solution, according to the Gibbs-Thomson equation, the curved particle/matrix interface solute concentration c_r varies with the interfacial energy γ and local curvature by:

$$c_r = c_e \exp\left(\frac{1-c_e}{c_p-c_e}\frac{2\gamma V_m}{RTr}\right) \tag{2.13}$$

where r is the equivalent radius describing the local curvature, c_e is the equilibrium solute concentration at the flat particle/matrix interface and V_m is the molar volume of the precipitate. This effect is often referred to as capillary effect or Gibbs-Thomson effect. The results obtained from the integration of Eq.(2.12) under some simplifying assumptions show that both the half-thickness of the plate and the radius of a spherical precipitate grow with time according to a parabolic growth law as: $r = k(Dt)^{1/2}$ [106], where the rate constant k increases with the increasing supersaturation.

The coarsening regime

Coarsening of the precipitates occurs by the growth of large precipitates at the expense of small ones. This process is driven by a reduction in the total interfacial energy. The classical theory of coarsening was developed based on the Gibbs-Thomson equation by Lifshitz and Slyozov [113] and Wagner [114], the so-called LSW theory. Assuming the precipitated volume fraction f is close to zero, i.e. the system is highly diluted and the particle interactions are ignored; and the precipitated volume fraction f is close to its equilibrium value, i.e. the precipitation is close to completion and thus the supersaturation is close to zero, the LSW theory predicts that during coarsening the average radius of spherical precipitates increases according to:

$$\bar{r}^3 - \bar{r}_0^3 = k_c t \tag{2.14}$$

where $\bar{r}$ is the average radius of the precipitates, $\overline{r_o}$ is the initial average radius of the precipitates at the start of coarsening and k_c is the rate constant for coarsening, which depends on temperature, the interfacial energy and the diffusion coefficient of precipitates as follows:

$$k_c = \frac{8}{9}\frac{V_m \gamma D c_e}{RT} \tag{2.15}$$

Several approximations made in deriving the above equation confine the validity of the LSW theory to the late stages of a precipitation reaction in dilute systems. Efforts have been made to extend the LSW theory to the case of finite volume fraction [106, 115, 116]. They all came to the same $\bar{r}^3 \propto t$ kinetic behaviour, but predicted the coarsening rate constant to increase, and the particle size distribution to flatten and to broaden with increasing volume fraction. Considering that the particles interact through their diffusion fields at finite volume fractions, the growth rate of an individual particle will depend on the details of its local environment. The competition among particles leads to an increase in the coarsening rates and thus a broader particle size distribution.

2.3.2.2 Models with numerical solutions for nucleation, growth and coarsening

The kinetic models described in Section 2.3.2.1 are usually restricted to idealized situations, which may differ from the real situation to varying extents. For a more practical description of homogeneous precipitation kinetics, one has to consider simultaneous nucleation, growth and coarsening stages of precipitation, which requires a full description of the particle size distribution. Langer and Schwartz [117] devised a numerical approach (LS model) which treated the nucleation, growth and coarsening as concomitant rather than consecutive processes. They calculated the evolution of particle size distributions in near critical fluids, accounting for supersaturation, nucleation of new particles and capillary effect. This treatment was

modified by Wendt and Haasen [118] and further improved by Kampmann and Wagner [119] (so-called modified LS model, i.e. MLS model).

Recently, based on the methodology of LS & MLS model, several precipitation kinetic models integrating nucleation, growth and coarsening in diluted alloy systems have been developed [108-111, 120-123]. By using classical kinetic equations, i.e. Eq.(2.7) to Eq.(2.13), these approaches calculate the evolution of volume fraction and particles with size distributions through the nucleation, growth and coarsening stages in discrete time steps, tracking the growth of a large number of different sized particles simultaneously and therefore require numerical solving. In this way, precipitate coarsening is implicitly embedded in the growth equation, i.e. Eq.(2.12), and occurs naturally as a result of the influence of precipitate curvature on the local composition at the particle/matrix interface (i.e. Gibbs-Thomson effect, which means that the equilibrium solute concentration in the solid solution at the curved particle/matrix interface differs from that of a flat interface, see Eq.(2.13)). These approaches predict the coarsening behaviour of precipitates and particle size distributions similar to the LSW theory.

These models treat the three stages simultaneously and are able to accurately describe the entire course of precipitation within the framework of classical nucleation and growth theories. The main advantage of this technique is that the traditional regimes of growth and coarsening arise as a natural consequence of changes in composition and driving forces during precipitation. A disadvantage of these iterative methods is that the basic relations between volume fraction/average precipitate size and heat treatment parameters (ageing time and temperature) are often difficult to assess, thus making inverse predictions from mechanical properties to compositions and heat treatments difficult to achieve [93].

2.3.2.3 Models with analytical solutions for nucleation and growth

The kinetics of isothermal transformations that proceed via nucleation and growth are often described by the classical Johnson-Mehl-Avrami-Kolmogorov (JMAK) model, which assumes random nucleation and uniform growth [103, 124-128]. The validity

of this approach was confirmed for the case of linear growth [129, 130]. The JMAK model is based on the so-called 'extended volume' concept which is the volume that new nuclei would occupy in the absence of impingement and overlap of adjacent transformed nuclei. Based on the assumption that the nuclei are randomly distributed in space, Avrami [103, 126] reasoned that the change in the actual transformed volume V_t, and that of the extended volume V_e are related by:

$$dV_t = (1 - \frac{V_t}{V})dV_e \tag{2.16}$$

where V is the total volume. This relation can be understood as follows: consider at time t a fraction of $(1\text{-}V_t/V)$ remains untransformed. During a further time dt, the extended volume will increase by dV_e and the actual volume by dV_t. Of the dV_e, a fraction of $(1\text{-}V_t/V)$ will lie in the previously untransformed region and thus contribute to dV_t, while the remainder of dV_e will be in already transformed region. That is, dV_e is proportional to V while dV_t is proportional to $(V\text{-}V_t)$ [131]. Introducing the fraction transformed $\alpha=V_t/V$, and the extended fraction transformed $\alpha_{ext}=V_e/V$, the above equation is equivalent to:

$$\frac{d\alpha}{d\alpha_{ext}} = 1 - \alpha \tag{2.17}$$

which results in the general expression:

$$\alpha = 1 - \exp(-[k(T)t]^n) \tag{2.18}$$

where n is the so-called Avrami exponent that is indicative of the transformation mechanism [103, 132] and $k(T)$ is temperature-dependent rate constant which can be expressed by an Arrhenius relation:

$$k(T) = k_0 \exp(-\frac{E_{eff}}{RT}) \tag{2.19}$$

where E_{eff} is the effective activation energy for isothermal nucleation and growth and k_0 is a pre-exponential constant. Eq.(2.18) can also be written as:

$$\ln[-\ln(1-\alpha)] = n\ln t + \ln k(T) \tag{2.20}$$

Thus the Avrami exponent n can be evaluated from the slope of the plot of ln[-ln(1-α)] against ln$t$.

In general, the JMAK equation is only valid for isothermal and linear growth kinetics under most circumstances and approximately valid for the early stages of diffusion-controlled precipitation reactions, i.e. at small fraction transformed, so its general application to all nucleation and growth reactions and to non-isothermal reactions is not justified [132, 133].

For a better description of diffusion-controlled precipitation reactions, Austin and Rickett [134] proposed a kinetic equation (AR equation):

$$\alpha = 1 - \left\{\left[k(T)t\right]^n + 1\right\}^{-1} \tag{2.21}$$

It has been shown that the AR equation is more appropriate in interpreting data of precipitation reactions than the JMAK equation [132, 135]. Thus to obtain a general kinetic equation, an impingement parameter is introduced to Eq.(2.17) [135]:

$$\frac{d\alpha}{d\alpha_{ext}} = (1-\alpha)^{1+c} \tag{2.22}$$

where c is an "impingement parameter", c=0 corresponds to JMAK equation, whilst c=1 corresponds to the AR equation.

Recently, Starink and Zahra proposed a general equation for diffusion-controlled precipitation reaction (SZ model) [107, 136, 137], and applied it to isothermal and non-isothermal transformations in age-hardening Al-based alloys [107, 136, 138-141]. The validity of the SZ model has been tested by a comparison between the predictions

and experimental isothermal calorimetry and DSC results, and excellent agreement between experiments and model was obtained. The SZ model incorporates both the JMAK and the AR model, takes the impingement into account, and has been proven to be better than JMAK model and AR model for diffusion-controlled precipitation kinetics. **Fig. 2.11** shows the comparisons of the normalised experimental heat flow for an Al-6.8at.% Zn alloy isothermally aged at 130°C with three fits using three kinetic equations. It is seen that the SZ kinetics is more accurate than the other two models especially at longer times. As this model will be adopted to describe the time evolution of volume fraction of precipitates in the present modelling work, a brief description of this model is given below in Section 2.3.2.4.

Comparing the models described in this section (JMAK, AR and SZ model) with the models mentioned in Section 2.3.2.2, the main advantage is that they provide approximate but adequate description of the phase transformations involving coupled nucleation and growth using analytical solutions. A drawback is that these models do not account for a further evolution of the precipitate size distribution with ageing time, hence they cannot describe the coarsening process.

2.3.2.4 Starink-Zahra model [107, 136]

Similar to the JMAK model, the transformation is described using the so-called 'extended volume' concept. By retaining the JMAK formalism, i.e. Eq.(2.17), and introducing an adjustable impingement parameter λ_i, a general kinetic equation is given as:

$$\frac{d\alpha}{d\alpha_{ext}} = (1-\alpha)^{\lambda_i} \tag{2.23}$$

where α is the fraction transformed and α_{ext} is the extended fraction transformed. The general solution of Eq.(2.23) for $\lambda_i \neq 1$ is:

$$\alpha(T,t)=1-\left(\frac{\alpha_{ext}}{\eta_i}+1\right)^{-\eta_i} \tag{2.24}$$

with the impingement exponent $\eta_i = 1/(\lambda_i-1)$. It is noted that the JMAK limit ($\eta_i \to \infty$) as well as the AR model ($\eta_i = 1$) is included.

The extended transformed fraction, α_{ext}, is given by [138]:

$$\alpha_{ext} = \int_0^t A_1 I(z)\left[G(t-z)\right]^m dz \tag{2.25}$$

where G is the growth rate, I is the nucleation rate, A_1 is a constant, z is the time at which the nucleus is formed and m is a constant related to the dimensionality of the growth and the mode of transformation, e.g. for diffusion-controlled growth in 3 dimensions, m=3/2. Both the growth rate and the nucleation rate can often be approximated by Arrhenius type dependencies:

$$G = G_0 \exp(-\frac{E_G}{RT}) \tag{2.26}$$

$$I = I_0 \exp(-\frac{E_N}{RT}) \tag{2.27}$$

where E_G and E_N are the activation energy for growth and for nucleation, respectively. G_0 and I_0 are constants. Under isothermal condition, the integral of Eq.(2.25) yields:

$$\alpha_{ext} = \frac{A_1}{m+1} I_0 G_0^m \exp(-\frac{E_N + mE_G}{RT}) t^{m+1} \tag{2.28}$$

Alternatively, for isothermal paths, the nucleation rate I will generally be constant or zero (so-called "site saturation"), for both cases a single general expression for the extended fraction can be derived [132]:

$$\alpha_{ext} = [k(T)t]^n \tag{2.29}$$

where n is the reaction exponent or Avrami exponent related to the dimensionality of the growth and the mode of transformation [103, 132], $k(T)$ is a temperature dependent factor determined by A_1, G and I, which can be expressed by an Arrhenius relation:

$$k(T) = k_0 \exp(-\frac{E_{eff}}{RT}) \tag{2.30}$$

The explicit expressions for n, E_{eff} and k_0 in Eqs. (2.29, 2.30) are obtained following Eq.(2.25) to Eq.(2.30), see **Table 2.4**.

For linear heating paths, α_{ext} can be approximated very accurately as [107, 136]:

$$\alpha_{ext} \cong \left(\frac{\beta R}{E_G} k_n \exp\left[\frac{-E_{eff}}{RT} \right] \left(\frac{T}{\beta} \right)^2 \right)^s \tag{2.31}$$

where

$$E_{eff} = \frac{mE_G + E_N}{m+1} \tag{2.32}$$

$$s = m + 1 \tag{2.33}$$

where β is the heating rate, k_n is a constant and s is the reaction exponent that corresponds to the reaction exponent n for isothermal transformation. It should be noted that the derivation of Eq.(2.31) is based on the assumptions that both the growth rate and the nucleation rate can be approximated by Arrhenius type dependencies, thus Eq.(2.31) is a good approximation which is valid if $E_N \approx E_G$, i.e. the driving force for the formation of nuclei is relatively large.

In summary, the SZ model includes three kinetic parameters: the reaction exponent n or s, which depends on the nucleation and growth mechanisms; the rate constant $k(T)$

which is an exponential Arrhenius type function depending on the effective activation energy, and the impingement exponent η_i which describes the impingement process.

2.4 Modelling of yield strength

2.4.1 Major mechanisms of strengthening

The introduction of dislocation theory in the 1930's provided a key step in the understanding of the hardening of metallic alloys. It is now well established that the strength of the metals is essentially due to the interaction between moving dislocations and obstacles. Due to the presence of the obstacles which reduce the mobility of dislocations, greater mechanical forces will be required to initiate plastic deformation, and thus the material will be harder. Precipitates, dispersoid particles, solute atoms, other immobile dislocations and grain boundaries are all effective obstacles to dislocation glide. The strengthening mechanisms for Al-based alloys are thus basically ascribed to five mechanisms: 1) precipitation strengthening, 2) dispersion strengthening, 3) solution strengthening, 4) work hardening (dislocation hardening) and 5) grain and subgrain strengthening.

For heat treatable Al-based alloys, the strength is enhanced mainly via precipitation strengthening. The precipitates act as the most effective obstacles to impede the movement of dislocations by various dislocation-obstacle interaction mechanisms. In terms of the specific obstacle strength, Kelly and Nicholson [12] distinguished between the "cutting" or "shearing" mechanism for "weak" shearable obstacles and "looping" or "bypassing" mechanism for "strong" non-shearable ones. Generally, in the early stages of age hardening when the precipitates are small and coherent with the matrix, such as GP zones, they may be sheared by moving dislocations. As ageing proceeds, the precipitates gradually lose their coherency with the matrix, they are large and widely spaced and cannot be cut. In these conditions, the moving dislocations have to bypass the precipitates and rejoin via the so-called Orowan looping mechanism [142]. The shearable precipitates may strengthen the alloys via a variety of interaction mechanisms including [14, 143, 144]:

1) chemical hardening, which results from the additional matrix-precipitate interface created by the dislocation shearing through a coherent particle;
2) stacking-fault hardening, which occurs when the stacking-fault energies of the precipitate and matrix differ substantially;
3) modulus hardening, which occurs when the shear moduli of the precipitate and the matrix differ;
4) order hardening, which occurs when a matrix dislocation shears a coherent ordered particle and creates an antiphase boundary on the slip plane within the precipitate phase;
5) coherency hardening, which results from the elastic interaction between the strain fields of the dislocations and a coherent precipitate whose lattice parameter differ from that of the matrix.

2.4.2 Models for the critical resolved shear stress and yield strength

Generally the solutions for structural hardening involve models for the interaction between hardening obstacles and dislocations, and the statistical summation of these individual interactions [145]. The quantitative models for the yield strength in age-hardened alloys date back to the pioneering work of Mott and Nabarro [146], Orowan [142] and the early review of Kelly and Nicholson [12]. When a glide dislocation encounters one of the obstacles in a random array, the critical resolved shear stress (CRSS), $\Delta\tau$, required to break the obstacle is [10, 143]:

$$\Delta\tau = F_m / bL \tag{2.34}$$

where b is the magnitude of the Burgers vector, L is the effective obstacle spacing in the slip plane along the bending dislocation and F_m is the maximum force exerted by the obstacle, i.e. the obstacle strength. **Fig. 2.12** shows the gliding dislocation bowing out between the obstacles in which Γ is the dislocation line tension and ψ_c is the breaking angle for a gliding dislocation to overcome the obstacles. F_m is related to Γ by:

$$F_m = 2\Gamma \cos\frac{\psi_c}{2} \tag{2.35}$$

When the breaking angle ψ_c=0, the particle behaves as a non-shearable obstacle, while for values of ψ_c>0, the particle can be sheared by the glide dislocation.

In order to correlate the precipitate microstructure with the increase in yield strength (YS) or critical resolved shear stress (CRSS), i.e. to model the CRSS as a function of the relevant precipitate parameters (volume fraction of the precipitate *f* and precipitate size *r*), the theoretical approach involves two steps:
1) the determination of the specific obstacle strength F_m, which is derived from the detailed mechanisms of the dislocation-obstacle interaction;
2) the estimation of the effective obstacle spacing *L* by statistical methods.
The approach had been used by Brown and Ham [143], Ardell [14], Nembach and Neite [147], Reppich [144] and Nembach [148] to derive equations for the CRSS.

For a dislocation interacting with a random array of particles in the slip plane, classical analysis using point-obstacle approximation of Friedel statistics shows the increment in CRSS is [10, 14, 144]:

$$\Delta\tau = \frac{F_m^{3/2}}{(2\Gamma)^{1/2} bL_s} \tag{2.36}$$

Where L_s is the average planar spacing of particles in the slip plane. For strong obstacles, F_m=2Γ, and $\Delta\tau$ becomes:

$$\Delta\tau = \frac{2\Gamma}{bL_s} \tag{2.37}$$

Which is the basis of the Orowan equation [142]. By calculating the specific obstacle strength F_m and choosing the average planar spacing L_s in Eq. (2.36), equations for the CRSS can be derived. **Table 2.5** lists the expressions for the CRSS of various strengthening mechanisms based on the point-obstacle approximation of Friedel

statistics for the dislocation–obstacle interaction. As seen from Table 2.5, the increment in CRSS due to the presence of the shearable particles is generally proportional to $(fr)^{1/2}$ except that for chemical hardening which predicts that the CRSS decreases as the particle size increases. The increment in CRSS due to the presence of the non-shearable particles is proportional to $\sqrt{f}/r$ [10, 14, 144].

In order to make comparison with measured yield strength obtained from tensile tests, the calculated microstructure-based critical resolved shear stress of a grain must be converted to equivalent uniaxial macroscopic yield strength of a polycrystalline material. Several models for the plastic deformation of polycrystals have been proposed to relate the macroscopic yield strength of a polycrystalline material to the CRSS of the grains [149-151]. Generally, the yield strength of a polycrystalline material, σ_y, is related to the CRSS increment, $\Delta\tau$, of the grains as follows:

$$\sigma_y = M\Delta\tau \tag{2.38}$$

where M is a constant which has been termed the Taylor factor. For a texture-free polycrystalline material, M ranges between a lower bound of 2.24 given by the Sachs model to an upper bound of 3.07 given by the Taylor model [3, 152]. In the Sachs model it is assumed that there is only one active slip system in each grain and that this system is the one with the highest Schmid factor. This leads to different strains in the different grains. In texture-free fcc materials the Sachs model gives M=2.24. In the Taylor model it is assumed that all the grains in the material deform uniformly. This is obtained by multiple slip, in each grain there are at least five active slip systems. In texture-free materials the Taylor model gives M=3.07. Work on self-consistent modelling of deformation of texture free polycrystalline aluminium indicates that on average about 3.5 slip systems are activated per grain and this leads to an intermediate value M=2.6 [149]. The average Taylor factor can be experimentally calculated from textures by the analysis of pole figures and orientation distribution functions (ODFs) which are obtained from electron backscatter diffraction (EBSD) [153] or from x-ray diffraction techniques [154].

2.4.3 Superposition of strengthening mechanisms

Materials are often simultaneously strengthened by various types of obstacles, e.g. different types of precipitates, various solute atoms and grain boundaries. Thus the total CRSS, $\Delta\tau_{tot}$, will be a superposition of different strengthening contributions. Various addition rules have been proposed [14, 143]. The most common expression is the linear addition law used in the case when a few strong obstacles are mixed with many weak obstacles:

$$\Delta\tau_{tot} = \sum_i (\Delta\tau_i) \tag{2.39}$$

The second expression is the root-mean-square addition law (or the so-called Pythagorean addition law) used in the case when the obstacles are of similar strength but may differ in their number density:

$$(\Delta\tau_{tot})^2 = \sum_i (\Delta\tau_i)^2 \tag{2.40}$$

Since no generally accepted model for the superposition of various obstacles of different strengths is available, an empirical relation is used:

$$(\Delta\tau_{tot})^q = \sum_i (\Delta\tau_i)^q \tag{2.41}$$

where the exponent q is between 1.0 and 2.0, depending on the ratio of the strengths of the obstacles and is usually treated as a parameter adjustable to fit the experimental data [147, 148, 155]. For a superposition of two obstacles, high values of q suppress the effect of the smaller one of the two CRSS increments $\Delta\tau_1$ and $\Delta\tau_2$. The higher q is, the closer is $\Delta\tau_{tot}$ to the larger one of $\Delta\tau_1$ and $\Delta\tau_2$. q=1 has been justified theoretically by Kocks *et al.* [145] and by Foreman and Makin's computer simulations [156] for two types of obstacles that differ strongly in their strength and number density. q=2 has been justified theoretically by Hanson and Morris [157] and by Foreman and

Makin's computer simulations [156] for two types of obstacles that are of similar strength.

A different type of rule of mixing as below has been introduced by Brown and Ham [143]:

$$\Delta\tau_{tot} = n_1^{1/2}\Delta\tau_1 + n_2^{1/2}\Delta\tau_2 \tag{2.42}$$

Where n_1 and n_2 correspond to the density fractions of two types of particles. Ardell [14] further proposed an equation which combines Eq.(2.41) and Eq.(2.42):

$$\Delta\tau_{tot}^{q} = n_1^{q/2}\Delta\tau_1^{q} + n_2^{q/2}\Delta\tau_2^{q} \tag{2.43}$$

The latter equation provides better agreement with the results of computer simulations of Foreman and Makin [156]. Using Eq.(2.43), Zhu *et al.* [158] determined the CRSS due to a mixture of two different particles by computer simulation of a dislocation passing through a random distribution of two types of particles. By comparison of the total strengthening effects due to the mixture of θ′, T_1 and δ′ obtained by computer simulation, by tensile tests and by calculation using Eq.(2.41), Zhu *et al.* indicated that the total strengthening effect can be well described by Eq.(2.43) and suggested that the computer simulation can be used to determine the value of q which varies between 1.0 and 2.0 [158].

Due to the difficulties in quantitative characterization, only very few experimental studies have been carried out to find out the value of q for the superposition of different obstacles. Huang and Ardell [154] showed that for the superposition of T_1 and δ′ strengthening contributions in Al–Li–Cu alloys using Eq.(2.41), where the total strengthening contribution due to both T_1 and δ′ particles and contribution due to T_1 particles had been extracted experimentally, q=1.4 gave the best agreement between the CRSS of δ′ precipitates obtained from Eq.(2.41) and the calculated CRSS of δ′ precipitates obtained from an order hardening model. Since there were two adjustable parameters in the calculation, i.e. q and the antiphase boundary energy, the criterion

for choosing the best values of q is that the antiphase boundary energy must be identical for two different alloys studied. For the superposition of solution strengthening due to dissolved atoms $\Delta\tau_s$ and order strengthening due to $Ni_3(Al,Ti)$ type γ' precipitates $\Delta\tau_p$ in a nickel based superalloy using Eq.(2.41), Nembach and Neite [147] derived from experimental CRSS data that q equals 1.23 for underaged and peakaged single crystal specimens. The derivation of q is based on the different temperature dependences of the total CRSS $\Delta\tau_{tot}$, $\Delta\tau_s$ and $\Delta\tau_p$, where $\Delta\tau_{tot}$ is the actually measured CRSS, $\Delta\tau_s$ can be calculated via the measured overall atomic fraction of solute atom and $\Delta\tau_p$ is known [147, 148, 155, 159]. The important point in this experimental derivation of q is that the procedure involves neither the radius nor the volume fraction of the precipitates. Even though the values of q were derived by the above methods, no convincing physical justification can be given and the values should still be considered as empirical ones [155]. In conclusion, any superposition law has yet to be verified by reliable and conclusive experiments.

2.5 Integrated models for yield strength

With respect to the modelling of the yield strength based on the microstructure development of aluminium alloys, the elementary mechanisms governing microstructural evolution as well as structural hardening are now reasonably well understood, and constitutive equations for these components can be obtained from well-established sources [14, 103, 106, 144]. Hence there is a need for developing integrated strength models to couple these components and provide a detailed and continuous description of strengthening in precipitation-hardened alloys. During the last fifteen years, various age hardening models, based on thermodynamics, kinetics and dislocation mechanics, have been developed to model complex relations between microstructural changes, mechanical properties and industrial processes *etc*. for wrought aluminium alloys. Among these models, the process model developed by Shercliff and Ashby [160] provides a simplified framework for overall strength modelling of age hardening Al alloys.

The Shercliff-Ashby model assumed a single type of precipitate in binary or pseudo-binary alloy systems, applied JMAK kinetics to describe the time dependent volume

fraction of precipitate, and applied classical LSW coarsening theory to describe the time evolution of the average particle radius. As for the yield strength, three contributions to the strength were added linearly: the intrinsic strength of the matrix (which included the contributions of grain boundaries and cold working), the solid solution contribution and the precipitation strengthening contribution; with the latter being calculated by simply taking the harmonic mean of shearable and non-shearable precipitate strengthening contributions. In this way, this model incorporated established physical models for the precipitation kinetics and the relationship between the microstructure and the strength of the alloy, providing a reasonable description of the ageing behaviour of some 2xxx Al-Cu alloys and 6xxx Al-Mg-Si alloys. However this model simply applied the LSW coarsening theory to the complete ageing process in which precipitation usually involves nucleation, growth and coarsening processes, and did not provide a description for the evolution of the average particle radius in the nucleation and growth stages. Thus this model was only accurate for alloys in an overaged condition (**Fig. 2.13)**. Following the approach of the Shercliff and Ashby model, a yield strength model for casting alloys was presented [161]. Several authors have made modifications to the Shercliff and Ashby model for instance by taking account of compositional variations in 7xxx Al-Zn-Mg-Cu alloys [162, 163] or by considering the effect of non-isothermal two step ageing treatments and the level of pre-deformation in 7xxx Al-Zn-Mg-Cu alloys [164, 165].

Deschamps and Brechet [108] developed a model for the prediction of precipitation kinetics and yield strength of Al-Zn-Mg alloys. The model simplified the ternary alloy as pseudo-binary with an equivalent solute having its own equilibrium concentration and diffusion coefficient, and replaced the complex sequence of precipitation by a single precipitation process. The kinetics sub-model includes two steps: a step combining nucleation and growth of precipitates, followed by a step combining growth and coarsening. For all steps the classical equations for the individual mechanisms were used. Simple criteria considering the evolution of the precipitate density were used to determine the transitions between these steps. Thus a continuous prediction of a precipitation process from nucleation to coarsening was obtained. The structural hardening sub-model took into account the particle size distribution to calculate the mean obstacle strength $\overline{F}_m$ in Eq.(2.34) and adopted the Friedel statistics

to give the effective obstacle spacing L. Therefore an expression for the yield strength in the general case where both shearable and non-shearable precipitates are present was derived. A critical radius for the shearing/bypassing transition was used to define the pure shearing mode or the pure bypassing mode. The precipitation hardening contribution and dislocation hardening contribution were added using the Pythagorean addition law (see Eq.2.40). **Fig. 2.14** shows the applications of the model to experimental data for an Al–Zn–Mg alloy ageing at 160°C after heating at 30°C/h to the ageing temperature. It is seen that the model underestimated the yield strength at short and long ageing times. The authors suggested that the discrepancy observed in the early stages of ageing can be explained by the presence of undissolved GP zones in the microstructure which contribute to the strength, and the discrepancy in the late overaging stage may be due to an incorrect description of the line tension [108].

Myhr *et al.* [166] proposed a precipitation hardening model for Al-Mg-Si alloys that is similar to the model developed by Deschamps and Brechet [108]. Compared with Deschamps and Brechet's model, Myhr *et al*.'s kinetic sub-model further involves a description of the evolution of the particle size distribution with time. Comparison between predicted and measured strength evolution of an AA6082 Al-Mg-Si alloy is presented in **Fig. 2.15**. It is noted that by using the classical equations, i.e. Eq.(2.7) to Eq.(2.13), both the model by Deschamps and Brechet [108] and the model by Myhr *et al.* [166] are highly sensitive to the values of the interfacial energy (or ΔG_0 in [108] and A_0 in [166]) as they enter in the term of the activation energy barrier for nucleation with an exponent of 3. The interfacial energy is usually unknown and it is treated as an adjustable parameter. Thus in the application of the models to other systems, re-adjustment of the interfacial energy would be needed.

Liu *et al.* [167] presented a modified model to predict the yield strength of Al-Cu, Al-Mg-Si and Al-Zn-Mg alloys by taking account of the precipitate shape in calculating the strengthening contribution of the precipitates. The evolution of volume fraction and the dimensions (i.e. the radius of a disc, or the thickness of a plate or the length of a rod) was described by classical nucleation and growth theory. The precipitates were assumed to grow with time according to the parabolic growth law. Although reasonable agreement was found between predictions and experiments (**Fig. 2.16**), the

model is not clearly described. For instance the contributions due to solution strengthening and dislocation strengthening (for deformed Al-Zn-Mg alloys) seem to be neglected.

Esmaeili *et al.* [168] developed a yield strength model for a solution treated and aged Al-Mg-Si-Cu alloy AA6111. Starting from the expression for the determination of the critical resolved shear stress, i.e. Eq.(2.34), Esmaeili *et al.* derived expressions for the contributions from precipitation hardening, σ_{ppt}, during various stages of ageing. For shearable precipitates in the underaged and peak-aged conditions, depending on whether the precipitates are strong or weak obstacles, σ_{ppt} can be proportional to $(f_r)^{1/2}$ (where f_r is the relative volume fraction normalised to the peak-aged state volume fraction) or to $(f_r r)^{1/2}$, respectively. For both strong and weak obstacles in the over-aged condition, the volume fraction was assumed constant and equal to the peak-aged state volume fraction, and thus σ_{ppt} is related to the average radius only. Evolution of the relative volume fraction of precipitates was described by the JMAK kinetics. The kinetic parameters were obtained from a calibration on the relative volume fractions which were obtained from isothermal calorimetry experiments. Evolution of the precipitate size was estimated by either a parabolic growth law in the underaged and peak-aged conditions or by the LSW theory in the over-aged condition. The calibration of the model requires yield strength measurements in the as-quenched, peak-aged and overaged conditions. The predicted yield strengths for an AA6111 alloy are shown in **Fig. 2.17**. Due to the way the calibration used, these calibration parameters may be unique to a given alloy composition and have no particular physical meanings. This yield strength model was further coupled with a kinetic model for the description of concurrent precipitate formation and cluster dissolution during artificial ageing to predict the yield strength of an AA6111 alloy with prior natural ageing [169].

Recently, Starink and Wang [153] presented a model for the yield strength of overaged Al–Zn–Mg–Cu alloys. In these alloys precipitation hardening is the main strengthening component, and coarsening of η precipitates and their maximum attainable volume fraction are the main factors determining the strength. To take into

account the composition dependency of yield strength in multi-component alloys (in this case quaternary Al–Zn–Mg–Cu alloys), it was assumed that an equivalent solute concentration is a linear combination of the concentrations of the main alloying elements. Using this equivalent solute concentration and a reference alloy with known maximum volume fraction, the volume fraction of precipitates after completion of precipitation in the alloys studied can be obtained. The evolution of average size of the precipitates (the thickness and the diameter of the disc-shaped precipitates) was described by the SZ model which has been extended to deal with the transition from the nucleation and growth stage to the coarsening stage. The model also considers the influence of supersaturation on precipitation rates and of volume fraction on coarsening rates. These effects were proved to be small (causing differences in yield strength up to about 3MPa) since the precipitate rate is greatly determined by the activation energy and the typical volume fraction of precipitates for an overaged alloy is small (about 4.3%). Effects of crystallographic texture and recrystallisation were taken account of through the determination of the Taylor factor. The modelling results are shown in **Fig. 2.18** for three Al–Zn–Mg–Cu alloys[*].

It is noted that in all of the above mentioned strength models, a single precipitate was assumed throughout the ageing process. Attempts have been made [152, 170, 171] to take into account the specific strengthening due to various precipitates in complex alloys. Gomiero *et al.* [170] calculated the yield strengths at two states (as-quenched and aged 12h at 150°C) of a 2091 Al-Li-Cu-Mg(-Zr) alloy, a Al-Cu-Mg(-Zr) alloy and a Al-Li(-Zr) alloy from measured microstructural parameters such as the precipitate size, volume fraction, the composition of remaining solid solution and grain size. Contributions to the yield strength include grain boundary strengthening, solution strengthening and precipitation strengthening due to δ′, GPB zones, Al_3Zr and S laths. The results obtained from a linear addition of all contributions were in good agreement with the measured values of the conventional yield strength. More recently, Genevois *et al*. [171] modelled the variation of yield stress through the 2024

[*] Due to the confidential nature of the work, only three alloys with very similar predicted volume fractions of precipitates were presented in the paper, from which the composition dependency of yield strength cannot be reflected. It was mentioned in the paper that the model successfully predicted the yield strength data of 21 Al–Zn–Mg–Cu alloys, with yield strengths ranging from 400MPa to 600MPa.

T351 friction stir weld from the quantitative results of the microstructure analysis. Following the structural hardening model developed by Deschamps and Brechet [108], strengthening contributions from shearable GPB zones and non-shearable S precipitates were considered and added according to a Pythagorean addition law. The predicted yield strengths agree well with the experimental yield strength (**Fig. 2.19**).

Starink *et al.* [152, 172] developed a model for the yield strength of Al-Li-Cu-Mg alloys and composites in which detailed strengthening contributions of different types of precipitates e.g. GPB zones, δ' (Al_3Li) and S′ (Al_2CuMg) were considered. The evolution of the volume fractions of these precipitates were obtained by fitting the SZ kinetic model (see Section 2.3.2.4) to measured volume fractions that were determined from the DSC curves [60, 172]. Thus the relation between alloy composition and precipitate volume fraction cannot be given in this model. A simple model was developed to predict the evolution of sizes of the S precipitates through the complete nucleation, growth and coarsening process. Although the description of the coarsening behaviour did not follow the LSW theory, this method demonstrated a satisfactory fit to the size data measured using TEM. For the sizes of δ' precipitates for which growth occurs by coarsening only, the classical LSW coarsening theory was applied. These obtained microstructural parameters (volume fractions, sizes, *etc*.) were then used in the strength model to calculate the specific strengthening contributions. However no evolution of solution strengthening due to dissolved Li, Cu and Mg atoms was given. A superposition law in the form of Eq.(2.41) was used to calculate the total CRSS, with the superposition exponents adopted from validated values in the literature. The modelling results are shown in **Fig. 2.20**.

In summary, since the development of the model by Shercliff and Ashby [160], quite a few works on modelling of the yield strength of Al based alloys on the basis of microstructural development have been presented. Theoretical expressions for most of the strengthening mechanisms are available in the literature and are generally adopted in the models. Thus the strength modelling is reduced to finding the time evolution of microstructural parameters such as volume fraction, size and remaining solute concentrations either by experiments or by modelling. As seen from the above-mentioned models, the modelling approaches for microstructural parameters are diverse depending on the problems to be solved and the required level of complexity.

Some models simply adopt the classical equations [160, 167, 168], some apply numerical calculations based on classical equations to make a continuous prediction [108, 166] and others use simple but efficient analytical methods to describe the complete precipitation process [152, 153]. So the emphasis in new model development will be in the microstructure modelling aspect.

It is also noted that while a typical precipitation sequence in aluminium based alloys involves several phases, very little work has been done to deal with the coexistence of different types of precipitates. Models for Al-Cu alloys have been developed by Shercliff and Ashby [160] and by Liu *et al.* [167] on the one precipitate assumptions. The published models for Al-(Li)-Cu-Mg alloys considered the contributions from different types of precipitates, but the microstructural parameters were obtained either from detailed experimental microstructure characterization [170, 171] or from the fits to microstructure data derived from DSC and TEM results [172]. It is the aim of this thesis to see if a model based on microstructural evolution for two precipitates competing for the available solute can provide good description for the two-stage ageing behaviour in Al-Cu-Mg based alloys.

Table 2.1 Chemical composition of some 2xxx aerospace alloys (wt.%) [4]

Alloy	Cu	Mg	Zn	Mn	Cr	Ti	Si	Fe
2014	3.9-5.0	0.20-0.8	<0.25	0.40-1.2	<0.1	<0.15	0.50-1.2	<0.7
2024	3.8-4.9	1.2-1.8	<0.25	0.30-0.9	<0.1	<0.15	<0.5	<0.5
2124	3.8-4.9	1.2-1.8	<0.25	0.30-0.9	<0.1	<0.15	<0.2	<0.3
2618	1.9-2.7	1.3-1.8	<0.1	(0.9-1.2 Ni)		0.04-0.10	0.10-0.25	0.9-1.3

Table 2.2 Typical tensile properties of some 2xxx aerospace alloys [2, 4]

Alloy	Temper	Solution treatment (°C)	Ageing treatment (h/°C)	Yield strength (MPa)	Tensile strength (MPa)	Elongation in 50mm (%)
2014	T4,T451	505	RT	290	425	18
2014	T6,T651	505	18/160	415	485	12
2024	T4, T351	495	RT	324	469	19
2024	T81, T851	495	12/190	448	483	7
2618	T61	530	20/200	372	440	10

Table 2.3 Basic characteristics of the precipitates

	Precipitates	Characteristics	References
Al-Cu (-Mg) (high Cu/Mg ratio)	GPI zone	monolayer of Cu atoms on $\{001\}_\alpha$	[18]
	GPII zone/θ″	fully coherent intermediate precipitate, two or more layers of Cu atoms on $\{001\}_\alpha$	[18]
	θ′(Al_2Cu)	tetragonal, I4/mcm, a=0.404nm, c=0.580nm; semicoherent intermediate precipitate forms as plate on $\{001\}_\alpha$ plane	[27]
	θ (Al_2Cu)	tetragonal, I4/mcm a=0.6066nm, c=0.4874nm, incoherent equilibrium phase	[173]
Al-Cu-Mg (low Cu/Mg ratio)	GPB zone	ordered Cu-and Mg-rich zone as thin rods along $<100>_\alpha$ direction	[32]
	S′ (Al_2CuMg)	orthorhombic, Cmcm, a=0.404 nm, b=0.925nm, c=0.718nm, semi-coherent intermediate precipitate, forms as lath along $<100>_\alpha$ on $\{021\}_\alpha$ habit plane, only a slightly distorted version of S	[26, 55, 61]
	S (Al_2CuMg)	orthorhombic, Cmcm, a=0.400 nm, b=0.923nm, c=0.714nm, incoherent equilibrium phase	[63]

Table 2.4 Expressions for kinetic parameters E_{eff}, n and k_0 for isothermal transformation

	Continuous nucleation	Site saturation
E_{eff}	$\frac{E_N + mE_G}{m+1}$	E_G
n	$m+1$	m
k_0	$(\frac{1}{m+1} A_1 I_0 G_0^m)^{1/(m+1)}$	$(A_1 N G_0^m)^{1/(m+1)}$

Table 2.5 Expressions for the CRSS of various strengthening mechanisms

Strengthening mechanism	Formula	Symbols	Ref.
chemical	$\Delta\tau_{ch}=\left(\frac{6bf}{\pi\Gamma}\right)^{1/2}\frac{\gamma^{3/2}}{r}$	γ interfacial energy	[14, 144]
stacking-fault	$\Delta\tau_{sf}=\Delta\gamma_{sf}^{3/2}\left(\frac{3\pi^2 fr}{32\Gamma b^2}\right)^{1/2}$	$\Delta\gamma_{sf}$ difference in stacking-fault energy between matrix and particle	[14, 144]
modulus	$\Delta\tau_{\mu}=\frac{\Delta\mu}{4\pi\sqrt{2}}f^{1/2}$ From [174] $\Delta\tau_{\mu}=0.9(rf)^{1/2}(\frac{\Gamma}{b})\left(\frac{\Delta\mu/\mu_{Al}}{2b\ln(\frac{2r}{bf^{1/2}})}\right)^{3/2}$ From [175] $\Delta\tau_{\mu}=0.0055\Delta\mu^{3/2}(\frac{f}{\Gamma})^{1/2}b\left(\frac{r}{b}\right)^{\frac{3m}{2}-1}$ From [176]	$\Delta\mu$ difference in modulus between matrix and particle m constant (≈0.85)	[14, 144]
order	$\Delta\tau_{o}=\frac{\gamma_{apb}}{2b}\left(\sqrt{\frac{3\pi^2\gamma_{apb}fr}{32\Gamma}}-f\right)$ for underaged alloys $\Delta\tau_{o}=0.81\frac{\gamma_{apb}}{2b}\left(\sqrt{\frac{3\pi f}{8}}-f\right)$ for peak aged alloys	γ_{apb} antiphase boundary energy	[14]
coherency	$\Delta\tau_{c}=\alpha_{\varepsilon}(\varepsilon\mu_{Al})^{3/2}\left(\frac{bfr}{\Gamma}\right)^{1/2}$	α_{ε} numerical factor ε misfit parameter	[14, 144]
Orowan	$\Delta\tau=\frac{0.81\mu_{Al}b}{2\pi(1-\upsilon)^{1/2}}\left[\frac{\ln(2r_s/r_0)}{L_s-2r_s}\right]$	ν Poisson's ratio r_s average planar radius r_0 dislocation inner cut-off radius (≈b)	[10]

Note: b Burgers vector; Γ dislocation line tension; μ_{Al} shear modulus of the matrix; L_s the average planar spacing of particles in the slip plane; f precipitate volume fraction; r precipitate radius.

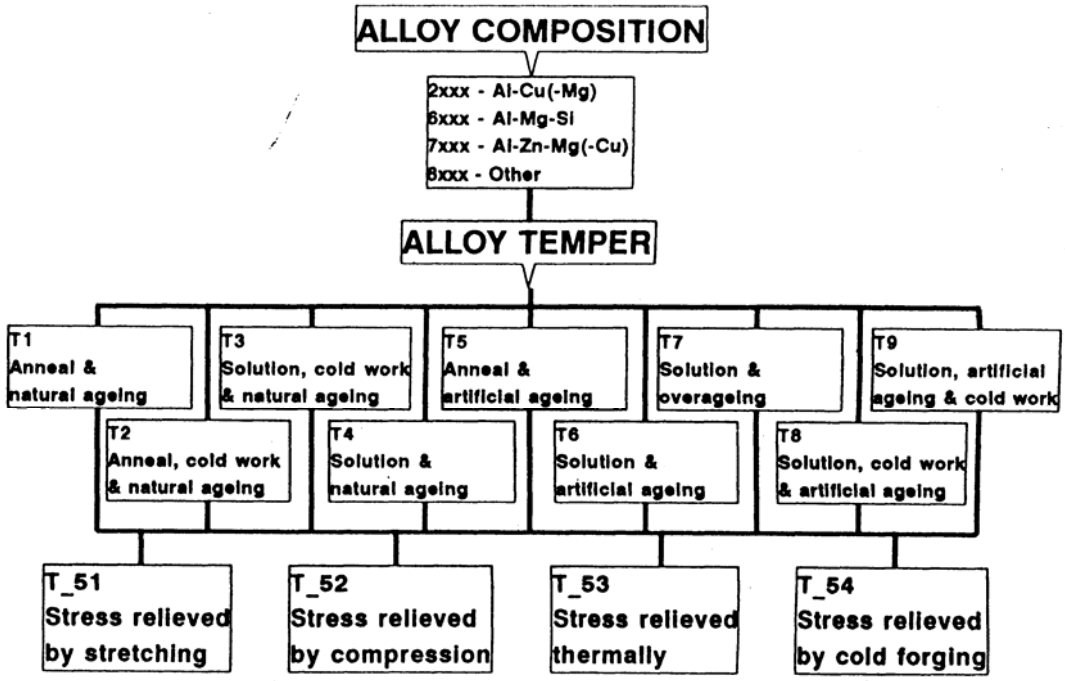

Fig. 2.1 Alloy and temper designation for heat-treatable aluminium alloys [2].

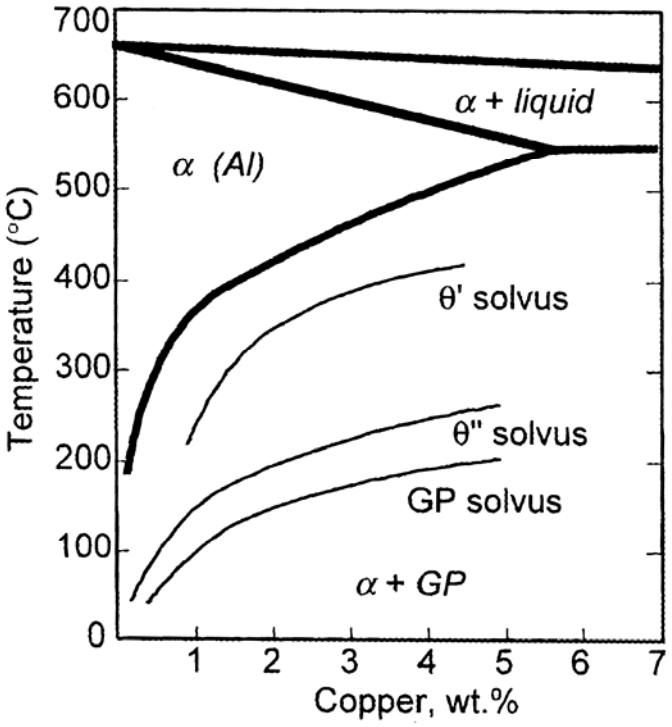

Fig. 2.2 Al-rich end of the Al-Cu phase diagram [18].

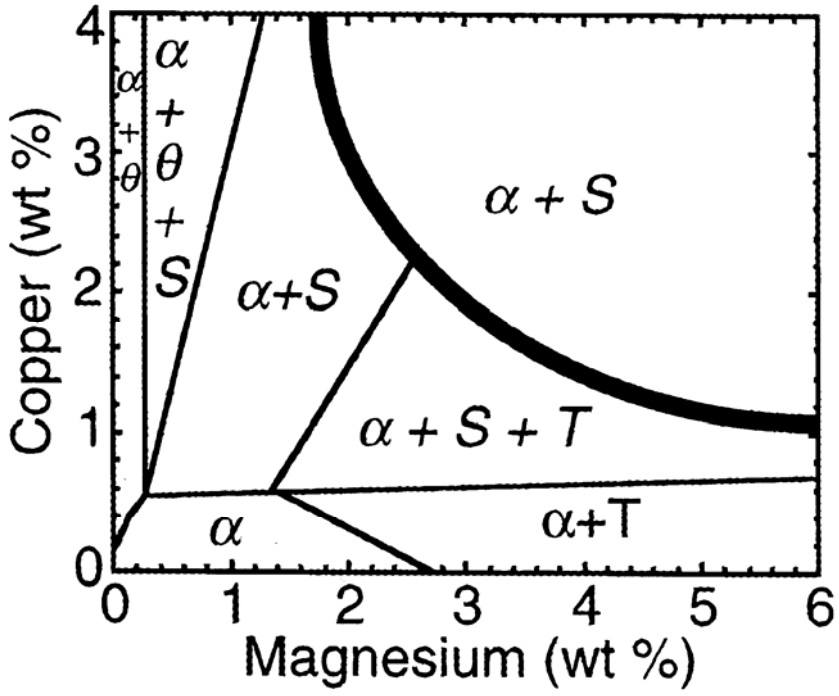

Fig. 2.3 Al-rich corner of the Al-Cu-Mg phase diagram at 190°C. The thick solid line defines the α/α+S phase boundary at 500°C [22].

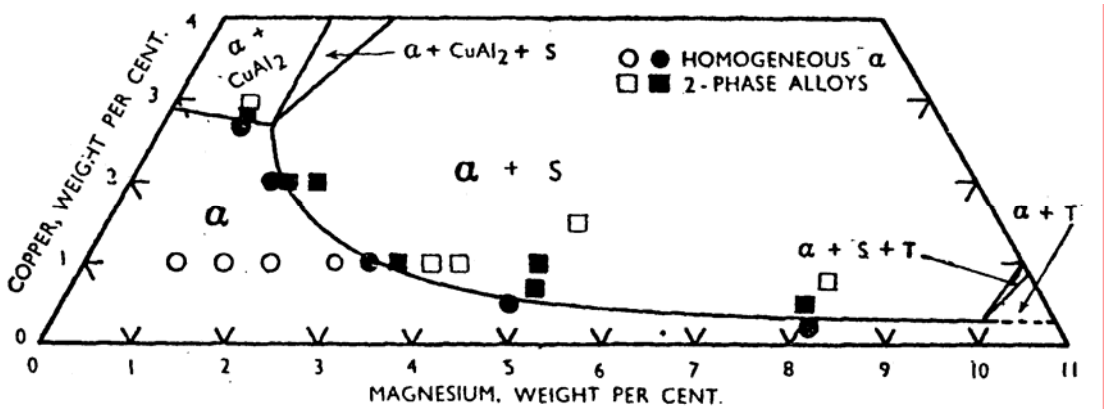

Fig. 2.4 The constitution of the ternary Al-Cu-Mg system at 460°C [19]. (open symbol: nominal compositions, solid symbol: compositions checked by chemical analysis after annealing at 460°C. From [177]).

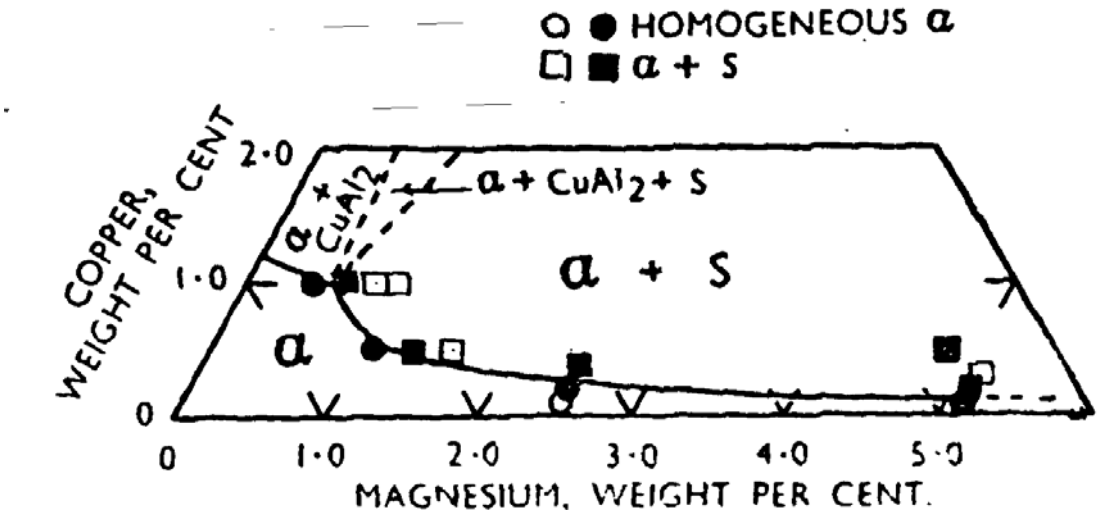

Fig. 2.5 The constitution of the ternary Al-Cu-Mg system at 375°C [19]. (Same symbols as in Fig. 2.4).

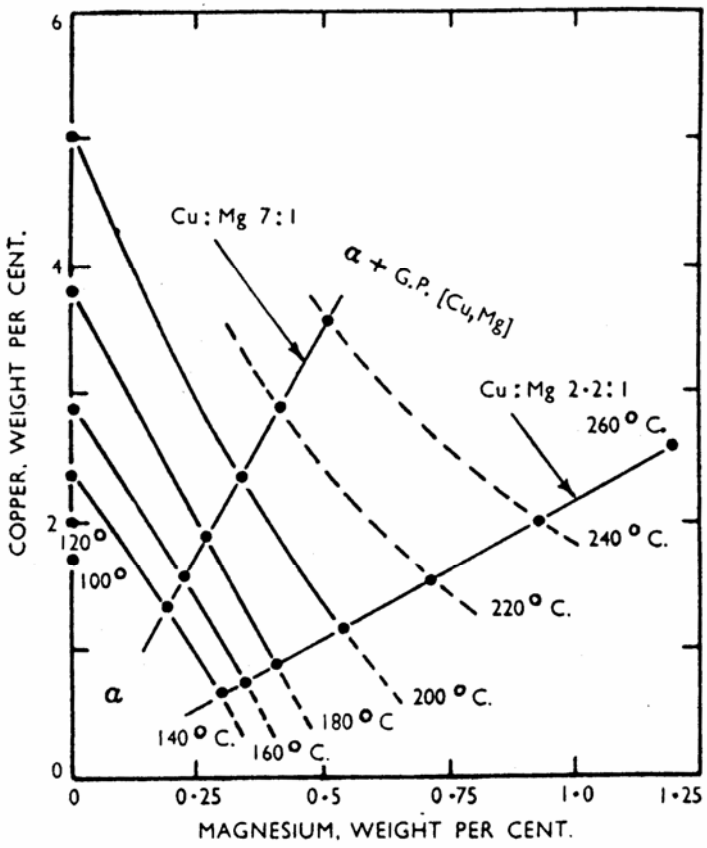

Fig. 2.6 Isothermals of the α/(α+GP [Cu,Mg] zones) metastable phase boundaries in the Al-Cu-Mg system [16].

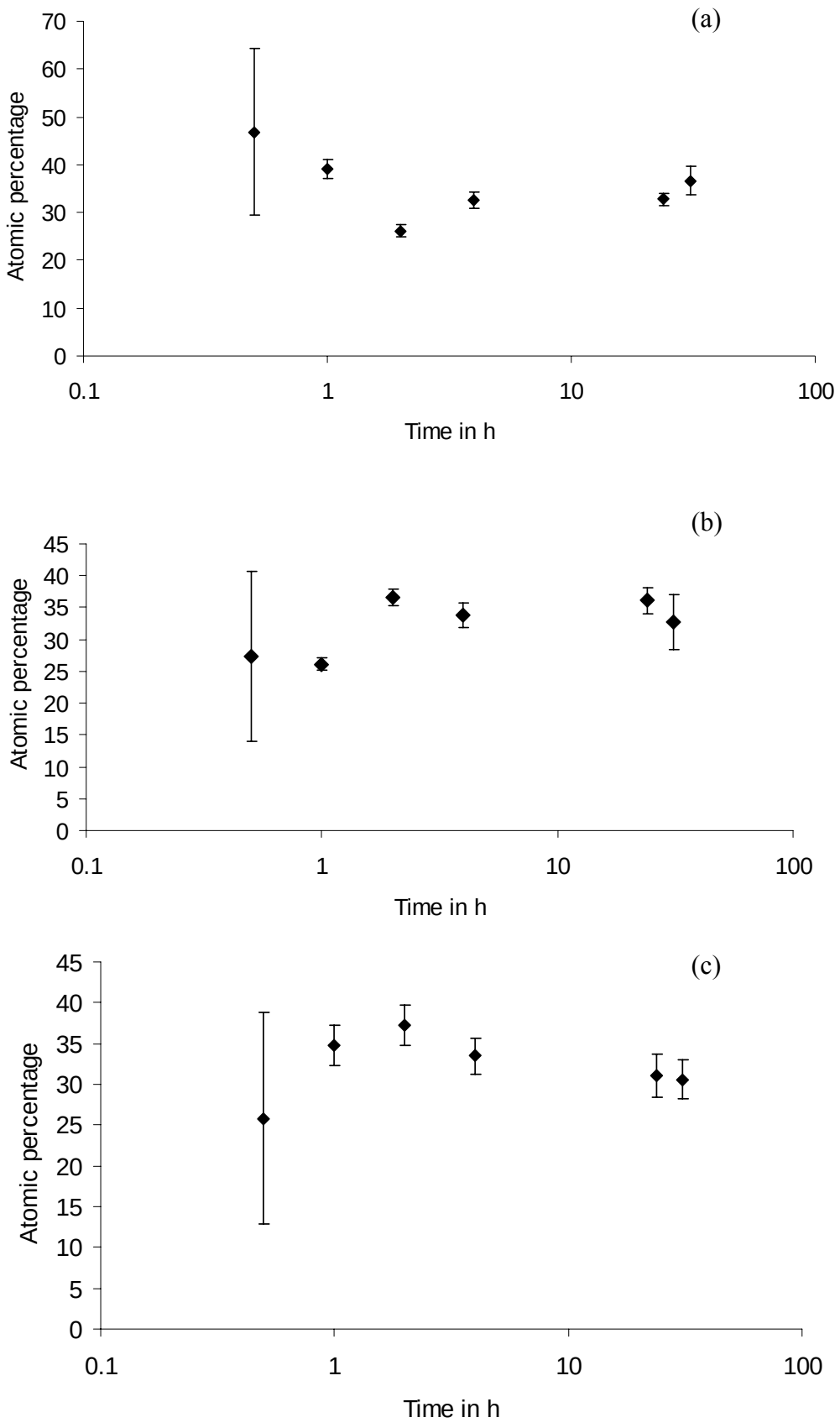

Fig. 2.7 (a) Mg, (b) Cu and (c) Al contents in the Cu-Mg co-clusters depending on the time of natural ageing in alloy B [49].

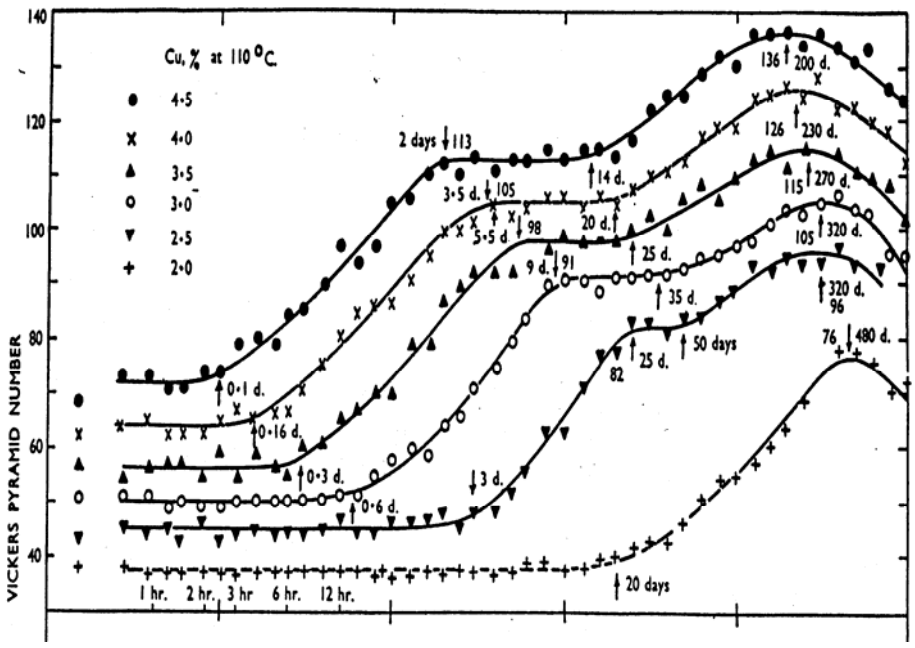

Fig. 2.8 Hardness/ageing curves for Al-Cu alloys aged at 110 °C [69].

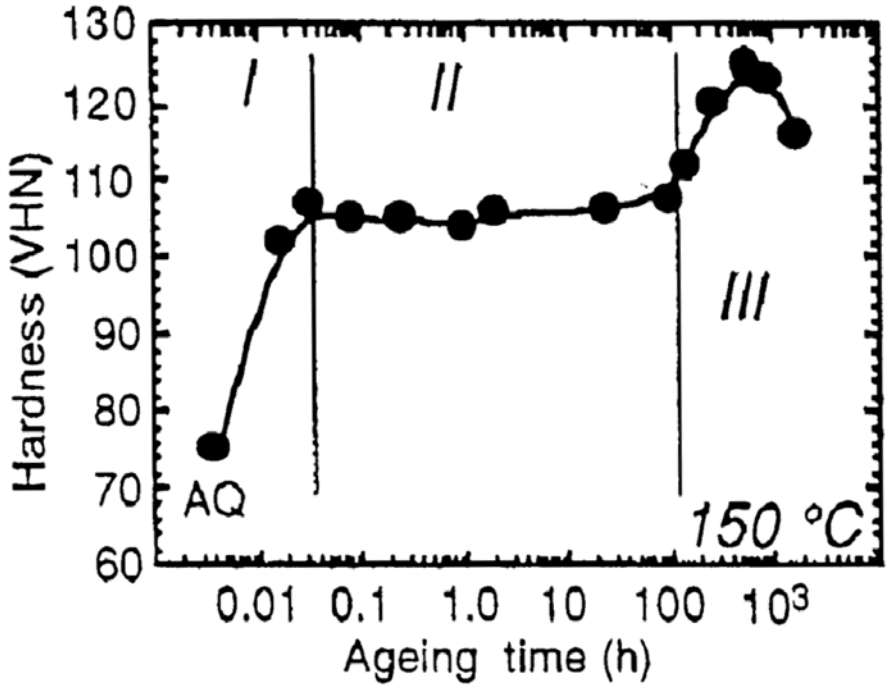

Fig. 2.9 Hardness-time plot for Al-1.1 at.% Cu-1.7 at.% Mg alloy aged at 150°C [33].

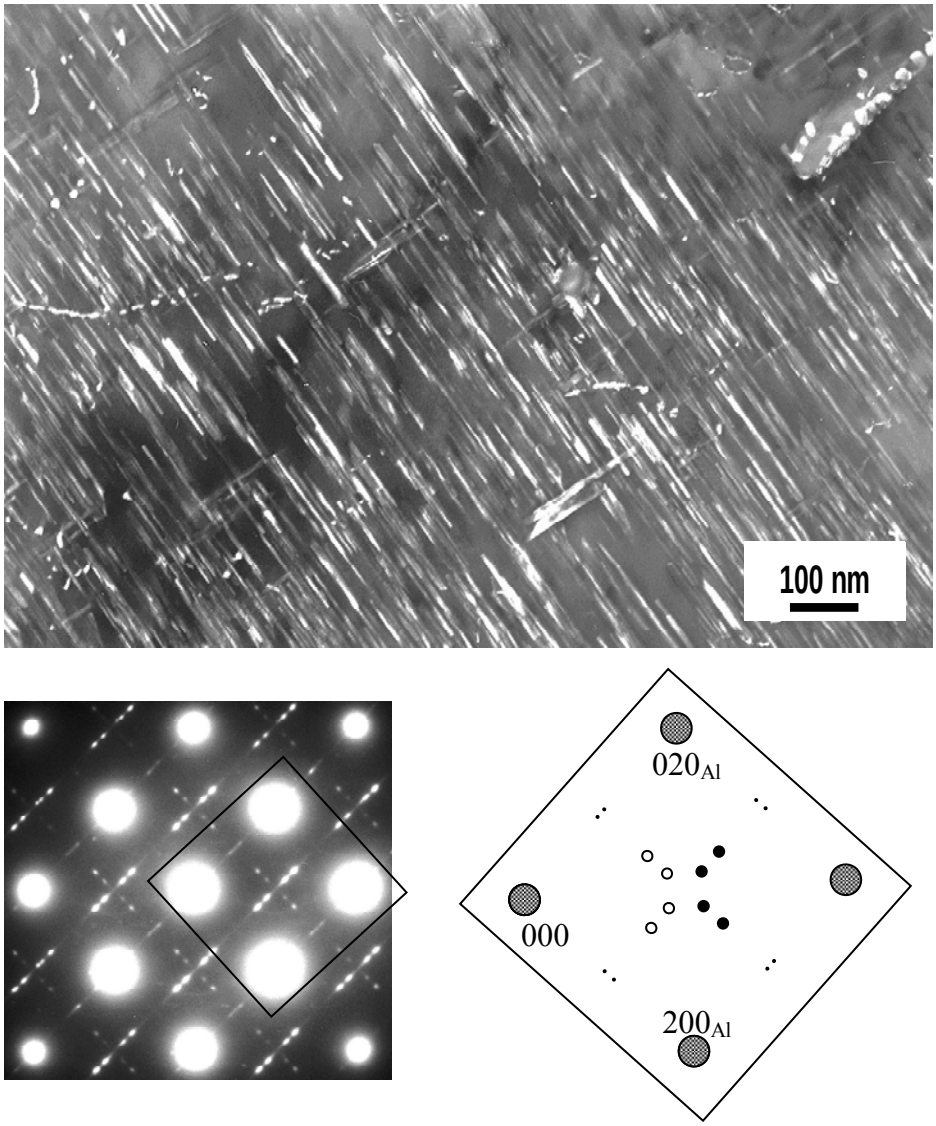

Fig. 2.10 TEM micrograph (dark field) of alloy B aged 12h/190°C (B=[100]), with corresponding SAD pattern (courtesy of Dr. N. Gao and Dr. S Wang).

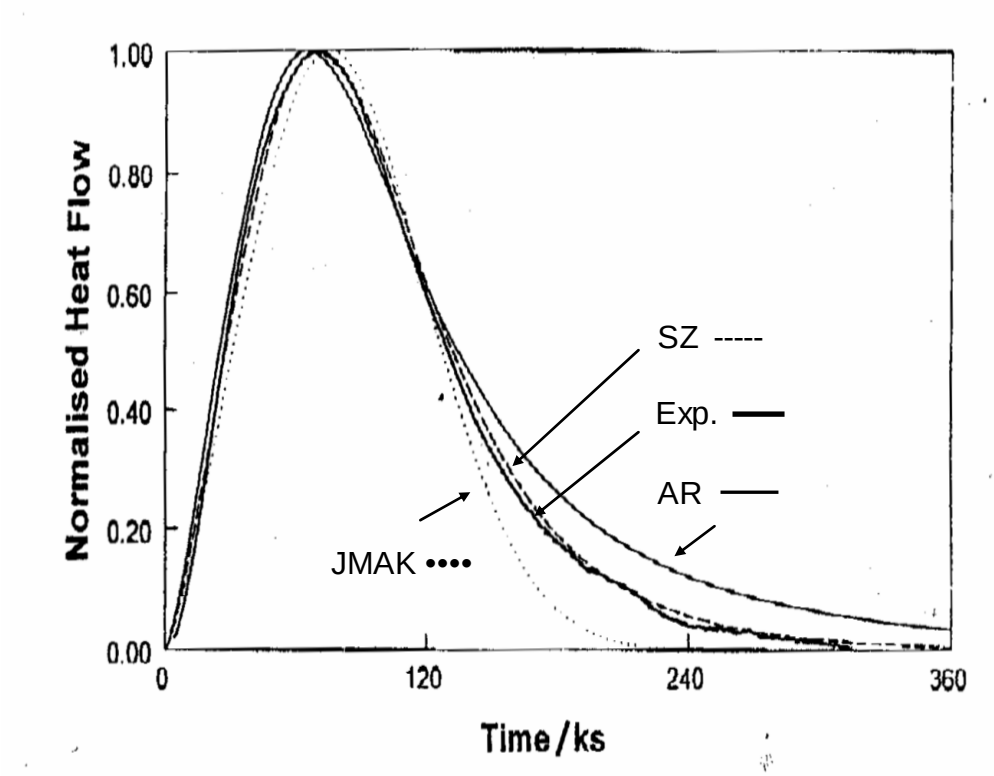

Fig. 2.11 Normalised experimental heat flow for the decomposition of an Al-6.8 at%Zn alloy during isothermal ageing at 130°C along with three fits according to the JMAK, the AR and the SZ models [140].

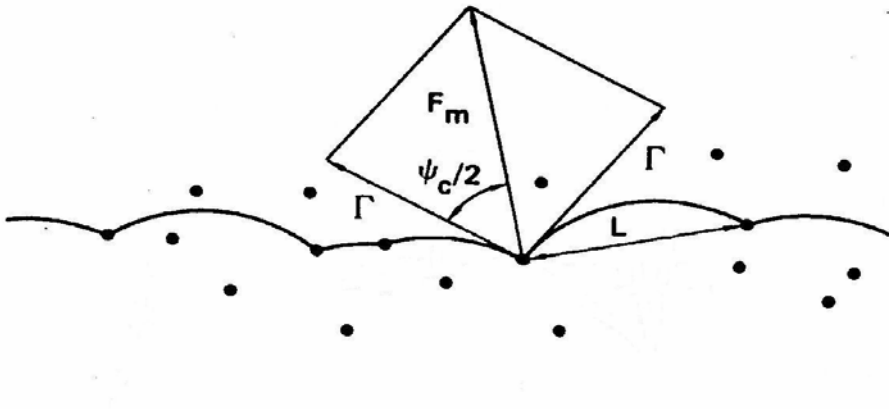

Fig. 2.12 Schematic illustration of the gliding dislocation bows out between the dislocations.

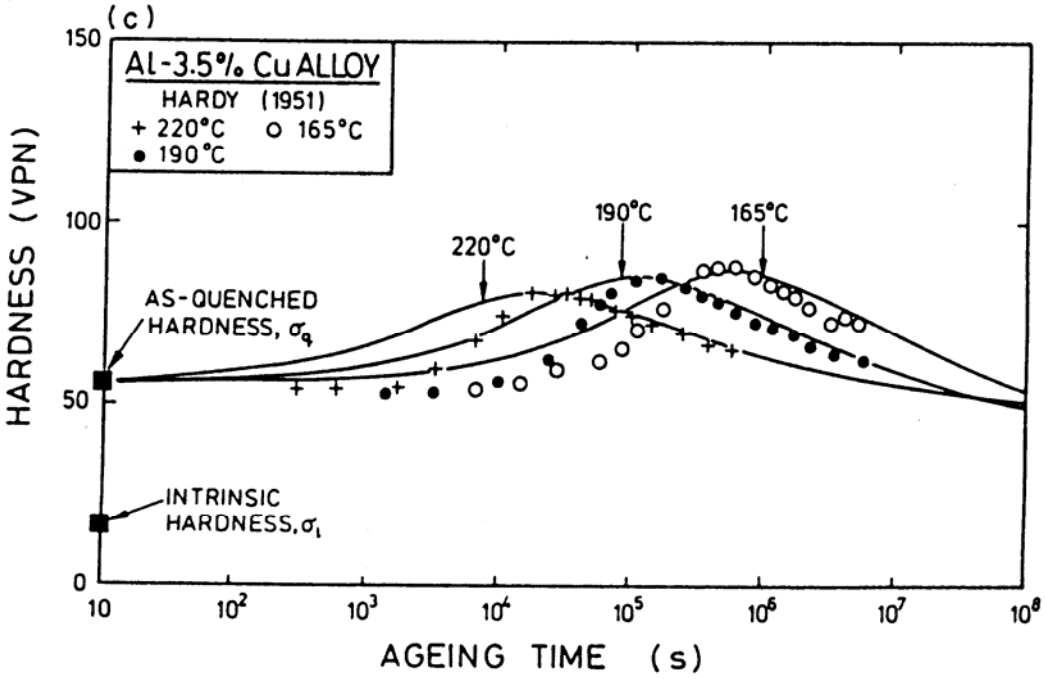

Fig. 2.13 Comparison between the experimental and predicted strength evolution of an Al-Cu alloy [160].

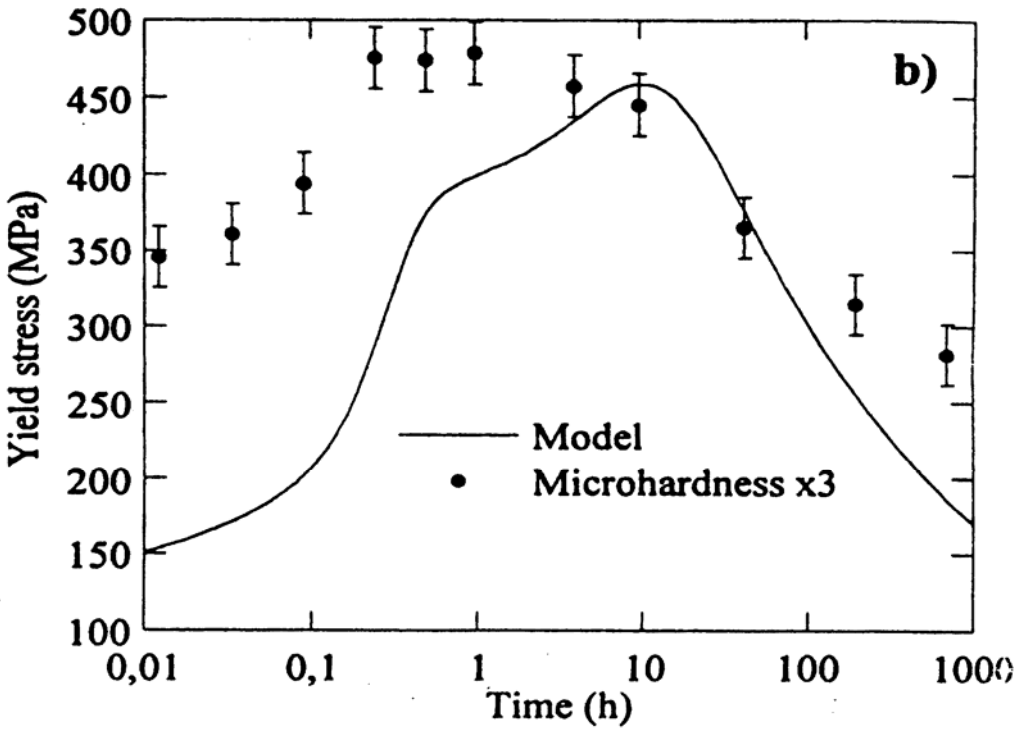

Fig. 2.14 Comparison between the experimental and predicted strength evolution of an Al-6.1Zn-2.35Mg-0.1Zr(wt%) alloy [108].

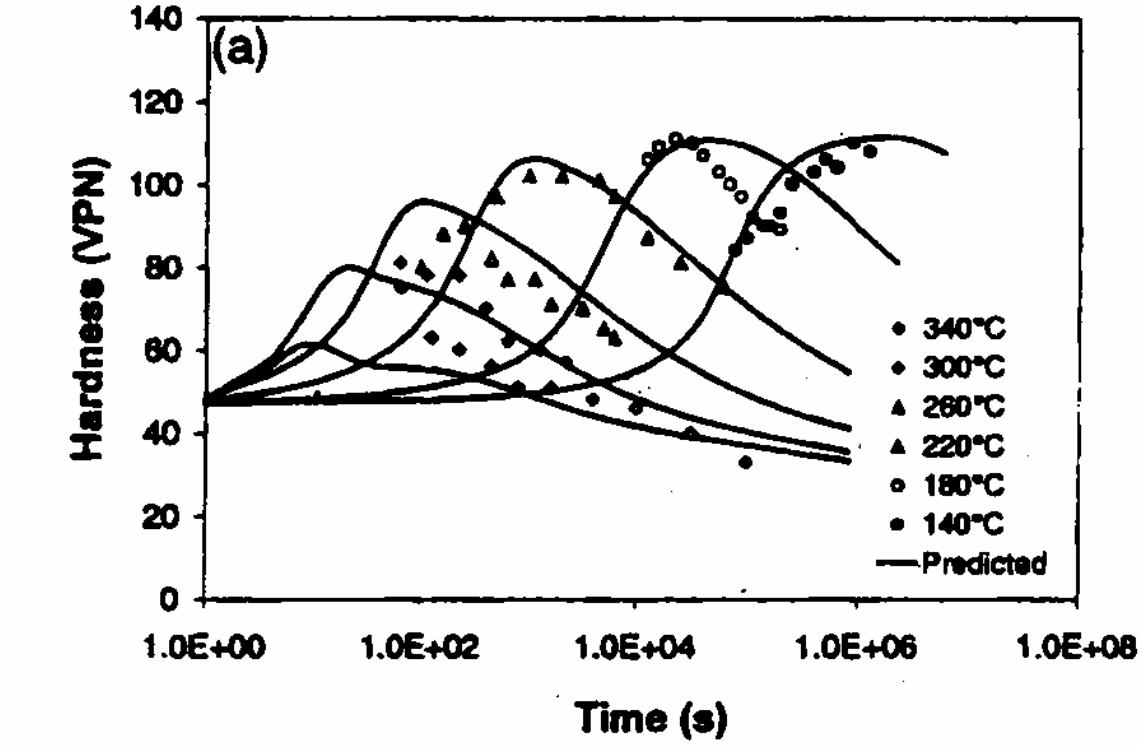

Fig. 2.15 Comparison between the experimental and predicted strength evolution of an AA6082 Al-Mg-Si alloy [166].

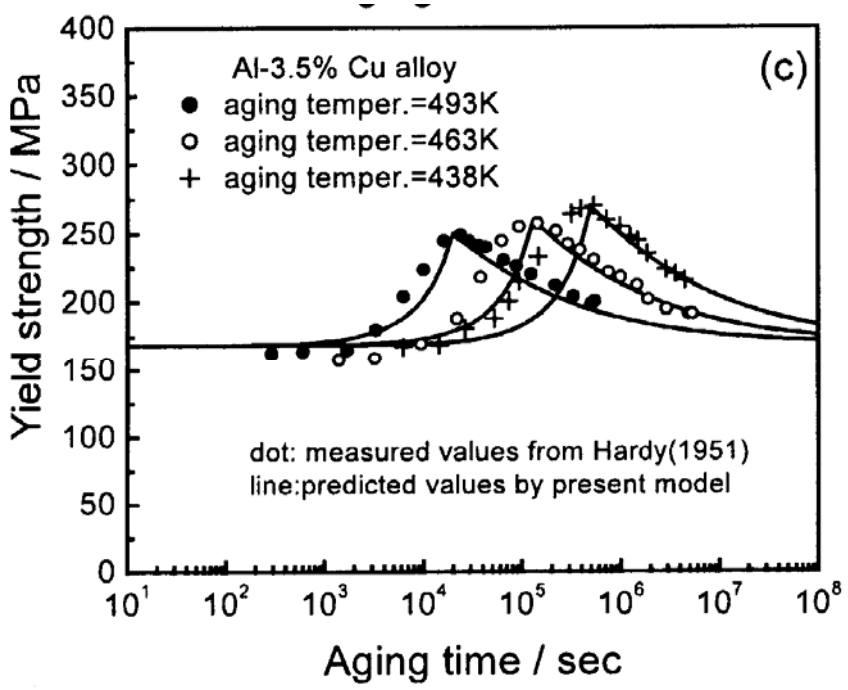

Fig. 2.16 Comparison between the experimental and predicted strength evolution of an Al-Cu alloy [167].

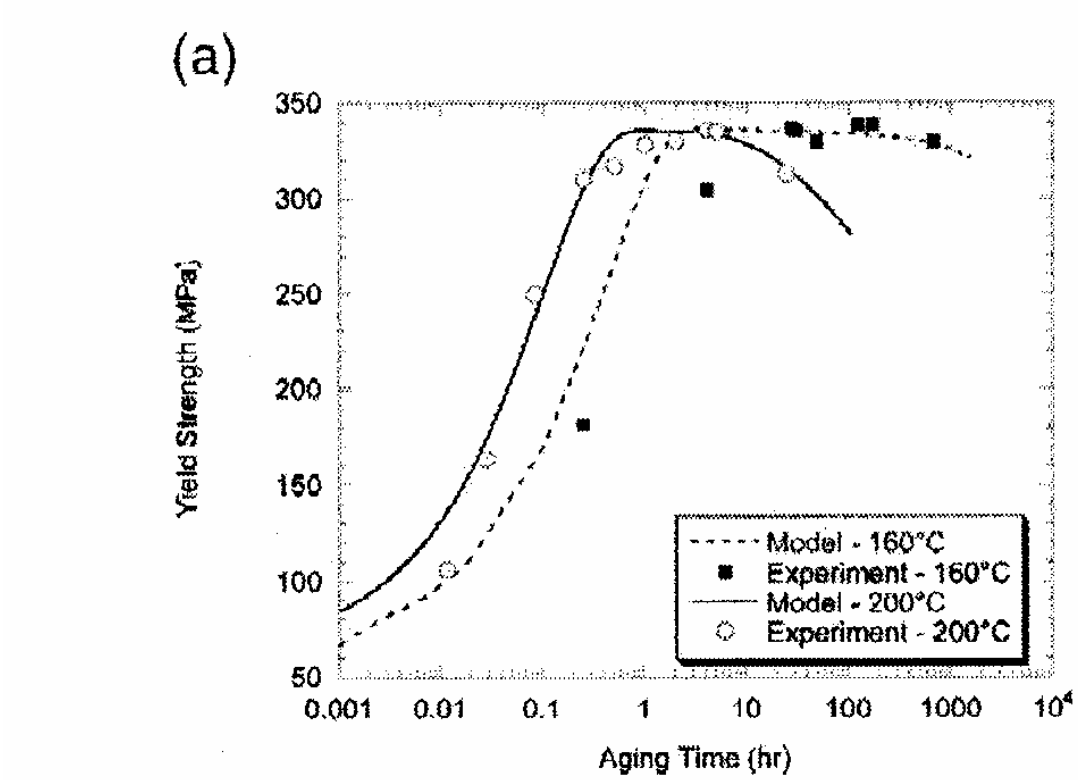

Fig. 2.17 Comparison of the model predictions and experimental results of an AA6111 alloy ageing at 160 °C and 200 °C [168].

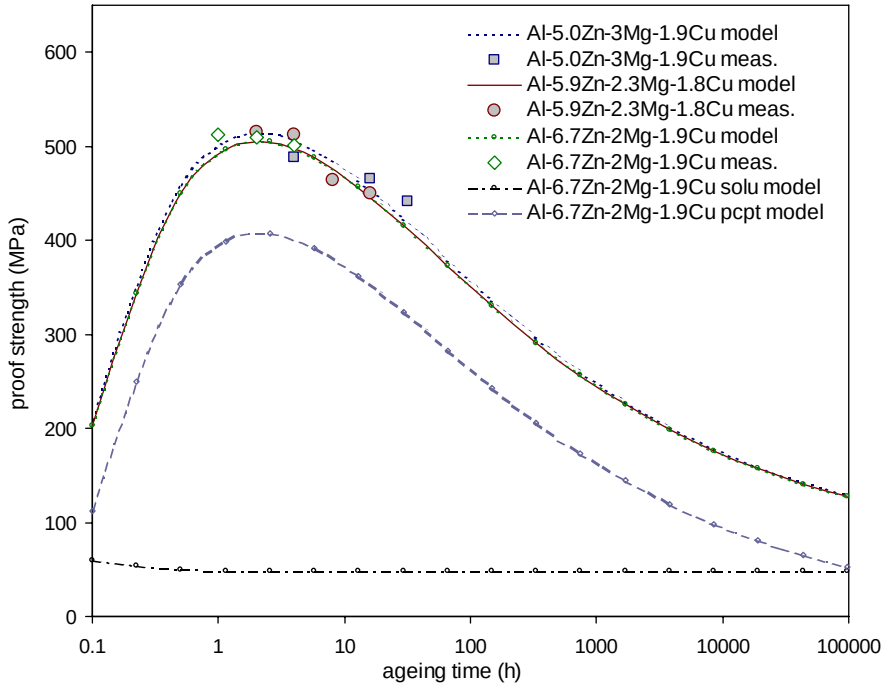

Fig. 2.18 Predicted and measured proof strengths for three Zr-containing Al-Zn-Mg-Cu alloys. Also presented are the predicted precipitate strengthening and solution strengthening contributions for one of the alloys [153].

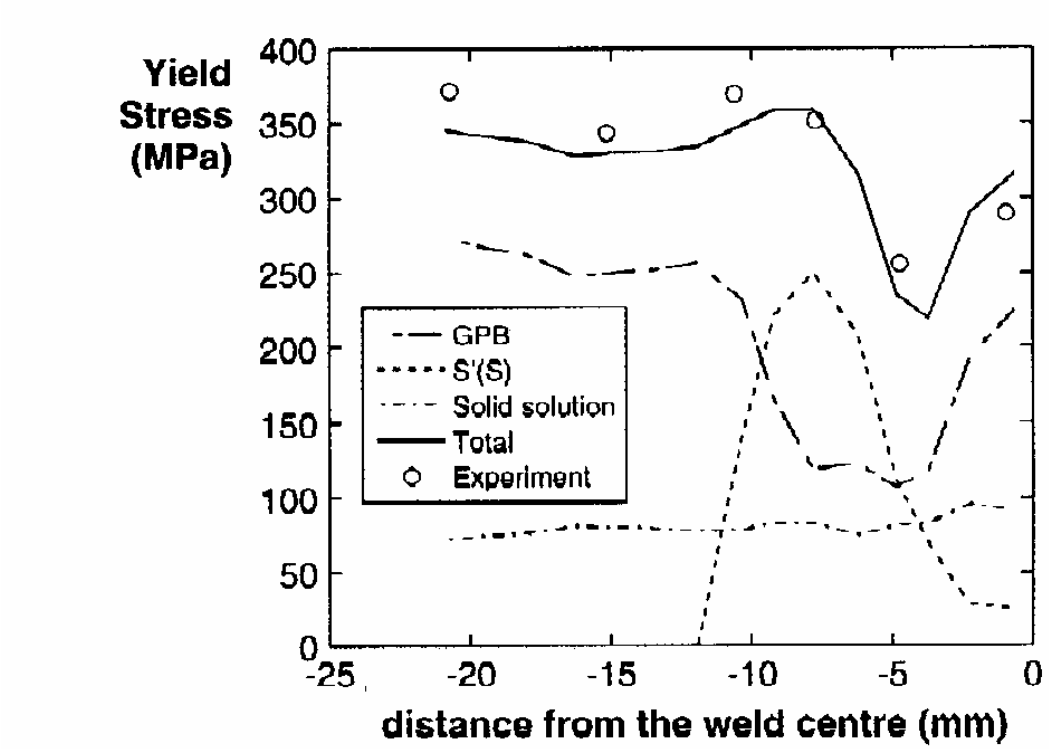

Fig. 2.19 Comparison of the calculated yield stress with the experimental yield stress along the advancing side of a 2024 T351 weld together with evolution of the different calculated contributions to strengthening [171].

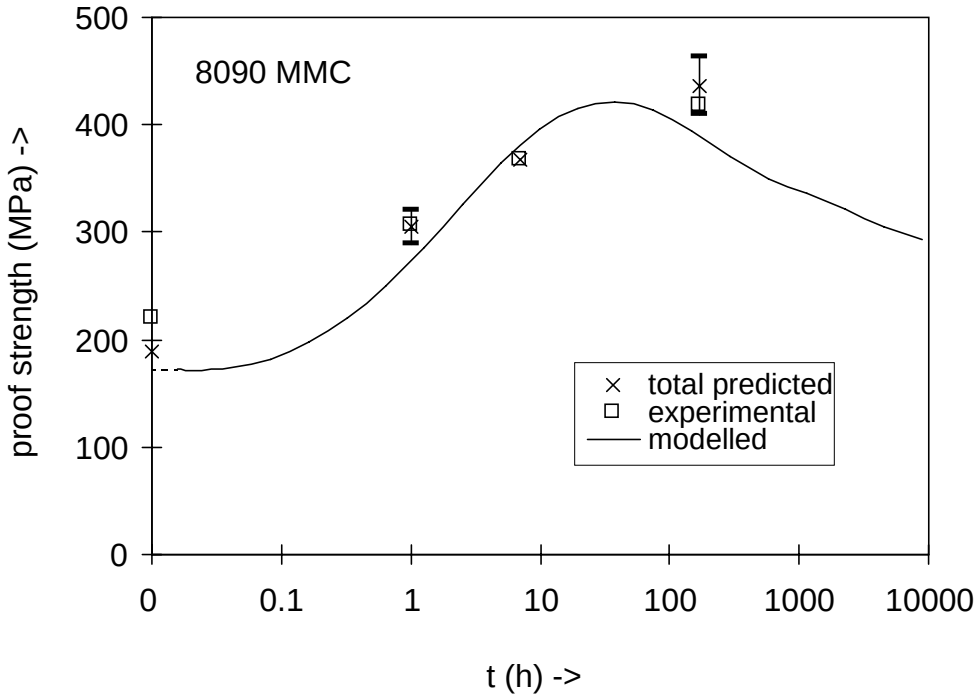

Fig. 2.20 Comparison between the experimental and predicted strength evolution of an 8090MMC Al-Li-Cu-Mg alloy [152].

References

[1] I. J. Polmear, *Light Alloys-Metallurgy of the Light Metals*, 3rd ed, Butterworth- Heinemann, Oxford, UK, 1995.

[2] P. J. Gregson, in: H. M. Flower (Ed.), *High Performance Materials in Aerospace*, p.40, 1995, Chapman & Hall, UK.

[3] A. K. Vasudevan and R. D. Doherty (Eds.), *Aluminium Alloys-Contemporary Research and Application*, Vol. **31**, Academic Press, London, 1989

[4] J. R. Davis (Ed.), *ASM Specialty Handbook: Aluminum and Aluminum Alloys*, Materials Park, OH: ASM International, 1993

[5] J. T. Staley, 'Metallurgical aspects affecting strength of heat treatable alloy products used in the aerospace industry', in: L. Arnberg, O. Lohne, E. Nes, and N. Ryum (Eds.), *Proc. 3rd Intl. Conf: Aluminium Alloys-Their Physical and Mechanical Properties (ICAA3)*, Vol. **3**, Norwegian Institute Of Technology, Trondheim, Norway, 1992, p.107-143.

[6] N. Sen and D. R. F. West, 'Some factors influencing S precipitation in Al-Cu-Mg and Al-Cu-Mg-Ag alloys', *J.Inst.Metals*, 1969, **97**, 87-92.

[7] J. T. Vietz and I. J. Polmear, 'The influence of small additions of silver on the ageing of aluminium alloys: observations on Al-Cu-Mg alloys', *J. Inst. Metals*, 1966, **94**, 410-419.

[8] H. Martinod, C. Renon, and J. Calvet, 'Influence of deformation after quenching on mechanical characteristics and resistance to creep of aluminium alloys used in aeronautics', *Rev. Metall.*, 1966, **63**, 815-821.

[9] H. K. Hardy, 'The ageing characteristics of some ternary aluminium-copper-magnesium alloys with copper : magnesium weight ratios of 7:1 and 2.2:1', *J. Inst. Metals*, 1954-55, **83**, 17-34.

[10] J. W. Martin, *Micromechanisms in Particle-Hardened Alloys*, Cambridge University Press, Cambridge, 1980.

[11] H. K. Hardy and T. J. Heal, 'Report on precipitation', *Prog. Met. Phys.*, 1954, **V**, 143-278.

[12] A. Kelly and R. B. Nicholson, 'Precipitation Hardening', *Prog. Mater. Sci.*, 1963, **10**, 149-391.

[13] J. W. Martin, *Precipitation Hardening*, Pergamon, Oxford, 1968.

[14] A. J. Ardell, 'Precipitation Hardening', *Metall. Trans. A*, 1985, **16**, 2131-2165.

[15] J. L. Murray, 'The Al–Cu system', *Int. Met. Rev.*, 1985, **30**, 211-233.

[16] R. H. Beton and E. C. Rollason, 'Hardness reversion of dilute alluminium-copper and alluminium-copper-magnesium alloys', *J. Inst. Metals*, 1957-58, **86**, 77-85.

[17] E. Hornbogen, *Aluminium*, 1967, **43**, 41-47.

[18] S. P. Ringer and K. Hono, 'Microstructural evolution and age hardening in aluminium alloys: Atom probe field-ion microscopy and transmission electron microscopy studies', *Mater. Charact.*, 2000, **44**, 101-131.

[19] A. T. Little, W. Hume-Rothery, and G. V. Raynor, 'The constitution of aluminium-copper-magnesium alloys at 460°C', *J. Inst. Metals*, 1944, **70**, 491-506.

[20] N. S. Brommelle and H. W. L. Phillips, 'The constitution of aluminium-copper-Magnesium alloys', *J. Inst. Metals*, 1949, **75**, 529-558.

[21] H. W. L. Phillips, *Equilibrium Diagrams of Aluminium Alloy Systems*, the Aluminium Development Assoc., London, UK, 1961.

[22] G. B. Brook, *Precipitation in Metals, Spec. Rep. No.3*, Fulmer Res. Inst., UK, 1963.

[23] P. Villars, A. Prince, and H. Okamoto (Eds.), *Handbook of ternary alloy phase diagrams*, ASM International, Materials Park, OH, 1994

[24] F. Laves and H. Witte, *Metallwirtschaft*, 1936, **15**, 5.

[25] V. Gerold, 'On the Structures of Guinier-Preston Zones in Al-Cu Alloys', *Scripta Metall.*, 1988, **22**, 927-932.

[26] L. F. Mondolfo, *Aluminium Alloys: Structure and Properties*, Butterworths, London, 1976.

[27] J. M. Silcock, T. J. Heal, and H. K. Hardy, 'Structural ageing characteristics of binary Al-Cu alloys', *J. Inst. Metals*, 1953-54, **82**, 239-248.

[28] T. Sato and T. Takahashi, 'High-Resolution Electron-Microscopy on the Layered Structures of GP Zones in an Al-1.7at-Percent-Cu Alloy', *Scripta Metall.*, 1988, **22**, 941-946.

[29] M. Karlik and B. Jouffrey, 'High resolution electron microscopy study of Guinier-Preston (GP1) zones in Al-Cu based alloys', *Acta Mater.*, 1997, **45**, 3251-3263.

[30] V. A. Phillips, 'High resolution electron microscope observations on precipitation in Al-3.0%Cu alloy', *Acta Metall.*, 1975, **23**, 751-767.

[31] R. W. Cahn, P. Haasen, and E. J. Kramer (Eds.), *Materials Science and Technology-Structure and Properties of Nonferrous Alloys*, Vol. **8**, VCH Publishers Inc., New York, USA., 1996

[32] J. M. Silcock, 'The structural ageing characteristics of Al-Cu-Mg alloys with copper:magnesium weight ratios of 7:1 and 2.2:1', *J. Inst. Metals*, 1960-61, **89**, 203-210.

[33] S. P. Ringer, K. Hono, I. J. Polmear, and T. Sakurai, 'Precipitation processes during the early stages of ageing in Al-Cu-Mg alloys', *Appl. Surf. Sci.*, 1996, **94-95**, 253-260.

[34] S. P. Ringer, K. Hono, I. J. Polmear, and T. Sakurai, 'Nucleation of precipitates in aged Al-Cu-Mg-(Ag) alloys with high Cu:Mg ratios', *Acta Mater.*, 1996, **44**, 1883-1898.

[35] S. P. Ringer, K. Hono, T. Sakurai, and I. J. Polmear, 'Cluster hardening in an aged Al-Cu-Mg alloy', *Scripta mater.*, 1997, **36**, 517-521.

[36] S. P. Ringer, T. Sakurai, and I. J. Polmear, 'Origins of hardening in aged Al-Cu-Mg-(Ag) alloys', *Acta Mater.*, 1997, **45**, 3731-3744.

[37] L. Reich, S. P. Ringer, and K. Hono, 'Origin of the initial rapid age hardening in an Al-1.7 at. % Mg-1.1 at.% Cu alloy', *Philos. Mag. Lett.*, 1999, **79**, 639-648.

[38] A. Charai, T. Walther, C. Alfonso, A. M. Zahra, and C. Y. Zahra, 'Coexistence of clusters, GPB zones, S "-, S '- and S-phases in an Al-0.9% Cu-1.4% Mg alloy', *Acta Mater.*, 2000, **48**, 2751-2764.

[39] S. P. Ringer, S. K. Caraher, and I. J. Polmear, 'Response to comments on cluster hardening in an aged Al-Cu-Mg alloy', *Scripta mater.*, 1998, **39**, 1559-1567.

[40] P. Ratchev, B. Verlinden, P. De Smet, and P. Van Houtte, 'Precipitation hardening of an Al-4.2wt%Mg-0.6wt%Cu alloy', *Acta Mater.*, 1998, **46**, 3523-3533.

[41] S. Abis, M. Massazza, P. Mengucci, and G. Riontino, 'Early ageing mechanisms in a high-copper AlCuMg alloy', *Scripta mater.*, 2001, **45**, 685-691.

[42] A. M. Zahra, C. Y. Zahra, C. Alfonso, and A. Charai, 'Comments on "Cluster hardening in an aged Al-Cu-Mg alloy"', *Scr. Mater.*, 1998, **39**, 1553-1558.

[43] Y. A. Bagaryatsky, 'On the nature of natural ageing of aluminium alloys', *Dokl. Akad. S.S.S.R.*, 1952, **87**, 559-562.

[44] H. C. Shih, N. J. Ho, and J. C. Huang, 'Precipitation behaviors in Al-Cu-Mg and 2024 aluminum alloys', *Metall. Mater. Trans. A*, 1996, **27**, 2479-2494.

[45] N. Gao, L. Davin, S. Wang, A. Cerezo, and M. J. Starink, 'Precipitation in stretched Al-Cu-Mg alloys with reduced alloying content studied by DSC, TEM and atom probe', *Mater. Sci. Forum*, 2002, **396-402**, 923-928.

[46] N. Gao, N. Kamp, I. Sinclair, and M. J. Starink, 'Innovation of age forming through development of novel damage tolerant alloys (report on DARP project)', University of Southampton, 2002.

[47] S. Wang, M. J. Starink, and N. Gao, 'Precipitation hardening in Al-Cu-Mg alloys revisited', *Scripta Mater.*, 2006, **54**, 287-291.

[48] V. Radmilovic, G. Thomas, G. J. Shiflet, and E. A. Starke, 'On the Nucleation and Growth of Al_2CuMg (S') in Al-Li-Cu-Mg and Al-Cu-Mg Alloys', *Scripta Metall.*, 1989, **23**, 1141-1146.

[49] L. F. Davin, 'Ultra-fine Characterisation of Nanostructures in Al-(Li)-Cu-Mg-(Zr) alloys by Three-Dimensional Atom Probe', PhD thesis, Oxford University, 2004.

[50] M. K. Miller, A. Cerezo, M. G. Hetherington, and G. D. W. Smith, *Atom probe field-ion microscopy*, Oxford University Press, 1996.

[51] M. J. Starink, N. Gao, L. Davin, J. Yan, and A. Cerezo, 'Room temperature precipitation in quenched Al–Cu–Mg alloys: a model for the reaction kinetics and yield strength development', *Philos. Mag.*, 2005, **85**, 1395-1417.

[52] Y. A. Bagaryatsky, 'Mechanism of artificial ageing of alloy Al-Cu-Mg', *Dokl. Akad. S.S.S.R.*, 1952, **87**, 397-401.

[53] F. Cuisiat, P. Duval, and R. Graf, 'Study on the 1st Stages of Decomposition of an Al-Cu-Mg Alloy', *Scripta Metall.*, 1984, **18**, 1051-1056.

[54] L. Kovarik, P. I. Gouma, C. Kisielowski, S. A. Court, and M. J. Mills, 'A HRTEM study of metastable phase formation in Al-Mg-Cu alloys during artificial aging', *Acta Mater.*, 2004, **52**, 2509-2520.

[55] R. N. Wilson and P. G. Partridge, 'The nucleation and growth of S' precipitates in an aluminium-2.5% copper-1.2% magnesium alloy', *Acta Metall.*, 1965, **13**, 1321-1327.

[56] L. Kovarik, P. I. Gouma, C. Kisielowski, S. A. Court, and M. J. Mills, 'Decomposition of an Al-Mg-Cu alloy - a high resolution transmission electron microscopy investigation', *Mater. Sci. Eng.A*, 2004, **387-89**, 326-330.

[57] S. C. Wang and M. J. Starink, 'The assessment of GPB2/S " structures in Al-Cu-Mg alloys', *Mater. Sci. Eng. A*, 2004, **386**, 156-163.

[58] S. Wang and M. J. Starink, ' Precipitates and intermetallic phases in precipitation hardening Al–Cu–Mg–(Li) based alloys', *Int. Mater. Rev.*, 2005, **50**, 193-215.

[59] M. J. Starink and P. J. Gregson, 'S' and delta' phase precipitation in SiCp reinforced Al- 1.2wt.%Cu-1wt.%Mg-xLi alloys', *Mater. Sci. Eng. A*, 1996, **211**, 54-65.

[60] M. J. Starink and P. J. Gregson, 'A Quantitative Interpretation of DSC Experiments on Quenched and Aged SiCp Reinforced 8090-Alloys', *Scripta Metall. Mater.*, 1995, **33**, 893-900.

[61] A. K. Gupta, P. Gaunt, and M. C. Chaturvedi, 'The Crystallography and Morphology of the S'-Phase Precipitate in an Al(Cumg) Alloy', *Philos. Mag. A*, 1987, **55**, 375-387.

[62] H. M. Flower and P. J. Gregson, 'Critical-Assessment - Solid-State Phase-Transformations in Aluminum-Alloys Containing Lithium', *Mater. Sci. Technol.*, 1987, **3**, 81-90.

[63] H. Perlitz and A. Westgren, 'The crystal structure of Al_2CuMg', *Ark Chem, Miner. Geol.*, 1943, **16B**, 1-5.

[64] Y. Jin, C. Z. Li, and M. G. Yan, 'On the Crystal-Structure of S' Phase in Al-Cu-Mg Alloy', *J. Mater. Sci. Lett.*, 1990, **9**, 421-424.

[65] V. Radmilovic, R. Kilaas, U. Dahmen, and G. J. Shiflet, 'Structure and morphology of S-phase precipitates in aluminum', *Acta Mater.*, 1999, **47**, 3987-3997.

[66] R. Kilaas and V. Radmilovic, 'Structure determination and structure refinement of Al_2CuMg precipitates by quantitative high-resolution electron microscopy', *Ultramicroscopy*, 2001, **88**, 63-72.

[67] C. Wolverton, 'Crystal structure and stability of complex precipitate phases in Al-Cu-Mg-(Si) and Al-Zn-Mg alloys', *Acta Mater.*, 2001, **49**, 3129-3142.

[68] H. K. Hardy, 'The ageing characteristics of binary aluminium-copper alloys', *J. Inst. Metals*, 1951, **79**, 321-369.

[69] H. K. Hardy, 'Ageing curves at 110°C on binary and ternary aluminium-copper alloys', *J. Inst. Metals*, 1953-54, **82**, 236-238.

[70] W. L. Fink, D. W. Smith, and L. A. Willey, 'Precipitation hardening of high purity binary and ternary aluminum-copper alloys', in: *Age hardening of metals*, p.31-55, 1940, ASM.

[71] Y. Nagai, M. Murayama, Z. Tang, T. Nonaka, K. Hono, and M. Hasegawa, 'Role of vacancy-solute complex in the initial rapid age hardening in an Al-Cu-Mg alloy', *Acta Mater.*, 2001, **49**, 913-920.

[72] A. Somoza, M. P. Petkov, K. G. Lynn, and A. Dupasquier, 'Stability of vacancies during solute clustering in Al-Cu-based alloys', *Phys. Rev. B*, 2002, **65**, art. no.-094107.

[73] T. Sato, 'Early stage phenomena and role of microalloying elements in phase decomposition of aluminum alloys', *Mater. Sci. Forum*, 2000, **331-7**, 85-96.

[74] R. Ferragut, A. Somoza, A. Dupasquier, and I. J. Polmear, 'Mechanisms of age-hardening in two Al-Cu-Mg alloys studied by Positron Annihilation Spectroscopy', *Mater. Sci. Forum*, 2002, **396-4**, 777-781.

[75] K. Raviprasad, C. R. Hutchinson, T. Sakurai, and S. P. Ringer, 'Precipitation processes in an Al-2.5Cu-1.5Mg (wt. %) alloy microalloyed with Ag and Si', *Acta Mater.*, 2003, **51**, 5037-5050.

[76] M. J. Starink, N. Gao, and J. L. Yan, 'The origins of room temperature hardening of Al-Cu-Mg alloys', *Mater. Sci. Eng. A*, 2004, **387-89**, 222-226.

[77] N. Gao, N. Kamp, I. Sinclair, and M. J. Starink, 'Innovation of age forming through development of novel damage tolerant alloys (report on DARP project)', University of Southampton, 2001.

[78] I. J. Polmear, 'The effects of small additions of silver on the aging of some aluminum alloys', *Trans. Met. Soc. AIME*, 1964, **230**, 1331-1339.

[79] R. N. Wilson, D. M. Moore, and P. J. E. Forsyth, 'Effect of 0.25% silicon on precipitation porcesses in an aluminium-2.5% copper-1.2% magnesium alloy', *J.Inst.Metals*, 1967, **95**, 177-183.

[80] C. R. Hutchinson and S. P. Ringer, 'Precipitation processes in Al-Cu-Mg alloys microalloyed with Si', *Metall. Mater. Trans. A*, 2000, **31**, 2721-2733.

[81] R. N. Wilson, 'The effect of 0.24% silicon upon the initial stages of ageing of an Aluminium-2.5%Copper-1.2% Magnesium alloy', *J.Inst.Metals*, 1969, **97**, 80-86.

[82] S. Hirosawa, T. Sato, A. Kamio, and H. M. Flower, 'Classification of the role of microalloying elements in phase decomposition of Al based alloys', *Acta Mater.*, 2000, **48**, 1797-1806.

[83] S. P. Ringer, I. J. Polmear, and T. Sakurai, 'Effect of additions of Si and Ag to ternary Al-Cu-Mg alloys in the alpha+S phase field', *Mater. Sci. Eng. A*, 1996, **217**, 273-276.

[84] K. Hono, 'Nanoscale microstructural analysis of metallic materials by atom probe field ion microscopy', *Prog. Mater. Sci.*, 2002, **47**, 621-729.

[85] R. D. Schueller, A. K. Sachdev, and F. E. Wawner, 'Identification of a Cubic Precipitate Observed in an Al-4.3Cu-2Mg/SiC Cast Composite', *Scripta Metall. Mater.*, 1992, **27**, 617-622.

[86] S. C. Barr, L. M. Rylands, H. Jones, and W. M. Rainforth, 'Formation and characteristics of coarsening resistant cubic sigma phase in Al-4 .2Cu-1.6Mg-0 .2Si', *Mater. Sci. Technol.*, 1997, **13**, 655-659.

[87] I. C. Barlow, W. M. Rainforth, and H. Jones, 'The role of silicon in the formation of the ($Al_5Cu_6Mg_2$) sigma phase in Al-Cu-Mg alloys', *J. Mater. Sci.*, 2000, **35**, 1413-1418.

[88] B. M. Gable, G. J. Shiflet, and E. A. Starke, 'The effect of Si additions on Omega precipitation in Al-Cu-Mg- (Ag) alloys', *Scripta Mater.*, 2004, **50**, 149-153.

[89] R. D. Schueller, F. E. Wawner, and A. K. Sachdev, 'Strengthening Potential of the Cubic-Sigma Precipitate in Al- Cu-Mg-Si Alloys', *J. Mater. Sci.*, 1994, **29**, 239-249.

[90] X. Gao, J. F. Nie, and B. C. Muddle, 'Effects of Si additions on the precipitation hardening response in Al-Cu-Mg(-Ag) alloys', *Mater. Sci. Forum*, 1996, **217**, 1251-1256.

[91] A. K. Mukhopadhyay, 'Coprecipitation of Ω and σ phases in Al-Cu-Mg-Mn alloys containing Ag and Si', *Metall. Mater. Trans. A.*, 2002, **33**, 3635-3648.

[92] Q. Li and F. E. Wawner, 'Characterization of a cubic phase in an Al-Cu-Mg-Ag alloy', *J. Mater. Sci.*, 1997, **32**, 5363-5370.

[93] M. F. Ashby, 'Physical Modeling of Materials Problems', *Mater. Sci. Technol.*, 1992, **8**, 102-111.

[94] M. J. Starink, I. Sinclair, P. A. S. Reed, and P. J. Gregson, 'Predicting the structural performance of heat-treatable Al- alloys', *Mater. Sci. Forum*, 2000, **331-3**, 97-110.

[95] P. Kolby, 'Applications of thermodynamically modelled phase diagram data in mathematical modelling of industrial processes', *Mater. Sci. Forum*, 1996, **217**, 661-666.

[96] F. L. Kaufman, 'Foreword', *CALPHAD*, 1977, **1**, 1-6.

[97] I. Ansara, 'Comparison of methods for thermodynamic calculation of phase diagrams', *Int. Metals Rev.*, 1979, **1**, 20-53.

[98] S. L. Chen, Y. Zuo, H. Liang, and Y. A. Chang, 'A thermodynamic description for the ternary Al-Mg-Cu system', *Metall. Mater. Trans. A*, 1997, **28**, 435-446.

[99] T. Buhler, S. G. Fries, P. J. Spencer, and H. L. Lukas, 'A thermodynamic assessment of the Al-Cu-Mg ternary system', *J. Phase Equilib.*, 1998, **19**, 317-333.

[100] D. H. Bratland, O. Grong, H. Shercliff, O. R. Myhr, and S. Tjotta, 'Modelling of precipitation reactions in industrial processing', *Acta Mater.*, 1997, **45**, 1-22.

[101] R. H. Brown and L. A. willey, 'Constitution of Alloys', in: K. R. Van Horn (Ed.), *Aluminium Vol.I: Properties, Physical Metallurgy and Phase Diagram*, p.31-54, 1967, ASM, ohio.

[102] M. J. Starink and P. J. Gregson, 'Thermodynamics and precipitation in 8090 (Al-Li-Cu-Mg-Zr) alloys studied by DSC and TEM', *Mater. Sci. Forum*, 1996, **217-222**, 673-678.

[103] J. W. Christian, *The Theory of Phase Transformations in Metals and Alloys*, 2nd edn, Pergamon, Oxford, 1975.

[104] R. D. Doherty, in: R. W. Cahn and P. Haasen (Eds.), *Physical Metallurgy, 3rd edn*, p.934, 1983, North-Holland Physics, Amsterdam.

[105] D. A. Porter and K. E. Easterling, *Phase Transformations in Metals and Alloys*, Chapman and Hall, London, 1992.

[106] R. Wagner and R. Kampmann, in: R. W. Cahn, P. Haasen, and E. J. Kramer (Eds.), *Materials Science and Technology: A Comprehensive Treatment Phase Transformations in Materials*, Vol. **5**, p.213, 1991, VCH, Weinheim.

[107] M. J. Starink and A. M. Zahra, 'An analysis method for nucleation and growth controlled reactions at constant heating rate', *Thermochim. Acta*, 1997, **292**, 159-168.

[108] A. Deschamps and Y. Brechet, 'Influence of predeformation and ageing of an Al-Zn-Mg alloy - II. Modeling of precipitation kinetics and yield stress', *Acta Mater.*, 1999, **47**, 293-305.

[109] O. R. Myhr and O. Grong, 'Modelling of non-isothermal transformations in alloys containing a particle distribution', *Acta Mater.*, 2000, **48**, 1605-1615.

[110] J. D. Robson and P. B. Prangnell, 'Dispersoid precipitation and process modelling in zirconium containing commercial aluminium alloys', *Acta Mater.*, 2001, **49**, 599-613.

[111] C. Sigli, 'Nucleation, growth and coarsening of spherical precipitates in aluminum alloys', *Mater. Sci. Forum*, 2000, **331-337**, 513-518.

[112] K. C. Russell, in: H. I. Aaronson (Ed.), *Phase Transformations*, p.219, 1970, Metals Park, Am.Soc. Metals.

[113] I. M. Lifshitz and V. V. Slyozov, 'The kinetics of precipitation from super-saturated solid solutions', *J. Phys. Chem.Solids*, 1961, **19**, 35-50.

[114] C. Wagner, 'Theorie der alterung von niederschlagen durch umlosen (Ostwald Reifung)', *Z. Elektrochem.*, 1961, **65**, 581-591.

[115] P. W. Voorhees, 'The Theory of Ostwald Ripening', *J. Stat. Phys.*, 1985, **38**, 231-252.

[116] A. Baldan, 'Review Progress in Ostwald ripening theories and their applications to nickel-base superalloys - Part I: Ostwald ripening theories', *J. Mater. Sci.*, 2002, **37**, 2171-2202.

[117] J. S. Langer and A. J. Schwartz, 'Kinetics of nucleation in near-critical fluids', *Phys. Rev. A.*, 1980, **21**, 948-958.

[118] H. Wendt and P. Haasen, 'Nucleation and Growth of γ'-Precipitates in Ni-14 at- Percent Al', *Acta Metall.*, 1983, **31**, 1649-1659.

[119] R. Kampmann and R. Wagner, in: P. Haasen, V. Gerold, R. Wagner, and M. F. Ashby (Eds.), *Decomposition of Alloys: the Early Stages*, p.91-103, 1984, Pergamon Press, New York.

[120] O. Grong and H. R. Shercliff, 'Microstructural modelling in metals processing', *Prog. Mater. Sci.*, 2002, **47**, 163-282.

[121] J. D. Robson, 'Optimizing the homogenization of zirconium containing commercial aluminium alloys using a novel process model', *Mater. Sci. Eng. A*, 2002, **338**, 219-229.

[122] J. C. Werenskiold, A. Deschamps, and Y. Brechet, 'Characterization and modeling of precipitation kinetics in an Al-Zn-Mg alloy', *Mater. Sci. Eng. A*, 2000, **293**, 267-274.

[123] M. Nicolas and A. Deschamps, 'Characterisation and modelling of precipitate evolution in an Al-Zn-Mg alloy during non-isothermal heat treatments', *Acta Mater.*, 2003, **51**, 6077-6094.

[124] W. A. Johnson and R. F. Mehl, 'Reaction kinetics in processes of nucleation and growth.' *Trans. Am. Inst. Min. Met. Engrs.*, 1939, **135**, 416.

[125] A. N. Kolmogorov, 'A statistical theory for the recrystallization of metals.' *Izv. Akad. Nauk SSSR, Ser. Mater.*, 1937, **1**, 355.

[126] M. Avrami, 'Kinetics of Phase Change. I: General Theory.' *J. Chem. Phys.*, 1939, **7**, 1103.

[127] M. Avrami, 'Kinetics of Phase Change. II: Transformation-Time relations for random distribution of nuclei.' *J. Chem. Phys.*, 1940, **8**, 212.

[128] M. Avrami, 'Kinetics of Phase Change. III: Granulation, Phase Change an Microstructures', *J. Chem. Phys.*, 1941, **9**, 177.

[129] V. Sessa, M. Fanfoni, and M. Tomellini, 'Validity of Avrami's kinetics for random and nonrandom distributions of germs', *Phys. Rev. B*, 1996, **54**, 836-841.

[130] G. Yu and J. K. L. Lai, 'Kinetics of transformation with nucleation and growth mechanism: Two- and three-dimensional models', *J. Appl. Phys.*, 1996, **79**, 3504-3511.

[131] G. Yu, 'General equation of the kinetics of phase transformations with a nucleation-and-growth mechanism', *Philos. Mag. Lett.*, 1997, **75**, 43-48.

[132] M. J. Starink, 'Kinetic equations for diffusion-controlled precipitation reactions', *J. Mater. Sci.*, 1997, **32**, 4061-4070.

[133] F. L. Cumbrera and F. SanchezBajo, 'The use of the JMAYK kinetic equation for the analysis of solid-state reactions: Critical considerations and recent interpretations', *Thermochim. Acta*, 1995, **266**, 315-330.

[134] J. B. Austin and R. L. Rickett, 'Kinetics of the decomposition of Austenite at constant tenperature', *Trans. Am. Inst. Min. Met. Engrs.*, 1939, **135**, 396.

[135] E. S. Lee and Y. G. Kim, 'A Transformation Kinetic-Model and Its Application to Cu-Zn-Al Shape Memory Alloys .1. Isothermal Conditions', *Acta Metall. Mater.*, 1990, **38**, 1669-1676.

[136] M. J. Starink and A. M. Zahra, 'Kinetics of isothermal and non-isothermal precipitation in an Al-6 at% Si alloy', *Philos. Mag. A*, 1998, **77**, 187-199.

[137] M. J. Starink, 'On the meaning of the impingement parameter in kinetic equations for nucleation and growth reactions', *J. Mater. Sci.*, 2001, **36**, 4433-4441.

[138] M. J. Starink and A. M. Zahra, 'β ' and β precipitation in an Al-Mg alloy studied by DSC and TEM', *Acta Mater.*, 1998, **46**, 3381-3397.

[139] M. J. Starink and A. M. Zahra, 'The kinetics of isothermal β ' precipitation in Al-Mg alloys', *J. Mater. Sci.*, 1999, **34**, 1117-1127.

[140] M. J. Starink, C. Y. Zahra, and A. M. Zahra, 'Analysis of precipitation in Al-based alloys using a novel model for nucleation and growth reactions', *J. Therm. Anal.*, 1998, **51**, 933-942.

[141] A. M. Zahra and M. J. Starink, in: R. Ciach (Ed.), *Advanced Light Alloys and Composites*, p.17, 1998, Kluwer Academic, Amsterdam.

[142] E. Orowan, in: *Symposium on Internal Stresses in Metals and Alloys. Session III Discussion.*, p.451, 1948, Institute of Metals, London.

[143] L. M. Brown and R. K. Ham, in: A. Kelly and R. B. Nicholson (Eds.), *Strengthening Methods in Crystals*, p.9, 1971, Elsevier, London.

[144] B. Reppich, 'Particle Strengthening', in: R. W. Cahn, P. Haasen, and E. J. Kramer (Eds.), *Materials Science and Technology: A Comprehensive Treatment Plastic Deformation and Fracture of Materials*, Vol. **6**, p.311-357, 1992, Wiley-VCH, Weinheim.

[145] U. F. Kocks, A. S. Argon, and M. F. Ashby, 'Thermodynamics and Kinetics of Slip', *Prog. Mater. Sci.*, 1975, **19**, 1-291.

[146] N. F. Mott and F. R. N. Nabarro, 'An attempt to estimate the degree of precipitation hardening with a simple model', *Proc. Phys. Soc.*, 1940, **52**, 86-89.

[147] E. Nembach and G. Neite, 'Precipitation Hardening of Superalloys by Ordered γ' Particles', *Prog. Mater. Sci.*, 1985, **29**, 177-319.

[148] E. Nembach, 'Order strengthening: recent developments, with special reference to aluminium-lithium-alloys', *Prog. Mater. Sci.*, 2000, **45**, 275-338.

[149] B. Clausen, T. Lorentzen, and T. Leffers, 'Self-consistent modelling of the plastic deformation of FCC polycrystals and its implications for diffraction measurements of internal stresses', *Acta Mater.*, 1998, **46**, 3087-3098.

[150] E. Sachs and Z. Ver, *Deutsch. Ing.*, 1928, **72**, 734.

[151] G. I. Taylor, *J. Inst. Metals*, 1938, **62**, 307.

[152] M. J. Starink, P. Wang, I. Sinclair, and P. J. Gregson, 'Microstrucure and strengthening of Al-Li-Cu-Mg alloys and MMCs: II. Modelling of yield strength', *Acta Mater.*, 1999, **47**, 3855-3868.

[153] M. J. Starink and S. C. Wang, 'A model for the yield strength of overaged Al-Zn-Mg-Cu alloys', *Acta Mater.*, 2003, **51**, 5131-5150.

[154] J. C. Huang and A. J. Ardell, 'Addition Rules and the Contribution of Delta' Precipitates to Strengthening of Aged Al-Li-Cu Alloys', *Acta Metall.*, 1988, **36**, 2995-3006.

[155] E. Nembach, *Particle Strengthening of Metals and Alloys*, John Wiley & Sons, New York, 1996.

[156] A. J. E. Foreman and M. J. Makin, 'Discolation movement through random arrays of obstacles', *Can. J. Phys.*, 1967, **45**, 511-518.

[157] K. Hanson and J. W. Morris, Jr., 'Estimation of the critical resolved shear stress for discolation glide through a random mixture of distinct obstacles', *J.Appl. Phys.*, 1975, **46**, 2378-2383.

[158] A. W. Zhu, A. Csontos, and E. A. Starke, 'Computer experiment on superposition of strengthening effects of different particles', *Acta Mater.*, 1999, **47**, 1713-1721.

[159] U. Lagerpusch, V. Mohles, D. Baither, B. Anczykowski, and E. Nembach, 'Double strengthening of copper by dissolved gold-atoms and by incoherent SiO2-particles: How do the two strengthening contributions superimpose?' *Acta Mater.*, 2000, **48**, 3647-3656.

[160] H. R. Shercliff and M. F. Ashby, 'A Process Model for Age Hardening of Aluminum-Alloys .1. The Model', *Acta Metall. Mater.*, 1990, **38**, 1789-1802.

[161] P. A. Rometsch and G. B. Schaffer, 'An age hardening model for Al-7Si-Mg casting alloys', *Mater. Sci. Eng. A.*, 2002, **325**, 424-434.

[162] X. M. Li, *PhD Thesis*, University of Southampton, 2001.

[163] M. J. Starink, X. M. Li, and S. C. Wang, 'Models for the yield strength of Al-Zn-Mg-Cu alloys', in: M. Tiryakioglu and L. A. Lalli (Eds.), *1st International Symposium on Metallurgical Modeling for Aluminum Alloys, ASM Materials Solution 2003*, Pittsburgh, PA, October 12-15, 2003, p.105-118.

[164] W. J. Poole, H. R. Shercliff, and T. Castillo, 'Process model for two step age hardening of 7475 aluminium alloy', *Mater. Sci. Technol.*, 1997, **13**, 897-904.

[165] W. J. Poole, J. A. Saeter, S. Skjervold, and G. Waterloo, 'A model for predicting the effect of deformation after solution treatment on the subsequent artificial aging behavior of AA7030 and AA7108 alloys', *Metall. Mater. Trans. A*, 2000, **31**, 2327-2338.

[166] O. R. Myhr, O. Grong, and S. J. Andersen, 'Modelling of the age hardening behaviour of Al-Mg-Si alloys', *Acta Mater.*, 2001, **49**, 65-75.

[167] G. Liu, G. J. Zhang, X. D. Ding, J. Sun, and K. H. Chen, 'Modeling the strengthening response to aging process of heat- treatable aluminum alloys containing plate/disc- or rod/needle- shaped precipitates', *Mater. Sci. Eng.*, 2003, **344**, 113-124.

[168] S. Esmaeili, D. J. Lloyd, and W. J. Poole, 'A yield strength model for the Al-Mg-Si-Cu alloy AA6111', *Acta Mater.*, 2003, **51**, 2243-2257.

[169] S. Esmaeili, D. J. Lloyd, and W. J. Poole, 'Modeling of precipitation hardening for the naturally aged Al- Mg-Si-Cu alloy AA6111', *Acta Mater.*, 2003, **51**, 3467-3481.

[170] P. Gomiero, Y. Brechet, F. Louchet, A. Tourabi, and B. Wack, 'Microstructure and Mechanical-Properties of a 2091 Al-Li Alloy .2. Mechanical-Properties - Yield Stress and Work-Hardening', *Acta Metall. Mater.*, 1992, **40**, 857-861.

[171] C. Genevois, A. Deschamps, A. Denquin, and B. Doisneau-cottignies, 'Quantitative investigation of precipitation and mechanical behaviour for AA2024 friction stir welds', *Acta Mater.*, 2005, **53**, 2447-2458.

[172] M. J. Starink, P. Wang, I. Sinclair, and P. J. Gregson, 'Microstructure and strengthening of Al-Li-Cu-Mg alloys and MMCs: I. Analysis and modelling of microstructural changes', *Acta Mater.*, 1999, **47**, 3841-3853.

[173] J. Bradley and P. Jones, 'An X-ray investigation of the Cu–Al alloys', *J. Inst. Metals*, 1933, **51**, 131-162.

[174] L. Cartaud, J. Guillot, and J. Grilhe, 'Influence of mode of zones formation on elastic limit', in: *Proc. ICSMA IV*, Vol. **1**, Nancy, 1976, p.214.

[175] A. Melander and P. A. Persson, 'The strength of a precipitation hardened AlZnMg alloy', *Acta Metall.*, 1978, **26**, 267-278.

[176] E. Nembach, 'Precipitation hardening caused by a difference in shear modulus between particle and matrix', *Physica status solidi (A)*, 1983, **78**, 571-581.

[177] D. J. Strawbridge, W. Hume-Rothery, and A. T. Little, 'The constitution of aluminium-copper-magnesium-zinc alloys at 460°C', *J. Inst. Metals*, 1948, **74**, 191-225.

Chapter 3 Experimental

This chapter presents the materials studied and the experimental techniques used for mechanical tests and microstructure characterisation. The aim of the experimental work is to provide data for model input and model validation. Vickers hardness and tensile tests were used to evaluate the ageing behaviour of the alloys. DSC and isothermal calorimetry were used to study the precipitation sequence and precipitation kinetics. TEM and image analysis were used to obtain the precipitate size distribution and mean equivalent radius of the precipitates. The experimental results and analysis will be given in Chapter 4.

3.1 Materials

Most of the experimental work in this study was carried out on a 12.5mm thick commercial 2024-T351 Al-Cu-Mg type aluminium alloy (referred to as alloy A). The T351 temper indicates the alloy has been solution treated, water quenched, stress relieved by stretching to about 1% to 3% plastic deformation and then naturally aged. In addition, two 2024 type alloys (referred to as alloys B and C) and an alloy with reduced Cu and Mg contents (referred to as alloy D) available from other projects at the University of Southampton [1, 2] were studied. Alloys B and D were supplied by QinetiQ as 20mm thick plate. They were solution treated at 495°C, cold water quenched and stretched by 2.5% prior to natural ageing [1]. Alloy C is a 12mm thick 2024-T351 plate taken from the central part (mid-thickness) of a 40mm thick plate [2]. The compositions are given in **Table 3.1**. It is seen that alloy C has relatively high Si and Fe contents compared with the other three alloys.

Grain structures of alloys B, C and D have been examined using optical microscopy [1-3]. All alloys exhibit similar plate-shaped grains. The grain size was measured using the conventional mean linear intercept method. Alloy B is fully recrystallised and has an average grain size in the transverse-short transverse (TS) plane of 157μm [3]. The mean grain dimensions of alloy C were measured as 312μm, 121μm and 57μm in the longitudinal (L), transverse (T) and short transverse (S) directions, respectively [2]. Scanning electron microscopy (SEM) investigation of alloys B, C and D showed coarse intermetallic particles. The main particles were identified by means of SEM and energy dispersive spectroscopy (EDS) as undissolved S particles and clusters of particles containing Cu, Fe and Mn. The clusters are most likely to be a mixture of Al_7Cu_2Fe and $Al_{20}Cu_2Mn_3$ with Al_7Cu_2Fe in the majority [1-3].

The age hardening behaviour of alloys B and D has been studied previously by collaborators (for details see [1, 3-5] and Chapter 2 in this thesis). **Table 3.2** gives the mechanical properties obtained from tensile tests on alloys B and D during ageing at 150°C and 190°C, together with data for alloy C in the as-received condition. The results show that alloy C has higher yield strength (YS) (the flow stress at 0.2% offset plastic strain) and ultimate tensile strength (UTS) compared with alloy B.

3.2 Heat treatments

3.2.1 Artificial ageing

Further artificial ageing on as-received samples was performed in an air-circulating furnace. Tensile samples of alloy A were aged at 120°C, 170°C and 220°C. Rectangular samples of alloy A, approximately 20mm long × 12mm wide × 12mm thick, were aged at 120°C, 150°C, 170°C, 200°C and 220°C for hardness tests and calorimetric studies. The samples were loaded into the furnace set at ageing temperature, and it took approximately 15-20min for the samples to heat up to temperature. To take this heating effect into account and provide a consistent measure of ageing time, the concept of an equivalent time or temperature compensated time [6] was used.

By definition, the equivalent time t_{eq} is the time at a certain isothermal temperature T_{iso} required to have the same amount transformed that can be obtained in a non-isothermal heat treatment, or in a different isothermal temperature. When the sample is held at a different isothermal temperature T for a time t, it is converted to t_{eq} at T_{iso} as:

$$t_{eq} = t\exp(-\frac{E_a}{RT})/\exp(-\frac{E_a}{RT_{iso}}) \tag{3.1}$$

where t is the time held at temperature T, E_a is the appropriate activation energy associated with the reaction process and R is the gas constant. For non-isothermal heat treatment, the extent of ageing can be expressed as [7]:

$$t_{eq} = \int \exp(-\frac{E_a}{RT})dt/\exp(-\frac{E_a}{RT_{iso}}) \tag{3.2}$$

In this study, after the samples were put into the furnace, the increase of the furnace temperature with time to reach the set temperature was recorded and the actual isothermal ageing time was calculated using Eq.(3.2) with E_a approximated by the activation energy for diffusion of solute atom (Cu or Mg) as 130kJ/mol. The ageing times reported in this thesis are corrected times according to Eq.(3.2).

To study the effect of Si addition on the age hardening and the coarsening of the precipitates, samples of alloys A and C, approximately 5mm × 5mm× 1mm, were cut from slices which were machined from the as-received samples using a precision saw. These small samples were aged (in the DSC cells) at 190°C for times up to 30 days. Vickers micro-hardness tests and TEM were conducted on these samples.

3.2.2 Natural ageing

To study the natural ageing response of 2024 type alloys, rectangular samples of alloys A and B were re-solution treated at 495°C for 30 min then water quenched and aged at room temperature.

3.2.3 Multi-stage ageing

Based on the ageing curves obtained from the above artificial ageing (Section 3.2.1), two sequences of multi-stage heat treatments were carried out in the DSC cells on two as-received T351 samples (approximately 5mm × 5mm× 1mm) of alloy A to identify the contributions of different precipitates to the overall strength in underaged condition, i.e. on the rise to the peak strength. For one heat treatment route, samples were aged at 170°C for 1h to reach the plateau hardness, and then aged at 220°C for 5min and 10 min to dissolve the pre-precipitates and to precipitate out some further precipitates, followed by room temperature ageing. The other route involved ageing of samples at 150°C from 0.5h to 8h, then ageing at 200°C from 5 min to 1h before natural ageing. The time interval between consecutive heat treatments was limited to around 15min. Vickers micro-hardness tests were carried out immediately after each step of heat treatments.

3.3 Vickers hardness tests

For larger samples, Vickers hardness tests were carried out using a standard testing machine with a load of 20 kg. For small size samples, Vickers micro-hardness tests were employed with a load of 1 kg for a dwell time of 15 seconds. For all the samples, tests were conducted immediately after heat treatments on the TS cross section of the plate. Measurements were made on the surfaces of samples ground to 1200 grit with SiC paper. Five indentations were made on each surface and the average hardness is reported.

3.4 Tensile tests

Tensile tests were carried out on an Instron 1196 tensile tests machine with a crosshead speed of 10mm/min at room temperature in accordance with ASTM standard E8 [8]. A strain gauge extensometer with a gauge length of 12.5 mm and a travel distance of 5mm was employed to measure strain. A digital data logger was used to collect data which correspond to load and elongation values directly from load cell and the extensometer every 0.8 second. Round tensile samples with shouldered ends were machined paralleled to the longitudinal (rolling) direction of the plates with

a 25mm gauge length and a 5mm diameter. Two samples for each heat treatment condition were tested. The obtained engineering stress and strain data up to the onset of necking were converted into true stress and strain data according to:

$$\varepsilon = \ln(e+1) \tag{3.3}$$

$$\sigma = s(e+1) \tag{3.4}$$

where σ and ε are the true stress and true strain, and s and e are engineering stress and strain, respectively. YS, UTS, elongation to fracture and the strain-hardening exponent were measured for each sample. The strain-hardening exponent was obtained from the slope of a log-log plot of true stress and true strain for strain between 1 and 5%.

3.5 Differential scanning calorimetry and isothermal calorimetry

Disc-shaped samples, 5 mm in diameter by approximately 1 mm thick, were punched from the slices machined from the as-received and the aged samples. Both DSC and differential isothermal calorimetry (DIC) measurements were carried out on a power-compensating Perkin-Elmer Pyris-1 calorimeter, using nitrogen gas as a protective atmosphere. An empty pure aluminium sample pan was used as a reference sample. For artificially aged samples and as-received samples, DSC runs were performed from 5°C to 540°C at a heating rate of 10°C/min. For the determination of the activation energy, three heating rates of 5°C/min, 10°C/min and 20°C/min were used for selected samples. For the study of cluster formation, the disc-shaped samples were re-solution treated at 495°C for 30 min, water quenched and aged at room temperature. For DSC runs on as-quenched samples, the samples were introduced into the calorimeter within three minutes of quenching.

All DSC traces were corrected by subtracting a baseline obtained from a DSC run with empty pans. A further correction was performed to correct for the combined effect of heat capacity differences and small baseline fluctuations. The method used here has been applied and validated for a range of alloys [6]. In this method, three points on the DSC curve where no reaction occurs, i.e. the heat flows are zero, need to

be identified. Then a second order polynomial function fit through these points is used to determine the heat flow due to heat capacity differences and small baseline fluctuations. The first point is readily defined as the initial part of the DSC curve which is after the transient period and before the start of first reaction. The second point is the temperature where all the precipitation and dissolution reactions are completed. In the case of the alloys studied, this point was taken as the temperature corresponding to maximum heat flow between the final dissolution effect and the incipient melting, which was around 498°C. The third point can be found at the transition from the first precipitation effect to its dissolution effect. This point was chosen so that for freshly quenched samples, the heat evolved of the exothermic peak due to cluster formation was equal to or slightly larger than that of the endothermic peak due to cluster dissolution considering the overlap of the endothermic effect with subsequent exothermic effect. The validity of this point was checked by the DSC curves of re-solution treated, water quenched and naturally aged samples, as at these stages the heats evolved due to cluster dissolution should be identical. The coefficients of the second order polynomial function were then obtained by fitting the heat flows at these three points. In the present studies, the three points were taken as 30°C, 140°C and 498°C for a heating rate of 10°C/min. Thus in the presented DSC curves, the heat effects are due to reactions only. An example for the second order polynomial correction is given in **Fig. 3.1**. The heat evolved ΔQ is obtained by integrating the heat flow dQ/dT (in J/g °C) of the peak over temperature T. This three-point heat capacity correction does not alter the position of the exothermic or endothermic peaks. Varying the second point temperature of 140°C by ±5°C led to deviations in the heat evolved for cluster formation effect (the exothermic peak centred at about 70°C) up to 0.5J/g and for S precipitation effect (the exothermic peak centred at about 270°C) up to 0.3J/g.

DIC experiments were performed in the temperature range of 200°C to 250°C. The samples were introduced into the DSC held at the desired temperature. Baseline drift was corrected for by continuing the experiments long after the completion of the precipitation process and then linearly extrapolating the baseline back to t=0 [9]. An example is given in **Fig. 3.2**. Generally, baseline drifts were small. The total heat

evolved, ΔQ, during the isothermal process is determined by integrating the heat flow dQ/dt (in W/g) over time t for the exothermic heat effect.

3.6 Transmission electron microscopy and image analysis

TEM studies were carried out on samples of alloys A and C aged at 190°C for 96h (4 days) and 720h (30 days) to investigate the coarsening of the precipitates. Slices of 0.4mm thickness were cut and mechanically ground with SiC paper down to about 0.2mm thickness. Thin foils were prepared by punching 3 mm diameter discs from the slices, which were then thinned by electropolishing in a 3:1 methanol-nitric acid solution cooled to about -30°C using a Struers Tenupol with an applied potential of 20-30V and subsequently rinsed in methanol.

Microstructural investigation was carried out on a JEOL JEM 3010 TEM operating at 300kV. Digital bright field (BF) images and corresponding selected area electron diffraction (SAD) patterns were taken near the [001] zone axis. The quantitative microstructural measurements were performed on BF images using Carl Zeiss KS300 image analysis software. For each ageing condition, several BF images from different locations were analysed to count as many precipitate particles as possible to provide good statistical significance. Morphological parameters such as filled area, minimum to maximum feret ratio and equivalent diameter for each end-on particle were measured. The equivalent diameter is defined as the diameter of circular precipitates with identical cross-sectional area to the non-circular precipitates. For images with good contrast between the particles and the matrix, a semi-automated procedure for image analysis was adopted, involving image filtering (smoothing, shading), segmentation (adaptive thresholding), binary image polishing (scrap, fill holes), particle selection and automatic measurement. A binary image showing features close to the original grey level image can be obtained by properly selecting the segmentation parameters. This was done manually by trial-and-error based on the visual comparison of the original image and the resulting binary image. An example is shown in **Fig. 3.3**. Incomplete particles at the edge of the image were excluded from the analysis. Particle selection was conducted in two modes. In the first mode, particles are selected automatically and subsequently a manual correction is applied

by eliminating side-on variants and coalesced end-on particles (referred to as semi-auto Mode I). The other is that particles are selected manually on the binary images (referred to as semi-auto Mode II). Images with poor contrast for semi-automated analysis were measured manually by selecting the particles of interest on the background corrected images using the interactive measurement method (referred to as manual). Particles with filled area larger than 2000 pixel^2 or smaller than 60 pixel^2, or particles with a maximum to minimum feret ratio larger than 5 were further excluded.

It is desirable to obtain a reliable estimate of precipitate volume fraction from TEM images for modelling of the mechanical properties. To this end, knowledge of foil thickness and precipitate length or aspect ratio are required to correct the overestimation of the volume fraction due to section effect (i.e. particles are cut by the surfaces of the foil). In this study, no foil thickness measurement was carried out, and the high density of side-on particles makes it difficult to measure the length. Therefore meaningful volume fraction of the precipitates cannot be derived from TEM images. Here only the equivalent diameter is reported and used for the evaluation of the precipitate size.

Table 3.1 Chemical composition of alloys studied in this work

Alloy	Cu	Mg	Mn	Si	Fe	Cu/Mg	
Alloy A[a]	4.20	1.36	0.58	0.06	0.08	3.09	(wt.%)
	1.83	1.55	0.29	0.06	0.04	1.18	(at.%)
Alloy B[b]	4.17	1.31	0.41	0.02	0.04	3.18	(wt.%)
	1.82	1.49	0.20	0.02	0.02	1.22	(at.%)
Alloy C[c]	4.07	1.36	0.54	0.12	0.20	2.99	(wt.%)
	1.77	1.55	0.27	0.12	0.10	1.14	(at.%)
Alloy D[b]	2.77	1.06	0.40	0.03	0.05	2.62	(wt.%)
	1.19	1.19	0.20	0.03	0.02	1.00	(at.%)

[a] Analysed by Bodycote Materials Testing Ltd using Inductively Coupled Plasma Optical Emission Spectroscopy (ICP-OES)

[b] Taken as average composition from QinetiQ analysis [1] and from ICP-OES analysis by Bodycote Materials Testing Ltd.

[c] From [2].

Table 3.2 Mechanical properties in longitudinal direction of alloys*

Alloy	Ageing treatment (h/°C)	Hv (VPN)	YS (MPa)	UTS (MPa)	Elongation (25mm)%
Alloy B	as-received		340	451	20.6
Alloy B	12/150	137	330	440	20.6
Alloy B	24/150	138	339	445	20.0
Alloy B	48/150	147	371	463	18.0
Alloy B	72/150	153	404	474	15.9
Alloy B	as-received		340	451	20.6
Alloy B	6/190	161	463	494	10.1
Alloy B	12/190	156	447	482	10.1
Alloy B	24/190	150	428	473	10.2
Alloy B	48/190	146	406	463	10.3
Alloy D	as-received	114	272	369	22.6
Alloy D	12/150	117	264	366	22.8
Alloy D	24/150	118	270	371	23.6
Alloy D	48/150	119	279	373	24.4
Alloy D	72/150	127	309	390	22.8
Alloy D	as-received	114	272	369	22.6
Alloy D	6/190	128	380	405	12.1
Alloy D	12/190	129	378	403	11.6
Alloy D	24/190	128	374	409	12.8
Alloy D	48/190	124	354	398	12.7
Alloy C	as-received		372	483	21.4

*Data for alloys B and D are from [1], data for alloy C are from [2].

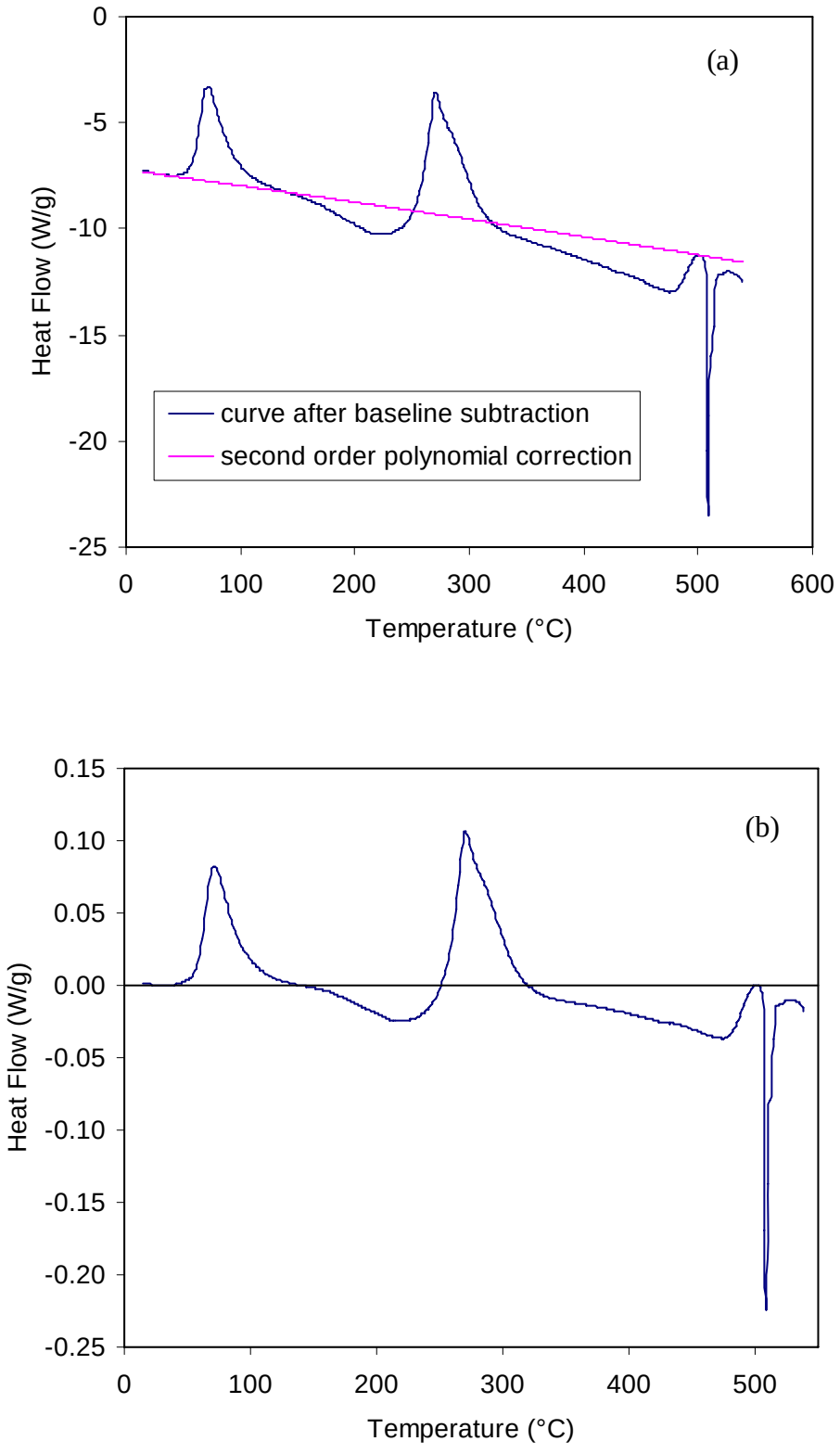

Fig. 3.1 Illustration of heat flow correction for DSC curve: (a) curve after baseline subtraction and second order polynomial correction; (b) final corrected curve.

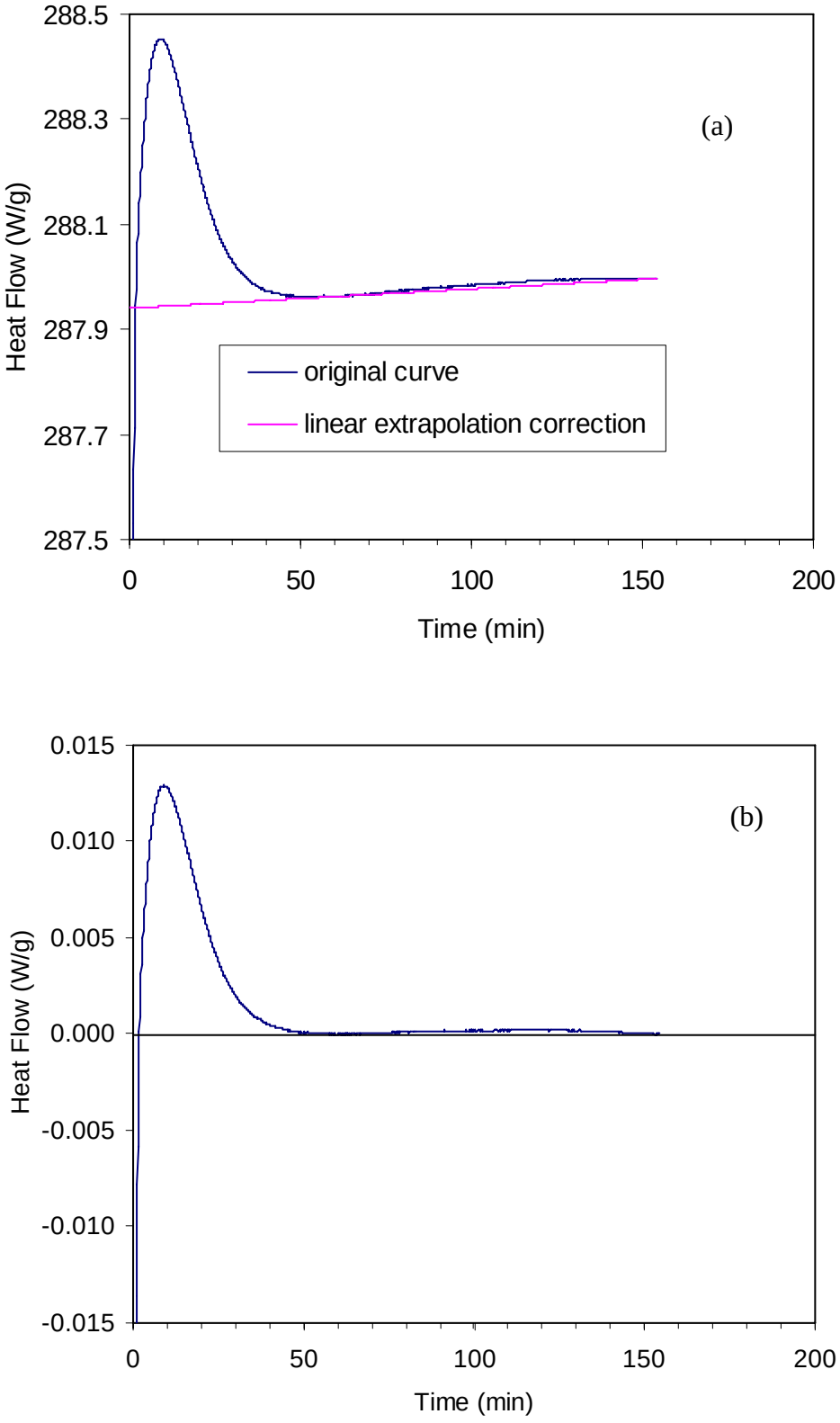

Fig. 3.2 Illustration of heat flow correction for DIC curve: (a) original curve and linear extrapolation correction; (b) final corrected curve.

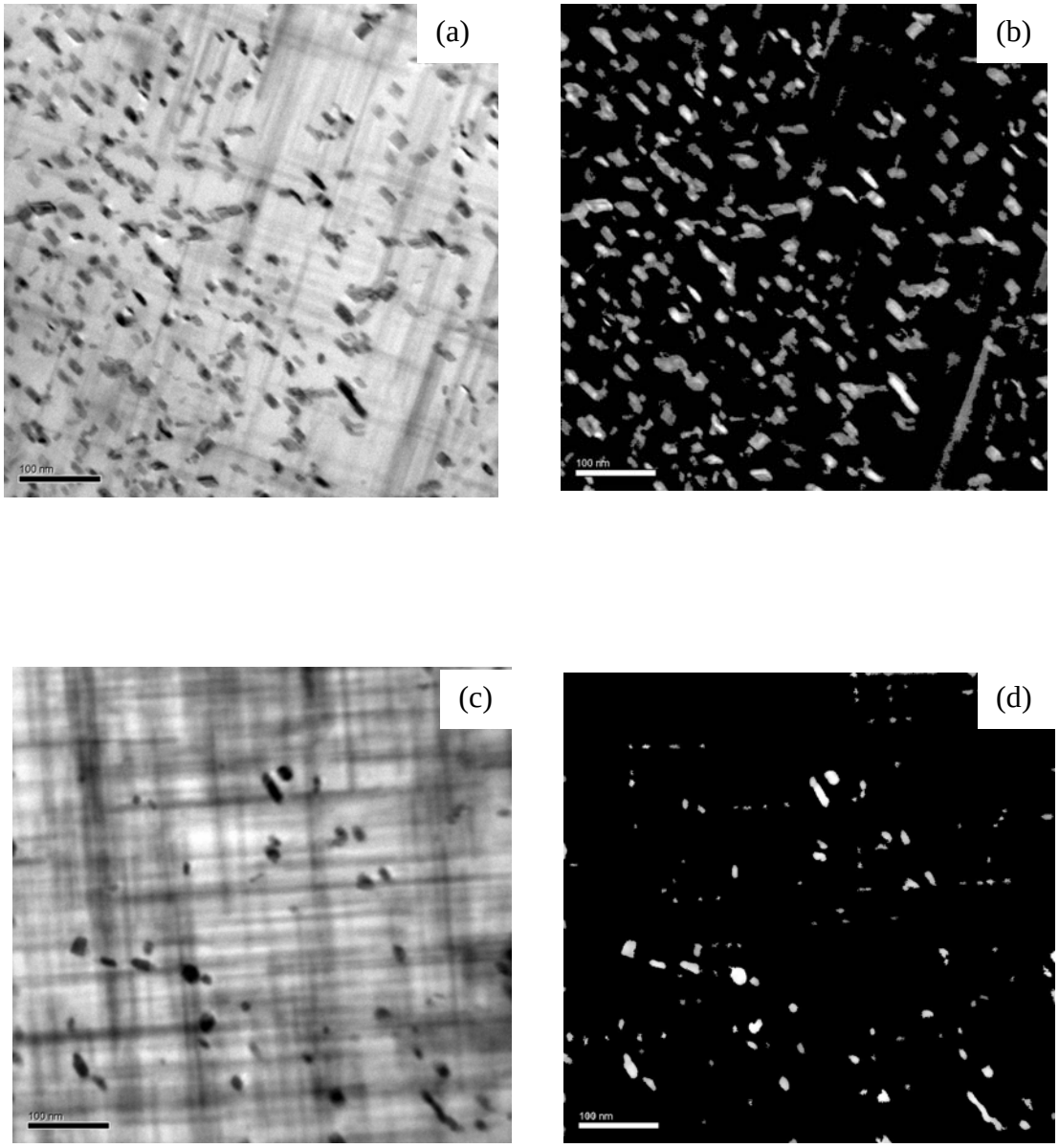

Fig. 3.3 Illustration of original bright field TEM images (a, c) and corresponding binary images (b, d) obtained from image analysis software.

References

[1] N. Gao, N. Kamp, I. Sinclair, and M. J. Starink, 'Innovation of age forming through development of novel damage tolerant alloys (report on DARP project)', University of Southampton, 2001.

[2] Y. Xu, 'Variable amplitude loading effects on damage tolerant airframe materials', PhD Thesis, University of Southampton, 2000.

[3] N. Kamp, N. Gao, I. Sinclair, and M. J. Starink, 'Innovation of age forming through development of novel damage tolerant alloys (report on DARP project)', University of Southampton, 2004.

[4] M. J. Starink, N. Gao, L. Davin, J. Yan, and A. Cerezo, 'Room temperature precipitation in quenched Al–Cu–Mg alloys: a model for the reaction kinetics and yield strength development', *Phil. Mag.*, 2005, **85**, 1395-1417.

[5] N. Gao, N. Kamp, I. Sinclair, and M. J. Starink, 'Innovation of age forming through development of novel damage tolerant alloys (report on DARP project)', University of Southampton, 2002.

[6] M. J. Starink, 'Analysis of aluminium based alloys by catorimetry: quantitative analysis of reactions and reaction kinetics', *Int. Mater. Rev.*, 2004, **49**, 191-226.

[7] R. Shahani, J. F. Verdier, P. Lassince, G. M. Raynaud, C. Sigli, and P. Sainfort, 'Thick AlZnMgCu alloy product with improved preperties', *US patent*, 2000, 6027582.

[8] 'Standard test methods for tension testing of metallic materials (Metric)', in: *Annual book of ASTM standards*, Vol. **03.01**, p.78-98, 1998, ASTM E8M.

[9] G. W. Smith, 'A method for determination of Avrami parameters directly from isothermal calorimetry data', *Thermochim. Acta*, 1997, **291**, 59-64.

Chapter 4 Results and Analysis

This chapter presents the experimental results obtained by means of Vickers hardness and tensile tests, DSC, isothermal calorimetry, TEM and image analysis. The ageing responses of Al-Cu-Mg type alloys have been studied for artificial ageing, natural ageing and multistage ageing treatments. A quantitative analysis for precipitation kinetics has been performed to obtain the activation energy and the reaction exponent. The measured yield strength/hardness data, the kinetic parameters and the equivalent diameter of precipitates will be used to calibrate and validate the model presented in Chapter 5. In Section 4.2, a newly derived method of converting Vickers hardness to yield strength is described. This method will be used throughout this thesis, unless stated otherwise, to relate the Vickers hardness number to the yield strength.

4.1 Mechanical properties

4.1.1 Artificial ageing

Vickers hardness-time ageing curves of two solution treated, stretched and naturally aged 2024 alloys (alloys A and B) over a temperature range of 120°C to 220°C are plotted in **Fig. 4.1,** also included is the ageing curve for alloy D aged at 150°C. The typical (i.e. the median value) standard deviation (STD) for these measurements is ±2Hv (maximum STD ±4Hv) for 20kg load tests. It is shown that with decreasing ageing temperature, the time to peak hardness increases and the height of the peak increases. Ageing curves at 150°C, 170°C and 200°C show an initial drop from the as-received (T351) values. Alloy D exhibits lower hardness level and slightly slower ageing kinetics compared with alloys A and B. This is due to lower solute contents

available for the formation of precipitates in alloy D. The true stress-true strain curves for alloy A aged at 120°C, 170°C and 200°C for various times are shown in **Fig. 4.2** to **Fig. 4.4**. As seen from these figures, the elongation decreases with increasing strength. Little change in strength and elongation occur on ageing at 120°C up to 336h; while for ageing at 170°C and 200°C, the strengths drop below the as-received strength level at the early ageing times, then increase as the ageing proceeds (underaged and peak aged). At long ageing time of 168h at 170°C, the strength decreases due to overageing. The development of yield strength and elongation are represented in **Fig. 4.5**. For a better illustration of age hardening as a function of ageing temperature, YS data for alloy B aged at 190°C and 150°C obtained by Gao *et al.* [1] is also presented in Fig. 4.5. This figure shows that alloys aged at lower temperature exhibit higher plateau strength. Similar observations have been reported in the literature [2-4]. The initial decrease in hardness/strength from the as-received (T351) values during the artificial ageing at 150°C to 200°C is thought to be due to the reversion of GPB zones/clusters formed at room temperature and the recovery of deformation [2]. Evidence for reversion can be found from the endothermic effect due to cluster dissolution on the DSC curves (Section 4.3.2). The YS, UTS, elongation, strain-hardening exponent, the Vickers hardness number and the ratio of YS to Hv for alloy A are summarized in **Table 4.1**.

Fig. 4.6 shows Vickers hardness ageing curves for alloys A and C at 190°C. The typical STD for the measurements is ±2Hv (maximum STD ±6Hv) for 1kg load tests. The ageing curve of alloy C resembles the one of alloy A, but possesses a higher hardness level by an average of 4Hv in the whole ageing curve. This observation is in line with the literature [2, 5-7], which indicate that Si addition raises the hardness during the complete ageing process. Compared with the difference in yield strength between these two as-received alloys, which is 28MPa (344MPa for alloy A (Table 4.1) and 372MPa for alloy C (Table 3.2)), the differences in hardness are very limited and are comparable to the typical error of ±2Hv for these measurements.

4.1.2 Natural ageing

The ageing curves for re-solution treated, quenched and naturally aged alloys A and B are presented in **Fig. 4.7.** The hardness data for alloy B were the average values from measurements on two samples. It appears that these two alloys exhibit identical ageing behaviour. The ageing curves show a rapid and appreciable increase in hardness from the as-quenched value to a plateau which is reached within 24h. **Fig. 4.8** shows the natural ageing curves of alloys B and D (The curve for alloy D was performed and reported by Dr. Gao in our group).

4.1.3 Multi-stage ageing

Fig. 4.9 shows the changes in hardness during the multi-stage heat treatments. As the as-received samples were in the T351 temper, softening by reversion was observed when the samples were aged at temperatures of 150°C to 220°C. With increasing ageing temperatures, the extent of softening increased and the time interval at the plateau of near constant hardness decreased. For example, the hardness remained at about 127Hv for ageing times of 0.5h to 8h at 150°C, whereas no hardness plateau was observed at 200°C for ageing times of 5min to 1h. At longer ageing times, the hardness increases. An interesting finding was the increase in hardness at room temperature (RT) after air cooling from short elevated temperature ageing. After RT ageing for 2 months, no further hardness increase was found, indicating the age hardening is completed within 2 months. This hardening implies that after a short elevated temperature ageing, there is still sufficient supersaturation in the matrix to promote precipitation at RT. This is similar to the phenomenon of the so-called secondary precipitation (see Lumley *et al*. [8]): age hardening occurs at RT or low temperature after quenching from short time ageing at elevated temperature. This phenomenon has been observed in a range of aluminium alloys, e.g. 2014, 6061, 7050 and 8090 alloys [9, 10]. It is shown by TEM and nuclear magnetic resonance (NMR) that secondary hardening is due to the formation of coherent nanoparticles (GP zones or coherent solute clusters) [9]. When the artificial ageing is resumed after RT or low temperature ageing, finer dispersed precipitates are observed and this leads to improvements in mechanical properties compared with those obtained using conventional T6 temper [9]. As the aim of this multi-stage heat treatment is to obtain relevant data to test the model against the complex isothermal/non-isothermal

conditions and to identify the contributions of the Cu-Mg co-clusters and the S phase to the strength in the underaged condition, no further work on the resumed artificial ageing and the corresponding microstructure changes was carried out. In Section 6.3.4.1, the changes in hardness during these consecutive heat treatments will be modelled by considering the dissolution/precipitation of the Cu-Mg co-clusters and the S phase.

4.2 Conversion of Vickers hardness to yield strength

4.2.1 Background

In the literature, substantial amounts of hardness data* are available on Al-Cu-Mg based alloys. To be able to use these data for verification of the present yield strength model, a hardness to yield strength conversion is required. There have been many efforts to develop relationships between hardness and strength. The hardness value is related to the flow stress of a material and to its work-hardening characteristics. Tabor [11] has shown that about one third of the Vickers hardness (Hv, in MPa) is equivalent to the tensile stress at a strain of 8%, and related the ratio of UTS to Hv of a material to the Meyer exponent *m* or the strain hardening exponent *n* of the material (The relation between *m* and *n* is given as $n=m-2$.). Following Tabor's analysis, Cahoon *et al.* [12] derived a relationship between YS and Hv (in MPa), which showed a good correlation for steels and age hardening aluminium alloys:

$$\frac{\sigma_y}{Hv} = \frac{1}{3}(0.1)^{(m-2)} \tag{4.1}$$

As this method involves the use of the Meyer exponent *m* or the strain hardening exponent *n*, whose values are different for different materials and heat treatment conditions, and since neither *m* obtained from spherical indentation hardness tests nor *n* obtained from tensile tests are readily available in the literature, the application of the above equation is limited. Therefore in practice a linear relationship is often

* Here the strength is given in MPa and hardness is given in kg/mm^2 unless otherwise stated.

assumed, e.g. the well known correlation that for a material which does not work harden, the YS is about one third of the Hv (in MPa) [13]. This proportionality has been used by a number of researchers to make a quantitative comparisons of the model predicted YS with the hardness calculated YS [14-16]. However, for materials with substantial work hardening ability such as the Al-Cu-Mg alloys, this method is likely to lead to significant inaccuracies due to the strain hardening behaviour.

4.2.2 New method for conversion of Vickers hardness to yield strength

In an attempt to obtain YS from hardness measurements available in the literature without the knowledge of *m* or *n* values, a new convenient method is derived. It has been experimentally shown that for the age-hardening Al-Cu-Mg-Mn alloys, linear relationships are observed for data in underaged condition (with a proportionality constant (YS to Hv ratio) of 2.3) and for data in peak aged and slightly overaged conditions (with a proportionality constant of about 3.0), respectively [17]. Data of YS to Hv ratio in Table 4.1 for alloy A aged at 120°C, 170°C and 200°C confirm the above finding about the two separate linear relations, and **Fig. 4.10** indicates two proportionality constants of 2.5 and 2.9. **Fig. 4.11** shows that the hardness ageing curves are similar to the yield strength ageing curves and they have nearly the same times to peak. As indicated in **Fig. 4.12** and **Fig. 4.13**, the strain hardening exponent shows the opposite behaviour to the change of the yield strength or hardness, while the YS/Hv ratio resembles the change of the yield strength or hardness. With the increase of the YS or Hv, the strain hardening exponent decreases, indicating the reduced work hardening ability. At peak YS or Hv, the value of *n* drops to a minimum, while the YS/Hv ratio approaches the limit value predicted by Tabor [13] for fully work hardened material. Considering the gradual change of the YS/Hv ratio from 2.3~2.5 to 2.9~3.0, which corresponds to the Hv changes from the underaged plateau value to the peak aged value in the ageing curves, it is possible to relate the YS/Hv ratio directly to the Hv value instead of the *n* value. Using two proportionality constants, λ_1 and λ_2, the yield strength can be estimated as:

$$\frac{\sigma_y}{Hv} = \lambda_1 + (\lambda_2 - \lambda_1)\frac{(Hv - Hv_l)}{(Hv_p - Hv_l)} \quad (4.2)$$

Where Hv_l and Hv_p are the plateau hardness (lower bound) and the peak hardness (upper bound), respectively. λ_1 and λ_2 are the YS/Hv ratios corresponding to Hv_l and Hv_p. Using Vickers hardness and yield strength data of alloy A aged at 120°C, 170°C and 200°C (Table 4.1), taking Hv_l = 130kg/mm^2, Hv_p = 160kg/mm^2, the best fit between measured and calculated YS was obtained by minimising the root mean squared error (RMSE), which is defined as:

$$RMSE = \sqrt{\frac{1}{N}\sum_{i=1}^{N}(YS_{\exp,i} - YS_{cal.i})^2} \quad (4.3)$$

This provides values of λ_1 and λ_2 equalling 2.3 and 3.0, respectively. The RMSE obtained is 13MPa (or the average relative error is 3%). **Fig. 4.14** shows a plot of calculated YS versus experimental YS for alloy A aged at 120°C, 170°C and 200°C. YS calculated from Eq.(4.1) (using *n* values in Table 4.1) and from simple linear relationship of YS=3Hv are also presented for comparison. A good agreement is observed for analysis using Eq.(4.1) and Eq.(4.2). As expected, linear conversion using YS=3Hv results in much higher calculated YS values. The average relative errors between the experimental and calculated YS are 3%, 2% and 15% for this new analysis (Eq.(4.2)), Cahoon's analysis (Eq.(4.1)) and the linear conversion, respectively. For comparison, variations in λ_1 and λ_2 of ±0.1 cause deviations in YS within 4% and variations of ±0.2 lead to deviations within 9%.

4.2.3 Analysis of the method

The validity of this method is checked by comparing the calculated yield strengths with the experimental results for alloys in the underaged and overaged conditions, as illustrated in **Fig. 4.15** and **Fig. 4.16.** Applying the above values (Hv_l = 130 kg/mm^2, Hv_p = 160 kg/mm^2, λ_1=2.3 and λ_2=3.0), the converted YS calculated from hardness measurements agree well with the corresponding experimental YS for alloy B aged at

150°C and 190°C (Hv and YS data are from Table 3.2) with an average relative error of 4%. For Hv-time curves for which no corresponding experimental YS-time data are available (Hv data for alloy B at 150°C in Fig. 4.1 and Hv data for alloy A at 190°C in Fig. 4.6), the calculated ageing curves using Eq.(4.2) are compared with those using YS=3Hv. It is seen from Fig. 4.15(a) that Eq.(4.2) gives better correlation between the yield strength and the Vickers hardness than the simple linear one of YS=3Hv.

The present method can also be applied to natural ageing curves of Al-Cu-Mg alloys. Data for analysis are Vickers hardness data and two YS data points of an Al-2.5Cu-1.2Mg alloy reported by Wilson *et al*. [6]. The lower bound and the upper bound hardness values were read from the hardness-time curves (Hv_l = 70 kg/mm^2, Hv_p = 105 kg/mm^2), λ_2 was taken as 2.3. λ_1 was obtained by fitting the calculated YS to the two experimental YS data points, which resulted in 1.35 ± 0.05. The converted yield strength-time curve is given in **Fig. 4.17** along with the hardness–time curve. Comparing the differences between the initial value and the plateau value of YS and of Hv, it is seen that yield strength is more sensitive to the ageing than hardness.

It is worth noting that in converting the hardness data available in the literature to the yield strength, while Hv_l and Hv_p can be read from the ageing curves as the plateau hardness and peak hardness, care should be taken in choosing λ_1 and λ_2 to ensure the accuracy of the converted data. Appropriate values of λ_1 and λ_2 can be obtained from the experimental YS to hardness ratios of similar materials as it has been shown that the accuracy of the conversion is not markedly affected by a small variation (± 0.1) of λ_1 and λ_2. It is also worth mentioning that as seen from Fig. 4.13, the evolution of the YS to Hv ratio in the overaged conditions shows a slower rate of decrease than that in the underaged conditions which shows relatively rapid increase. Therefore applying the value of λ_1, which is obtained from the underaged conditions, to the overaged data may lead to underestimation of the yield strength.

4.3 Calorimetric studies

4.3.1 Isothermal calorimetry

As shown in **Fig. 4.18,** the isothermal calorimetry curves for the as-received alloy A in the temperature range from 200°C to 250°C exhibit a single exothermic heat effect and the heat flow peaks shift to shorter times with increasing isothermal temperature. The time to peak heat flow t_p, the total heat evolved ΔQ and the end time t_e, which is defined as the time when the heat flow is 0.5% of the maximum heat flow, are listed in **Table 4.2**. It is found that the t_e values for 200°C and 220°C are close to the time to peak hardness in the ageing curves (Fig. 4.1), which are around 2-4h and 0.8-1.2h, respectively. This indicates that the reactions involved in the isothermal process, i.e. the dissolution of the clusters and the precipitation of S phase, are responsible for the peak hardness in the ageing curves and suggests that precipitation strengthening provides the most significant contribution to the hardness. It is clear from Fig. 4.18 and Table 4.2 that the temperature range suited for the study of 2024 alloy using isothermal calorimetry is rather limited. At high T, the precipitation is too rapid to record due to the stabilisation of the calorimeter; at low T, it takes a long time to complete the reaction and to obtain a baseline, and the heat release is too small to be accurately measured. Thus isothermal calorimetry study is not considered to be the best suited technique for kinetic analysis in Al-Cu-Mg alloys studied in this work.

4.3.2 DSC

DSC curves for as-received and re-solutionized samples are presented in **Fig. 4.19**. Five heat effects, marked as A to E, are observed for the re-solutionized sample. For the as-received sample, the first exothermic peak A has disappeared, indicating that the formation of the precipitate associated with effect A has completed during long natural ageing. Previous DSC studies on Al-Cu-Mg alloys in the (α+S) phase field attributed effect A and effect B to the formation and dissolution of GPB zones, and effect C and effect D to the precipitation and dissolution of S phase [3, 18-21]. The assignment of effect C to S phase precipitation received support from a direct TEM/SAD observation of a sample of an Al-1.1Cu-1.7Mg (at.%) alloy heated in the DSC to the peak of the effect C [22]. For effect A, Abis *et al*. [23] supported that it is associated with GPB zone formation by DSC and TEM/SAD studies on quenched Al-4.4Cu-1.7Mg (wt.%) alloy naturally aged between 15min and 2760min (48h),

whereas Ringer *et al*. [22] found no evidence of GPB zones in TEM/SAD studies on a sample of an Al-1.1Cu-1.7Mg (at.%) alloy heated in the DSC to the peak of effect A. 3DAP results of alloys B and D aged between 15min and 48h at room temperature [24, 25] clearly showed that no pre-precipitates which could be interpreted as GPB zones were observed. Instead a high density of small Cu-Mg co-clusters was detected. In addition, no evidence of the presence of any precipitates were found by TEM/SAD on a 2024-T351 alloy [26]. Based on the above results and the review in Section 2.2.2.2 which highlighted the difficulty in detecting the GPB zones by TEM/SAD and the difference between Cu-Mg co-clusters and GPB zones, it is preferable to use the nomenclature of Cu-Mg co-clusters for the pre-precipitate structure formed during effect A. Thus the exothermic effect A between 40°C and 150°C is ascribed to the formation of Cu-Mg co-clusters, and the endothermic effect B between 140°C and 250°C is ascribed to the dissolution of the Cu-Mg co-clusters. The exothermic effect C between 220°C and 350°C is ascribed to the precipitation of S phase and the endothermic effect D between 300°C and 500°C is ascribed to the dissolution of the S phase. The effect E starting at about 500°C is due to the incipient melting of intermetallic phases in the alloys.

It is seen from **Fig. 4.19** that the stretching by 2~3% after quenching causes the S precipitation peak to shift to a lower temperature by about 10°C[*], indicating an acceleration of the S precipitation. This is consistent with other observations [27] which showed that for samples of an Al-2.1Cu-1.3Mg alloy (wt.%) which had been solution treated, quenched and aged at room temperature for 77 days, cold deformation before RT ageing led to a shift of the S peak to lower temperature. This can be explained by the dislocations introduced by stretching. The dislocations act as preferential nucleation sites to facilitate heterogeneous nucleation of S phase and may act as short circuit diffusion paths to accelerate the precipitation rates by dislocation core diffusion, i.e. fast diffusion of vacancies and solute along dislocations.

---

[*]The influence of punching versus cutting and grinding of DSC samples was also checked and it was found that the punching sample preparation method led to a further small shift of heat effect to lower temperatures (from T_p=259°C to T_p=257°C for a heating rate of 10°C/min), indicating that additional dislocations from punching have limited effect on the precipitation as a high density of dislocation from stretching already existed.

DSC curves for discs of re-solution treated, quenched and naturally aged samples are shown in **Fig. 4.20**. It is observed that the exothermal effect due to Cu-Mg co-cluster formation decreases with ageing time, indicating that Cu-Mg co-clusters form during ageing at room temperature. The time interval corresponds well to the rapid rise in hardness reported in Fig. 4.7. It is therefore suggested that the formation of the Cu-Mg co-clusters is responsible for the hardness increase during natural ageing. **Fig. 4.21** indicates that there is little S phase precipitated up to 336h at 120°C. Correspondingly the ageing curve at 120°C as shown in Fig. 4.5 exhibits little change in YS. At 170°C a substantial decrease in the amount of S phase is seen from 6h to 24h in the DSC curves (**Fig. 4.22**), and the decrease in the heat effect due to S precipitation corresponds well to the rapid increase in yield strength shown in Fig. 4.5. At 48h/170°C a very small exothermic effect is detected, and at 168h/170°C this exothermic effect disappears completely. The reduction in S phase precipitation effect shown in **Fig. 4.23** for alloy A aged at 200°C also corresponds well to the progressive increase in yield strength shown in Fig. 4.5. This indicates that the precipitation of S phase is responsible for the rise to peak hardness/strength.

Closer study of the Cu-Mg co-cluster dissolution effect in Fig. 4.22 revealed evidence for reversion of the Cu-Mg co-clusters. It is seen from the curves for as-received sample and for sample aged 0.5h at 170°C, that during ageing at 170°C for 0.5h no S phase forms, while the amount of the Cu-Mg co-clusters decreases. The dissolution of the Cu-Mg co-clusters is due to the retrogressive nature of the solvus curve, leading to the drop in the hardness/strength. It is evident from Fig. 4.20 to Fig. 4.23 that the S precipitation effect is correlated with the Cu-Mg co-cluster dissolution effect: the S precipitation peak decreases with the decrease of the Cu-Mg co-cluster dissolution peak. This suggests that Cu-Mg co-clusters dissolve and are replaced by S phase during the artificial ageing.

The area under the DSC curve at a particular heat effect gives the total heat evolved ΔQ due to the formation or dissolution of the precipitate, which is proportional to the volume fraction of the precipitate formed or dissolved [28, 29]. The values of heat

evolved*, ΔQ, for S precipitation in alloy A aged at 120°C, 170°C and 200°C (Fig. 4.21-Fig. 4.23) are given in **Table 4.3.** As seen from Fig. 4.23, DSC traces of samples aged at 200°C for 0.38h, 2h and 4.6h show greater areas for S dissolution effect as compared with the others. This indicates a baseline drift, since for these aged samples the endothermic effects due to S dissolution should be identical to those shown in Fig. 4.21 and Fig. 4.22. The baseline shift will lead to smaller ΔQ for S precipitation in these curves (Table 4.3). These ΔQ values will be used in Section 6.3.3.2 for a comparison of the changes in heat evolved and the volume fraction predicted by the model. It is noted that due to the overlap of the Cu-Mg co-cluster dissolution effect and the S precipitation effect, ΔQ for S precipitation will be treated as a semi-quantitative indicator of the precipitation process only; it is not used for calculation of the exact amount of S phase.

4.3.3 Determination of kinetic parameters

4.3.3.1 Determination of the activation energy

Modelling of precipitation kinetics usually starts with the determination of the activation energy E_a. Methods for the extraction of E_a from experiments at various linear heating rates have been proposed in the literature, e.g. the generalised Kissinger methods [30, 31], Ozawa method [32], Starink method [33, 34] and Gupta method [35]. All the methods require the determination of the temperature at which a fixed fraction transformed is obtained for various heating rates [29]. Due to overlapping of the Cu-Mg co-cluster dissolution effect and the S precipitation effect, such a stage of fixed fraction transformed cannot be determined accurately for the S precipitation

* To estimate the standard error in the reported heat evolved ΔQ values, the following procedure was used. From a consideration of the various sources of deviation (calibration error, noise, baseline, sample mass), it became clear that the baseline is the dominant source of error. The choice of the point at about 140°C in the determination of the second order polynomial baseline correction (see Section 3.5) is dominant in determining baseline error as the other two points can be established relatively accurately. Thus in this work, the errors in ΔQ were estimated by recalculating ΔQ values after various realistic choices of the temperature for the third point temperature (values from 135°C to 145°C were chosen).

peak. Thus the popular Kissinger peak reaction method is applied to obtain E_a for Cu-Mg co-cluster formation and S phase precipitation. This method can be expressed as follows [29, 30]:

$$\ln\left(\frac{T_p^2}{\beta}\right) = \frac{E_a}{RT_p} + C \qquad (4.4)$$

where β, E_a, R and T_p are the heating rate, activation energy, gas constant and peak temperature, respectively and C is a constant. According to Eq.(4.4), a plot of $\ln(T_p^2/\beta)$ versus $1/T_p$ should give a straight line with a slope of E_a/R.

DSC traces for re-solution treated alloy A at three heating rates are presented in **Fig. 4.24**. It can be seen that all the heat effects except for the incipient melting peak shift to higher temperatures with increasing heating rates, which indicates that these reactions are thermally activated. The first exothermic peak will be used for the determination of the activation energy of cluster formation. As stretching results in the shift of S precipitation peak, as seen in Fig. 4.19, one may expect different values of E_a for S precipitation in stretched and non-stretched alloys. Hence in this work, E_a for S precipitation was determined from DSC runs of as-received T351 samples, **Fig. 4.25**.

As discussed in [34], the main source of potential errors of the Kissinger peak method comes from the use of peak temperature T_p, at which the fraction transformed is not exactly at constant amount transformed. To check the applicability of the Kissinger analysis, the heat evolved, ΔQ, and the heat evolved at peak temperature, ΔQ_{Tp}, for the exothermic peak of cluster formation were calculated. The fraction transformed at T_p is then taken as $\Delta Q_{Tp}/\Delta Q$. The results are given in **Table 4.4** together with the peak temperature T_p. It is found from Table 4.4 that the state of transformation at T_p is indeed approximately at a fixed fraction transformed. Thus the Kissinger method should be valid and accurate. Kissinger plots for cluster formation reaction and for S precipitation reaction in alloy A are given in **Fig. 4.26** and **Fig. 4.27**, respectively. From the slopes it is found that E_a^{cl} =75±2kJ/mol for cluster formation,

E_a^S=144±15kJ/mol for S precipitation in 2024 T351 alloy (alloy A, samples were prepared by punching) and E_a^S=113±9kJ/mol for S precipitation in re-solutionized alloy A. (The errors were estimated based on the accuracy of determination of the slope which was obtained from a linear regression analysis.) It is known that for cluster formation reaction in as-quenched samples with excess vacancies, the activation energy for the reaction is to a large extent determined by the migration energy of vacancies. For comparison, the migration energy of vacancies in Al is 0.6eV (58kJ/mol) [36]. Within the limits of experimental errors, the value of 75±2kJ/mol for cluster formation in the present 2024 alloy compares well with a value of 73.3±2.5kJ/mol for GPB zone formation in a 2124 alloy reported by Smith [37], and broadly agrees with measurements reported in the literature for other Al-Cu-Mg alloys, which are in the range of 56-76kJ/mol [18, 19, 38, 39]. For the determination of the activation energy for S precipitation from DSC measurements, Smith [37] reported E_a^S=131.0±5.9kJ/mol for a solutionized 2124 alloy as determined from DSC runs at five heating rates of 1.2, 2.5, 5, 10 and 20°C/min. Using the data provided by Smith [37], E_a^S will be 115.7±8.7kJ/mol if determined from three heating rates of 5, 10 and 20°C/min. This is in fairly good agreement with E_a^S=113±9kJ/mol obtained in this work for re-solutionized alloy A (Fig. 4.27). Charai *et al*. [19] obtained E_a^S=134±5kJ/mol for an Al-2.03Cu-1.28Mg (wt.%) alloy, while Jena *et al*. derived E_a^S=129.9J/mol for an Al-1.53Cu-0.79Mg (wt.%) alloy. All these reported E_a^S values for non-stretched alloys are close to the activation energies for diffusion of Cu or Mg in Al, which are about 125-135kJ/mol [36]. The activation energy determined for the present stretched 2024 alloy (alloy A, E_a^S=144±15kJ/mol) is however greater than the above values. In a further experiment DSC samples were cut from as-received samples of alloy A and DSC runs were performed at four heating rates of 5, 10, 20 and 25°C/min from 120°C to 500°C. The peak temperatures for S exothermic effects with various heating rates are given in Table 4.4. A Kissinger plot for S precipitation for the cut samples is also presented in Fig. 4.27. A value of E_a^S=133±6kJ/mol was obtained. It is seen from the above analysis of the activation energy for S precipitation (Table 4.4 and Fig. 4.27) that a shift in peak temperature and a change in the range of heating rates used (therefore the range of peak

temperatures) cause variations in E_a^S. It is expected that a wider range of peak temperatures will give a more accurate value for E_a^S. In Chapter 6, the E_a^S values for S precipitation in 2024 T351 alloy will be further discussed.

4.3.3.2 Determination of the transformation exponent for cluster formation

To investigate the mechanism of cluster formation, the reaction exponent which describes the nucleation and growth mechanisms is needed. The reaction exponent can be obtained from isothermal experiments or from linear heating experiments [40]. Different symbols *n* and *s* are used in this thesis to indicate the reaction exponent for isothermal path and for linear heating path, respectively. In this section, both *n* and *s* will be determined.

The isothermal calorimetry experiments at 25°C on alloys B and D were performed by Dr. Gao in our group and reported in [24]. The results as presented in **Fig. 4.28** are used to determine the reaction exponent *n.* The fraction transformed α was obtained from the isothermal calorimetry curves by normalizing the heat evolved at a certain time. **Fig. 4.29** shows the Avrami plots of ln(-ln(1-α)) versus ln*t* for α in the range of 0.05 to 0.95 (open symbols labelled JMAK model), where α is the fraction transformed and *t* is the time. For a reaction which obeys JMAK kinetics, the Avrami plot should yield a straight line with a slope being equal to *n*. It is seen from Fig. 4.29 that the later stages of transformation (α >0.4) deviate from the expected straight line. This means that JMAK kinetics is not valid for the present reaction. This should come as no surprise as it has been noted in various publication [29, 41, 42] that the JMAK model is generally not valid for precipitation reactions and the AR model (Eq.(2.21)) is considered a better description for precipitation reactions. From Eq.(2.21), it follows that *n* can be obtained from the slope of a plot of ln(1/(1-α)-1) versus ln*t*. Such plots are also shown in Fig. 4.29 (solid symbols labelled AR model) for alloys B and D. Linear fits for α in the range of 0.05 to 0.95 yielded *n*=2.51±0.03 for alloy B and *n*=2.52±0.03 for alloy D.

For the initial stages of the reaction at which impingement is negligible (the stage should be situated well before the first inflection point in the heat release), the reaction exponent *s* can be obtained from DSC curves by application of a simple method as follows [40]:

$$R\frac{d(\ln HF)}{d(1/T)} \cong s(E_{eff} + 2RT_{av}) + 2RT_{av} \qquad (4.5)$$

where *HF* stands for the heat flow in a DSC curve and E_{eff} is the activation energy for cluster formation, taken to be 75kJ/mol. Taking the DSC data between 5% to 25% of the maximal exothermic heat flow, T_{av} represents the average temperature of the temperature range corresponding to 5 to 25% of the maximal exothermic heat flow. *s* can then be calculated from the slope of plot of ln*HF* versus *1/T*. The validity of this method for the determination of *s* has been verified by DSC studies of precipitation in a quenched Al-6at.% Si alloy and an Al-Cu-Mg-Zr alloy [40].

This analysis is applied to the cluster formation effects in Fig. 4.24 and the cluster formation effects for as-quenched sample in Fig. 4.20. A value close to 2.5 is obtained (**Table 4.5**). These values are in good agreement with those obtained from the above isothermal calorimetry studies. The value of 2.5 for reaction exponent indicates that cluster formation during isothermal room temperature ageing and during DSC runs for as-quenched samples (which have undergone very limited room temperature ageing) is a nucleation and growth process with continuous nucleation. This is consistent with 3DAP observations [25] of the increase in cluster density up to about 4-5h for alloy B aged at RT. Applying this method, the *s* values obtained by Starink *et al.* [39] from DSC curves of different heating rates for as-quenched samples of an Al-0.9 at%Cu-1.4 at% Mg alloy are in the range from 1.74 to 1.47. These results seem different from the present analysis. However, the authors pointed out that although the samples were in the as-quenched stages, due to the rapid formation of the zones, zone formation had occurred prior to the calorimetry studies, as the total heat effect of zones formation is about 18% smaller than that of zone dissolution. The decrease in *s* is in line with transformation theory [29, 41, 42]. When substantial amounts of clusters/zones have formed during RT ageing, the formation of clusters/zones during the subsequent DSC run will occur first via nucleation with decreasing nucleation rate

(n=2.5-1.5) then via growth of pre-existing clusters (n=1.5-0.5) as the prior RT ageing proceeds.

4.4 TEM and image analysis

TEM bright-field micrographs and corresponding SAD patterns taken on the $[100]_\alpha$ zone axis of alloys B and C aged 96h at 190°C are shown in **Fig. 4.30**. The SAD patterns for alloys B and C show diffraction spots attributed to S phase (see [43-45]), no extra reflections by other phases, e.g. σ phase, were resolved. Most of the S precipitates are seen end-on as individual precipitates with lath or spot shapes. Some S precipitates appear to have formed on a dislocation line but are separated from each other. The differences in morphology between Fig. 4.30(a) and Fig. 4.30(c) may be due to the increased number of heterogeneous nucleation sites introduced by the silicon and iron impurities. **Fig. 4.31** shows TEM BF micrographs and corresponding SAD patterns taken on the $[100]_\alpha$ zone axis of alloys A and C aged 720h at 190°C. Again the S phase is the only precipitate identified by SAD patterns in both alloys A and C at this ageing condition. It is seen that with increasing ageing time, S precipitates grow larger in both alloys; with the S precipitates in alloy A showing a more pronounced coarsening. It is assumed that alloy A shows similar precipitate size and reaction kinetics as alloy B in view of their similar composition and thermal processes, and no TEM was performed on alloy B in this work.

Image analysis using KS300 image analysis software has been performed on the end-on S precipitates to characterize the evaluation of the equivalent diameter. The distributions of the equivalent diameters are shown in **Fig. 4.32** and data are tabulated in **Table 4.6.** It is noted that different methods (semi-automated method and manual method) were applied to measure the sizes of S precipitates for alloy A and alloy C aged 720h at 190°C. To check the comparability of these two methods, a BF image of alloy C aged for 96 h at 190°C was analysed using both methods. The results given in **Table 4.7** show that difference in measured mean diameters from these two methods is less than 1nm, indicating that these two methods introduce no significant variation in the measurements of mean equivalent diameters. **Table 4.6** shows that, at the

ageing condition of 96h at 190°C, the mean equivalent diameters for S precipitates in alloys B and C are identical within experimental error. At the ageing condition of 720h at 190°C, the mean equivalent diameter for S precipitates in alloy C is smaller than that in alloy A by 3nm. This suggests that the growth of the S precipitates is retarded in alloy C which has a higher Si content. However, difference in size of S precipitates is small.

Table 4.1 Mechanical properties from hardness tests and tensile tests for alloy A

Ageing treatment (h/°C)	YS (MPa)	STD[c]	UTS (MPa)	STD	Elongation (25mm)%	STD	n	STD	Hv (VPN)	STD	YS/Hv
AR(T351)	344	0	451	0	20.1	0.5	0.126	0.001	138	2	2.5
6/120[a]	340	—	451	—	21.2	—	0.128	—	137	2	2.5
72/120[b]	348	4	454	—	21.6	—	0.124	0.001	140	1	2.5
168/120	346	2	456	2	20.1	0.6	0.125	0.001	140	2	2.5
336/120	350	0	457	2	20.1	0.0	0.122	0.000	141	3	2.5
AR(T351)	344	0	451	0	20.1	0.0	0.126	0.001	138	0	2.5
0.5/170	323	1	440	0	19.1	0.1	0.134	0.001	134	2	2.4
1.6/170	322	1	442	2	22.4	0.8	0.136	0.001	132	3	2.4
6/170[b]	341	9	448	—	23.8	—	0.123	0.006	139	2	2.5
24/170	450	2	481	2	12.0	0.9	0.064	0.000	155	4	2.9
48/170	463	2	486	1	10.2	0.6	0.058	0.001	159	1	2.9
168/170	423	0	467	1	10.3	0.5	0.088	0.001	148	2	2.9
AR(T351)	344	0	451	0	20.1	0.0	0.126	0.001	138	0	2.5
0.38/200	306	1	431	1	21.7	2.5	0.144	0.001	130	1	2.3
0.6/200	333	1	440	0	18.8	1.2	0.128	0.001	134	3	2.5
1/200	360	4	449	4	18.0	1.0	0.111	0.002	141	2	2.6
1.5/200[b]	420	1	464	—	12.6	—	0.077	0.001	145	4	2.9
2/200[b]	441	1	472	—	11.1	—	0.066	0.001	154	2	2.9
4.6/200	449	1	477	0	9.9	0.0	0.066	0.001	153	1	2.9

[a]. Only one tensile sample.

[b]. Fracture occured outside the extensometer in one of the two samples and these values are excluded for UTS and elongation.

[c]. The standard deviation (STD) for a set of N values is $\sqrt{\frac{1}{N-1}\sum_{i=1}^{N}(x_i-\bar{x})^2}$. For two tests, the STD reduces to $\frac{|x_1-x_2|}{\sqrt{2}}$.

Table 4.2 The time to peak t_p, the end time t_e and the total heat evolved ΔQ for the isothermal calorimetry curves of as-received alloy A (calculated from Fig. 4.18)

T (°C)	t_p (min)	t_e (min)	ΔQ (J/g)
250	0.9	15	21.1
240	1.8	32	21.0
230	3.6	34	18.9
220	7.7	48	17.0
210	16.0	89	14.2
200	33.8	182	13.8

Table 4.3 The heat evolved ΔQ for S precipitation in alloy A aged at 120°C, 170°C and 200°C (calculated from Fig. 4.21-Fig. 4.23)

Ageing treatment (h/°C)	ΔQ (J/g)	STD		Ageing treatment (h/°C)	ΔQ (J/g)	STD
AR-T351	17.1	0.1		AR-T351	17.1	0.1
6/120	17.12	0.01		0.38/200	14.7	0.1
336/120	15.95	0.02		0.6/200	15.7	0.1
				1/200	13.3	0.1
AR-T351	17.1	0.1		1.5/200	10.8	0.2
0.5/170	16.26	0.05		2/200	3.1	0.2
1.6/170	16.9	0.1		4.6/200	0	—
6/170	15.8	0.2				
24/170	6.0	0.3				
48/170	1.3	0.3				
168/170	0	—				

Table 4.4 The peak temperature T_p, heat evolved ΔQ, heat evolved at peak temperature ΔQ_{Tp} and the fraction transformed at T_p for alloy A at various heating rates (calculated from Fig. 4.24 and Fig. 4.25)

	Heating rate (°C/min)	T_p (°C)[a]	ΔQ (J/g)	ΔQ_{Tp} (J/g)	Transformed fraction at T_p
Cu-Mg co-clusters	5	63.82	14.5±0.2	5.17±0.02	0.36
	10	71.83	14.2±0.2	5.28±0.06	0.37
	20	80.89	14.2±0.3	4.93±0.07	0.35
S (punching)	5	244.88			
	10	256.87			
	20	265.83			
S (cutting)	5	248.32			
	10	259.37			
	20	272.35			
	25	274.39			
S (re-solutionized)	5	258.82			
	10	270.83			
	20	286.89			

[a]. The accuracy of temperature measurement is ±0.01°C for Pyris-1 calorimetry.

Table 4.5 The transformation exponent *s* obtained from DSC experiments for Cu-Mg co-cluster formation in alloy A

Heating rate (°C/min)	5	10	20	10
s	2.45±0.02[a]	2.08±0.05[a]	2.43±0.06[a]	2.24±0.04[b]

[a.] From Fig. 4.24.

[b]. From 3min/RT curve in Fig. 4.20.

Table 4.6 The measured mean equivalent diameters of end-on S precipitates as obtained from TEM

Alloy	Ageing treatment (h/°C)	Mean diameter (nm)	Standard deviation (nm)	Standard error* (nm)	No. measured precipitates	Image analysis method
Alloy B	96/190	14.3	5.8	0.3	487	Semi-auto Mode I
Alloy C	96/190	14.2	3.4	0.3	164	Semi-auto Mode II
Alloy A	720/190	25.0	4.9	0.9	32	Manual
Alloy C	720/190	22.0	5.7	0.6	105	Semi-auto Mode II

*Standard error = standard deviation / (number of measured precipitates)$^{0.5}$

Table 4.7 Comparison of the measurements of mean equivalent diameters of S precipitates made by manual and semi-automated methods

Alloy	Ageing treatment (h/°C)	Mean diameter (nm)	Standard deviation (nm)	Standard error (nm)	No. measured precipitates	Image analysis method
Alloy C	96/190	14.4	3.1	0.7	20	Manual
Alloy C	96/190	13.7	2.7	0.6	19	Semi-auto Mode II

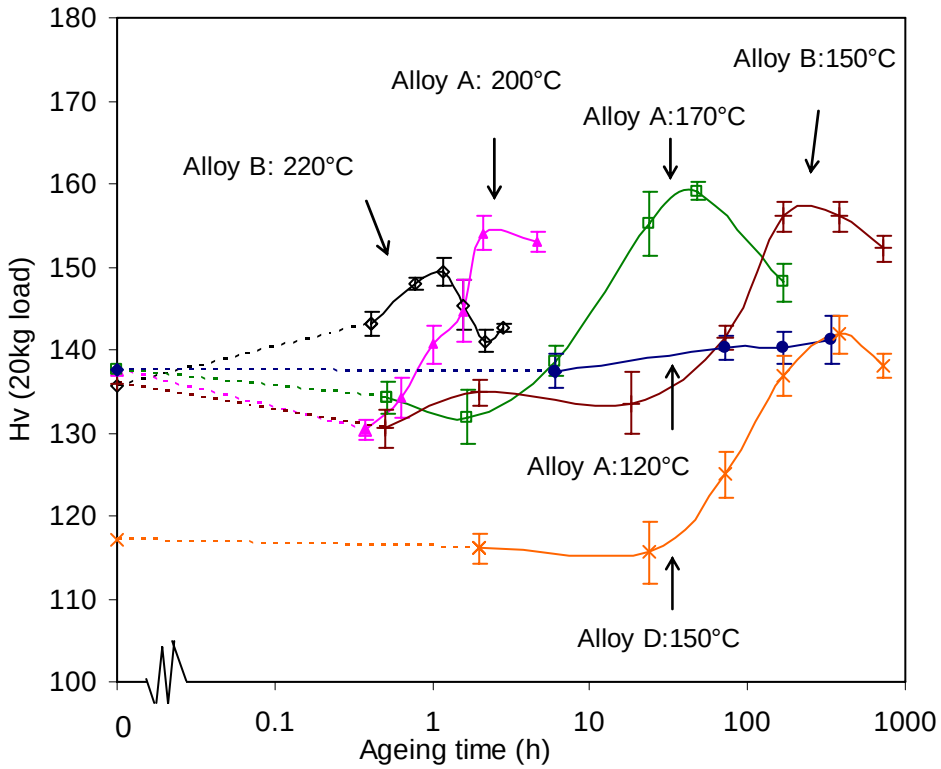

Fig. 4.1 Vickers hardness ageing curves for three Al-Cu-Mg alloys.

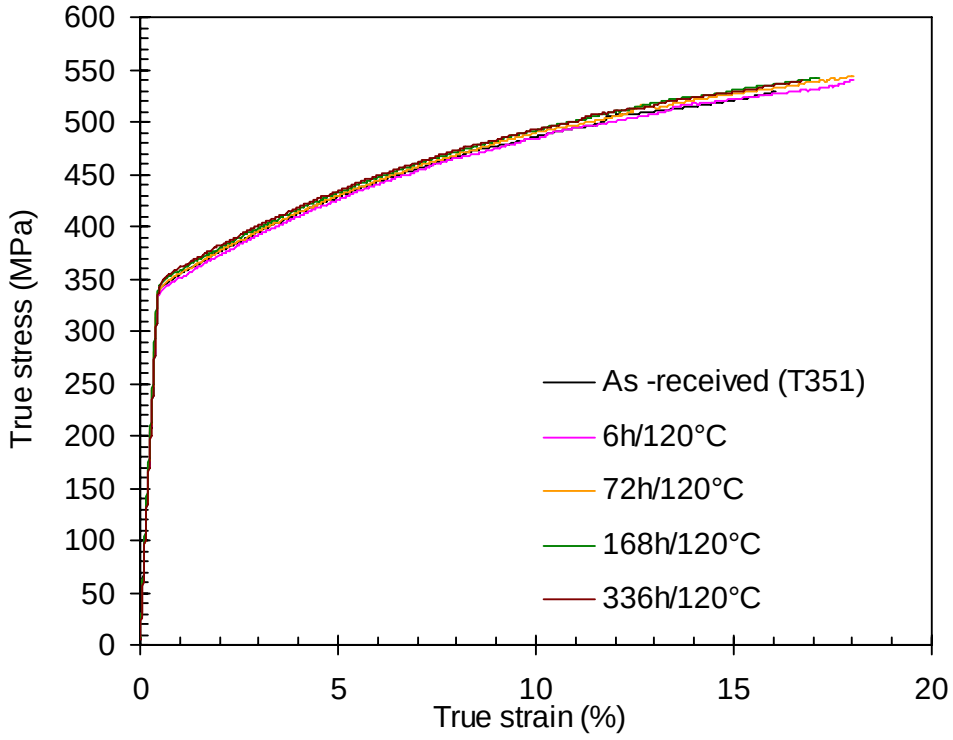

Fig. 4.2 True stress-true strain curves for alloy A (2024-T351) aged at 120°C.

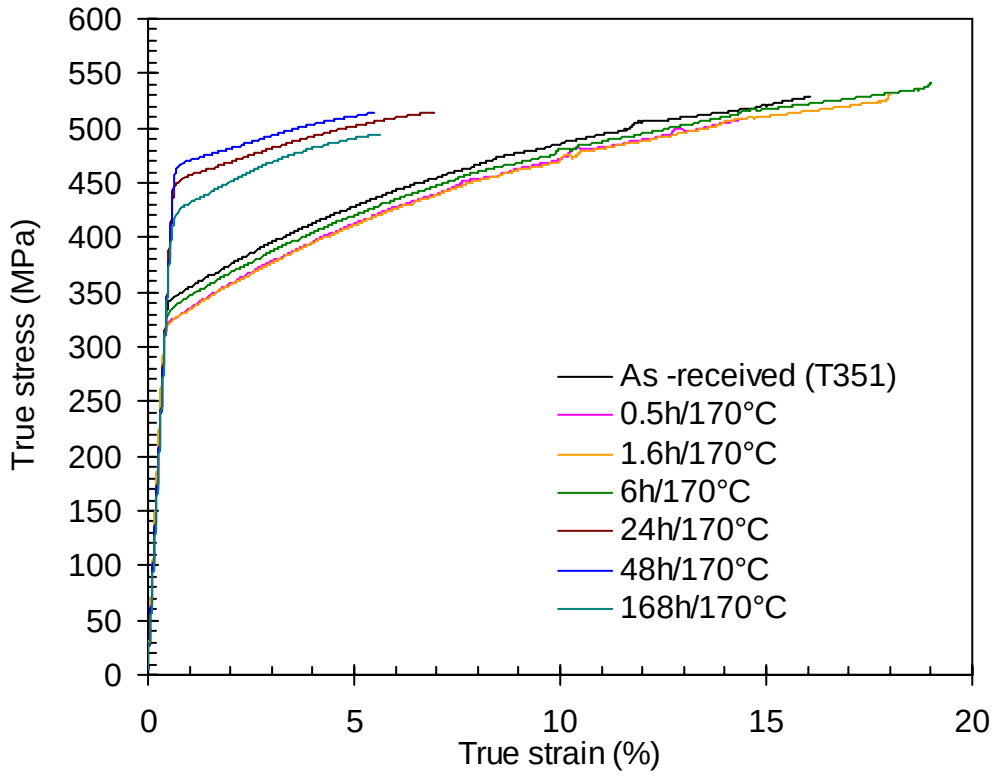

Fig. 4.3 True stress-true strain curves for alloy A (2024-T351) aged at 170°C.

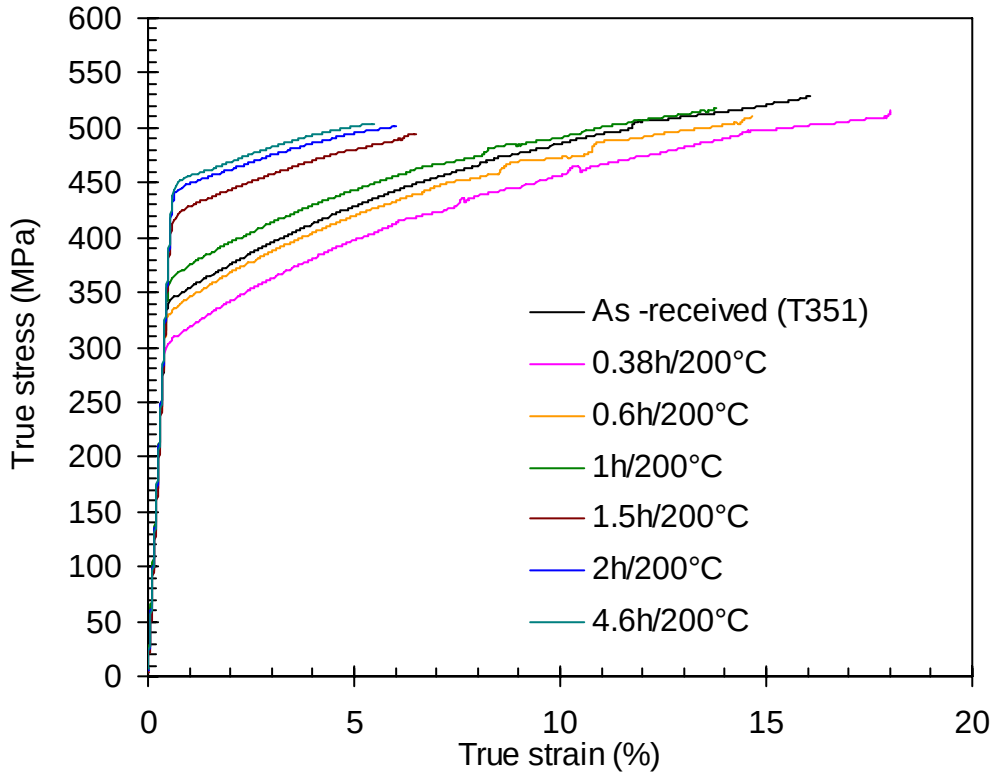

Fig. 4.4 True stress-true strain curves for alloy A (2024-T351) aged at 200°C.

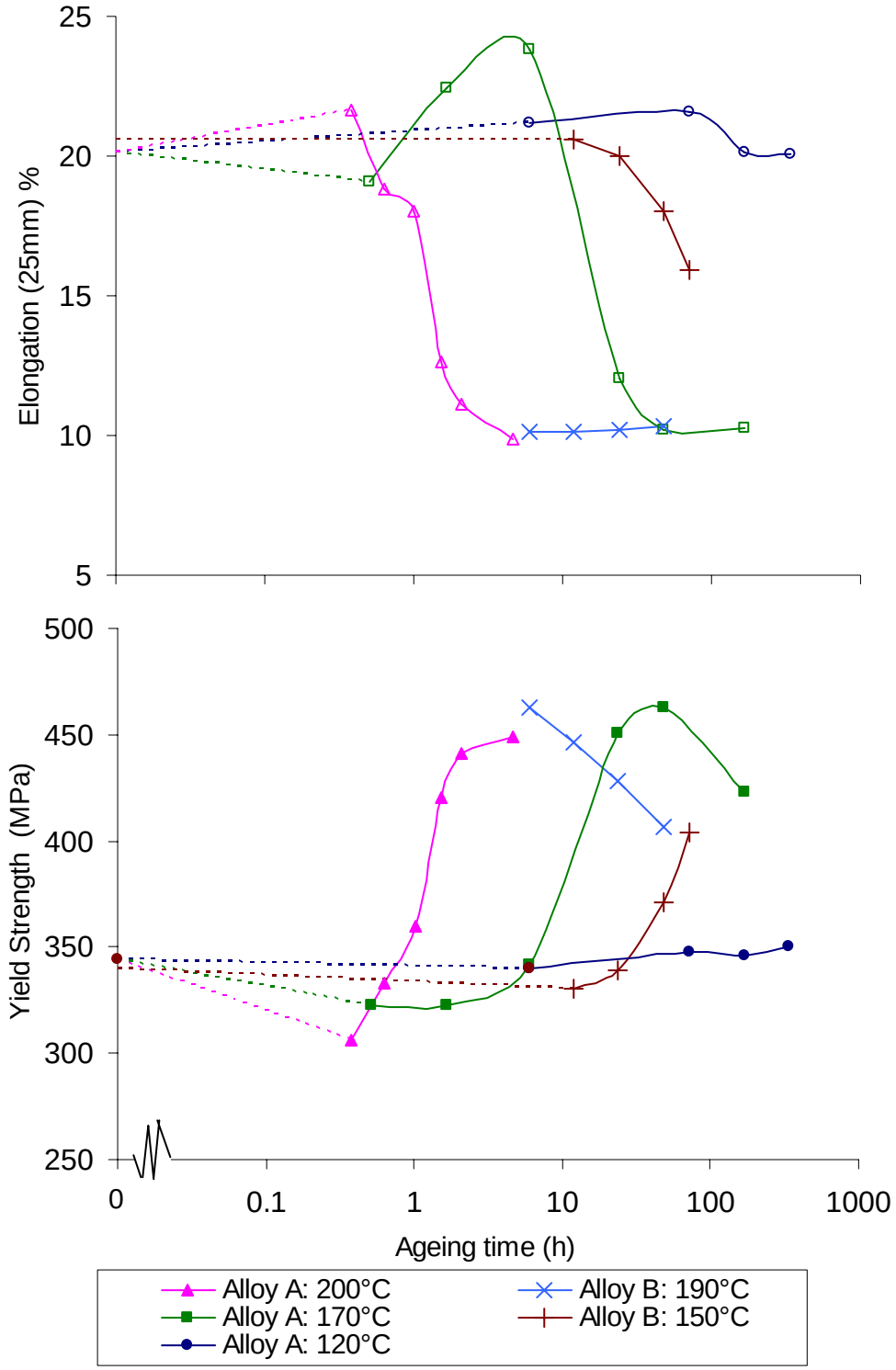

Fig. 4.5 Yield strength and elongation ageing curves for two 2024 alloys. Data for alloy B are from [1].

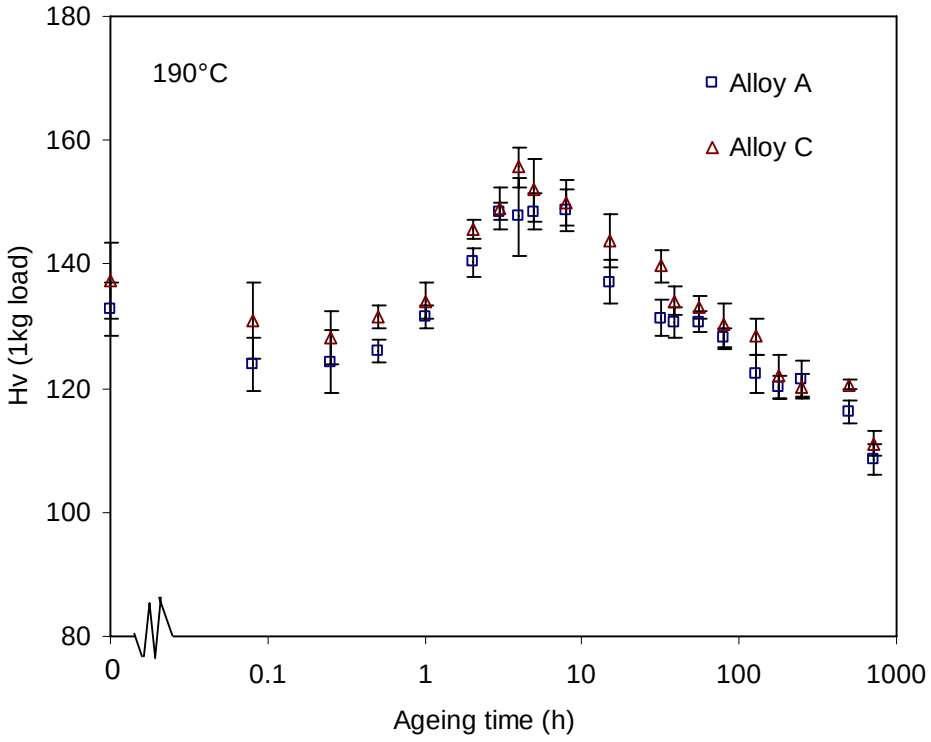

Fig. 4.6 Vickers hardness ageing curves for alloy A and alloy C at 190°C.

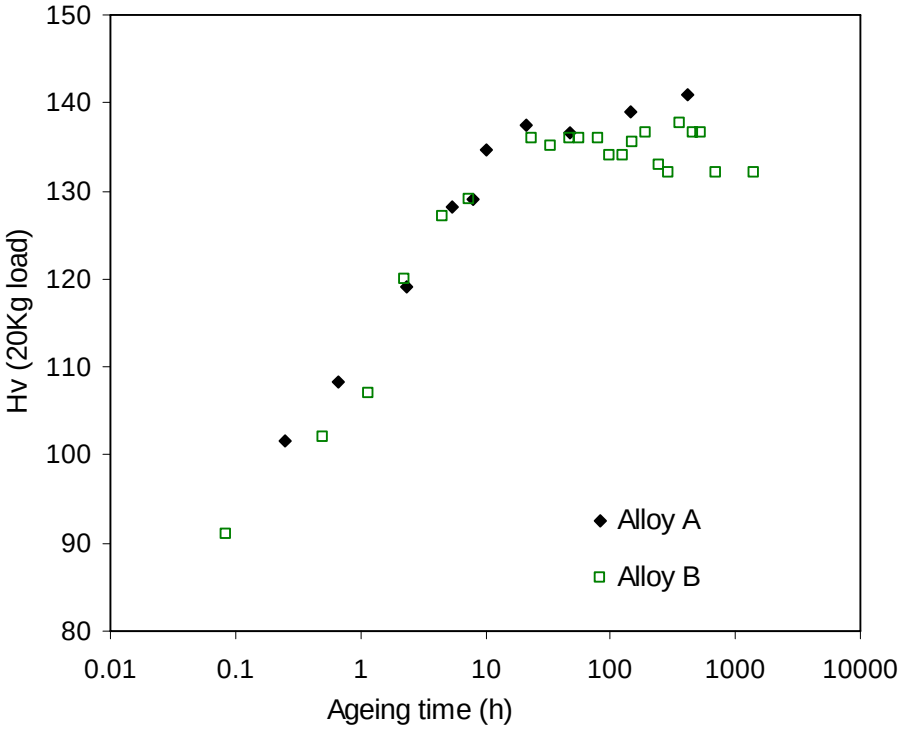

Fig. 4.7 Vickers hardness ageing curves for alloys A and B at room temperature. Typical standard deviation is ±2Hv (Error bars are omitted for clarity).

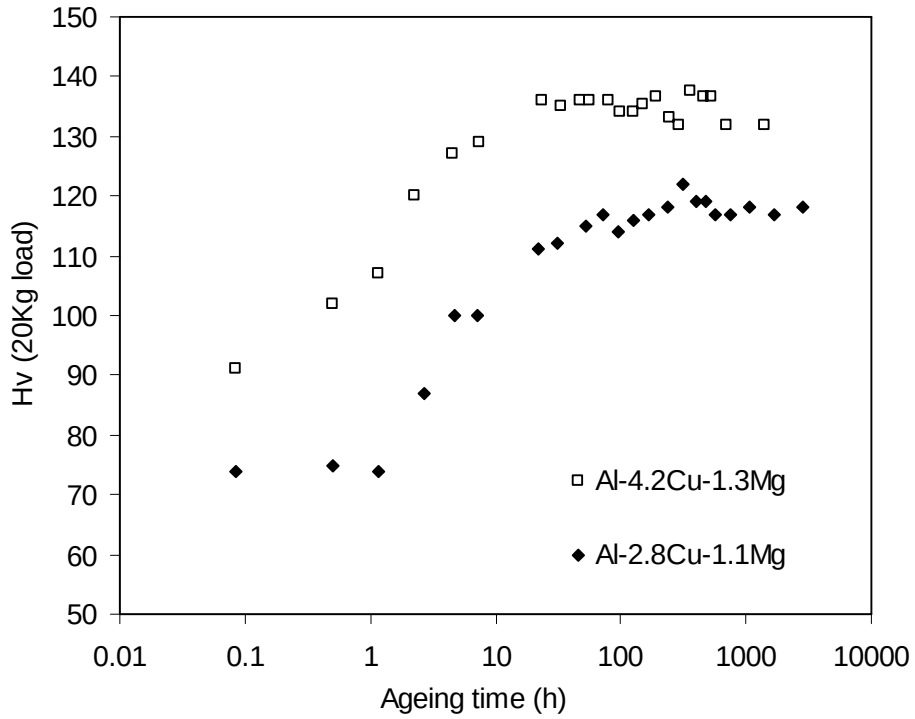

Fig. 4.8 Vickers hardness ageing curves for alloy B (Al-4.2Cu-1.3Mg wt.%) and alloy D (Al-2.8Cu-1.1Mg wt.%) at room temperature. Typical standard deviation is ±2Hv.

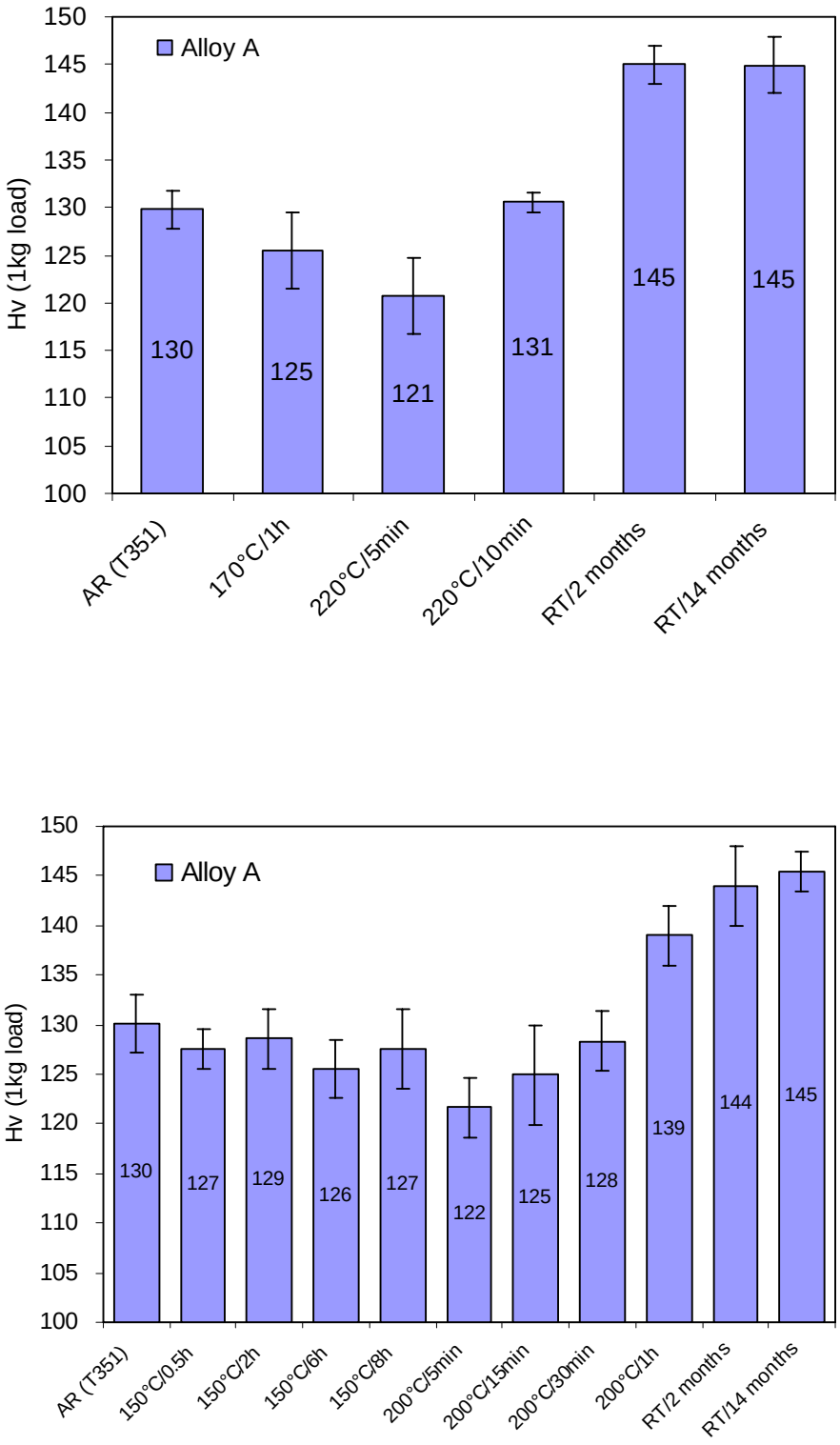

Fig. 4.9 Changes in Vickers hardness with heat treatments for alloy A (2024-T351).

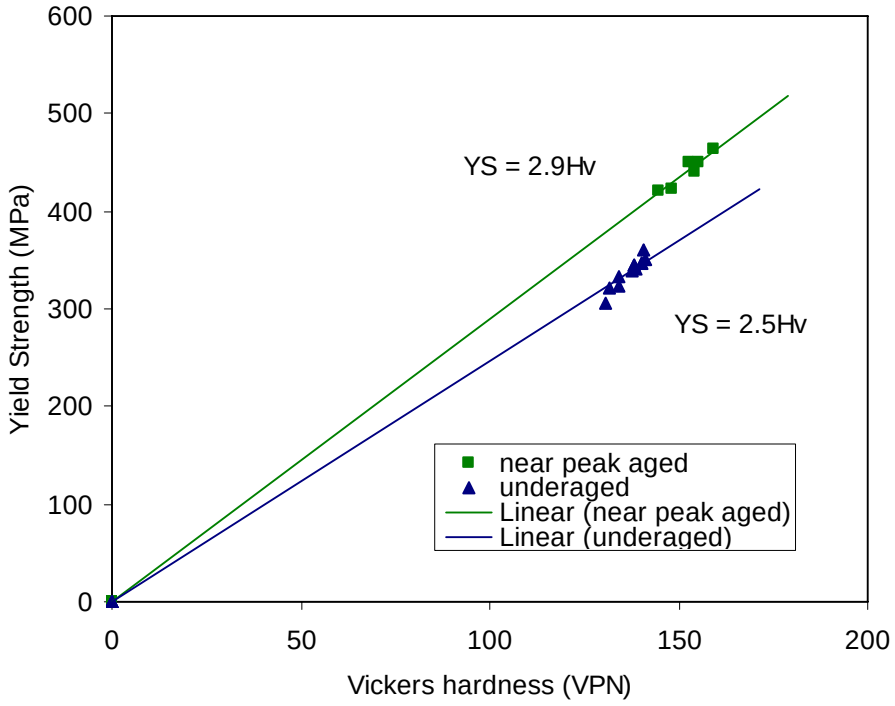

Fig. 4.10 Correlation between the yield strength and the Vickers hardness for alloy A (2024-T351) aged at 120°C, 170°C and 200°C.

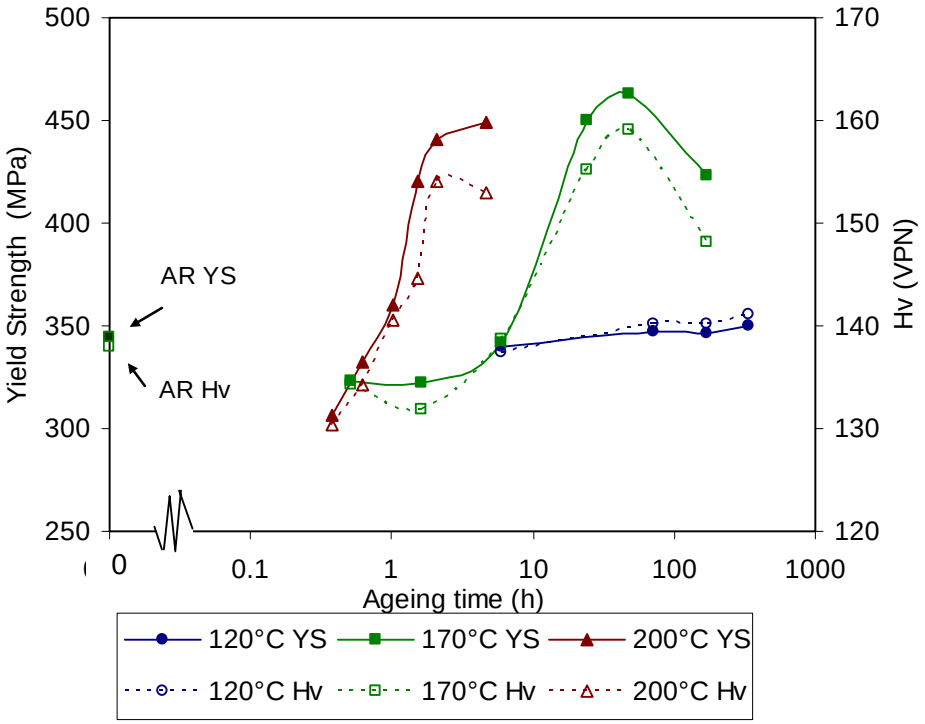

Fig. 4.11 Evolution of the yield strength and the Vickers hardness for alloy A (2024-T351).

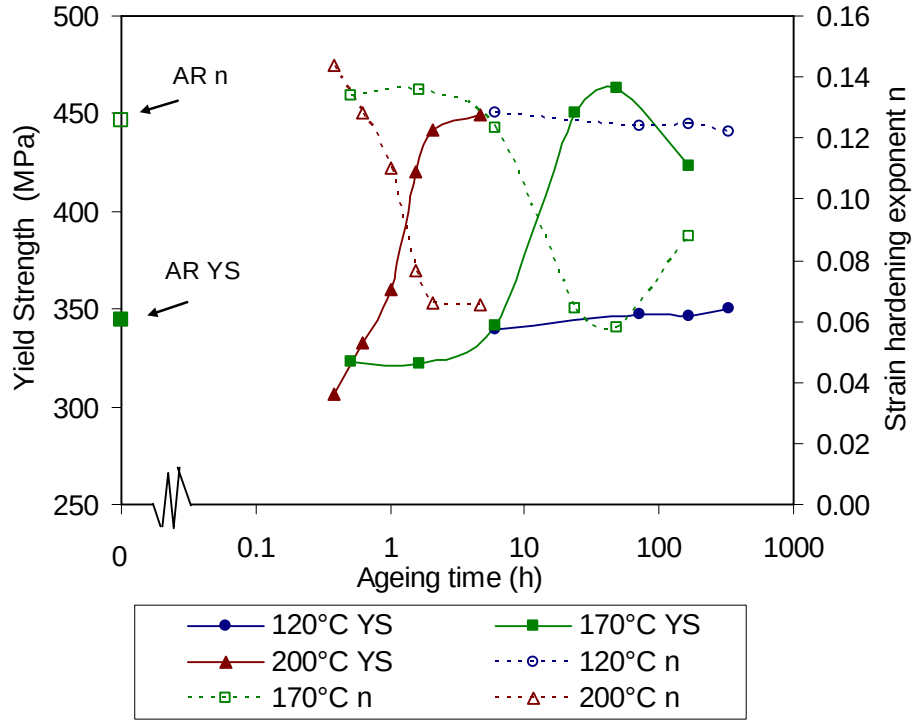

Fig. 4.12 Evolution of the yield strength and the strain hardening exponent for alloy A (2024-T351).

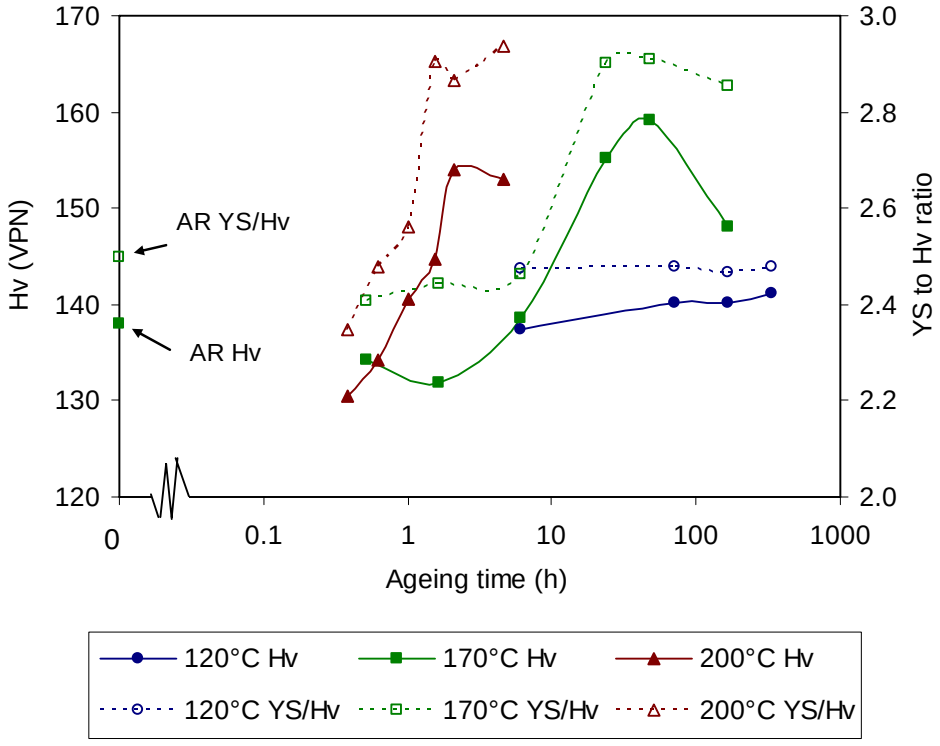

Fig. 4.13 Evolution of the Vickers hardness and the YS to Hv ratio for alloy A (2024-T351).

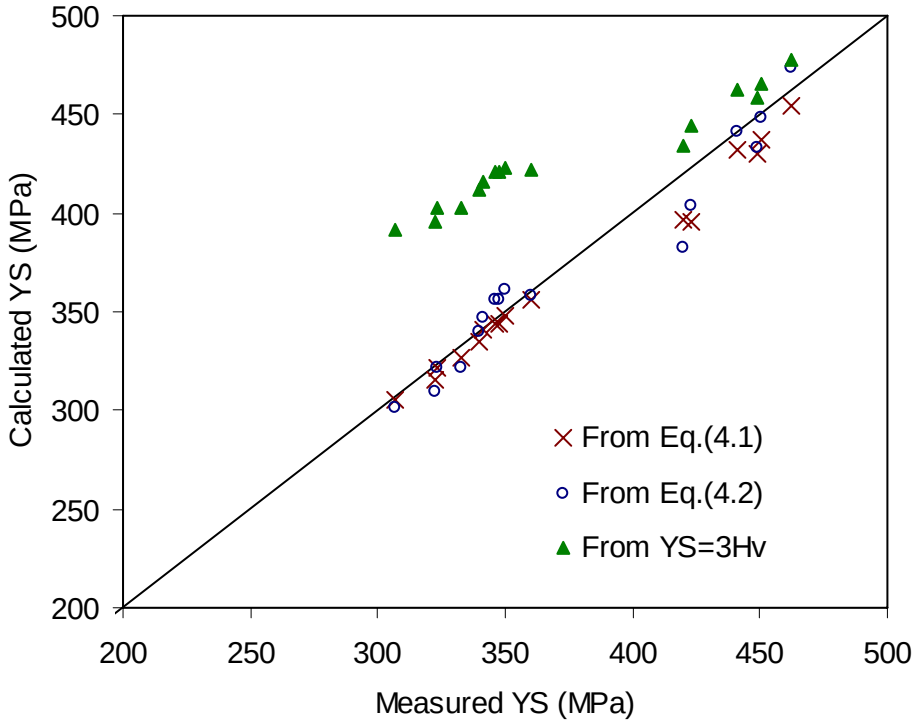

Fig. 4.14 Comparison of calculated and experimental yield strengths for alloy A (2024-T351) aged at 120°C, 170°C and 200°C. Calculated yield strengths from Eq.(4.1), Eq.(4.2) and the linear relationship of YS=3Hv are presented.

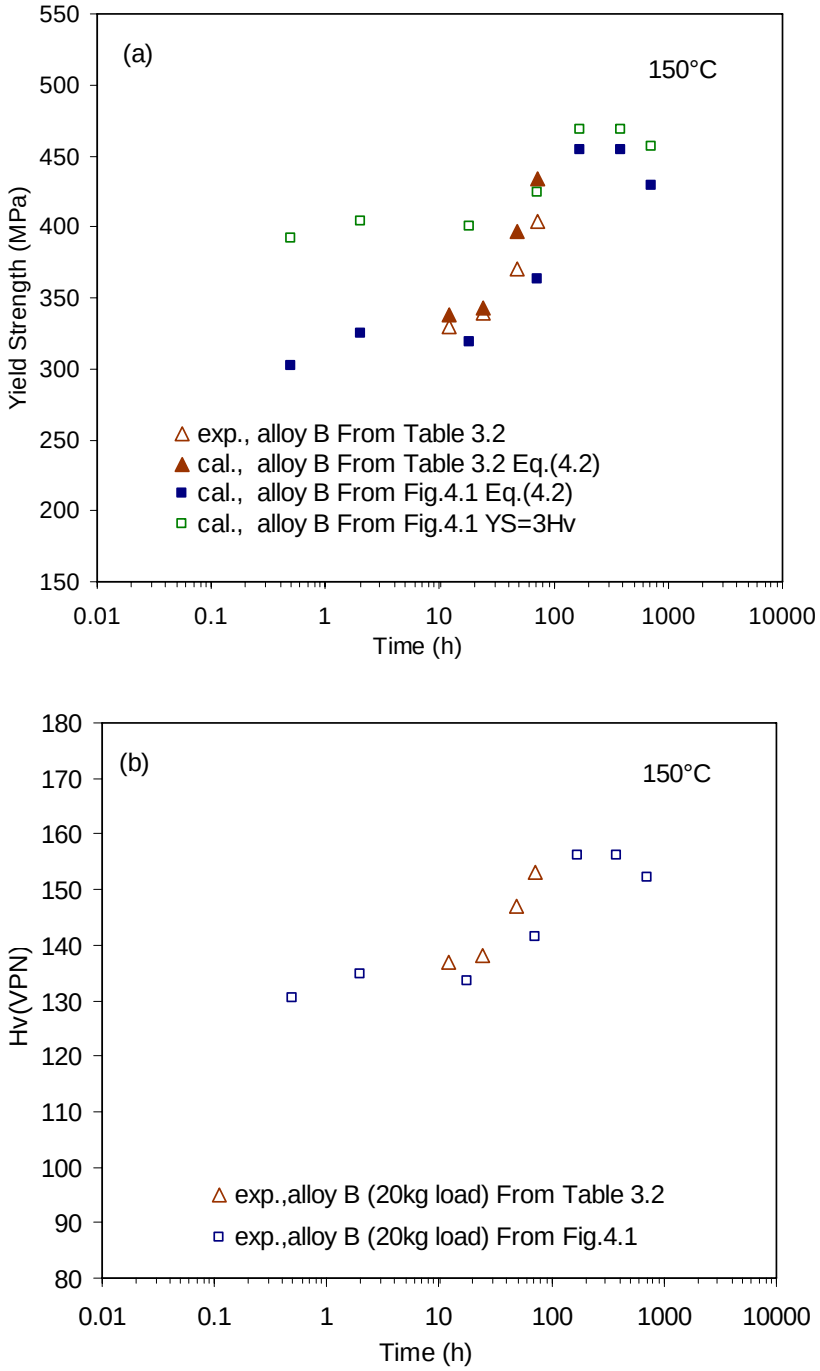

Fig. 4.15 (a) Comparison of calculated YS-time ageing curve by Eq.(4.2) with λ_1=2.3 and λ_2=3.0 (solid triangles) with the experimental one from Table 3.2 (open triangles) for alloy B. Calculated YS-time curves by Eq.(4.2) (solid squares) and by YS=3Hv (open squares) from Hv data in Fig.4.1 for alloy B are also presented. (b) Corresponding experimental Vickers hardness data at 150°C.

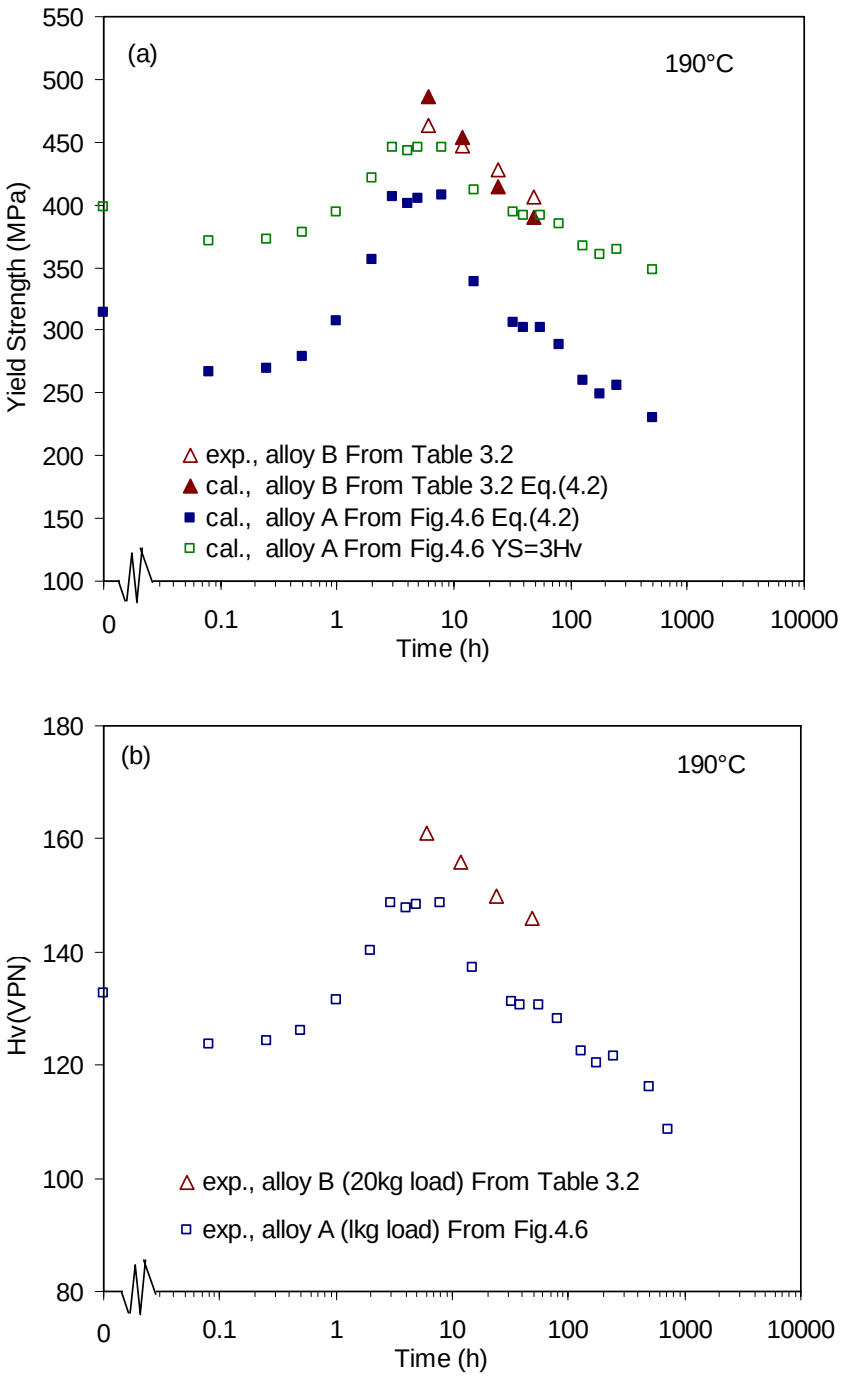

Fig. 4.16 (a) Comparison of calculated YS-time ageing curve by Eq.(4.2) with λ_1=2.3 and λ_2=3.0 (solid triangles) with the experimental one from Table 3.2 (open triangles) for alloy B. Calculated YS-time curves by Eq.(4.2) (solid squares) and by YS=3Hv (open squares) from Hv data in Fig.4.6 for alloy A are also presented. (b) Corresponding experimental Vickers hardness data at 190°C.

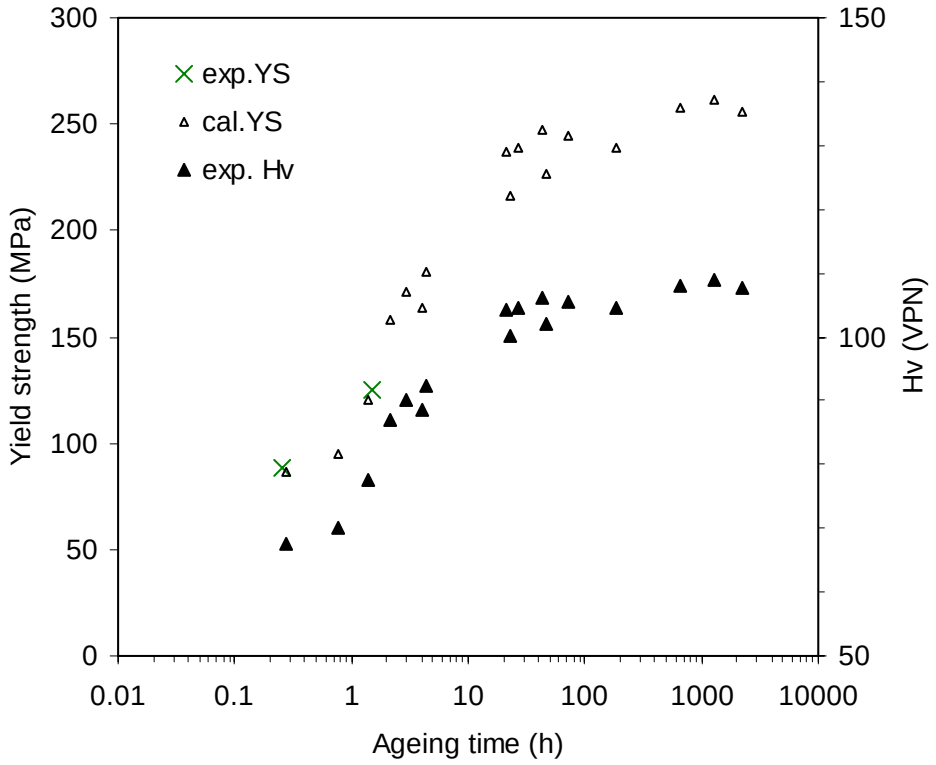

Fig. 4.17 Natural ageing curve of an Al-2.5Cu-1.2Mg alloy. Converted yield strength was calculated from Vickers hardness data in [6] using Eq.(4.2) with λ_1=1.35 ± 0.05 and λ_2=2.3.

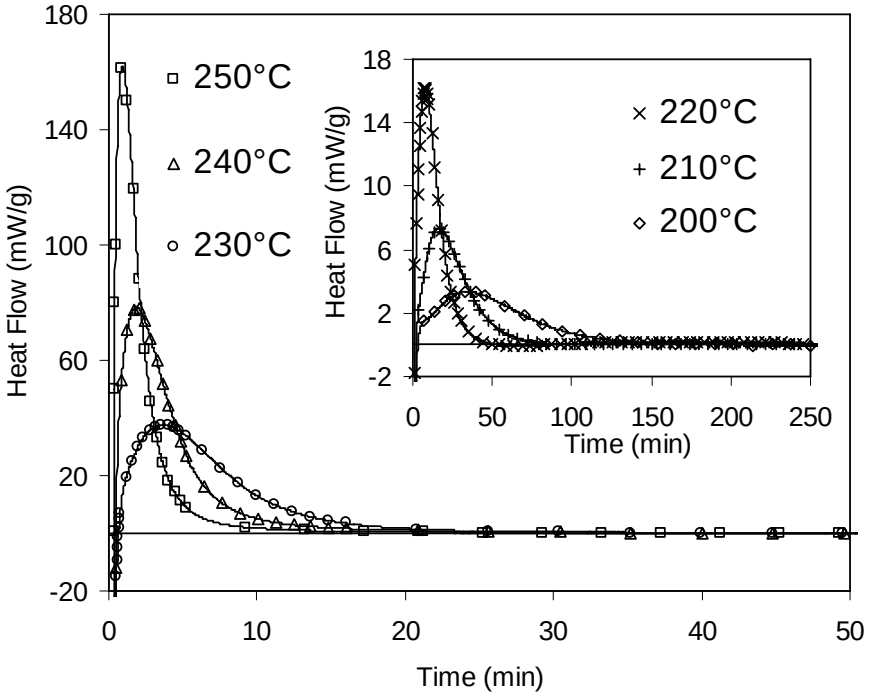

Fig. 4.18 The isothermal calorimetry curves for alloy A (2024-T351).

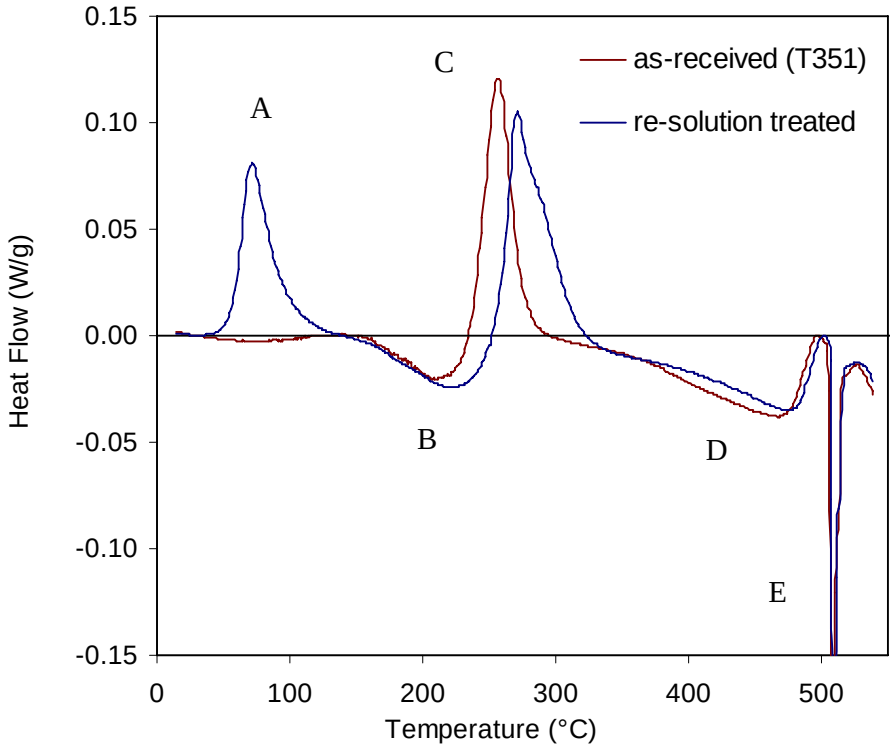

Fig. 4.19 Effect of stretching on DSC results for alloy A (2024-T351). Heating rate: 10°C/min.

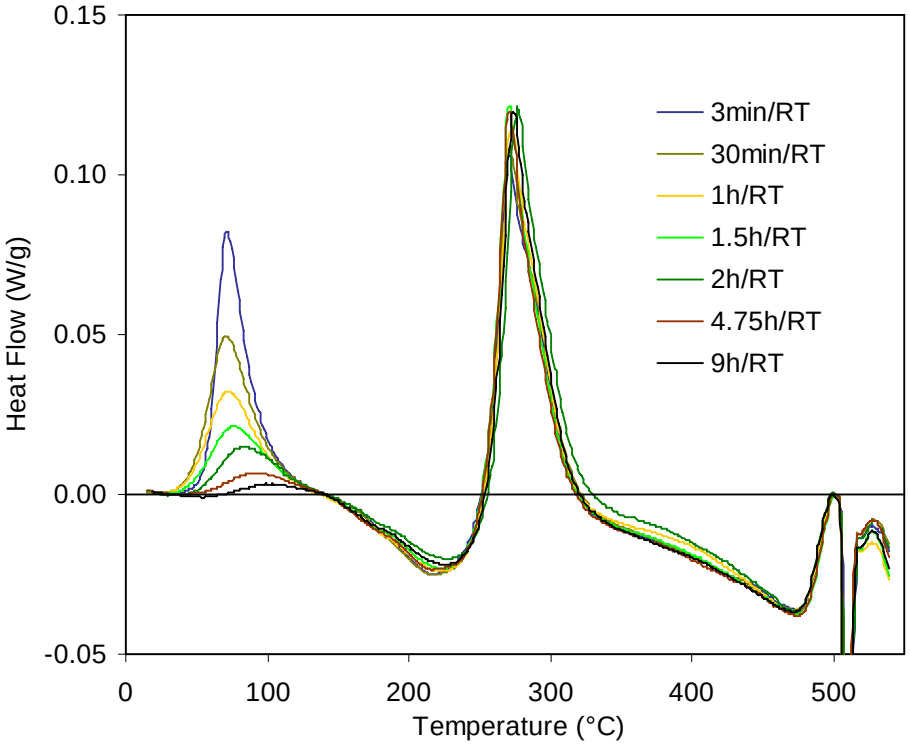

Fig. 4.20 DSC curves of re-solution treated and quenched alloy A aged at room temperature. Heating rate: 10°C/min.

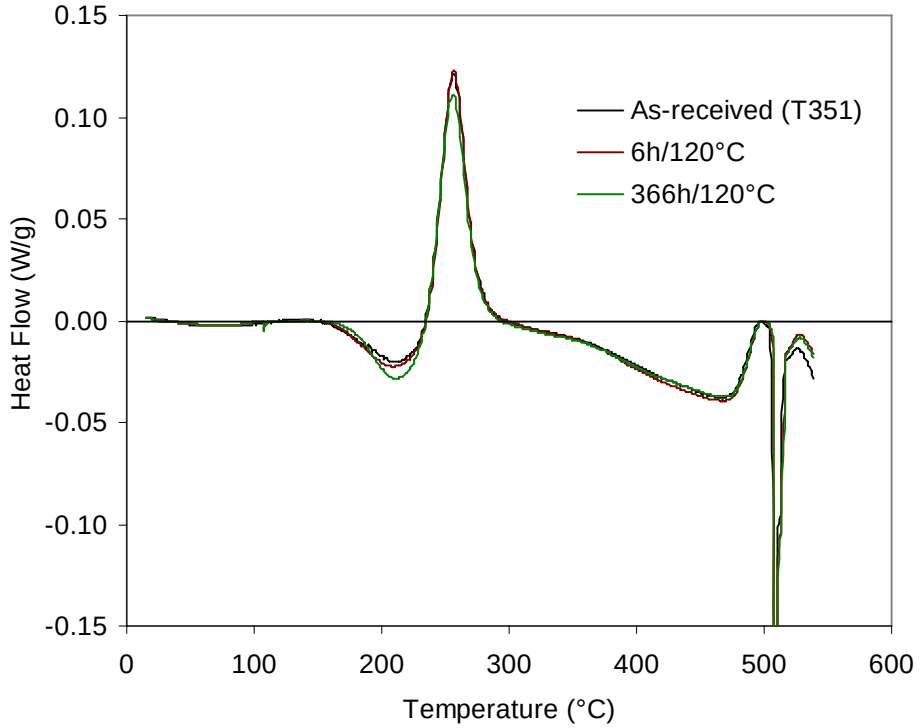

Fig. 4.21 DSC curves of alloy A (2024-T351) aged at 120°C. Heating rate: 10°C/min.

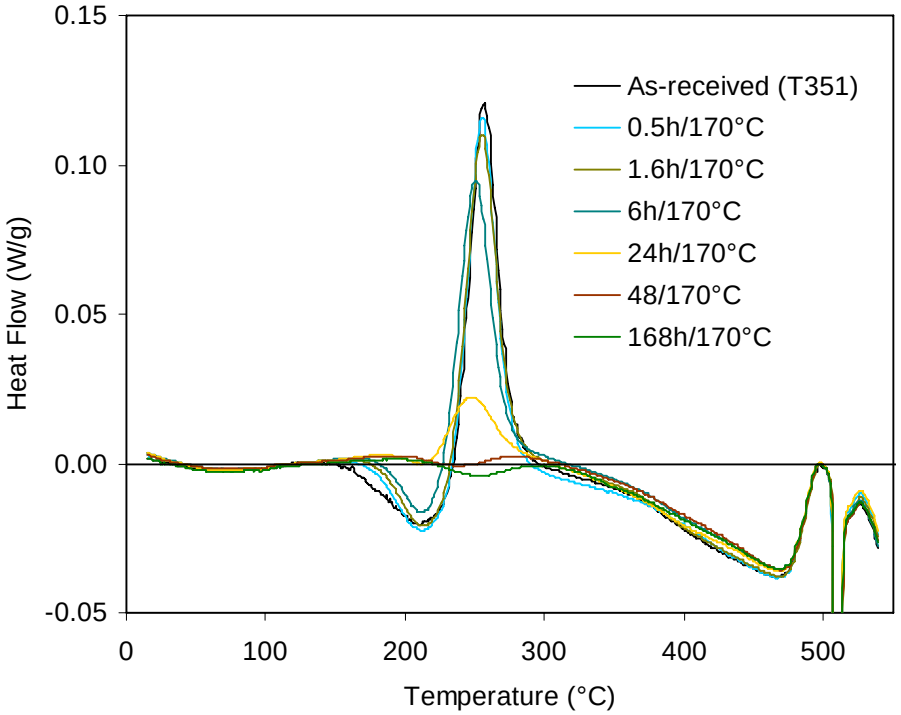

Fig. 4.22 DSC curves of alloy A (2024-T351) aged at 170°C. Heating rate: 10°C/min.

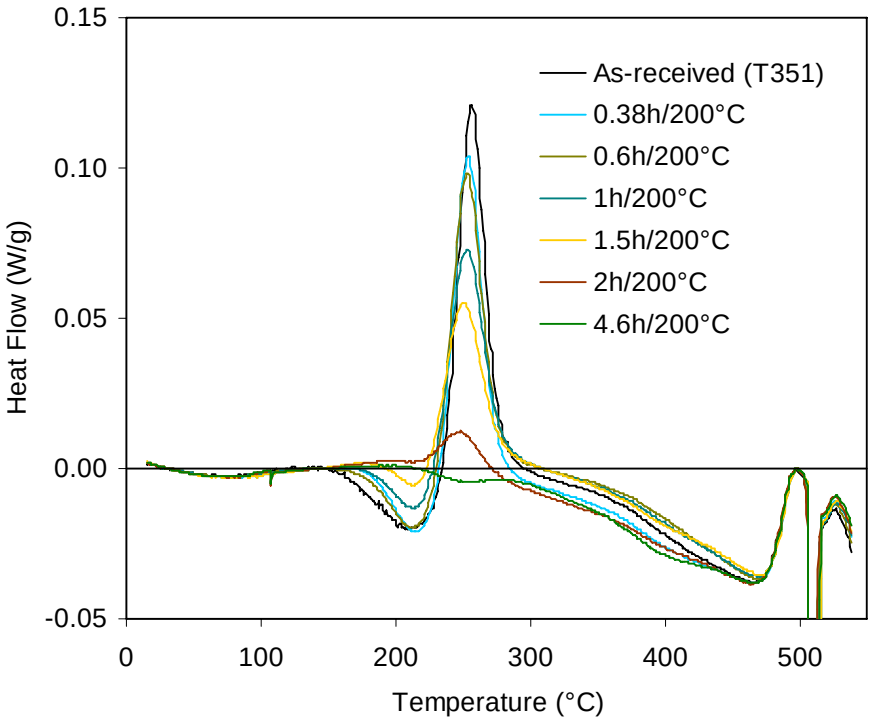

Fig. 4.23 DSC curves of alloy A (2024-T351) aged at 200°C. Heating rate: 10°C/min.

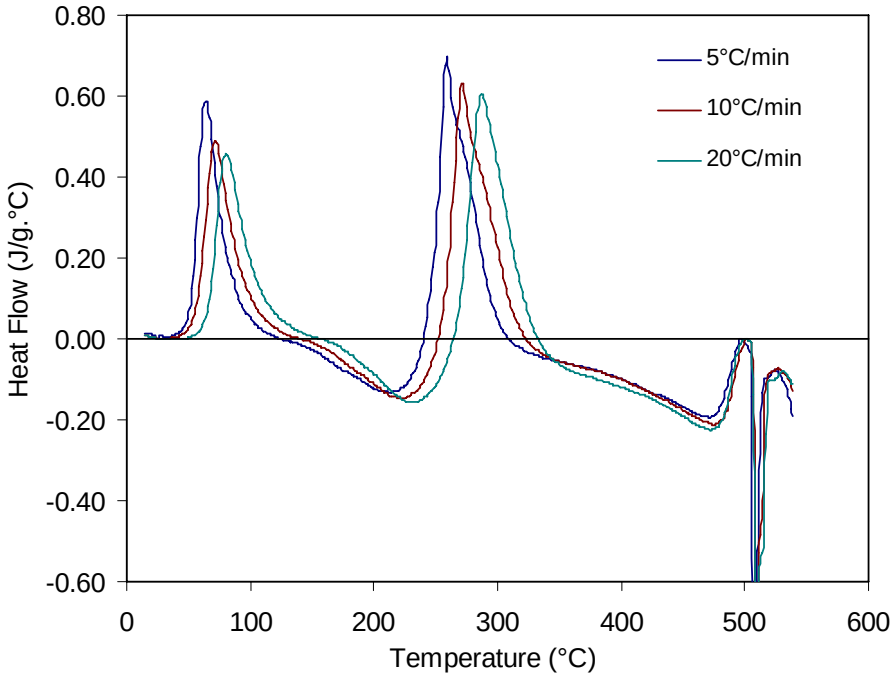

Fig. 4.24 DSC curves of re-solution treated and quenched alloy A at three heating rates.

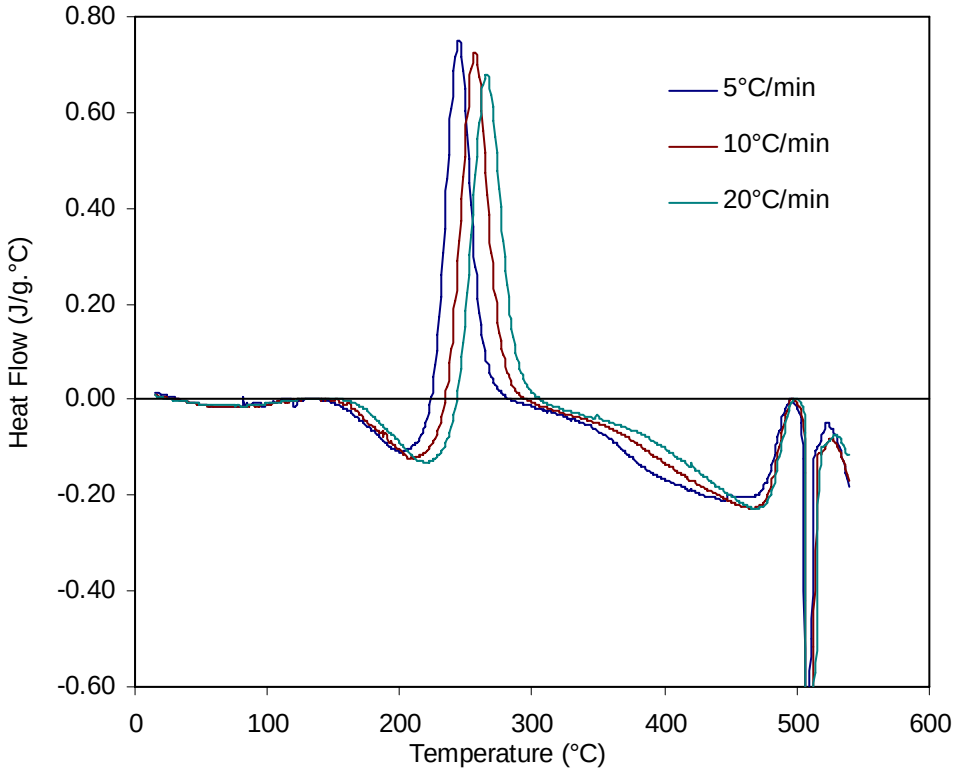

Fig. 4.25 DSC curves of alloy A (2024-T351) at three heating rates.

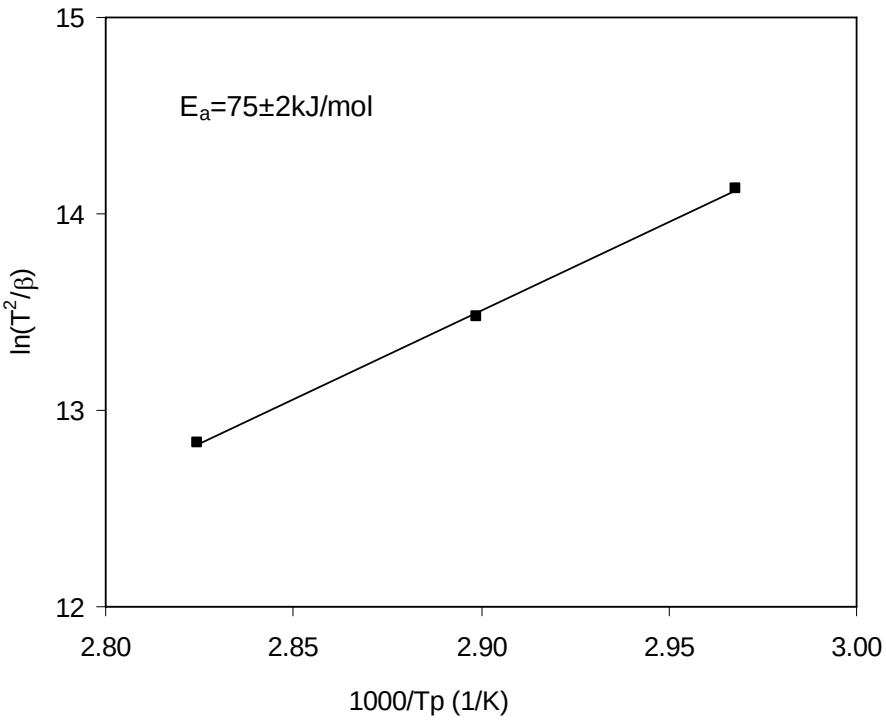

Fig. 4.26 Determination of the activation energy for cluster formation in alloy A using the Kissinger peak method.

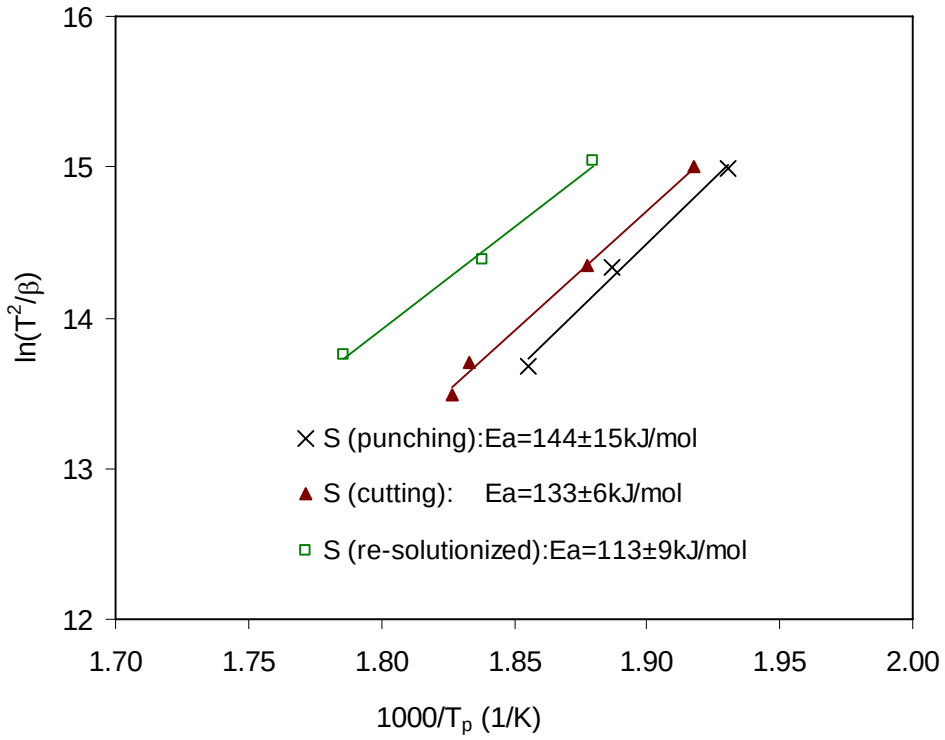

Fig. 4.27 Determination of the activation energy for S phase precipitation in alloy A using the Kissinger peak method.

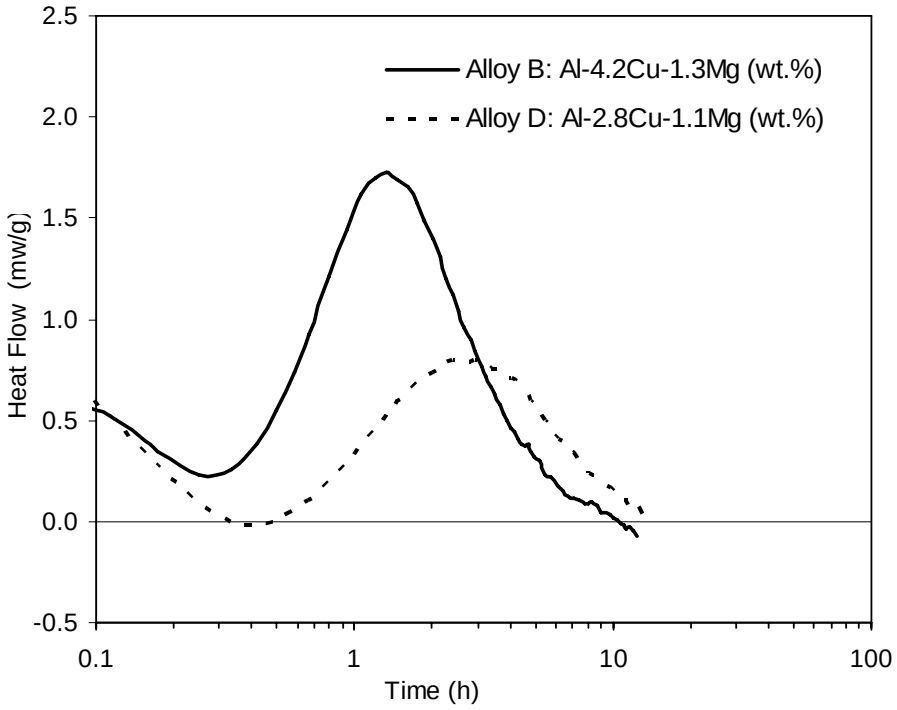

Fig. 4.28 Isothermal calorimetry curves of the Al-4.2Cu-1.3Mg (alloy B) and the Al-2.8Cu-1.1Mg alloy (alloy D) during ageing at 25ºC. (Courtesy of Dr. N. Gao).

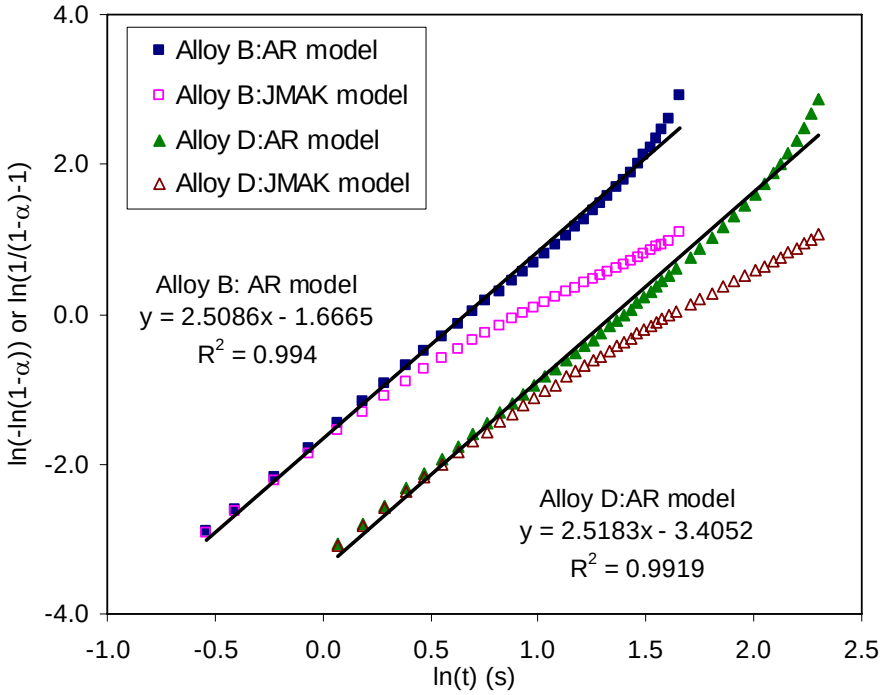

Fig. 4.29 Plots of ln(-ln(1-α)) versus ln$t$ for n using JMAK model and plots of ln(1/(1-α)-1) versus ln$t$ for n using AR model for alloys B and D aged at 25ºC.

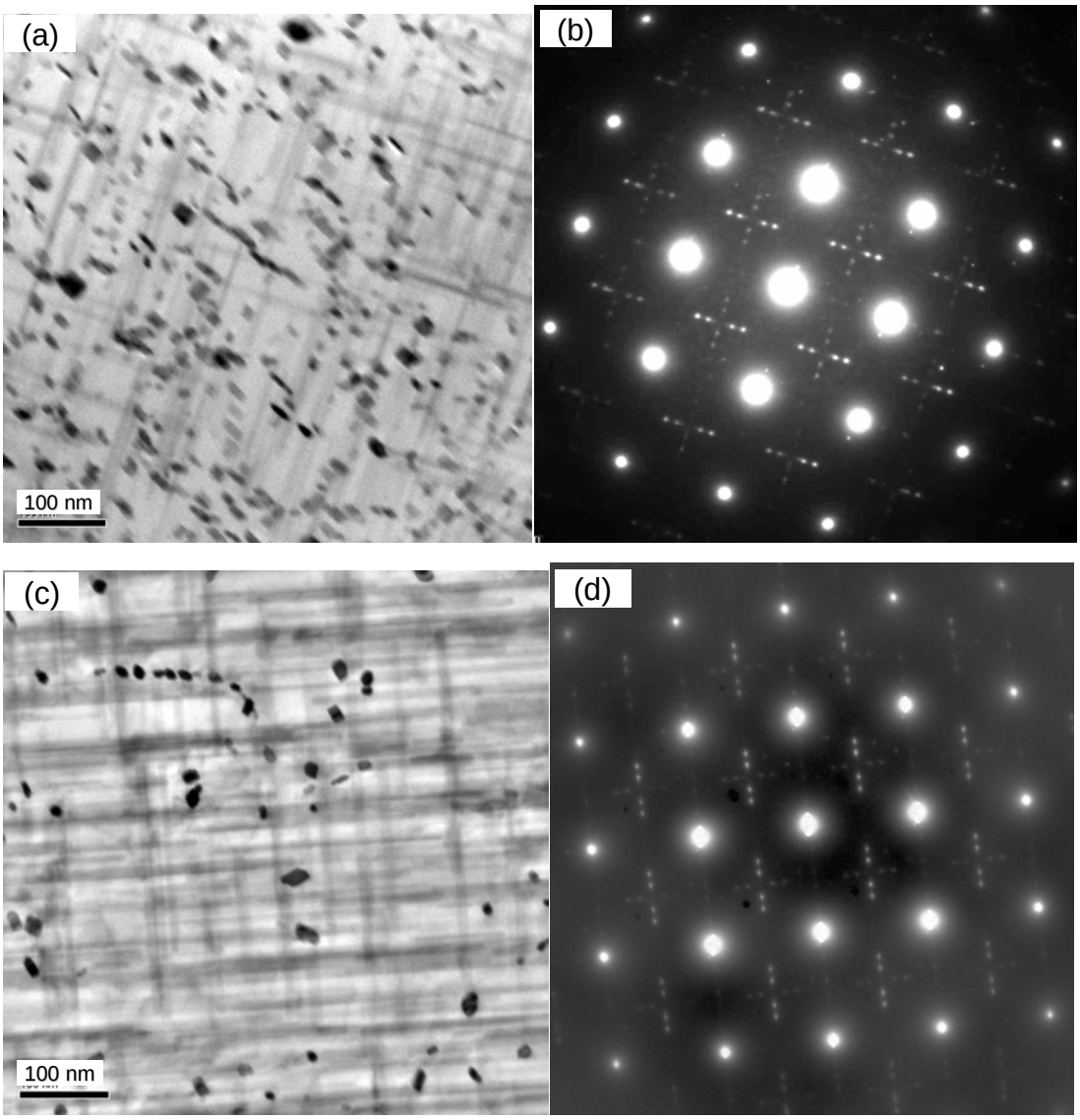

Fig. 4.30 TEM micrographs and corresponding SADs for alloy B (a-b) and alloy C (c-d) aged for 96 h at 190°C (bright field, B= [001]). Results for alloy B (a-b) are from [1].

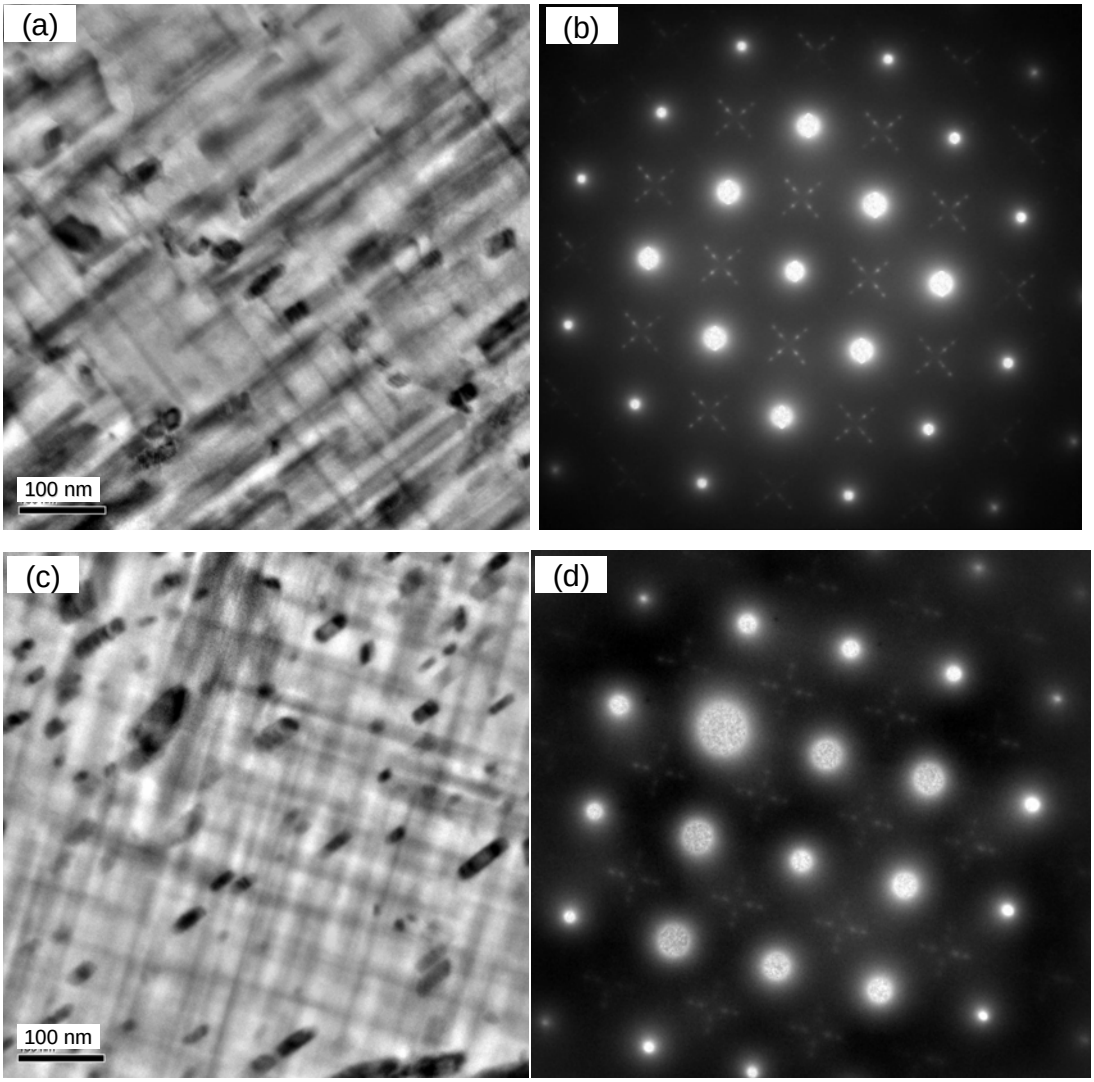

Fig. 4.31 TEM micrographs and corresponding SADs for alloy A (a-b) and alloy C (c-d) aged for 720 h at 190°C (bright field, B=[001]).

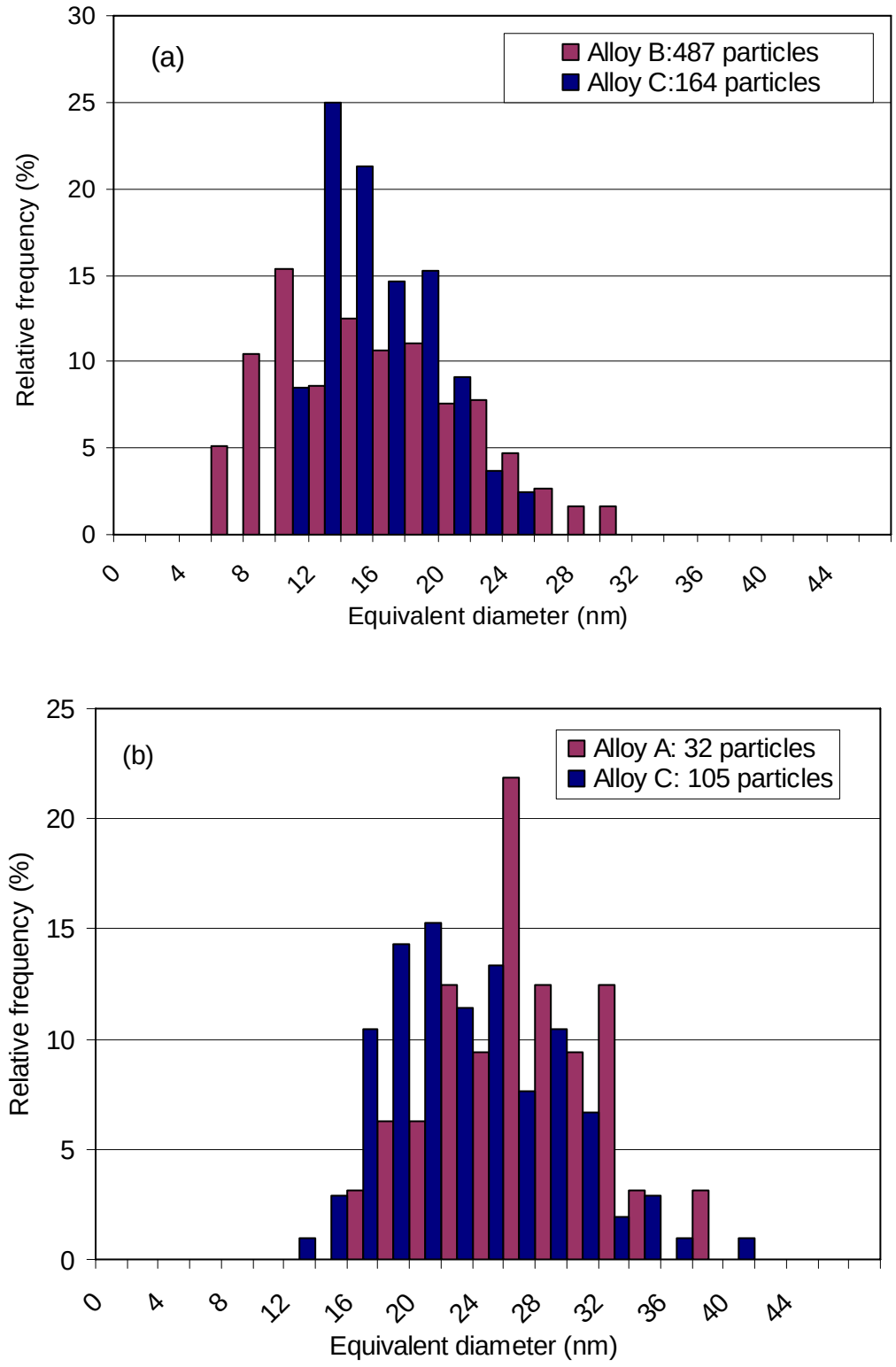

Fig. 4.32 Distributions of the equivalent diameters for (a) alloy B and alloy C aged at 190°C for 96h; (b) alloy A and alloy C aged at 190°C for 720h.

References

[1] N. Gao, N. Kamp, I. Sinclair, and M. J. Starink, 'Innovation of age forming through development of novel damage tolerant alloys (report on DARP project)', University of Southampton, 2001.

[2] H. K. Hardy, 'The ageing characteristics of some ternary aluminium-copper-magnesium alloys with copper : magnesium weight ratios of 7:1 and 2.2:1', *J. Inst. Metals*, 1954-55, **83**, 17-34.

[3] H. C. Shih, N. J. Ho, and J. C. Huang, 'Precipitation behaviors in Al-Cu-Mg and 2024 aluminum alloys', *Metall. Mater. Trans. A*, 1996, **27**, 2479-2494.

[4] H. Martinod, C. Renon, and J. Calvet, 'Influence of deformation after quenching on mechanical characteristics and resistance to creep of aluminium alloys used in aeronautics', *Rev. Metall.*, 1966, **63**, 815-821.

[5] J. T. Vietz and I. J. Polmear, 'The influence of small additions of silver on the ageing of aluminium alloys: observations on Al-Cu-Mg alloys', *J. Inst. Metals*, 1966, **94**, 410-419.

[6] R. N. Wilson, D. M. Moore, and P. J. E. Forsyth, 'Effect of 0.25% silicon on precipitation porcesses in an aluminium-2.5% copper-1.2% magnesium alloy', *J.Inst.Metals*, 1967, **95**, 177-183.

[7] C. R. Hutchinson and S. P. Ringer, 'Precipitation processes in Al-Cu-Mg alloys microalloyed with Si', *Metall. Mater. Trans. A*, 2000, **31**, 2721-2733.

[8] R. N. Lumley, I. J. Polmear, and A. J. Morton, 'Control of secondary precipitation to improve the performance of aluminium alloys', *Mater. Sci. Forum*, 2002, **396-402**, 893-898.

[9] R. N. Lumley, I. J. Polmear, and A. J. Morton, 'Interrupted aging and secondary precipitation in aluminium alloys', *Mater. Sci. Technol.*, 2003, **19**, 1483-1490.

[10] R. N. Lumley, I. J. Polmear, and A. J. Morton, 'Temper developments using secondary ageing', in: J. F. Nie, A. J. Morton, and B. C. Muddle (Eds.), *Proc. 9th International Conference on Aluminium Alloys (ICAA9)*, Brisbane, Australia, 2004, p.85-95.

[11] D. Tabor, *J.Inst.Metals*, 1951, **79**, 1.

[12] J. R. Cahoon, W. H. Broughton, and A. R. Kutzak, 'The Determination of Yield Strength From Hardness Measurements.' *Metall. Trans.*, 1971, **2**, 1979-1983.

[13] D. Tabor, *The Hardness of Metals*, Clarendon Press, Oxford, 1951, p.102.

[14] A. Deschamps and Y. Brechet, 'Influence of predeformation and ageing of an Al-Zn-Mg alloy - II. Modeling of precipitation kinetics and yield stress', *Acta Mater.*, 1999, **47**, 293-305.

[15] O. R. Myhr, O. Grong, and S. J. Andersen, 'Modelling of the age hardening behaviour of Al-Mg-Si alloys', *Acta Mater.*, 2001, **49**, 65-75.

[16] G. Liu, G. J. Zhang, X. D. Ding, J. Sun, and K. H. Chen, 'Modeling the strengthening response to aging process of heat- treatable aluminum alloys containing plate/disc- or rod/needle- shaped precipitates', *Mater. Sci. Eng.*, 2003, **344**, 113-124.

[17] M. J. Starink, I. Sinclair, N. Gao, N. Kamp, P. J. Gregson, P. D. Pitcher, A. Levers, and S. Gardiner, 'Development of new damage tolerant alloys for age-forming', *Mater. Sci. Forum*, 2002, **396-402**, 601-606.

[18] A. K. Jena, A. K. Gupta, and M. C. Chaturvedi, 'A Differential Scanning Calorimetric Investigation of Precipitation Kinetics in the Al-1.53 Wt-Percent Cu-0.79 Wt- Percent Mg Alloy', *Acta metall*, 1989, **37**, 885-895.

[19] A. Charai, T. Walther, C. Alfonso, A. M. Zahra, and C. Y. Zahra, 'Coexistence of clusters, GPB zones, S "-, S '- and S-phases in an Al-0.9% Cu-1.4% Mg alloy', *Acta Mater.*, 2000, **48**, 2751-2764.

[20] A. M. Zahra, C. Y. Zahra, C. Alfonso, and A. Charai, 'Comments on "Cluster hardening in an aged Al-Cu-Mg alloy"', *Scr. Mater.*, 1998, **39**, 1553-1558.

[21] A. M. Zahra and C. Y. Zahra, 'Comment on 'Positron lifetime study of an Al-1.7 at.% Mg-1.1 at.% Cu alloy", *Philos. Mag. Lett.*, 2002, **82**, 9-12.

[22] S. P. Ringer, S. K. Caraher, and I. J. Polmear, 'Response to comments on cluster hardening in an aged Al-Cu-Mg alloy', *Scripta mater.*, 1998, **39**, 1559-1567.

[23] S. Abis, M. Massazza, P. Mengucci, and G. Riontino, 'Early ageing mechanisms in a high-copper AlCuMg alloy', *Scripta mater.*, 2001, **45**, 685-691.

[24] M. J. Starink, N. Gao, L. Davin, J. Yan, and A. Cerezo, 'Room temperature precipitation in quenched Al-Cu-Mg alloys: a model for the reaction kinetics and yield strength development', *Philos. Mag.*, 2005, **85**, 1395-1417.

[25] L. Davin, *PhD thesis*, Oxford University, 2004.

[26] F. Lefebvre, S. Wang, M. J. Starink, and I. Sinclair, 'Microstructural features of fusion welded 2024-T351', *Mater. Sci. Forum*, 2002, **396-402**, 1555-1600.

[27] A. M. Zahra and C. Y. Zahra, 'Conditions for S'-Formation in an Al-Cu-Mg Alloy', *J. Therm. Anal.*, 1990, **36**, 1465-1470.

[28] J. M. Papazian, 'Effects of SiC Whiskers and Particles on Precipitation in Aluminum Matrix Composites', *Metall.Trans. A*, 1988, **19**, 2945-2953.

[29] M. J. Starink, 'Analysis of aluminium based alloys by catorimetry: quantitative analysis of reactions and reaction kinetics', *Int. Mater. Rev.*, 2004, **49**, 191-226.

[30] H. E. Kissinger, 'Reaction kinetics in differential thermal analysis', *Anal. Chem.*, 1957, **29**, 1702-1706.

[31] E. J. Mittemeijer, 'Analysis of the Kinetics of Phase-Transformations', *J. Mater. Sci.*, 1992, **27**, 3977-3987.

[32] T. Ozawa, 'Estimation of Activation-Energy by Isoconversion Methods', *Thermochim. Acta*, 1992, **203**, 159-165.

[33] M. J. Starink, 'A new method for the derivation of activation energies from experiments performed at constant heating rate', *Thermochim. Acta*, 1996, **288**, 97-104.

[34] M. J. Starink, 'The determination of activation energy from linear heating rate experiments: a comparison of the accuracy of isoconversion methods', *Thermochim. Acta*, 2003, **404**, 163-176.

[35] A. K. Gupta, A. K. Jena, and M. C. Chaturvedi, 'A Differential Technique for the Determination of the Activation-Energy of Precipitation Reactions from Differential Scanning Calorimetric Data', *Scr. Metall.*, 1988, **22**, 369-371.

[36] C. J. Smithells, *Metals Reference Book*, 7th edn, Butterworths-Heinemann, London, 1992.

[37] G. W. Smith, 'Precipitation kinetics in solutionized aluminum alloy 2124. Determination by scanning and isothermal calorimetry', *Thermochim. Acta*, 1998, **317**, 7-23.

[38] I. N. A. Oguocha and S. Yannacopoulos, 'Precipitation and dissolution kinetics in Al-Cu-Mg-Fe-Ni alloy 2618 and Al-alumina particle metal matrix composite', *Mater. Sci. Eng. A*, 1997, **231**, 25-33.

[39] M. J. Starink, C. Y. Zahra, and A. M. Zahra, 'Analysis of precipitation in Al-based alloys using a novel model for nucleation and growth reactions', *J. Therm. Anal.*, 1998, **51**, 933-942.

[40] M. J. Starink and A. M. Zahra, 'Determination of the transformation exponent s from experiments at constant heating rate', *Thermochim. Acta*, 1997, **298**, 179-189.

[41] F. L. Cumbrera and F. SanchezBajo, 'The use of the JMAYK kinetic equation for the analysis of solid-state reactions: Critical considerations and recent interpretations', *Thermochim. Acta*, 1995, **266**, 315-330.

[42] M. J. Starink, 'Kinetic equations for diffusion-controlled precipitation reactions', *J. Mater. Sci.*, 1997, **32**, 4061-4070.

[43] S. Wang, M. J. Starink, and N. Gao, 'Precipitation hardening in Al-Cu-Mg alloys revisited', *Scripta Mater.*, 2006, **54**, 287-291.

[44] S. Wang and M. J. Starink, ' Precipitates and intermetallic phases in precipitation hardening Al–Cu–Mg–(Li) based alloys', *Int. Mater. Rev.*, 2005, **50**, 193-215.

[45] M. J. Starink and J. Yan, 'A model for strengthening of Al-Cu-Mg alloys by S phase', in: M. Tiryakioglu and L. A. Lalli (Eds.), *1st International Symposium on Metallurgical Modeling for Aluminum Alloys, ASM Materials Solution 2003*, Pittsburgh, PA, October 12-15, 2003, p.119-126.

Chapter 5 The model

5.1 Introduction

As reviewed in Section 2.2, for alloys lying in the (α+S) phase region of the Al-Cu-Mg phase diagram, the precipitation sequence is described as:

$$\alpha_{SS} \rightarrow \text{Cu-Mg co-clusters/GPB zones} \rightarrow (\text{GPB2/S}'') \rightarrow \text{S } (Al_2CuMg)$$

To limit the model complexity and only consider the minimum number of phases necessary to model the ageing curves, a simplification on the sequence is made in the present model. Following the discussion in Section 2.2.2.2, in this thesis the term Cu-Mg co-clusters instead of GPB zones will be used to indicate the structure evolved in the early stages of the decomposition. As GPB2 or S″ phase is not generally observed and accepted, it is omitted from the model. Thus in the model a simplified precipitation sequence which involves the formation of the Cu-Mg co-clusters followed by S phase is adopted.

To model the competing precipitation reactions of the Cu-Mg co-clusters and S phase in Al-Cu-Mg alloys, it is assumed that for heat treatment below the solvus of the Cu-Mg co-clusters, the S phase forms at the expense of the Cu-Mg co-clusters. This assumption is supported by experimental evidence from TEM studies [1, 2] which show the dissolution of the GPB zones and the growth of the S phase, and by DSC studies which show that the Cu-Mg co-clusters dissolve and are replaced by the S phase (see Section 4.3.2). Based on 3DAP results of Al-Cu-Mg alloys from collaborators at Oxford University [3, 4] and from the literature [5], which show that

the Cu:Mg atomic ratios of the Cu-Mg co-clusters are close to 1, the Cu:Mg atomic ratio of the Cu-Mg co-clusters in the model is taken as 1:1.

In this chapter, firstly, a thermodynamic model for the solvi of Cu-Mg co-clusters and S phase is presented, and the effective solute concentrations are calculated to take account of the amounts of Cu and Mg present in undissolved intermetallic phases. Then a kinetics model is developed to quantitatively describe the precipitation as a function of precipitation temperature, time and alloy composition. The output parameters, such as the mean solute concentration in the matrix, the average precipitate size and the volume fraction of precipitates, are of most interest, and they will be used as input parameters in the strength model to predict the development of yield strength.

5.2 Thermodynamic Model

5.2.1 Solvi of Cu-Mg co-clusters and S phase

The regular solution model described in Section 2.3.1 will be applied to calculate the solvi of Cu-Mg co-clusters and S phase in the Al-rich matrix. Following Eq.(2.5), the solubility limits of Cu and Mg in the matrix for Cu-Mg co-clusters and for S phase can be expressed respectively as:

$$(c_e^{Cu})(c_e^{Mg}) = c_1 \exp[\frac{-\Delta H^{cl}}{RT}] \tag{5.1}$$

$$(c_e^{Cu})(c_e^{Mg}) = c_2 \exp[\frac{-\Delta H^{S}}{RT}] \tag{5.2}$$

where ΔH is the formation enthalpy, c_1 and c_2 are constants. The superscripts *cl* and *S* stand for Cu-Mg co-clusters and S phase, respectively.

The solvus of S phase has been constructed by combining the data for ΔH^S, which is taken as an average value (77 kJ/mol) from [6-8] and the solubility data from Little *et al*. [7]. The parameter c_2 is determined by least-square fitting of Eq (5.2) to

experimental solubility data. The best fit results in $c_2 = 5.0 \times 10^5 (\text{at.}\%)^2$ with $\Delta H^S = 77 kJ/mol$, see **Fig. 5.1**. These values are used throughout the model.

The metastable solvus of Cu-Mg co-clusters has been estimated by Beton and Rollason [9] (see Fig.2.6) using a hardness reversion method, i.e. reversion of the Al-Cu-Mg alloys from the natural aged hardness to the as-quenched hardness (in [9] the Cu-Mg co-clusters were termed GP[Cu, Mg] zones). However, full reversion of clusters/zones without forming any S phase is difficult to achieve, especially at high temperature (in their work, Beton and Rollason did not verify S phase was absent). This will cause the method of hardness reversion in [9] to overestimate the solution temperature.

A practical way to find the solvus temperature of Cu-Mg co-clusters, T_s^{cl}, in Al-Cu-Mg alloys is to estimate it from the ageing curves. Hardy [8] reported that two-stage ageing curves were observed in alloys with a Cu to Mg weight ratio of 2.2:1 aged at the temperature range of 110°C to 240°C (**Fig. 5.2**). As seen in Fig. 5.2, for an Al-3.4Cu-1.6Mg (wt.%) alloy aged at 260°C the rise to peak hardness occurs rapidly and peak hardness is reached within 3 min of ageing. No obvious plateau is present and therefore no two-stage age hardening is observed. Considering the rapid formation of S precipitates at this high temperature and the competing reactions of S and Cu-Mg co-cluster formation for the same solute atoms, it is reasonable to assume that the range of stability of Cu-Mg co-clusters lies between 240°C and 260°C for the Al-3.4Cu-1.6Mg (wt.%) alloy. Ageing curves for an Al-3.98Cu-1.38Mg (wt.%) alloy shown in **Fig. 5.3** indicate that at 240°C some hardening due to the Cu-Mg co-clusters occurs, whereas there is almost no hardening during the initial 10 min of ageing for an Al-2.62Cu-1.35Mg (wt.%) alloy, as the hardness values were only slightly larger than the as-quenched value [10]. This suggests that the upper limit for the solution temperature of Cu-Mg co-clusters is about 240°C for the Al-2.62Cu-1.35Mg (wt.%) alloy. Based on these data, the parameter c_1 used in the regular solution model (Eq.5.1) can be obtained under the assumption that ΔH^{cl} be taken as 38kJ/mol from [6, 11]. c_1 values ranging from $1.3 \times 10^4 (\text{at.}\%)^2$ to $1.9 \times 10^4 (\text{at.}\%)^2$ correspond to a solution temperature of Cu-Mg co-clusters of 260°C to 240°C for the Al-3.4Cu-1.6Mg (wt.%) alloy, and of 240°C to 215°C for the Al-2.62Cu-1.35Mg (wt.%) alloy.

These temperature ranges correspond well with the temperature limits given in [8] at which two-stage ageing curves were obtained for a specific alloy (with predicted accuracy of about ±15°C). For example, Hardy [8] reported that two-stage ageing curves were obtained for an alloy with copper content as low as 2.35wt.% when ageing at 240°C. The model predicts a temperature limit of 225°C for this alloy to show two-stage ageing behaviour. Thus in the present model an average value of 1.6×10^4 (at.%)^2 is taken for c_1. The predicted solvus lines are shown in **Fig. 5.4.** Using this c_1 value, it is obtained that the solvus temperatures of the Cu-Mg co-clusters are 255°C for alloy A (Al-4.20Cu-1.36Mg wt.% alloy) and 215°C for alloy D (Al-2.77Cu-1.06Mg wt.% alloy). The effect of T_s^{cl} on the amount of Cu-Mg co-clusters formed is illustrated in **Fig. 5.5**. It is seen that greater amounts of Cu-Mg co-clusters can be obtained when the alloys are aged at lower temperature. At a certain ageing temperature, higher T_s^{cl} leads to greater amount of Cu-Mg co-clusters formed. Furthermore, Fig. 5.5 shows that the relative difference in the amounts of the Cu-Mg co-clusters formed for two T_s^{cl} limits is smaller for alloys aged at 170°C than that at 220°C. The model to be presented in Section 6.3.2 predicts that a variation in T_s^{cl} of ±15°C produces a maximum deviation (at 200°C) in plateau yield strength of about 4% for alloy A.

5.2.2 Undissolved intermetallic phases

It is reported that insoluble or undissolved particles and dispersoids, such as ω-Al_7Cu_2Fe, S-Al_2CuMg and T-$Al_{20}Cu_2Mn_3$, which form during solidification or homogenisation, are presented in 2x24 alloys [4, 12, 13]. Since the presence of these particles will remove some Cu and Mg from the solid solution, it is necessary to calculate the effective solute concentration in the matrix after solution heat treatment (SHT). A description of the calculation method which is similar to those used in [14] is given below.

The atomic fraction of undissolved S phase is obtained by the regular solution model. The solid solubilities of Cu and Mg, i.e. c_e^{Cu} and c_e^{Mg}, at T_{SHT} can be calculated using

the S solvus determined in Section 5.2.1, and the amount of undissolved S phase is given by:

$$x^S = 4*(c_g^{Cu} - c_e^{Cu}) \tag{5.3}$$

where c_g^{Cu} is the gross Cu content of the alloy.

It is difficult to calculate the amount of ω-Al_7Cu_2Fe using the regular solution model because little solubility data for ω-Al_7Cu_2Fe phase in the Al-Cu-Fe-Mg system is available. Alternatively, the amount of ω-Al_7Cu_2Fe can be calculated based on the solubility of Fe in Al matrix, since the solubility of Fe is not significantly influenced by the additions of Cu or Mg [15]. At typical T_{SHT} for 2024 alloys, which is about 500°C, the maximum solubility of Fe in Al, c_e^{Fe}, is 0.0055 wt.% [16]. The amount of ω-Al_7Cu_2Fe in the alloy is then given by:

$$x^{\omega} = 10*(c_g^{Fe} - c_e^{Fe}) \tag{5.4}$$

where c_g^{Fe} is the gross Fe content of the alloy. A similar treatment is applied to obtain the amount of $Al_{20}Cu_2Mn_3$. Based on the solvus of $Al_{20}Cu_2Mn_3$ in the Al-Cu-Mn system**,** at 500°C the solubility of Mn in Al with a Cu content of 4 wt%, c_e^{Mn}, is about 0.2wt% [17]. Thus the amount of T-$Al_{20}Cu_2Mn_3$ in the alloy is given by:

$$x^T = 25/3*(c_g^{Mn} - c_e^{Mn}) \tag{5.5}$$

where c_g^{Mn} is the gross Mn content of the alloy. Consequently, the effective solute concentration in the matrix after SHT can be obtained from:

$$c_{eff}^{Cu}(t=0) = \frac{c_g^{Cu} - \frac{2}{10}x^{\omega} - \frac{1}{4}x^S - \frac{2}{25}x^T}{1 - x^{\omega} - x^S - x^T} \tag{5.6}$$

$$c_{eff}^{Mg}(t=0)=\frac{c_g^{Mg}-\frac{1}{4}x^S}{1-x^{\omega}-x^S-x^T} \tag{5.7}$$

The validity of the calculation method was checked against the composition data of high purity Al-Cu alloys with different level of Fe impurity given by Fink *et al.* [18]. The measured Cu content in solid solution from [18] and the calculated Cu contents using the above method are in a good agreement (see Table 5.1).

5.3 Kinetic Model

In this section, the Starink and Zahra model (SZ model, see Section 2.3.2.4) is applied to describe the precipitation kinetics, and it is extended to incorporate the evolution of average particle sizes to describe the entire nucleation-growth-coarsening process. An attempt has been made to find an expression in which the dependence of the fraction transformed on temperature and concentration is included in an explicit form.

5.3.1 Evolution of volume fraction and mean solute concentration

As precipitation is a nucleation and growth process, the precipitation kinetics of Cu-Mg co-clusters and S phase can be described by the SZ model. The fraction transformed of precipitates during isothermal ageing is given as [19, 20] (see Eq. (2.24)):

$$\alpha(T,t)=1-\left(\frac{[k(T)t]^n}{\eta_i}+1\right)^{-\eta_i} \tag{5.8}$$

where *k(T)* is the rate constant which can be expressed by an Arrhenius relation depending on the effective activation energy and the pre-exponential constant. Assuming that S phase forms and grows at the expense of Cu-Mg co-clusters, the fraction transformed of Cu-Mg co-clusters, α^{cl}, can be expressed as:

$$\alpha^{cl} = \alpha_0^{cl}(1-\alpha^S) \tag{5.9}$$

where α_0^{cl} stands for the fraction transformed of Cu-Mg co-clusters without the formation of S phase and α^S is the fraction transformed of S phase. Subsequently, the amounts of the Cu-Mg co-clusters and the S phase are given as:

$$x^{cl}(t) = \alpha^{cl}(t,T)\left[c_{eff}^{Cu}(t=0) - c_e^{Cu}(t=\infty)\right] / c_{cl}^{Cu} \tag{5.10}$$

$$x^{S}(t) = 4 * \alpha^{S}(t,T)\left[c_{eff}^{Cu}(t=0) - c_e^{Cu}(t=\infty)\right] \tag{5.11}$$

where c_{cl}^{Cu} and c_{cl}^{Mg} are the atomic fraction of Cu and Mg in the Cu-Mg co-clusters. The amount of precipitates, e.g. amount of S phase, x^S, can be converted to the volume fraction, f^S, by:

$$f^S(t) = \frac{x^S V_{at}^S}{x^S V_{at}^S + x^{cl} V_{at}^{cl} + (1 - x^S - x^{cl}) V_{at}^m} \approx x^S \frac{V_{at}^S}{V_{at}^m} \tag{5.12}$$

where V_{at} is the atomic volume, the superscripts *cl*, *s* and *m* stand for Cu-Mg co-clusters, S phase and matrix, respectively. The crystal structure of S phase is orthorhombic, space group *Cmcm* with a=0.400nm, b=0.923nm, c=0.714nm, containing 16 atoms per unit cell [21]. The average atomic volume of S phase is nearly the same as that of FCC Al matrix (V_{at}^S =1.68x10^{-2}nm^3, V_{at}^m =1.65x10^{-2}nm^3), and the coherent Cu-Mg co-clusters are thought to retain the structure of the matrix with an atomic volume equal to that of the matrix. Hence, to a good approximation, the atomic fractions of S phase and Cu-Mg co-clusters can be considered to be equal to the volume fraction.

As the precipitation process proceeds, the matrix is depleted of solute, so the instantaneous concentration of Cu or Mg in the matrix during the precipitation process is related to the volume fraction of precipitates as:

$$c^{Cu}(t) = c_{eff}^{Cu}(t=0) - x^S(t)/4 - c_{cl}^{Cu} * x^{cl}(t) \tag{5.13}$$

$$c^{Mg}(t) = c_{eff}^{Mg}(t=0) - x^{S}(t)/4 - c_{cl}^{Mg} * x^{cl}(t) \tag{5.14}$$

The obtained solute concentration will be used to calculate the strengthening contribution due to solid solution strengthening.

5.3.2 Evolution of average precipitate size

To model the evolution of the average size of the precipitates in the transition from the growth stage to the coarsening stage, a novel, simple analytical treatment is used.

Nuclei grow by transformation of the parent phase and by dissolution of other nuclei. In the nucleation and growth stages, for the case in which the amount of growing particles is constant during most of the growth stage (the so-called site saturation case, the reaction exponent *n* will equal 1.5), the average volume of a single nucleus is simply given by [22]:

$$\overline{v_N} = \frac{V_t}{\rho_N} \tag{5.15}$$

where V_t is the actual transformed volume, ρ_N is the number density of growing nuclei. If the nuclei grow in three dimensions and retain their original shape throughout the growth process, the average size of the nucleus in a particular direction, $\bar{l}_g$, grows according to:

$$\bar{l}_g = A_a \left(\overline{v_N}\right)^{1/3} = A_a' \left(\frac{\alpha}{\rho_N}\right)^{1/3} \tag{5.16}$$

where A_a and A_a' are constants which depend on the aspect ratio of the nuclei. If $\bar{l}_0$ is defined as the average size that is reached in the limit of α approaching 1, it gives:

$$\bar{l}_g(t) = \bar{l}_o \alpha^{1/3} \tag{5.17}$$

In the case of continuous nucleation, *n* will equal 2.5 and the number density of growing nuclei will not be constant. A treatment has been proposed to take into account this situation [23], but in this work, to limit the complexity of the model, it will be assumed that Eq.(5.17) holds for any *n* between 1½ and 2½.

If it is assumed that the LSW coarsening equation (Eq.(2.14)) is also valid for coarsening of precipitates with a fixed shape, the following equation holds:

$$\bar{l}_c^3 - \bar{l}_0^3 = k_c t \tag{5.18}$$

where $\bar{l}_c$ is the average size of the precipitates in a particular direction during the coarsening stage (for instance the diameter or length of a rod, or the thickness of a plate). The rate constant for coarsening k_c is expressed as an Arrhenius type temperature dependency:

$$k_c = k_{o,c} \exp(-\frac{E_{a,c}}{RT}) \tag{5.19}$$

where $E_{a,c}$ is the activation energy for coarsening and $k_{o,c}$ is the pre-exponential factor.

Having described the basic equations for nucleation and growth and for coarsening, the next step is to describe the transition between the two stages. It should be mentioned that the implicit assumption in defining $\bar{l}_0$ in Eq.(5.17) and Eq.(5.18) is that the phase transformation (nucleation/growth) is essentially completed before the onset of coarsening. Therefore there is no overlap between the nucleation/growth stage and the coarsening stage, and due to this the average particle size is nearly constant in the transition stage (see [24]). Thus it is possible to devise a simple way of dealing with the transition without considering the preferential growth and dissolution in an assembly of particles with different sizes, by taking:

$$\bar{l}(t) = \bar{l}_g(t) + \bar{l}_c(t) - \bar{l}_0 \tag{5.20}$$

The summation is schematically illustrated in **Fig. 5.6**. Basically, the value of $\bar{l}_0$, as inferred from the Gibbs-Thomson equation and the LSW theory, may be a function of temperature and composition. In the present model $\bar{l}_0$ is treated as a fitting parameter and a single value of $\bar{l}_0$ is used for modelling of yield strength at a temperature range of 100°C to 260°C. The effect of $\bar{l}_0$ on the yield strength will be presented in Section 6.3.2. It is found that the change in $\bar{l}_0$ does not significantly affect the prediction. A variation in $\bar{l}_0$ of about 10% produces a deviation in peak yield strength of about 4%.

By combining the thermodynamic model for the solvi with the present kinetic model, the evolution of the volume fraction of precipitate *f(t)*, the average precipitate size $\bar{l}(t)$ and the solute concentrations *c(t)* can be modelled throughout the complete nucleation-growth-coarsening process.

5.3.3 Effect of solute content on homogeneous precipitation kinetics

Studies of the natural age hardening behaviour of alloys B and D by hardness tests, DSC, isothermal calorimetry and 3DAP have shown that the Cu-Mg co-cluster formation reaction is slower in the more dilute alloy [4, 25]. The difference in precipitation rate is thought to be mainly due to the difference in composition. To model the precipitation kinetics of different alloys during isothermal ageing, an attempt is made to correlate the precipitation rate to the solute concentration in the matrix within the framework of the SZ model by using the expressions given by the classical precipitation kinetic theories.

The formation of Cu-Mg co-clusters during isothermal ageing is a process of homogeneous nucleation and growth. According to the classical nucleation theory, the steady state nucleation rate *I* may be written as [26, 27]:

$$I = N_0 Z\beta^* \exp\left(-\frac{\Delta G^*}{RT}\right) \tag{5.21}$$

where N_0, Z, β^* and ΔG^* have the same meaning as in Section 2.3.2.1. For a dilute alloy, the activity of the alloying element can be replaced by its concentration, and the driving force ΔF_v can be written as [27]:

$$\Delta F_v = \frac{RT}{V_m} \ln\left(\frac{c}{c_e}\right) \tag{5.22}$$

where V_m is the molar volume, c_e is the equilibrium solute concentration in the matrix and c is the current solute concentration in the matrix. Following Eq.(2.8), the activation energy barrier ΔG^* for homogeneous nucleation is given by:

$$\Delta G^* = \frac{16\pi\gamma^3}{3\left[\frac{RT}{V_m}\ln\left(\frac{c}{c_e}\right)\right]^2} \tag{5.23}$$

Thus ΔG^* is related to the solubility limit via the supersaturation c/c_e. Using the expressions for Z and β^* (see Eq.(2.9-2.10)), Eq.(5.21) for the nucleation rate can be approximated as:

$$I = I_0 \exp\left(-\frac{\Delta G^* + Q_d}{RT}\right) \tag{5.24}$$

with

$$I_0 = N_0 \sqrt{\frac{4\gamma}{k_B T}} \frac{D_0 c V_{at}}{a^4} \tag{5.25}$$

where the symbols have the same meaning as in Section 2.3.2.1. The pre-exponential factor I_0 is proportional to the concentration c and has relatively weak temperature dependence compared with the exponential term.

From the established equation for diffusion controlled growth [27], the growth rate is given by:

$$G = \frac{c - c_r}{c_p - c_r}\frac{D}{r} = G_0 \exp(-\frac{Q_d}{RT}) \tag{5.26}$$

where the diffusion coefficient D is calculated by an Arrhenius type temperature dependence. Eq. (5.26) shows that G_o is proportional to (c-c_r). Seeing that I_0 is proportional to the concentration c and in general precipitate rates depend on the supersaturation (c-c_e) whilst c_e is mostly much smaller than c, following Eqs. (2.25-2.30) and Eqs.(5.21-5.26), the rate constant $k(T)$ in Eqs.(5.8) can be expressed as a function of temperature and supersaturation:

$$k(T,c) \cong k_0 (c - c_e) \exp(-\frac{E_{eff}}{RT}) \tag{5.27}$$

where

$$E_{eff} = \frac{mE_G + E_N}{m+1} = Q_d + \frac{\Delta G^*}{m+1} \tag{5.28}$$

The validity of the above expressions will be checked by fitting the isothermal calorimetry curves. This will be shown in Section 6.2.1. However, it should be noted that the assumption, that both the growth rate and the nucleation rate can be approximated by Arrhenius type dependencies, may become invalid if the undercooling or driving force for the formation of nuclei is small [28, 29].

5.4 Strength Model

Having obtained the microstructure parameters from the kinetic model, the yield strengths of Al-Cu-Mg based alloys for various heat treatment conditions can then be calculated using the strength model described below.

Precipitation strengthening in Al-Cu-Mg alloys is associated with the formation of Cu-Mg co-clusters and the precipitation of S phase. The present model takes

precipitation strengthening (by Cu-Mg co-clusters and S phase), solution strengthening (by Cu and Mg atoms) and dislocation hardening (caused by stretching) into account. Grain boundary strengthening is assumed to be constant throughout the ageing process, i.e. the grain structure is considered to be stable.

5.4.1 Cluster strengthening

As mentioned in Section 2.4.1, shearable precipitates can impede the movement of gliding dislocations through a variety of interaction mechanisms, including modulus hardening, order hardening, coherency hardening, chemical hardening and stacking-fault hardening. Cu-Mg co-clusters are coherent with the matrix, retain the matrix structure and have no internal ordering, thus coherency hardening, order strengthening and stacking fault strengthening should be very limited, and only chemical hardening and modulus hardening are expected to occur. As cluster-matrix interfaces are diffuse, chemical hardening is expected to be relatively small, and hence Cu-Mg co-clusters are thought to strengthen alloys as a result of modulus strengthening. The validity of neglecting possible contribution of chemical hardening will be tested by considering the accuracy of the model predictions. A further estimate of the contribution due to chemical hardening is presented in Section 6.4.2, which shows that this contribution accounts for only about 5% of the strengthening due to cluster shearing.

Theories of modulus strengthening have been proposed [30-32] and it has been demonstrated that modulus strengthening is difficult to deal with theoretically, leading to quite complex expressions. A satisfactory general solution for the problem of deriving the obstacle strength F_m has not yet been given. Approximate calculations for F_m gave expressions for the increment in CRSS due to modulus strengthening as those listed in Table 2.5. However, as pointed out by Ardell [33] and Reppich *et al*. [34], so far there are no ideally suited alloy systems in which modulus strengthening is the dominant mechanism to test these theories of modulus strengthening. In addition, one of the major difficulties in comparing theory with experiment is that the shear modulus of the precipitates is not known with certainty, and its value may then be considered as an adjustable parameter which leads to an agreement between experiment and theoretical estimate. As the expressions in Table 2.5 derived by

Melander and Persson [31] and by Nembach [32] are applicable to particles with sizes significantly larger than the magnitude of the Burgers vector b (>8b [32]), these expressions seem to be inappropriate for the present Cu-Mg co-clusters for which the sizes are about 0.6nm [3]. Also during natural ageing and artificial ageing of Al-Cu-Mg alloys, a constant hardness is observed which may indicate a very weak size dependency of the hardening contribution due to the Cu-Mg co-clusters. Furthermore, experimental studies of the GPB zones in a stretched Al-2.1Cu-1.4Mg (wt.%) alloy aged at 150°C by SAXS showed that the radius of the GPB zones remains nearly constant for ageing times up to 48h, and for longer ageing times the dissolution of GPB zones was observed [35]. 3DAP analysis of the Cu-Mg co-clusters in alloys B and D aged at room temperature showed that the variations in the size of the Cu-Mg co-clusters during ageing are limited [3]. Hence in this work the simplified equation for modulus strengthening derived by Cartaud *et al*. [30] is adopted as:

$$\Delta\tau_{cl} = \frac{\Delta\mu}{4\pi\sqrt{2}} f_{cl}^{\frac{1}{2}} \tag{5.29}$$

where $\Delta\mu$ is the difference in shear modulus between Al-rich matrix, $\mu_{Al,}$ and the Cu-Mg co-clusters, μ_{cl}, f_{cl} is the volume fraction of the Cu-Mg co-clusters. The accuracy of the above equation has been justified by comparing the model predictions with experimental data for Al-(Li)-Cu-Mg alloys [36, 37]. Further justification will be presented in Chapter 6 (Section 6.2.2, 6.3.3, 6.3.4.1 and 6.3.4.2), where the predictions on unseen data based on a single set of parameters will be compared with experimental data for Al-Cu-Mg alloys with different compositions during natural ageing or artificial ageing.

5.4.2 S phase strengthening

Depending on the degree of coherency, two different dislocation-particle interactions, i.e. shearing or bypassing, may occur [34]. Due to the semi-coherent or incoherent nature of the S precipitates, they are considered to be non-shearable and bypassed by an Orowan mechanism [36, 37]. In addition, the measured diameter of S needles/rods in under-aged condition [10, 22, 38] are generally larger than the critical diameter for

shearing of S precipitates, which has been determined to be about 2nm [39]. Thus the S precipitate strengthening is described by the Orowan mechanism for alloys in both underaged and overaged conditions.

S precipitates formed during low temperature ageing are needle/rod-shaped particles with a very high length-to-diameter ratio (>10) [22, 40]. The S rods are known to form along <100> matrix directions, and therefore the cross-section of the S rod in the $\{111\}_\alpha$ slip plane has an approximately ellipsoidal shape which is nearly equiaxed. For equiaxed particles of diameter *d*, the classical Orowan expression listed in Table 2.5 becomes [36, 38]:

$$\Delta\tau_S = \frac{0.81\mu_{Al}b}{2\pi(1-\upsilon)^{1/2}}\left[\frac{\ln\left(d/b\right)}{0.615d\sqrt{\frac{2\pi}{3f}}-d}\right] \tag{5.30}$$

where *b* is the magnitude of the Burgers vector, ν is the Poisson's ratio for Al and *f* is the volume fraction of the particles. Recently modified Orowan equations have been suggested by taking account of the effects of precipitate shape and orientation [41, 42]. For $\langle 100\rangle_\alpha$ oriented rod-shaped precipitates of diameter D_r, length l_r ($l_r >> D_r$) and volume fraction *f*, Nie *et al*. proposed that the increment in CRSS is as follows based on the regular triangular arrays of precipitates on the slip plane [41]:

$$\Delta\tau = \frac{\mu_{Al}b}{2\pi(1-\upsilon)^{1/2}}\left[\frac{\ln\left(1.316D_r/r_0\right)}{(1.075\sqrt{\frac{0.433\pi}{f}}-1.316)D_r}\right] \tag{5.31}$$

where r_0 is the dislocation inner cut-off radius. While Zhu *et al.* [42] suggested the following equation based on computer simulations of a dislocation slip process through circular unshearable obstacles and by means of two-order polynomial regression analysis:

$$\Delta\tau = \frac{0.15\mu_{Al}b}{D_r}(f^{1/2} + 1.84f + 1.84f^{3/2})\ln(\frac{1.316D_r}{r_0}) \quad (5.32)$$

For comparison, the increment in CRSS calculated using the above three equations are presented in **Fig. 5.7** (r_0 is taken as equal in magnitude to the Burgers vector of the dislocation, b). In these calculations the evolution of volume fraction f and particle diameter d (or D_r) are taken from model predictions of evolution for alloy A aged at 190°C (see Section 6.3.1). It is seen that no significant differences are observed for the resulting S strengthening contributions calculated from Eq.(5.30), Eq.(5.31) and Eq.(5.32). For the present work it is assumed that Eq.(5.30) is a valid approximation for S strengthening contribution and d is taken as the diameter of the S rods.

5.4.3 Solid solution strengthening

Solid solution strengthening comes from the restriction of dislocation movement due to interaction of dislocations with the internal strained lattice surrounding the solute atoms. A general equation for the increment in yield strength due to binary solid solution strengthening is given by:

$$\Delta\sigma_{ss} = k_j c_j^m \quad (5.33)$$

Where c_j is the concentration of solute j in solid solution and k_i is the corresponding strengthening coefficient related to the nature of the solute–dislocation interaction for solute j. m is a constant and its value of either 2/3 [43-45] or 1 [46] has been reported.

In this work, contributions for solution strengthening from Cu and Mg atoms are considered and the value of k_j was estimated from binary Al-Cu and Al-Mg aluminium alloys. Mn is usually added to precipitate as dispersoids for the control of grain and subgrain structures in commercial Al alloys. Due to the formation of dispersoids in Al-Cu-Mg alloys, the amount of Mn in solid solution is very low, only about 0.2-0.3 wt.% Mn [17, 47]. Although the strengthening coefficient of Mn is higher than those for Cu and Mg atoms, which is 30MPa/wt.% from the ASM

Handbook [46], the maximum contribution of Mn atom is estimated to be about 6-9MPa. This small contribution is then considered to be constant and is included in the intrinsic strength.

Strengthening in non-heat-treatable Al-Mg alloys comes mainly from solid solution strengthening due to Mg atoms in solid solution, work hardening and grain size strengthening. Here, the yield strengths of Al-Mg plates [48] and of high purity Al-Mg alloys [49] at various Mg concentrations in an annealed condition (O temper) are used to calibrate the strengthening coefficient for Mg, k_{Mg}. It is seen from the data points in **Fig. 5.8**(a) that the yield strength increases approximately linearly with increasing Mg concentration, thus a linear dependence of strength on the concentration was applied. The high purity Al-Mg alloys [49] were reported to have a constant grain size of 200μm, i.e. the grain boundary strengthening is constant. No information on the grain size of the Al-Mg plates was given in [48], and it is assumed that the grain boundary strengthening is also constant, so the strengthening coefficient for Mg can be obtained from the slope of the fit to the data points. A value of 15.0±0.4MPa/wt.%Mg (or 13.6±0.4MPa/at.%Mg) was obtained for k_{Mg} from the average of two slopes which are shown in Fig. 5.8(a). This value is in agreement with that of 15.5MPa/wt.%Mg determined over the range from 2wt.% Mg to 7wt.% Mg in binary Al-Mg alloys in the O temper by Burger *et al*. [50] and with that of 18.6MPa/wt.%Mg given in [46]. Relatively less information is available regarding the solution strengthening due to Cu atoms in aluminium. In this work the yield strength curve of high purity Al-Cu alloys in the as-quenched condition given in [51] (Fig. 5.8(b)) was used to calibrate the strengthening coefficient for Cu, k_{Cu}. A value of 22±1MPa/wt.%Cu (or 50±2MPa/at.%Cu) was obtained for k_{Cu} from a linear fit. This value indicates that the strengthening from Cu is greater than that from Mg. Recently a value of approximately 33MPa/wt.%Cu was reported by Court *et al*. [52] based on Al-3wt.%Mg alloys containing from 0.2 to 0.6wt.%Cu. To check whether a $c^{2/3}$ concentration dependence could yield a better fit than a linear fit, the least squares fits of Eq.(5.33) with m=2/3 to the data points/curve in Fig. 5.8 were carried out. The best fits yield 28MPa/wt.%$^{2/3}$ Mg for k_{Mg} and 45MPa/wt.%$^{2/3}$ Cu for $k_{Cu.}$ These values are found to be consistent with those used in a yield strength model by Myhr *et al*. [53].

The results are also presented in Fig. 5.8. It is seen that a linear law fit the data better than a 2/3 power law, and thus in this work a linear law is adopted.

The addition of strength contributions from two different solute atoms can follow the rules as indicated in Section 2.4.3. Specifically equations for superposition of solid solution strengthening in ternary alloys have been listed in [54]. Considering that solute atoms are much weaker obstacles compared with precipitates, the solution strengthening contribution is very limited compared with contributions due to the precipitates, and it is expected that the uses of different addition rules have little effect on the prediction of the yield strength. Thus a linear addition of contributions from Cu and Mg atoms is used, i.e. the solution strengthening effect is given as:

$$\Delta\sigma_{ss} = k_{Cu}c_{Cu} + k_{Mg}c_{Mg} \tag{5.34}$$

5.4.4 Dislocation strengthening

The dislocation strengthening introduced by a small amount of stretching prior to the ageing treatment can be adequately described by the Ashby model, which is valid for a limited strain range, roughly for imposed plastic strain ε between about 0.01 to 0.05 [36, 37, 55, 56]. The increment in CRSS due to dislocation strengthening is thus taken as:

$$\Delta\tau_d = \frac{K_A}{M}\sqrt{\varepsilon} \tag{5.35}$$

where K_A is the strain hardening factor which depends on microstructural parameters and M is the Taylor factor. In the present work, K_A was obtained by fitting the Ashby model to experimental stress-strain curves in the strain range of 0.01-0.05 [4]. For simplicity, K_A is treated as a constant in the model and an initial value of about 450MPa for a 2024 alloy in the as-received condition is taken [4]. Recovery during ageing is expected to be very limited as the imposed strain by stretching is low, about 2-3%.

5.4.5 Grain boundary strengthening

The strengthening increment, $\Delta\sigma_{GB}$, due to grain boundaries can be described well by the Hall-Petch relationship [57, 58], which holds for materials with grain sizes over 50μm:

$$\Delta\sigma_{GB} = k_{HP} d_{GB}^{-1/2} \tag{5.36}$$

where k_{HP} is the Hall-Petch coefficient and d_{GB} is the average grain size. As mentioned in Section 3.1, the average grain size in the transverse-short transverse (TS) plane were measured as around 89μm [59] to 157μm [40]. The value of k_{HP} has been reported to range from 0.065MPa$\sqrt{m}$ for pure Al [60] to 0.22MPa$\sqrt{m}$ for Al-Mg alloys [50]. Taking a typical k_{HP} value of 0.15MPa$\sqrt{m}$ [50], the grain boundary strengthening contribution is estimated between about 20MPa to 10MPa for average grain sizes between 50μm to 200μm, respectively. This is only a very small contribution to the yield strength, and thus it is considered constant and included in the intrinsic strength.

5.4.6 Overall strength

Finally the various components of the CRSS increment must be combined to obtain the overall yield strength. As both the dislocations introduced by stretching and S particles are strong obstacles to impede the movement of dislocations, the dislocation strengthening, $\Delta\tau_d$, and S phase strengthening, $\Delta\tau_S$, are added with the superposition exponent $q = 2$ (see Section 2.4.3):

$$\Delta\tau_{\Sigma}^2 = \Delta\tau_d^2 + \Delta\tau_S^2 \tag{5.37}$$

The Cu-Mg co-clusters are thought to be weaker obstacles compared with S particles and the dislocations introduced by stretching, thus the exponent q for superposition of

$\Delta\tau_{\Sigma}$ and cluster strengthening $\Delta\tau_{cl}$ is taken as an adjustable parameter between 1.0 and 2.0:

$$\Delta\tau_{ppt} = (\Delta\tau_{\Sigma}^{q} + \Delta\tau_{cl}^{q})^{1/q} \tag{5.38}$$

The yield strength of the alloy is related to the CRSS by the Taylor factor *M* [36]:

$$\sigma_y = \sigma_i + \Delta\sigma_{ss} + M\Delta\tau_{ppt} \tag{5.39}$$

where σ_y is the conventionally measured yield strength of the alloy, σ_i is the intrinsic strength of the Al matrix and is considered constant. σ_i in this model consists of the yield strength for pure aluminium which is 10MPa, the contribution of the grain boundary strengthening and possible contributions from other solutes such as Mn in Al. $\Delta\sigma_{ss}$ is the contribution due to the solid solution strengthening. *M* is the Taylor factor. As mentioned in Section 2.4.2, *M* ranges between a lower bound of 2.24 given by the Sachs model to an upper bound of 3.07 given by the Taylor model [36, 61]. Work on self-consistent modelling of deformation of texture free polycrystalline Al indicates that on average about 3.5 slip systems are activated per grain and this leads to *M*=2.6 [62]. The value of 2.6 will be used throughout the model to relate the CRSS to the yield strength.

5.5 Summary

A model has been developed for two-stage age hardening of Al-Cu-Mg alloys with composition in the (α+S) phase field. It considers two types of strengthening precipitates, Cu-Mg co-clusters and S phase, with the S phase forming at the expense of the Cu-Mg co-clusters. The model consists of three components: a thermodynamic model, with the solvi of Cu-Mg co-clusters and S phase approximated by the regular solution model; a kinetic model which describes the evolution of the average size and volume fraction of the precipitates and the solute concentration in the matrix during the precipitation process; and a strength model which considers the superposition of various strengthening contributions from precipitation strengthening, solution

strengthening and dislocation strengthening. The first stage of hardening is attributed to Cu-Mg co-clusters via modulus hardening mechanism and the second stage of hardening is attributed to S phase via Orowan bypassing mechanism. The composition dependency of precipitation rate for homogeneous precipitation of the Cu-Mg co-clusters, as well as the amount of Cu and Mg present in undissolved intermetallic phases, are taken into account. Therefore the model is capable of predicting the microstructure evolution and the yield strength of Al-Cu-Mg alloys as a function of composition and heat treatments.

Table 5.1 The nominal, measured and calculated Cu in solid solution (wt.%)

Nominal composition:Cu*	Nominal composition:Fe*	Measured composition:Cu*	Calculated composition:Cu
4	0.25	3.40	3.59
4	0.5	3.02	3.07
4	1.0	1.90	1.96

* From [18].

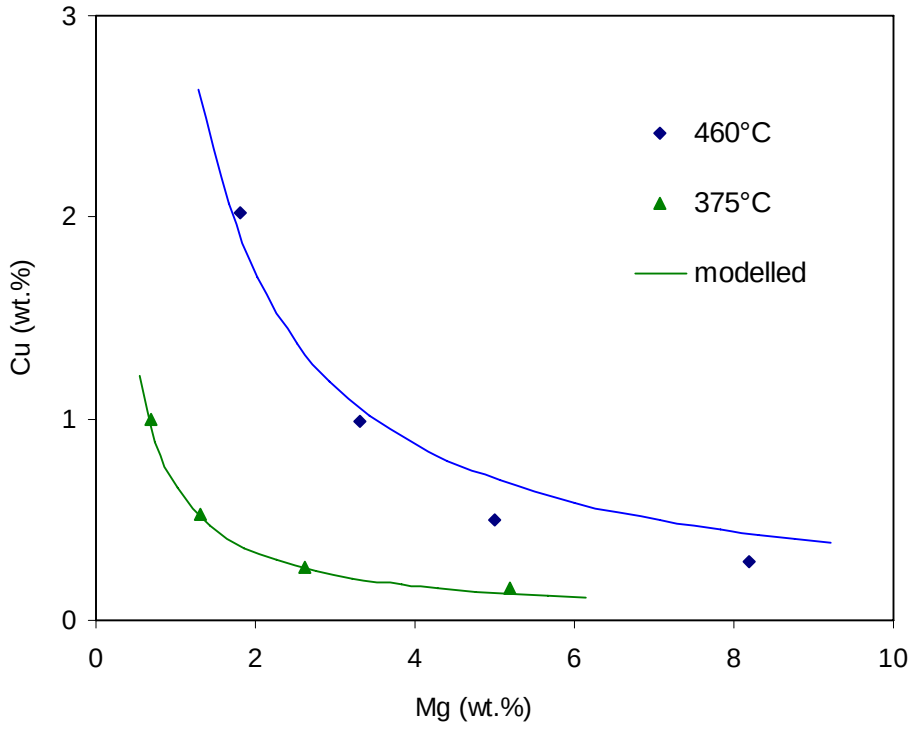

Fig. 5.1 Comparison of the fitted solvi of S phase at 375°C and 460°C together with the experimental data from [7].

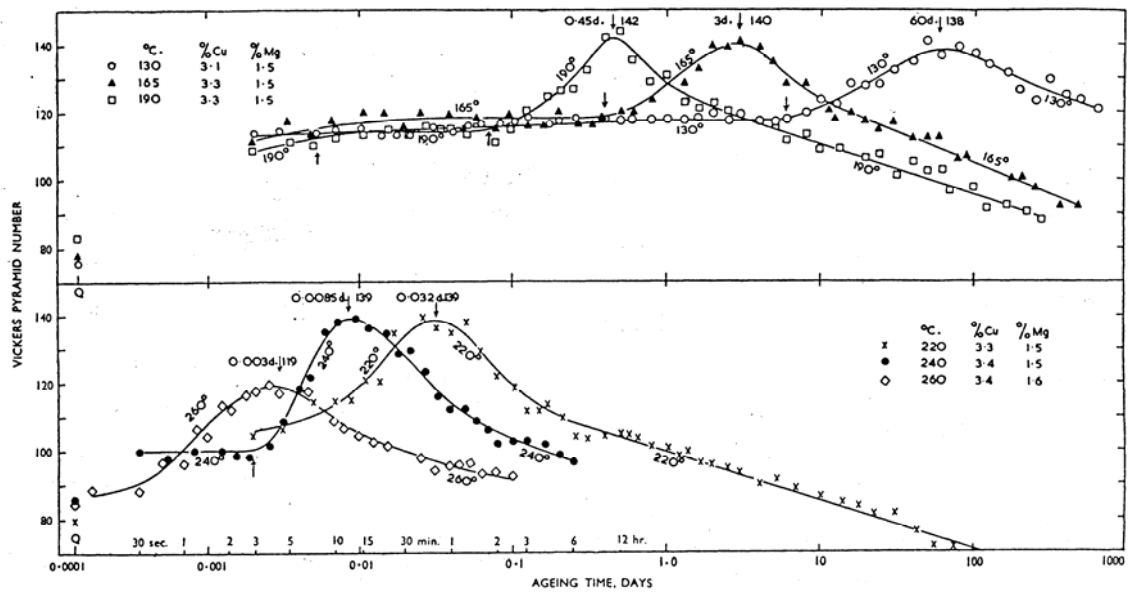

Fig. 5.2 Vickers hardness versus ageing time curves for alloys with a Cu: Mg weight ratio of 2.2:1 aged at various temperature after solution treatment (From [8]).

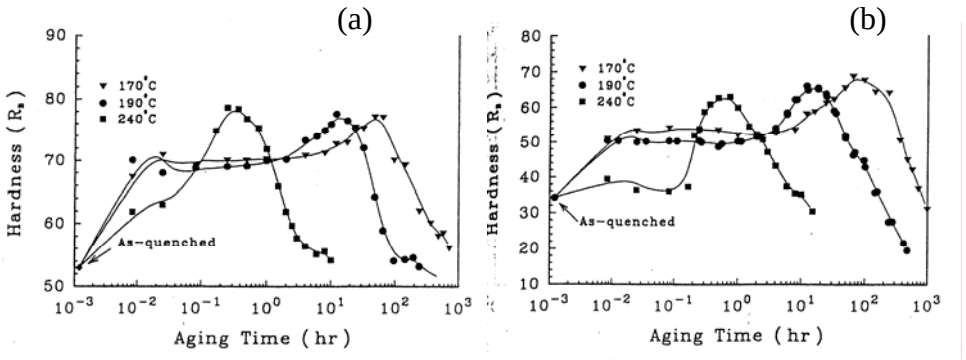

Fig. 5.3 Rockwell B hardness versus ageing time curves for (a) an Al-3.98Cu-1.38Mg (wt.%) alloy and (b) an Al-2.62Cu-1.35Mg (wt.%) alloy aged at 170°C, 190°C and 240°C after solution treatment (From [10]).

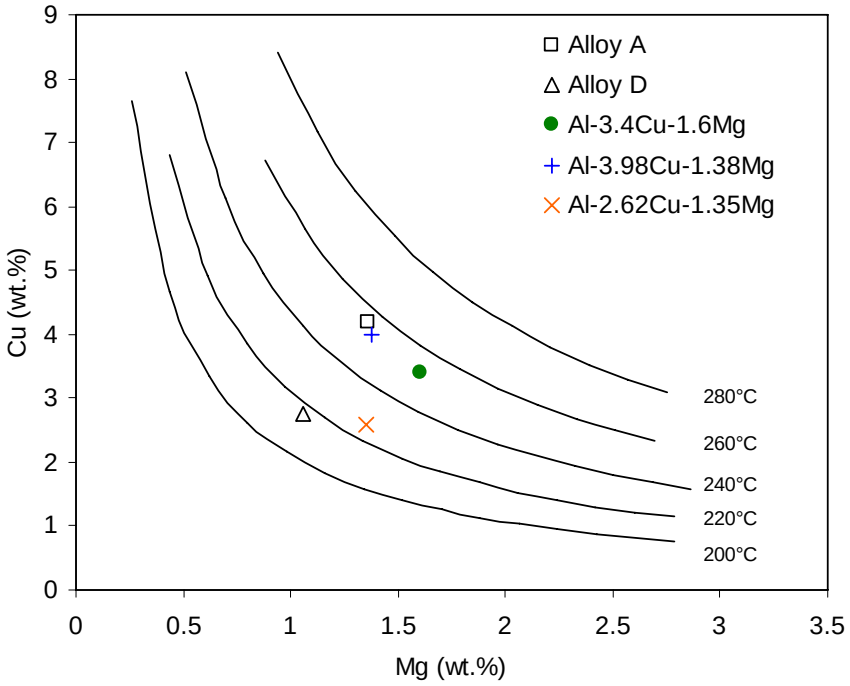

Fig. 5.4 Calculated solvus of Cu-Mg co-clusters in Al-Cu-Mg alloys constructed by using regular solution model (Eq.5.1) with c_1=1.6×10^4 (at.%)^2 and ΔH^{cl} =38kJ/mol.

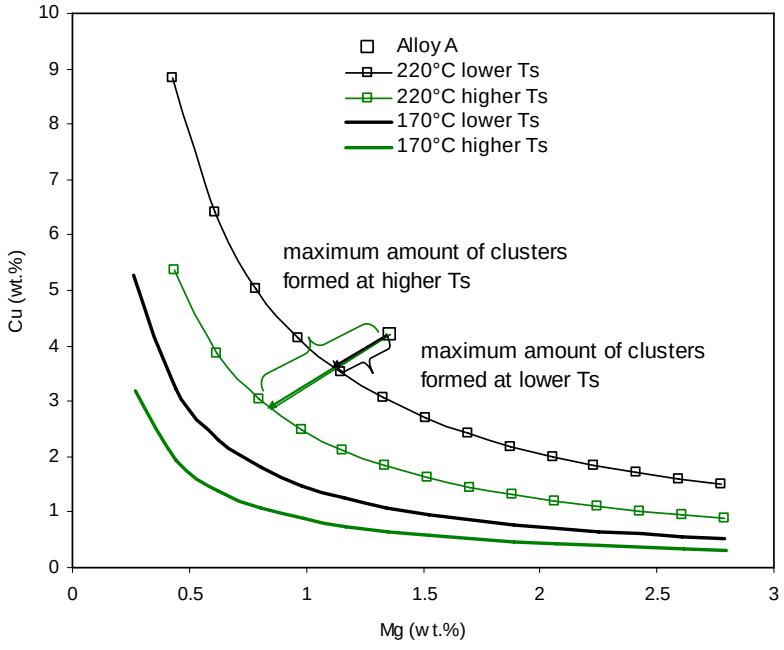

Fig. 5.5 Illustration of potential amounts of Cu-Mg co-clusters formed in alloy A aged at 220°C for two estimated T_s^{cl} limits. The relative difference in the amounts of the Cu-Mg co-clusters formed for two T_s^{cl} limits is smaller for alloys aged at 170°C than that at 220°C.

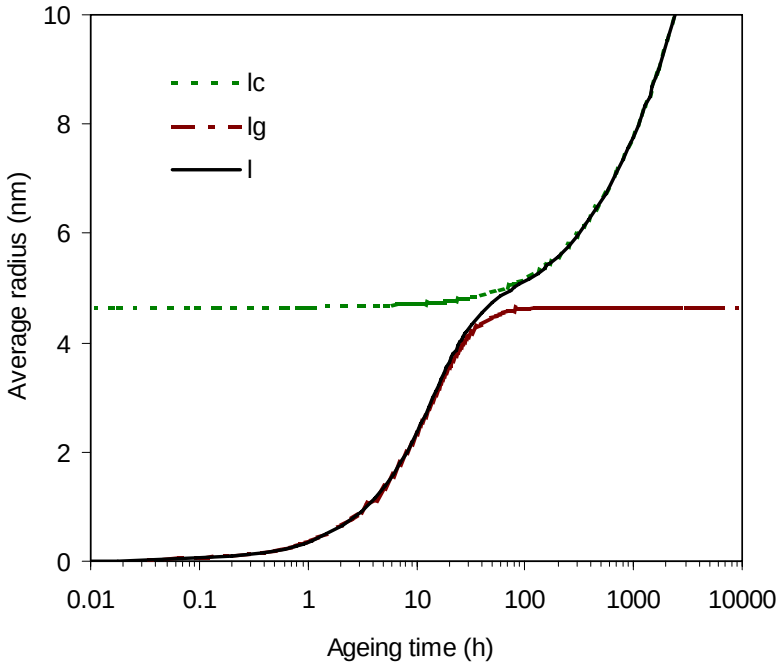

Fig. 5.6 Schematic illustration of evolution of the average precipitate size in the nucleation & growth stages, l_g, the average precipitate size in the coarsening stage, l_c and the average precipitate size through the whole nucleation, growth and coarsening stages, l.

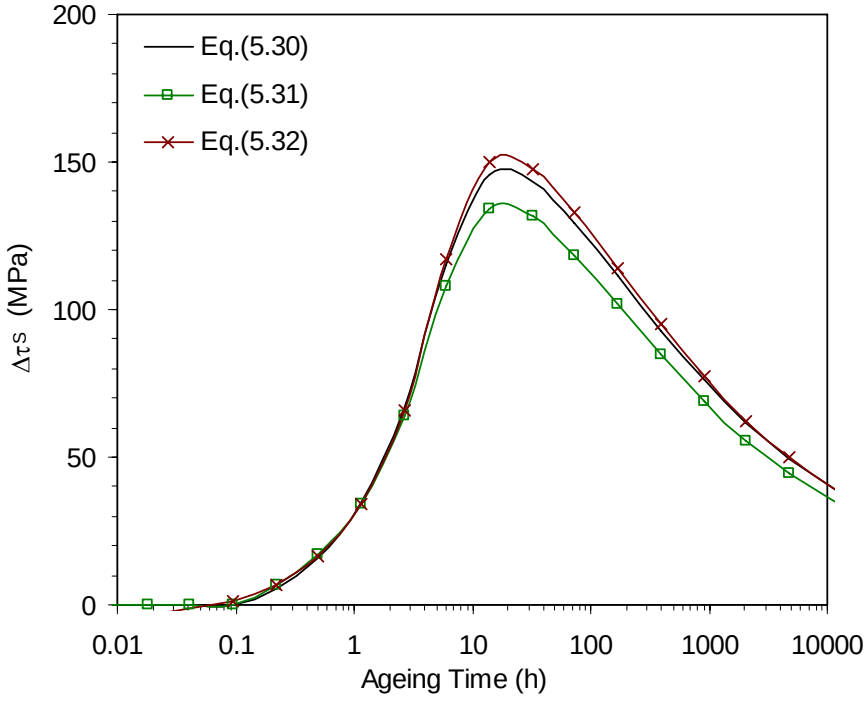

Fig. 5.7 Comparison of S strengthening contributions calculated from Eq.(5.30), Eq.(5.31) and Eq.(5.32).

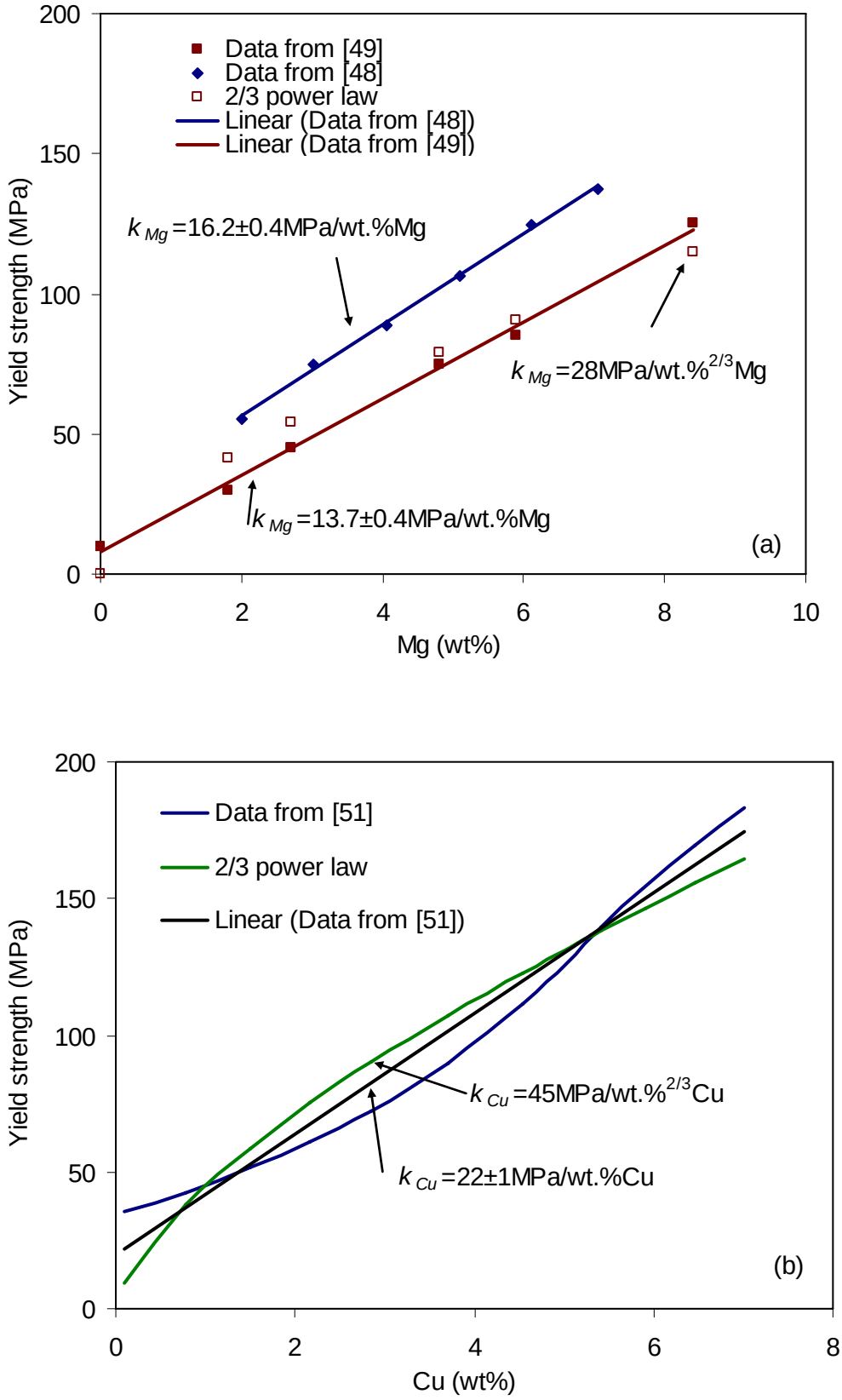

Fig. 5.8 Calibration of the strengthening coefficient (a) k_{Mg} and (b) k_{Cu} based on a linear solute concentration dependence of the yield strength.

References

[1] S. P. Ringer, T. Sakurai, and I. J. Polmear, 'Origins of hardening in aged Al-Cu-Mg-(Ag) alloys', *Acta Mater.*, 1997, **45**, 3731-3744.

[2] S. P. Ringer, K. Hono, I. J. Polmear, and T. Sakurai, 'Precipitation processes during the early stages of ageing in Al-Cu-Mg alloys', *Appl. Surf. Sci.*, 1996, **94-95**, 253-260.

[3] L. F. Davin, 'Ultra-fine Characterisation of Nanostructures in Al-(Li)-Cu-Mg-(Zr) alloys by Three-Dimensional Atom Probe', PhD thesis, Oxford University, 2004.

[4] N. Gao, N. Kamp, I. Sinclair, and M. J. Starink, 'Innovation of age forming through development of novel damage tolerant alloys (report on DARP project)', University of Southampton, 2002.

[5] K. Raviprasad, C. R. Hutchinson, T. Sakurai, and S. P. Ringer, 'Precipitation processes in an Al-2.5Cu-1.5Mg (wt. %) alloy microalloyed with Ag and Si', *Acta Mater.*, 2003, **51**, 5037-5050.

[6] M. J. Starink and P. J. Gregson, 'A Quantitative Interpretation of DSC Experiments on Quenched and Aged SiCp Reinforced 8090-Alloys', *Scr. Metall. Mater.*, 1995, **33**, 893-900.

[7] A. T. Little, W. Hume-Rothery, and G. V. Raynor, 'The constitution of aluminium-copper-magnesium alloys at 460°C', *J. Inst. Metals*, 1944, **70**, 491-506.

[8] H. K. Hardy, 'The ageing characteristics of some ternary aluminium-copper-magnesium alloys with copper : magnesium weight ratios of 7:1 and 2.2:1', *J. Inst. Metals*, 1954-55, **83**, 17-34.

[9] R. H. Beton and E. C. Rollason, 'Hardness reversion of dilute alluminium-copper and alluminium-copper-magnesium alloys', *J. Inst. Metals*, 1957-58, **86**, 77-85.

[10] H. C. Shih, N. J. Ho, and J. C. Huang, 'Precipitation behaviors in Al-Cu-Mg and 2024 aluminum alloys', *Metall. Mater. Trans. A*, 1996, **27**, 2479-2494.

[11] M. J. Starink and P. J. Gregson, 'Thermodynamics and precipitation in 8090 (Al-Li-Cu-Mg-Zr) alloys studied by DSC and TEM', *Mater. Sci. Forum*, 1996, **217-222**, 673-678.

[12] J. T. Staley, 'Metallurgical aspects affecting strength of heat treatable alloy products used in the aerospace industry', in: L. Arnberg, O. Lohne, E. Nes, and N. Ryum (Eds.), *Proc. 3rd Intl. Conf: Aluminium Alloys-Their Physical and*

Mechanical Properties (ICAA3), Vol. **3**, Norwegian Institute Of Technology, Trondheim, Norway, 1992, p.107-143.

[13] A. K. Mukhopadhyay, 'Coprecipitation of Ω and σ phases in Al-Cu-Mg-Mn alloys containing Ag and Si', *Metall. Mater. Trans. A.*, 2002, **33**, 3635-3648.

[14] M. J. Starink and X. M. Li, 'A model for the electrical conductivity of peak-aged and overaged Al-Zn-Mg-Cu alloys', *Metall. Mater. Trans. A*, 2003, **34A**, 899-911.

[15] L. F. Mondolfo, *Aluminium Alloys: Structure and Properties*, Butterworths, London, 1976.

[16] H. W. L. Phillips, 'The constitution of alloys of aluminium, copper and iron', *J. Inst. Met.*, 1953-54, **82**, 197-212.

[17] P. Villars, A. Prince, and H. Okamoto (Eds.), *Handbook of ternary alloy phase diagrams*, ASM International, Materials Park, OH, 1994

[18] W. L. Fink, D. W. Smith, and L. A. Willey, 'Precipitation hardening of high purity binary and ternary aluminum-copper alloys', in: *Age hardening of metals*, p.31-55, 1940, ASM.

[19] M. J. Starink and A. M. Zahra, 'An analysis method for nucleation and growth controlled reactions at constant heating rate', *Thermochim. Acta*, 1997, **292**, 159-168.

[20] M. J. Starink and A. M. Zahra, 'Kinetics of isothermal and non-isothermal precipitation in an Al-6 at% Si alloy', *Philos. Mag. A*, 1998, **77**, 187-199.

[21] H. Perlitz and A. Westgren, 'The crystal structure of Al_2CuMg', *Ark Chem, Miner. Geol.*, 1943, **16B**, 1-5.

[22] M. J. Starink, P. Wang, I. Sinclair, and P. J. Gregson, 'Microstructure and strengthening of Al-Li-Cu-Mg alloys and MMCs: I. Analysis and modelling of microstructural changes', *Acta Mater.*, 1999, **47**, 3841-3853.

[23] M. J. Starink and S. C. Wang, 'A model for the yield strength of overaged Al-Zn-Mg-Cu alloys', *Acta Mater.*, 2003, **51**, 5131-5150.

[24] J. D. Robson, 'Modelling the overlap of nucleation, growth and coarsening during precipitation', *Acta Mater.*, 2004, **52**, 4669-4676.

[25] M. J. Starink, N. Gao, L. Davin, J. Yan, and A. Cerezo, 'Room temperature precipitation in quenched Al–Cu–Mg alloys: a model for the reaction kinetics and yield strength development', *Philos. Mag.*, 2005, **85**, 1395-1417.

[26] J. W. Christian, *The Theory of Phase Transformations in Metals and Alloys*, 2nd edn, Pergamon, Oxford, 1975.

[27] R. Wagner and R. Kampmann, in: R. W. Cahn, P. Haasen, and E. J. Kramer (Eds.), *Materials Science and Technology: A Comprehensive Treatment Phase Transformations in Materials*, Vol. **5**, p.213, 1991, VCH, Weinheim.

[28] A. T. W. Kempen, F. Sommer, and E. J. Mittemeijer, 'Determination and interpretation of isothermal and non- isothermal transformation kinetics; the effective activation energies in terms of nucleation and growth', *J. Mater. Sci.*, 2002, **37**, 1321-1332.

[29] M. J. Starink and A. M. Zahra, 'β ' and β precipitation in an Al-Mg alloy studied by DSC and TEM', *Acta Mater.*, 1998, **46**, 3381-3397.

[30] L. Cartraud, J. Guillot, and J. Grilhe, 'Influence of mode of zones formation on elastic limit', in: *Proc. ICSMA IV*, Vol. **1**, Nancy, 1976, p.214.

[31] A. Melander and P. A. Persson, 'The strength of a precipitation hardened AlZnMg alloy', *Acta Metall.*, 1978, **26**, 267-278.

[32] E. Nembach, 'Precipitation hardening caused by a difference in shear modulus between particle and matrix', *Physica status solidi (A)*, 1983, **78**, 571-581.

[33] A. J. Ardell, 'Precipitation Hardening', *Metall. Trans. A*, 1985, **16**, 2131-2165.

[34] B. Reppich, 'Particle Strengthening', in: R. W. Cahn, P. Haasen, and E. J. Kramer (Eds.), *Materials Science and Technology: A Comprehensive Treatment Plastic Deformation and Fracture of Materials*, Vol. **6**, p.311-357, 1992, Wiley-VCH, Weinheim.

[35] P. Gomiero, F. Livet, Y. Brechet, and F. Louchet, 'Microstructure and Mechanical-Properties of a 2091 AlLi Alloy .1. Microstructure Investigated by SAXS and TEM', *Acta Metall. Mater.*, 1992, **40**, 847-855.

[36] M. J. Starink, P. Wang, I. Sinclair, and P. J. Gregson, 'Microstrucure and strengthening of Al-Li-Cu-Mg alloys and MMCs: II. Modelling of yield strength', *Acta Mater.*, 1999, **47**, 3855-3868.

[37] P. Gomiero, Y. Brechet, F. Louchet, A. Tourabi, and B. Wack, 'Microstructure and Mechanical-Properties of a 2091 Al-Li Alloy .2. Mechanical-Properties - Yield Stress and Work-Hardening', *Acta Metall. Mater.*, 1992, **40**, 857-861.

[38] R. D. Schueller, F. E. Wawner, and A. K. Sachdev, 'Strengthening Potential of the Cubic-Sigma Precipitate in Al- Cu-Mg-Si Alloys', *J. Mater. Sci.*, 1994, **29**, 239-249.

[39] C. P. Blankenship, E. Hornbogen, and E. A. Starke, 'Predicting Slip Behavior in Alloys Containing Shearable and Strong Particles', *Mater. Sci. Eng. A*, 1993, **169**, 33-41.

[40] N. Kamp, N. Gao, I. Sinclair, and M. J. Starink, 'Innovation of age forming through development of novel damage tolerant alloys (report on DARP project)', University of Southampton, 2004.

[41] J. F. Nie, B. C. Muddle, and I. J. Polmear, 'The effect of precipitate shape and orientation on dispersion strengthening in high strength aluminium alloys', *Mater. Sci. Forum*, 1996, **217-222**, 1257-1262.

[42] A. W. Zhu and E. A. Starke, 'Strengthening effect of unshearable particles of finite size: A computer experimental study', *Acta Mater.*, 1999, **47**, 3263-3269.

[43] R. Labush, 'A statistical theory of solid solution hardening', *Phys Status Solidi.*, 1970, **41**, 659.

[44] U. F. Kocks, A. S. Argon, and M. F. Ashby, 'Thermodynamics and Kinetics of Slip', *Prog. Mater. Sci.*, 1975, **19**, 1-291.

[45] H. R. Shercliff and M. F. Ashby, 'A Process Model for Age Hardening of Aluminum-Alloys .1. The Model', *Acta Metall. Mater.*, 1990, **38**, 1789-1802.

[46] J. R. Davis (Ed.), *ASM Specialty Handbook: Aluminum and Aluminum Alloys*, Materials Park, OH: ASM International, 1993, p.33: Table 3 of Chapter 'Introduction to Aluminum and Aluminum Alloys'

[47] I. J. Polmear, *Light Alloys-Metallurgy of the Light Metals*, 3rd ed, Butterworth- Heinemann, Oxford, UK, 1995.

[48] J. R. Davis (Ed.), *ASM Specialty Handbook: Aluminum and Aluminum Alloys*, Materials Park, OH: ASM International, 1993, p.43: Fig.24 of Chapter 'Introduction to Aluminum and Aluminum Alloys'.

[49] T. Mukai, K. Higashi, and S. Tanimura, 'Influence of the Magnesium Concentration on the Relationship between Fracture Mechanism and Strain-Rate in High-Purity Al-Mg Alloys', *Mater. Sci. Eng. A*, 1994, **176**, 181-189.

[50] G. B. Burger, A. K. Gupta, P. W. Jeffrey, and D. J. Lloyd, 'Microstructural Control of Aluminum Sheet Used in Automotive Applications', *Mater. Charact.*, 1995, **35**, 23-39.

[51] J. R. Davis (Ed.), *ASM Specialty Handbook: Aluminum and Aluminum Alloys*, Materials Park, OH: ASM International, 1993, p.42: Fig.18 of Chapter 'Introduction to Aluminum and Aluminum Alloys'.

[52] S. A. Court, K. P. Hicklin, and D. J. Lloyd, 'The ageing and thermal recovery behaviour of Al-Mg-Cu alloys', *Mater. Sci. Forum*, 2002, **396-4**, 1031-1036.

[53] O. R. Myhr, O. Grong, and S. J. Andersen, 'Modelling of the age hardening behaviour of Al-Mg-Si alloys', *Acta Mater.*, 2001, **49**, 65-75.

[54] L. A. Gypen and A. Deruyttere, 'Multicomponent Solid-Solution Hardening .1. Proposed Model', *J. Mater. Sci.*, 1977, **12**, 1028-1033.

[55] M. F. Ashby, 'Work hardening of dispersion-hardened crystals', *Philos. Mag.*, 1966, **14**, 1157-1178.

[56] M. F. Ashby, 'The deformation of plastically non-homogeneous alloys', in: K. A. and N. R. B. (Eds.), *Strengthening Methods in Crystals*, p.137-192, 1971, Elsevier, Amsterdam, the Netherlands.

[57] E. O. Hall, *Proc. Phys. Soc. London*, 1951, **B64**, 747.

[58] N. J. Petch, *J. Iron Steel Inst.*, 1953, **174**, 25.

[59] Y. Xu, 'Variable amplitude loading effects on damage tolerant airframe materials', PhD Thesis, University of Southampton, 2000.

[60] J. D. Embury, D. J. Lloyd, and T. R. Ramachandran, 'Strengthening mechanisms in aluminum alloys', in: A. K. Vasudevan and R. D. Doherty (Eds.), *Aluminium Alloys-Contemporary Research and Application*, Vol. **31**, p.579-601, 1989, Academic Press, London.

[61] A. K. Vasudevan and R. D. Doherty (Eds.), *Aluminium Alloys-Contemporary Research and Application*, Vol. **31**, Academic Press, London, 1989

[62] B. Clausen, T. Lorentzen, and T. Leffers, 'Self-consistent modelling of the plastic deformation of FCC polycrystals and its implications for diffraction measurements of internal stresses', *Acta Mater.*, 1998, **46**, 3087-3098.

Chapter 6 Model Assessment and Discussion

6.1 Introduction

In this Chapter, the model presented in Chapter 5 will be used to fit and predict the yield strength of Al-Cu-Mg alloys within the (α+S) phase field during natural ageing and artificial ageing. When possible, parameters are either taken from the literature or calibrated by experiments to minimize the number of adjustable variables. The parameters related to the solvi of Cu-Mg co-clusters and S phase, the values of the solution strengthening coefficients k_j, the strain hardening factor K_A and the Taylor factor M have been defined in Chapter 5. They are fixed throughout the model, as listed in **Table 6.1**. Parameters which cannot be determined accurately from literature are found by minimising the root mean square error (RMSE) to give the best agreement between experimental yield strength data and model predictions. They are the shear modulus of the Cu-Mg co-clusters μ_{cl}, the pre-exponential factor for precipitation k_0, the pre-exponential factor for coarsening $k_{0,c}$, the average radius of S precipitates at the start of coarsening $\bar{l}_0$ and the superposition exponent q. The model is tested by predicting unseen strength data, i.e. data not used in defining the parameters. Also the fitting parameters will be discussed, and compared against available quantitative and semi-quantitative data.

6.2 Modelling of natural age hardening

Natural age hardening of alloys B and D has been studied by hardness tests (Fig. 4.8), DSC (similar to Fig.4.20), isothermal calorimetry (Fig. 4.28) and 3DAP analysis (Fig.

2.7) (for details see [1]). The main experimental results are summarized here. For samples naturally aged for times between 15 min and 48h, 3DAP analysis indicates the presence of Cu clusters and Cu-Mg co-clusters at the very early stage of ageing (t<1h). As the ageing proceeds, Mg is co-clustering with the Cu clusters, forming Cu-Mg co-clusters with Cu:Mg atomic ratios approximately unity. The estimated number density of the clusters shows an increase up to about 4-5h, and for longer ageing times the density stays stable or decreases slightly. The composition of the clusters is variable, but clusters that are predominantly rich in Cu or Mg form a small minority of the total number of clusters. Thus clusters are predominantly Cu-Mg co-clusters. This time interval for Cu-Mg co-cluster formation corresponds well to the time interval for hardness increase in ageing curves (Fig. 4.8), also to the time interval for the exothermic heat release in isothermal calorimetry curves (Fig. 4.28) and to the time interval for the decreasing exothermic heat effect between about 25°C and 170°C on ageing samples in DSC curves (Fig. 4.20). These results indicate that the formation of the Cu-Mg co-clusters is responsible for the natural age hardening and the heat effects in calorimetry studies. In addition, it is shown that the rate of Cu-Mg co-cluster formation is slower in the more dilute alloy (alloy D).

In this section, natural ageing curves of alloys B and D will be modelled by considering the strengthening due to the formation of Cu-Mg co-clusters. Isothermal calorimetry curves of these alloys will be used to study the kinetics of Cu-Mg co-cluster formation during ageing at 25°C. In the present work, it is assumed that the Cu:Mg atomic ratios can be taken to be 1:1 and the content of Al atoms in the Cu-Mg co-clusters is taken as 40% according to 3DAP analysis [1, 2]. This assumption is used in the following to calculate the volume fraction and therefore the yield strength, and for the calibration of the shear modulus of the Cu-Mg co-clusters.

6.2.1 The kinetics of cluster formation

The kinetics of Cu-Mg co-cluster formation is analysed based on the extended SZ model described in Section 5.3.3. The kinetic parameters are calibrated using the isothermal calorimetry curves presented in Fig.4.28. From the isothermal calorimetry curve, the fraction transformed α is defined as the ratio of the heat evolved at a certain

ageing time t to the heat evolved of the peak on the thermogram, i.e. the total area of the peak A_e:

$$\alpha = \frac{\int_0^t \frac{dQ}{dt} dt}{\int_0^{t_e} \frac{dQ}{dt} dt} = \frac{\int_0^t \frac{dQ}{dt} dt}{A_e} \tag{6.1}$$

Where t_e is the end time of the exothermic peak. The heat flow dQ/dt is therefore related to the transformation rate $d\alpha/dt$ by:

$$HF = \frac{dQ}{dt} = \frac{d\alpha}{dt} A_e \tag{6.2}$$

In the process of modelling, first the fraction transformed is calculated using Eq.(5.8) and Eq.(5.27-5.28), then the calculated heat flow is obtained by Eq.(6.2) and is normalised and fitted to the normalised experimental heat flow using the least squares method.

Amongst the input parameters, Q_d in Eq.(5.28) is taken to be 75kJ/mol as determined in Section 4.3.3 for the activation energy of Cu-Mg co-cluster formation. The reaction exponent n has been determined from DSC and isothermal calorimetry studies as 2.5 (Section 4.3.3). The molar volume of the Cu-Mg co-clusters is taken as the molar volume of fcc Al. As either Cu or Mg can be the excess atom for the alloys used in the present work, the solute concentration in the matrix refers to the non-excess atom. The current solute concentration in the matrix c is taken as the initial solute concentration. The parameters which needed to be calibrated are the pre-exponential factor k_0, the impingement exponent η_i and the interfacial energy γ. The effects of these parameters are different. The position of the exothermic peak is mainly given by the rate constant via k_0. A large k_0 value indicates fast formation rate. The rate of decay of the exothermic effect is mainly described by η_i. A low η_i value represents a long lasting growth and coarsening processes. The difference in formation rates between alloys B and D is determined by γ.

Fig. 6.1 shows the best fit to the isothermal calorimetry curves. The fitting yields the interfacial energy of the clusters/α interface γ=0.07±0.01J/m^2. This low value is reasonable, as for metastable, fully coherent precipitates, γ is generally indicated to be between 0.01 and 0.10 J/m^2 [3]. The obtained rate constants at 25°C for alloy B and alloy D are 13×10^{-5} s^{-1} and 8.0×10^{-5} s^{-1}, respectively. This shows that the rate of Cu-Mg co-cluster formation for alloy B is nearly twice as fast as that for alloy D at 25ºC. The parameters used in the prediction are listed in **Table 6.2.** The validity of the value of γ will be checked in Section 6.2.2 and Section 6.3.4.2 by comparing the predicted YS with the experimental data for alloys with different compositions.

6.2.2 Modelling of yield strength development

During the room temperature ageing, the Cu-Mg co-clusters are the only structure observed that contribute to the precipitation hardening. Considering that the Cu-Mg co-clusters differ from the solute atoms in either obstacle strength or number density, it is reasonable to assume that the contributions from cluster hardening and solution hardening are added linearly. The kinetic parameters obtained above are used as input data in the strength model. The shear modulus of the Cu-Mg co-clusters is unknown. It has been suggested that the shear modulus of the Cu-Mg co-clusters can be approximated as a weighted average of the moduli of the individual pure substances [4] and for the present Cu-Mg co-clusters this would mean:

$$\mu_{cl} = c_{cl}^{Cu}\mu_{Cu} + c_{cl}^{Mg}\mu_{Mg} + c_{cl}^{Al}\mu_{Al} \tag{6.3}$$

where μ_{Cu}, μ_{Mg}, μ_{Al} are the shear moduli of Cu, Mg and Al fcc crystals. c_{cl} represents the atomic fraction of the respective atoms in the Cu-Mg co-clusters, which is assumed to be 30%, 30% and 40% for Cu, Mg and Al atoms (see Section 2.2.2.2). The value obtained from Eq.(6.3) give an estimation of $\mu_{cl,}$ which is 30GPa using μ_{Al} = 26.2GPa, μ_{Cu} = 48.3GPa and μ_{Mg} = 17.3GPa from [5]. However, it is not thought to be a reliable estimate. (For example, the shear modulus of Al_3Li does not correspond

to this type of estimate [6]). Therefore the value for μ_{cl} is obtained here by fitting to strength data.

The experimental yield strength data of an Al-4.0Cu-1.5Mg (wt.%) alloy from [7] aged at room temperature has been used to calibrate the shear modulus of the Cu-Mg co-clusters. The samples were solution treated for 16h at 495ºC and quenched in water at 25ºC. Grain boundary strengthening is expected to be very small due to long time solution heat treatment. For this high purity ternary alloy, σ_i was taken as 10MPa. The rate constant for Cu-Mg co-cluster formation was kept similar to that for alloy B, i.e. the rate constant at 25°C is 13×10^{-5} s^{-1}. Optimizing μ_{cl} for best fit provides μ_{cl} =34.2GPa with a RMSE of 13MPa. The comparison between model prediction (curves) and the experimental data (symbols) is presented in **Fig. 6.2,** which also includes the predicted contributions from the solution strengthening due to Cu and Mg and from the cluster strengthening to the yield strength. It is seen that as the solute depletes with ageing time, the Cu-Mg co-clusters form and contribute to the strengthening. It should be pointed out that the fitted value of μ_{cl} depends on the amount of Al assumed to be present in the Cu-Mg co-clusters. Taking Al content in the Cu-Mg co-clusters to be 20% to 90%, μ_{cl} would be 35GPa to 29GPa, respectively. The values fall between the shear modulus of Al (26.2GPa) and Cu (48.3GPa), and are lower than the values for θ phase (36GPa) and S phase (44GPa) from [8]. These comparisons show that the present assessment of μ_{cl} provides values that are broadly in the expected range.

Using the parameters in Table 6.2 which were obtained by calibration on the isothermal calorimetry curves (Fig.4.28) for kinetic parameters and on the ageing curve (Fig. 6.2) for the shear modulus of the Cu-Mg co-clusters, the model is then tested against the experimental hardness data as shown in Fig.4.8 and from the literature [9, 10]. σ_i is taken as 30MPa for commercial purity alloys B and D, and taken as 10MPa for experimental high purity alloys Al-2.5Cu-1.2Mg (wt.%) from [9] and Al-2.5Cu-1.5Mg (wt.%) from [10]. The model predictions are compared with experimental data of alloys B and D in **Fig. 6.3** and with literature data in **Fig. 6.4**. The resulting RMSE for data in Fig. 6.3 is 22MPa and for data in Fig. 6.4 is 17MPa. These results indicate that the model is not only able to describe the final plateau

strength, but is also able to model the rise in hardness during the age hardening process for alloys of different compositions with a single set of parameters.

Fig. 6.5 shows the evolution of the predicted volume fraction of the Cu-Mg co-clusters f_v in alloys B and D. It appears that the final f_v is about 5% for alloy B and about 3.5% for alloy D. This is consistent with the measured volume fraction of GPB zones of 5.5%, obtained by Genevois *et al*. [11] using DSC and small angle X-ray scattering (SAXS) for a 2024-T351 alloy. Based on the composition assumption of the Cu-Mg co-clusters, these f_{cl} values will mean that the final amounts of Cu or Mg in the Cu-Mg co-clusters are about 1.5at% and 1.0at% for alloy B and alloy D, respectively (see Eq.5.10). Using SAXS, Gomiero *et al*. [12] determined that about 80% of the Cu atoms are in the GPB zones for an Al-2.1wt%Cu-1.35wt%Mg (Al-0.9at%Cu-1.5at%Mg) alloy after 2 years room temperature ageing. That means the amount of Cu in the GPB zones is about 0.72at%. The predicted values of 1.5at% and 1.0at% are in good agreement with Gomiero *et al*.'s results.

6.3 Modelling of artificial age hardening

During the artificial ageing, two precipitates, namely Cu-Mg co-clusters and S phase, compete for the available solute, resulting in two-stage age hardening. A key point in the model is the assumption that the S phase forms at the expense of the Cu-Mg co-clusters. In this section, the two-stage age hardening model will be calibrated and validated by comparing the predictions with measured yield strength/hardness data and microstructure data in terms of volume fraction obtained from DSC and precipitate size obtained from TEM measurements on stretched Al-Cu-Mg alloys. Parametric studies have been carried out to investigate how variations in input parameters influence the resulting yield strength predictions and to provide a better understanding of the coupling between the parameters. The model is then applied to study the strength evolution during multistage heat treatment and the early stages of age hardening. Finally, by adjusting the appropriate parameters, the model is extended to fit and predict the ageing curves from the literature for alloys with small additions of Si.

6.3.1 Calibration of the model

The model has been calibrated on the yield strength data of alloy A aged at 120°C, 170°C and 200°C, which cover the underaged, peak aged and short term overaged conditions. A range of parameters is required as input data to describe the ageing curves. To model the precipitation kinetics, the activation energy E_{eff}, the pre-exponential factor for precipitation k_0, the reaction exponent n and the impingement exponent η_i need to be determined for the Cu-Mg co-clusters and S phase, respectively. It is reported that a pre-age stretch slows down the formation of clusters or GP zones in an Al-5.0Cu-0.5Mg (wt.%) alloy [13] and in an Al-4.0Cu-0.3Mg (wt.%) alloy [14] when aged at room temperature. However, when aged at 170°C to 240°C, it has been shown that the hardness increases rapidly from the as-quenched value to the plateau value within 1 minute for stretched 2024 and Al-2.62Cu-1.35Mg (wt.%) alloy [15], similar to the rapid rise found in non-stretched alloys [15-17]. Thus it is safe to assume that the cluster formation reaction has been completed within 1 min for stretched 2024 type alloys aged at temperatures between 120°C and 220°C, and the rate of cluster formation is not considered for these stretched alloys. For modelling of S precipitation kinetics, the activation energy E_{eff}, has been determined by calorimetry studies, taken as 133kJ/mol (Section 4.3.3). The pre-exponential factor k_0 determines to a large extent the rate of precipitation or the time to peak and was treated as a fitting parameter. According to phase transformation theory, the reaction exponent n can only take the value of 1.5 or 2.5. n=1.5 reflects three-dimensional diffusion-controlled growth with zero nucleation rate and n=2.5 reflects three-dimensional diffusion-controlled growth with constant nucleation rate. For the present alloys, DSC studies have shown that the S phase forms via dissolution of the Cu-Mg co-clusters (see Section 4.3.2). As Cu-Mg co-clusters and S precipitates compete for the same elements, n for S precipitation cannot be predicted from transformation theory [18]. The value of n was thus determined by fitting the ageing curves. The results showed that n=2.5 provides a better fit to the data and in the following n was fixed at 2.5. η_i lies between 0.5 and 1 for Al-Cu-Mg alloys [19] and has little effect on model predictions. It was chosen as 1. To limit the model complexity, the activation energy for S coarsening was taken as equal to the activation energy for S precipitation. The average radius of S precipitates at the start of the coarsening,

$\bar{l}_0$, was estimated from measurements on TEM micrograph of alloy B aged at 190°C for 12h (see Fig.2.10). The radii of the rods, as measured from the edge on view**,** range from about 2.5 to 6nm, with an average of 4.4nm. The value of 4.4nm was initially used in the modelling and was further refined to give the best fit. The superposition exponent *q* was treated as a fitting parameter varying between 1 and 2. In summary, 4 parameters were fitted to the experimental data. They were the pre-exponential factor for precipitation k_0, the pre-exponential factor for coarsening $k_{0,c}$, the average radius of S rods at the start of coarsening $\bar{l}_0$ and the superposition exponent *q*.

Fig. 6.6 shows the model prediction compared with the experiment for alloy A at 120°C, 170°C and 200°C. A very good agreement is obtained with RMSE=12MPa. The parameters which gave the best fit are summarized in **Table 6.2**. As seen in Fig. 6.6, the model predicts that with reducing ageing temperature, the plateau strength increases, which is consistent with the experimental results presented in [15, 16, 20]. This is due to a higher volume fraction of Cu-Mg co-clusters precipitated at lower temperature resulting from the retrograde solvus. Single-precipitate models such as those developed by Shercliff and Ashby [21] (see Fig.2.13) and Liu *et al*. [22] (see Fig.2.16), are unable to predict the differences in plateau strength. This indicates that for these alloys it is necessary to consider a strengthening component due to a second precipitate that is dependent on solute concentration.

The obtained parameters for $\bar{l}_0$ and *q* are reasonable when compared with literature values [11, 23]. As the strength of the Cu-Mg co-clusters is much lower than that of S phase, it is expected that *q* should vary between 1 and 1.5. The fitting value of *q* falls within the expected range and is similar to the value (q=1.24) used in [23] for superposition of precipitate and GPB zone strengthening in Al–Li–Cu–Mg alloys. The fitting value of $\bar{l}_0$ =4.7nm for S precipitates corresponds reasonably well to the measured average radius of about 4nm given in [11] for an 2024-T351 alloy aged 10h at 190°C. This ageing condition corresponds to peak aged or slightly overaged stages. The radius of S rods at these stages is thought to represent the radius at the onset of the coarsening. Further validation of the model in terms of the size of precipitate and the rates of S precipitation are given in Section 6.3.3.

The various strengthening contributions to the CRSS for samples aged at 170°C are presented in **Fig. 6.7**. It can be seen that precipitation strengthening in the alloy is due to the Cu-Mg co-clusters in the first stage (the plateau portion). With increasing ageing time, the Cu-Mg co-clusters dissolve and its contribution declines, while S phase contribution becomes the main source of continued strengthening in the rise to the peak strength. It is observed that the time to reach peak of the total CRSS is shorter than the time to reach peak CRSS due to S phase alone. This reflects the contributions from the Cu-Mg co-clusters and the solute atoms, and arises from the superposition of the cluster strengthening and S phase strengthening. It is seen that the precipitation of S phase has not finished at the time to reach the peak strength; therefore the contribution from the solute atoms keeps on decreasing to reach a steady value well after the start of overageing.

6.3.2 Parametric study

Before testing the validity of these calibrated parameters, it is of interest to study the effects of the variations in these parameters on the yield strength. Parametric studies were carried out by varying one of the parameters used in the model while holding all the others constant in order to demonstrate the effect of varying a single parameter[*]. In this work, the effects of the following parameters were studied: the activation energy for S precipitation and coarsening E_{eff}^{S}, the shear modulus of the Cu-Mg co-clusters $\mu_{cl,}$, the solvus temperature of the Cu-Mg co-clusters T_s, the pre-exponential factor for precipitation k_0, the pre-exponential factor for coarsening $k_{0,c}$, the average radius of S precipitates at the start of coarsening $\bar{l}_0$ and the superposition exponent q.

Fig. 6.8 shows the variation of the yield strength with the change in E_{eff}^{S} for alloy A. Ageing curves at three ageing temperatures (120°C, 170°C and 200°C) are presented to demonstrate this effect. The values of E_{eff}^{S} were chosen from those obtained from DSC experiments as presented in Section 4.3.3 (133kJ/mol and 144kJ/mol) and from

[*] Except for the parametric study of E_{eff}^{S} where k_0 and $k_{0,c}$ have been re-adjusted. See the text.

[24] (160kJ/mol). k_0 and $k_{0,c}$ have been re-adjusted such that the peak hardness for alloy A aged at 170°C is maintained at constant ageing time. In applying these values of E_{eff}^{S}, it is seen that changing the activation energy changes the time axis and a high E_{eff}^{S} value enlarges the gap between the ageing curves for different temperatures. A variation in E_{eff}^{S} of about 10% from 133kJ/mol to 144kJ/mol produces a deviation in RMSE from the best fit of 12MPa to 14MPa, and a variation of about 20% from 133kJ/mol to 160kJ/mol produces a deviation in RMSE from the best fit of 12MPa to 21MPa.

It is evident from Fig. 6.7 that the plateau strength is mainly due to the cluster strengthening. In the present model, the increment in CRSS due to the Cu-Mg co-clusters is proportional to the shear modulus of the Cu-Mg co-clusters μ_{cl} and the square root of the volume fraction (see Eq.(5.29)). It is thus expected that a small variation in μ_{cl} will lead to a significant change in the YS. As seen from **Fig. 6.9**, varying μ_{cl} by about 6% (or varying $\Delta\mu$ by 25%) results in a deviation in the plateau yield strength of about 15%. The value of μ_{cl} listed in Table 6.2 was calibrated on the natural age curve of a high purity experimental alloy (see Section 6.2.2), and the use of a higher value of μ_{cl} will be discussed in Section 6.3.4.3.

The effect of the solvus temperature T_s of the Cu-Mg co-clusters on the yield strength is relatively small (**Fig. 6.10**). As previously indicated in Fig.5.5, no noticeable change in the YS is observed at low temperature due to the difference in the amount of the Cu-Mg co-clusters formed being nearly negligible. At 200°C, it is seen that higher T_s leads to higher plateau strength. A variation in T_s of ±15°C produces a maximum deviation in plateau yield strength of about 4% for alloy A aged at 200°C.

Variations of the yield strength with the changes in four fitting parameters are indicated in **Fig. 6.11**. It is seen that each parameter affects different stages of the ageing curve. Increasing k_0 shifts the time to peak to an earlier time and increases the yield strength at the rise to peak strength stage due to a faster rate of S precipitation. The peak strength increases by about 2% when the rate constant for S precipitation is double. Decreasing $k_{0,c}$ increases the overaged yield strength as the rate of S

coarsening decreases. Changing $\bar{l}_0$ affects the yield strength close to the peak, and a decrease in $\bar{l}_0$ leads to an increase in the peak yield strength. A variation in $\bar{l}_0$ of about 10% produces a deviation in peak yield strength of about 4%. A large value of q suppresses the contribution of the Cu-Mg co-clusters and causes a decrease in the yield strength. No change in the overaged yield strength is observed because at this stage the Cu-Mg co-clusters dissolve and are replaced by the S phase (see Fig. 6.7). A variation in q of about 15% produces a deviation in peak yield strength of about 5%.

6.3.3 Validation of the model

6.3.3.1 Evolution of the yield strength

Parameters listed in Table 6.1 and Table 6.2 were used to predict the yield strength for Al-Cu-Mg based alloys. **Fig. 6.12** shows the comparison between the predicted and measured strength evolutions for alloys B and D aged at 150°C, 190°C and 220°C. A reasonable agreement is obtained with RMSE=16MPa for the comparison of experimental YS data points and the corresponding modelled points for alloys B and D aged at 150°C and 190°C. The agreement in Fig. 6.12(b) indicates that the model is capable of predicting the ageing response for alloys with different compositions. The predictions show that the model correctly predicts the time to peak and the variations associated with the changes in composition and temperature based on a single set of parameters. It is found that the effect of increasing alloying elements, i.e. increasing Cu and Mg contents, on the ageing mainly serves to increase the magnitude of the ageing response due to the increasing volume fractions of the precipitates, although the increasing alloying elements are likely to increase the formation rate for the precipitates. As seen from Fig. 6.12(b), compared with experimental data for alloy D, the model predicts a slightly slower rate at 190°C, whereas it predicts a slightly faster rate at 150°C. Considering the effect of the activation energy of S phase on the yield strength (Fig. 6.8), it is suggested that larger activation energy would provide a better agreement with the experiments for alloy D.

Further verification of the model was performed on the YS ageing curves of 2024-T3 alloys. Data was taken from [25]. In modelling of these curves, a nominal

composition of Al-4.4Cu-1.5Mg-0.6Mn-0.25Fe (wt.%) was applied and the Si content was not considered. Changes in solute concentrations (Cu, Mg, Mn and Fe) will result in the ageing curves shifting slightly upwards or downwards. Comparison between measured and predicted yield strengths for 2024-T3 alloys aged at a range of temperatures is presented in **Fig. 6.13**. It is evident from Fig. 6.13 that the model results are in reasonable agreement with the measured ones for all ageing conditions. This exhibits the predictive power of the model.

6.3.3.2 Evolution of the volume fraction of S precipitates and the rate of S precipitation

It has been shown in Section 4.3.2 that the reduction in the S phase formation effect during DSC runs (Fig.4.22 and Fig.4.23**)** is associated with the amount of S phase formed during the isothermal ageing. The predicted volume fractions of S phase for alloy A aged at 170°C and 200°C are therefore compared with the change in the heat evolved of the S phase formation effects. Using the data in Table 4.3, the results are shown in **Fig. 6.14,** where ΔQ is the heat evolved of the S formation peak, the subscripts *AR* and *t* are for as-received samples and samples artificially aged for time *t*. The data point for sample aged 168h at 170°C is at the overaged stage (see Fig.4.5) and is excluded in Fig. 6.14. As mentioned previously in Section 4.3.2, DSC curves of samples aged 0.38h, 2h and 4.6h at 170°C show slight baseline drifts, which result in deviation of the heats evolved. Therefore these data points (shown as encircled points in Fig. 6.14) are not comparable with other data points. A linear approximation for the other data points, as seen from the figure, indicates the good correspondence between the predicted volume fractions and the changes in the heats evolved. This shows that the model correctly describes the evolution of the volume fraction of precipitates. It is thus suggested that the rate for S precipitation can be estimated from DSC data, and this will be described in the following.

The fraction transformed for S precipitation during the isothermal ageing can be estimated from DSC data for samples aged for various times. The method involves conducting DSC runs on several samples that have aged for various times at a certain temperature, and then calculating the heat evolved, i.e. the area of the exothermic

peak for S precipitation. For a sample aged at temperature T for time t, the fraction transformed α can be estimated from the heat evolved during DSC runs using:

$$\alpha^s = \frac{\Delta Q_{AR} - \Delta Q_t}{\Delta Q_{AR} - \Delta Q_\infty} \tag{6.4}$$

where ΔQ is the heat evolved of the S formation peak, the subscripts AR, t and ∞ are for as-received samples, samples artificially aged for time t and samples artificially aged for very long time, respectively. Obviously ΔQ_∞=0. Using the heat evolved data in Table 4.3, the obtained α versus t curves for 170°C and 200°C isothermal ageing are presented in **Fig. 6.15** as data points.

To determine the rate of S precipitation, the SZ model was applied to fit the above α versus t curves using Eq.(5.8). For a comparison with the rate obtained from fitting the yield strength data in Fig. 6.6, the kinetic parameters for S precipitation such as the activation energy E_{eff}, the reaction exponent n and the impingement exponent η_i were taken as identical to those listed in Table 6.2. The fitting results, shown in Fig. 6.15 as curves, yielded the pre-exponential factor k_0=7.6×10^{10} s^{-1}. Comparing this value with that obtained from the optimization of the yield strength curves in Fig. 6.6 (k_0=4.3 ×10^{10} s^{-1}) and taking into account the superposition of the Cu-Mg co-clusters and S phase (q=1.3), it is found that these two values correspond with each other very well. Given q=2 (i.e. the contribution due to the Cu-Mg co-clusters is suppressed), k_0=7.6×10^{10} s^{-1} will accurately predict the time to peak in the ageing curves. Hence the optimised value of k_0 from the ageing curves can be verified by DSC experiments. In other words, the k_0 value can be estimated from DSC data and the rate for S precipitation during an isothermal ageing process can be modelled.

6.3.3.3 Evolution of the radius of S precipitates

Fig. 6.16 presents the predicted evolution of the average radius of S rods in alloy A during ageing at 190°C, compared with the measured results obtained from quantitative TEM analysis on alloys A and B (see Table 4.6). (This figure also

includes the predicted and measured data for alloys C and E, for which a discussion will be given in Section 6.3.4.3). Good agreement is observed. This indicates that the model, particularly the part of the analytical treatment for the evolution of average precipitate size (Section 5.3.2), is sound and the fitting value of $k_{0,c}$ is reasonable. Compared to the iterative numerical treatment employed in [26, 27] based on the so-called Kampmann-Wagner treatment, the present treatment is straightforward and transparent, and has a predictive capacity similar to the Kampmann-Wagner treatment.

6.3.4 Applications of the model

6.3.4.1 Modelling of the hardness during multi-stage heat treatment

It has been shown in the above section that the model is capable of describing the concurrent dissolution of the Cu-Mg co-clusters and precipitation of the S phase. For alloys in the underaged condition, two precipitates, the Cu-Mg co-clusters and the S phase, are present and contribute to the strength. Thus the changes in the hardness during multi-stage heat treatment (see Section 4.1.3) can be better understood through model predictions, which show the simultaneous evolution of each hardening component. In applying the model to the multi-stage heat treatment which includes isothermal and non-isothermal conditions, the effects of prior artificial ageing on subsequent ageing were not considered for simplicity. This simplification is justified by a comparison of the hardness values at 200°C during multi-stage heat treatments (see Fig.4.9) with those aged at 200°C from as-received T351 (see Table 4.1). Considering the difference in their as-received hardness values, it shows little difference between these two sets of values within experimental error (typical STD ±2Hv, maximum STD ±6Hv). It is thus presumed that the preceding heat treatments at 150°C or at 170°C have little influence on subsequent ageing at 200°C or at 220°C. For the extended natural ageing after a short high temperature ageing (so-called secondary ageing), the initial microstructure contains both the Cu-Mg co-clusters and the S phase. As the S precipitates formed at high temperature remain stable at room temperature, the hardening occurring at room temperature (RT) after underageing at high temperature is due to the additional Cu-Mg co-clusters that form at RT. The re-formation of the Cu-Mg co-clusters will depend on whether there is sufficient

remaining solute concentration in the matrix to overcome the energy barrier ΔG^*. Also the rate of the Cu-Mg co-cluster formation in the underaged condition (re-quenched from the ageing temperature into water or air cooled) will be slower than that in the as-quenched condition (quenched from the solution heat treatment temperature into water) due to the reduced supersaturation and vacancy concentration. The kinetics of secondary ageing in an Al-4.5Cu-0.56Mg (wt.%) alloy has been studied by combined measurements of positron annihilation spectroscopy (PAS), DSC and microhardness tests [28, 29]. It is shown that secondary hardening at RT after quenching from 5 min at 190°C occurs at a rate about 10 times slower than natural ageing after quenching from the solution heat treatment temperature. In the present case, 2 months RT ageing was applied and it is relatively simple to calculate the amount of additional Cu-Mg co-clusters as formation of Cu-Mg co-clusters should be completed.

Fig. 6.17 and **Fig. 6.18** show the comparisons of the predicted hardness with the experimental data for two consecutive heat treatment routes as well as the predicted different contributions to the CRSS. The ratio of the yield strength to the Vickers hardness number is taken to be 2.5 as calculated from the yield strength and the hardness data of alloy A in the underaged condition (see Fig 4.10). It is seen that the predicted hardness is consistent with the experiments. In the as-received state only one precipitate, the Cu-Mg co-clusters, is present and their contribution to the hardening is at a maximum. The Cu-Mg co-clusters partially dissolve with the increasing temperature. At the same time, S phase starts to precipitate and at the early ageing stage its contribution is very small due to limited volume fraction, thus the overall hardness decreases. At longer ageing times, the amount of the S precipitates increases and the hardness increases accordingly. On subsequent RT ageing, the model predicts that the Cu-Mg co-clusters re-form from the available solute in the matrix, leading to the increase in the overall hardness with an increased cluster strengthening contribution and a decreased solution strengthening contribution, while the S phase strengthening contribution remains unchanged.

This multi-stage heat treatment was initially designed to identify the contributions of the Cu-Mg co-clusters and the S phase to the strength in the underaged condition, and

the possibility of re-formation of the Cu-Mg co-clusters at room temperature after the alloy has been underaged at high temperature. Data in Fig. 6.17 and Fig. 6.18 confirm that the changes in the hardness can be well interpreted by considering a microstructure that contains the Cu-Mg co-clusters and the S phase. The hardness changes during the multi-stage heat treatment are to some extent similar to those occurring during welding of 2024-T351 alloys [11, 30, 31]. Genevois *et al.* [11] have modelled the variation of yield strength through a 2024-T351 weld using measured microstructural data (i.e. the evolution of volume fractions and size of the precipitates). The modelling presented in this section may be regarded as a preliminary assessment of the suitability of the model for modelling more complex thermal cycle in the welding process. Applying the present model, the evolutions of volume fraction and size can be predicted based on alloy composition and heat treatment without quantitative microstructural characterization and the yield strength can be predicted. Considering the encouraging results shown in Fig. 6.17 and Fig. 6.18, the model can then be further extended to incorporate several sub-models to describe the microstructure and hardness profile of a 2024-T351 variable polarity plasma arc (VPPA) weld. This is beyond the scope of the present PhD work. The work has however been performed by researchers in our group and results presented in [32] show that the extension of the present model can predict hardness profiles in these welds quite well.

6.3.4.2 Modelling of the early stages of age hardening

In order to check the predictive capability of the model for the rapid hardening during the early stages of ageing, experimental data for the change in hardness during the course of the first rise to plateau hardness for a range of alloys are needed. Such data were obtained from Dr. K. Raviprasad [*] of Monash University, Australia, who studied four alloys with nominal compositions of Al-xCu-1.7Mg (x=0.2, 0.5, 0.8 and 1.1) (at.%) (The ageing behaviour of Al-0.2Cu-1.7Mg and Al-0.8Cu-1.7Mg alloys can be found in [33]). The compositions of the alloys were chosen so that the Al-0.2Cu-1.7Mg alloy is on the boundary of the (α+S) region and α region, and the other alloys

[*] Dr. K. Raviprasad is now with Nanotechnology Victoria, Australia.

are in the (α+S) region based on the phase diagram of the Al-Cu-Mg system at 190°C (see Fig.2.3). The alloys were solution treated in a salt bath for 1h at 525°C, quenched rapidly into cold water and then aged in an oil bath maintained at 150°C. Vickers hardness was measured with a 5kg load and the average value of ten indentations was reported. As shown in **Fig. 6.19,** alloys with Cu contents of 0.5at.% to 1.1at.% exhibit the first rapid hardening and the rates for the rise decreased with the decreasing Cu content, while alloy with Cu content of 0.2at.% exhibits no rapid hardening but a gradual increase to peak hardness.

Using the parameters given in Table 6.1 (the intrinsic strength σ_i was taken as 10MPa) and Table 6.2, the modelling results are compared with the experimental data in Fig. 6.20. The accuracy of the prediction is RMSE=32MPa between the modelled YS and the hardness converted YS for alloys with Cu contents of 0.5at.% to 1.1at.%. It is seen that the features of two-stage age hardening are well reproduced by the model, and the slower rates for the first rise in more dilute alloys are correctly modelled. Large discrepancy is observed in the modelling of 0.2at.% Cu alloy, as the model predicts that no Cu-Mg co-clusters form during ageing at 150°C for this alloy. Considering that the 0.2at.% Cu alloy lies on the boundary of the (α+S) region and α region, it is likely that other precipitates not considered in the present model are responsible for the gradual rise to peak hardness. For the other three alloys which are well within the (α+S) region, reasonable agreements are observed. These results verify the validity of the analysis for homogeneous precipitation kinetics of alloys with different compositions as described in Section 5.3.3.

Fig. 6.21 shows the evolution of Cu and Mg concentrations and volume fractions of the Cu-Mg co-clusters and the S phase during ageing at 150°C in the 0.5at.% Cu and 0.8at.% Cu alloys. For each alloy, the parallel decreases of the Cu and Mg concentration are observed because the Cu: Mg atomic ratios in the Cu-Mg co-clusters and in the S phase are one to one. The first drop is related to the formation of the Cu-Mg co-clusters and the second one to the precipitation of the S phase. The plateau corresponds to the metastable equilibrium concentration of the solute at 150°C. In correspondence with the decrease in solute concentration, the Cu-Mg co-clusters and the S phase form and reach their equilibrium volume fractions. Higher

solute contents result in a higher volume fraction. Fig. 6.21 indicates that the precipitation of the S phase occurs by dissolution of the Cu-Mg co-clusters and by transformation of the solid solution.

It should be noted that by using the parameters in Table 6.2 for S precipitation, which were calibrated on alloy with pre-stretch, the description of the second stage of hardening is actually in line with those for alloys with pre-stretch. As pre-stretch is known to result in an accelerated rate of age hardening and an increased yield strength or hardness [15, 24, 34], it is expected that the predicted peak strength and the time to peak are likely to be higher and shorter than the experimental values, respectively. Thus it is somewhat surprising to find that these parameters give reasonably good predictions for the peak strength and the time to peak to alloys without pre-stretch. It is however noted that other measurement of the hardness (see Fig.2.9) [35, 36] for an Al-1.1Cu-1.7Mg (at.%) alloy during ageing at 150°C indeed shows longer times to peak as compared with the curve in Fig. 6.19. It partly reflects the complicated dependence of the mechanical properties on alloy composition and process history. Nevertheless, the modelling of the first rapid hardening which is due to the formation of the Cu-Mg co-clusters is not affected by the use of the parameters for S precipitation.

6.3.4.3 Modelling of age hardening of alloys with small additions of silicon

Alloys studied so far contain less than 0.1at.% Si. In this section, the ageing behaviour of alloys with small additions of silicon will be modelled. The YS-time ageing curves of an Al-4.25Cu-1.68Mg-0.71Mn-0.14Si-0.24Fe (wt.%) alloy (referred to as alloy E) measured by Martinod *et al.* [24] were used, see data points in **Fig. 6.22.** This alloy was solution treated, deformed by 2% immediately after quenching, room temperature aged for an unknown time and then aged at temperatures from 150°C to 225°C. In a first attempt to model the curves using the parameters in Table 6.2, it was found that the predicted yield strengths were smaller than the experimental ones throughout the whole ageing curves by a nearly constant value. These results are consistent with the experimental observations that the addition of small amounts of Si to the Al-Cu-Mg alloys significantly enhances the age hardening, as mentioned in Section 2.2.4. In

view of the fact that Si addition affects the whole ageing process (i.e. first decreases the as-quenched hardness by removing Mg from solid solution, then increases the response to artificial ageing, leading to enhanced plateau and peak hardness [37]), the effect of Si cannot be incorporated in the model in a way similar to that of Fe and Mn. A practical way is to simply apply a separate set of parameters on the ageing curves. The present approach is not aimed at describing the detailed relation between the amounts of Si content and the hardening, but rather to show the resulting changes in the model parameters, and the possible physical insight inferred from the modelling results.

To model these ageing curves, the activation energy for S precipitation and coarsening was taken as 158 kJ/mol which was measured from the times to peak in the ageing curves by Martinod *et al.* [24]. It was found that the best fit was obtained with RMSE=10MPa (**Fig. 6.22**) when the shear modulus of the Cu-Mg co-clusters, $\mu_{cl,}$ is increased by about 2GPa to 36.5GPa and the rate constant for S coarsening, $k_c(T)$, is decreased from $k_c(200°C)=1.4\times10^{-3}nm^3/s$ calculated from Table 6.2 to $k_c(200°C)=5.2\times10^{-4}nm^3/s$. The S precipitation rate for this alloy is similar to that calculated from Table 6.2. Within the present model, this would imply that the Si addition influences the shear modulus of the Cu-Mg co-clusters and the rate of S coarsening. The changes in μ_{cl} and $k_c(T)$ can be interpreted by experimental observations. As seen from Fig. 6.9, an increase in μ_{cl} from 34.2GPa to 36.2GPa causes an increase of about 50MPa in the plateau yield strength. Hutchinson and Ringer [37] reported that addition of 0.1wt.%Si to an experimental alloy Al-2.5Cu-1.5Mg (wt.%) led to an increase of the plateau hardness from 90Hv to 110Hv when the alloys were aged at 200°C. An increase of 20Hv in hardness is equivalent to 46MPa if a conversion of YS=2.3Hv is used. This comparison indicates that the higher level of the strength presented by alloy E compared with alloys A and B is indeed due to the presence of Si. Some support for the increase in μ_{cl} may be derived from the observations of the so-called Si-modified GPB zones reported in [37, 38]. Although the precise mechanism by which Si-modified GPB zones enhance age hardening remains unknown, it is likely that the addition of Si increases the perfection of cluster/zone structure which may well increase μ_{cl}.

The modelling of the ageing curves indicates that the rate of S phase coarsening is slowed down by Si additions. The model therefore predicts a smaller average radius of S precipitates in alloy E compared with that in alloy A during the coarsening stage (**Fig. 6.16**). This is consistent with the measured results which indicate that the sizes of S precipitates in alloy C are smaller than those in alloys A and B, and is in line with TEM observations reported by Wilson *et al*. [9, 39, 40] and Hutchinson and Ringer [37] which demonstrated a refinement of the S precipitates in Si-containing alloys. In this work, an attempt was made to quantify the effect of Si addition on the size of the S precipitates by quantitative TEM analysis of alloy C (Al-4.07Cu-1.36Mg-0.54Mn-0.12Si-0.20Fe wt.%), which is similar in chemical composition to alloy E (Al-4.25Cu-1.68Mg-0.71Mn-0.14Si-0.24Fe wt.%). The average radii of S rods in alloy C aged at 190°C for 96h and 720h are compared with the predicted radius of alloy E in Fig. 6.16. The agreement is reasonable, as the predicted sizes fall within the experimental errors. Thus the change in $k_c(T)$, which was obtained by fitting the ageing curves, is justified by the size measurements of the S precipitates.

6.4 Discussion

6.4.1 Coarsening kinetics of S precipitates

In a further attempt to verify the coarsening rate of S phase, the predicted rate constants of coarsening, $k_c(T)$, are compared with the experimental ones. Although extensive microstructural characterization of Al-Cu-Mg alloys is available in the literature, very few publications concerning the quantitative analysis of the coarsening of S precipitates in Al-Cu-Mg alloys can be found. Limited experimental data on the coarsening of S phase in non-stretched Si-free Al-Cu-Mg alloys has been reported for an Al-3.3Cu-1.6Mg (wt%) alloy at 260°C, 280°C and 300°C [34], for an Al-2.0Cu-1.1Mg (wt%) alloy at 200°C and 230°C [41] and for an Al-4.1Cu-1.6Mg (wt%) alloy at 200°C [42]. For the three sets of data, measurements were made on the length, thickness and width of S laths, and average particle volume, V, and surface area, A, were calculated. An "effective particle radius", r_e, was used to compare the experimental particle size data with the LSW theory. According to Wagner [43], r_e is defined as $(2dV/dA)$, where dV is the change in volume $(V_2\text{-}V_1)$ and dA is the change in surface area $(A_2\text{-}A_1)$ occurring over time $(t_2\text{-}t_1)/2$. A plot of r_e^3 versus ageing time is

expected to be a straight line, with slope determined by $k_c(T)$. This treatment allows the coarsening rate of S laths from different data to be compared. However, the above three sets of data exhibit discrepancies, varying by 1 to 2 orders of magnitude in $k_c(T)$ for a given temperature. As can be seen in **Fig. 6.23**, at 200°C, $k_c(T)$ for the Al-2.0Cu-1.1Mg (wt%) alloy is $2.8\text{x}10^{-2}\text{nm}^3/\text{s}$ (data taken from [44]), $k_c(T)$ for the Al-3.3Cu-1.6Mg (wt%) alloy is one order of magnitude less at $3.25\text{x}10^{-3}\text{nm}^3/\text{s}^*$ and $k_c(T)$ for the Al-4.1Cu-1.6Mg (wt%) alloy is $3.2\text{x}10^{-4}\text{nm}^3/\text{s}$ [42]. Nonetheless, it is found that the predicted $k_c(200°\text{C})=1.4\times10^{-3}\text{nm}^3/\text{s}$ for alloy A (the low Si content alloy) and $k_c(200°\text{C})=5.2\times10^{-4}\text{nm}^3/\text{s}$ for alloy E (the high Si content alloy) lie within the range obtained from these literature data as illustrated in Fig. 6.23, and it clearly shows that alloy E exhibits a lower coarsening rate as compared with alloy A. This agrees well with experimental results that the rate of S coarsening is reduced by small additions of Si [9, 39, 40].

6.4.2 Mechanisms for cluster strengthening

In the literature on modelling of precipitation hardening of heat treatable aluminium alloys, little work has been done to consider the strengthening due to GP/GPB zones or Cu-Mg co-clusters. This is thought to be partly because of lack of knowledge of the structures, morphologies and volume fractions of the zones/clusters and therefore the strengthening mechanisms. However, it has been shown in this work (see Fig. 6.20) that, in order to model two-stage age hardening in Al-Cu-Mg alloys, it is necessary to include a zone/cluster strengthening term that is dependent on solute concentration, ageing time and temperature. Also the experimental observations that the plateau hardness increases with decreasing ageing temperature can only be reflected by consideration of the zone/cluster strengthening.

For shearable Cu-Mg co-clusters, the possible strengthening mechanisms are modulus hardening and chemical hardening, as indicated previously in Section 5.4.1. In the

---

* This value was obtained from an Arrhenius expression of $k_c(T)$ with parameters Q=117kJ/mol and $k_{0,c}=2.7\text{x}10^{-2}\text{nm}^3/\text{s}$ determined from plot of $ln(k_c)$ versus $1/T$ using $k_c(T)$ data on T=260°C, 280°C and 300°C ($k_c(T)$ data were taken from [44]).

present approach to calculate the cluster strengthening contribution, it was assumed that chemical hardening is relatively small and is neglected. This assumption was justified by the good agreement between the model and the experiments, which suggests that any potential contribution will not be significant. Actually, with the interfacial energy of 0.07J/m^2 obtained in Section 6.2.1, one can estimate the chemical hardening contribution using the equation derived by Brown and Ham [3, 45]:

$$\Delta\tau_{ch} = \left(\frac{6bf}{\pi\Gamma}\right)^{1/2} \frac{\gamma^{3/2}}{r} \tag{6.5}$$

Where b is the magnitude of the Burgers vector, $\Gamma=\beta_{LT}\mu_{Al}b^2$ is the dislocation line tension (β_{LT} is a constant close to 0.5), μ_{Al} is the shear modulus of the aluminium matrix, γ is the interfacial energy, f is the volume fraction and r is the radius of the Cu-Mg co-clusters. The average radius of the Cu-Mg co-clusters, as estimated from the radius of gyration using 3DAP in naturally aged alloys B and D, is in the range of 0.5nm to 0.7nm for ageing time from 1h to 6 months [2]. Thus a radius of 0.6nm is used to calculate the contribution. Given the equilibrium volume fraction f=0.05 (assuming Cu content in the Cu-Mg co-clusters to be 30%) for naturally aged alloy B (see Fig. 6.5), Eq.(6.5) provides $\Delta\tau_{ch} \approx$ 5MPa. The value is clearly very small compared with $\Delta\tau_{cl}$ obtained from the present model for naturally aged alloy B using Eq.(5.29), which is typically ~100MPa (see Fig. 6.3). Genevois *et al*. [11] reported that the hardening contribution due to the GPB zones during the natural ageing equals 278MPa, which is consistent with the above predicted value of about 100MPa for $\Delta\tau_{cl}$. This result indicates that chemical hardening is not the dominant mechanism. Thus the present approach which considered modulus hardening only is reasonable. If this small $\Delta\tau_{ch}$ term is taken into account, Eq.(6.5) can then be approximated as $A_1f^{1/2}$ because the radius of the Cu-Mg co-clusters is relatively stable during ageing. Similarly Eq.(5.29) can be regarded as $A_2f^{1/2}$. Therefore a general expression of $Af^{1/2}$ can be used to describe the strengthening contribution due to shearable Cu-Mg co-clusters, regardless of the detailed strengthening mechanisms involved. The constant A then reflects predominantly modulus hardening with a small increase (~5%) due to chemical hardening.

6.5 Limitations of the model and suggestions for further work

A model for the prediction of the yield strength of Al-Cu-Mg alloys based on microstructural evolution has been presented in this thesis. The model predictions are in good agreement with the experimental data in terms of the yield strength evolution, the volume fraction and the average particle size evolution. In order to deal with problems such as the complicated precipitation process which may involve several metastable phases competing for the available solute atoms whilst limiting the model complexity, and to provide a model that is relatively straightforward and accurate, some approximations and assumptions were made. Improvements of the model therefore can be suggested from consideration of the following limitations:

- The dislocation strengthening due to pre-stretch was described by the Ashby model with a strain hardening factor assumed to be a constant. The model can be improved with a better description of the work hardening behaviour, which accounts for the evolution of work hardening rate or strain hardening factor with ageing time due to the change in microstructure, especially when the amount of cold work is larger than 5%. The effect of dislocation recovery on nucleation rate may need to be considered.
- The solvus of the Cu-Mg co-clusters was estimated from the ageing curves and the shear modulus of the Cu-Mg co-clusters needs calibration. Difficulties exist in experimental determination of the solvus and the shear modulus. Considering the uncertainties and sparse studies on cluster strengthening in the literature, it is thought that the present model gives a satisfactory analysis of the cluster strengthening. Further work is needed on both the experimental and modelling aspects to address the detailed mechanism for cluster strengthening.
- The evolution of the average particle size was simplified by taking a parameter $\bar{l}_0$ which was assumed to be a constant in the temperature range studied. Although this treatment gives reasonable agreement between the predicted and measured average particle size, improvement on the nucleation-growth-coarsening kinetics, which allows consideration of the size distribution of the particles, may be worth trying. This work is currently carried out in our group [46].

6.6 Summary

A model developed for the age hardening behaviour of Al-Cu-Mg alloys has been calibrated and validated against yield strength measurements and microstructural data obtained by TEM and DSC studies. It has been shown that the model is capable of predicting accurately the ageing response of Al-Cu-Mg alloys to heat treatment (solution temperature, ageing temperature and ageing time) and alloy composition (the Cu, Mg, Fe and Mn contents). The two-stage age hardening is well represented by considering the strengthening due to Cu-Mg co-clusters and S phase with a minimum of fitting parameters. The model provides a good prediction of the yield strength during the early stages of hardening. It is shown that the model is applicable to describe the ageing behaviour of Al-Cu-Mg alloys with Si contents at levels of 0.1-0.2wt.%. Modelling results indicating increased shear modulus of the Cu-Mg co-clusters and decreased coarsening rate of the S phase for Si containing alloys are supported by experimental evidence in the literature. Finally, the limitations of the model and areas for improvements in future studies are discussed with respect to nucleation-growth-coarsening kinetics, cluster strengthening and work hardening.

Table 6.1 Fixed parameters used in the model predictions

Symbol	Definition	Value	Comments
b	Magnitude of the Burgers vector	0.286 nm	
μ_{Al}	Shear modulus of the Al matrix	26.2 GPa	From [5]
ν	Poisson's ratio	0.33	
ΔH^{cl}	Formation enthalpy of the Cu-Mg co-clusters	38 kJ/mol	See Section 5.2.1 Eq.(5.1)
c_1	Pre-exponential factor	$1.6\text{x}10^4$ (at.%)^2	See Section 5.2.1 Eq.(5.1)
ΔH^S	Formation enthalpy of S phase	77kJ/mol	See Section 5.2.1 Eq.(5.2)
c_2	Pre-exponential factor	5.0×10^5 (at.%)^2	See Section 5.2.1 Eq.(5.2)
V_m	Molar volume of the Cu-Mg co-clusters	10^{-5} m^3/mol	Taken as the molar volume of Al
σ_i	Intrinsic strength	30 MPa*	For commercial purity alloys
k_{Cu}	Strengthening coefficient for Cu	50MPa/at % Cu	See Section 5.4.3
k_{Mg}	Strengthening coefficient for Mg	13.6MPa/at % Mg	See Section 5.4.3
K_A	Strain hardening factor	450 MPa	See Section 5.4.4
M	Taylor factor	2.6	See Section 5.4.6

* The intrinsic strength σ_i is taken to be 10 MPa for high purity alloys.

Table 6.2 Parameters used in the model predictions

Symbol	Parameter	Value	Comments
E_{eff}^{cl}	Activation energy for Cu-Mg co-cluster formation	75 kJ/mol	From DSC measurement, See Section 4.3.3
k_0^{cl}	Pre-exponential factor for Cu-Mg co-cluster formation	1.9×10^{9} 1/s	Obtained by fitting to isothermal calorimetry curves, see Section 6.2.1
n^{cl}	Reaction exponent for Cu-Mg co-cluster formation	2.5	From calorimetry studies, see Section 4.3.3
η_i^{cl}	Impingement exponent for Cu-Mg co-cluster formation	0.6	Obtained by fitting to isothermal calorimetry curves, see Section 6.2.1
γ	Interfacial energy of the clusters/α interface	0.07 J/m^2	Obtained by fitting to isothermal calorimetry curves, see Section 6.2.1
μ_{cl}	Shear modulus of the Cu-Mg co-clusters	34.2 GPa*	Obtained by fitting to natural ageing curve, see Section 6.2.2
E_{eff}^{S}	Activation energy for S precipitation	133 kJ/mol	From DSC measurement, See Section 4.3.3
k_0^{S}	Pre-exponential factor for S precipitation	4.3×10^{10} 1/s	Fitting parameter
n^{S}	Reaction exponent for S precipitation	2.5	Chosen by curve-fitting
η_i^{S}	Impingement exponent for S precipitation	1	Chosen based on the literature
$k_{0,c}^{S}$	Pre-exponential factor for S coarsening	7.0×10^{11} nm^3/s	Fitting parameter
$\bar{l}_0$	Average radius of S rods at the start of coarsening	4.7 nm	Fitting parameter
q	Superposition exponent	1.3	Fitting parameter

* Based on the assumption that the Cu, Mg and Al contents in the Cu-Mg co-clusters are 30at.%, 30at.% and 40at.%.

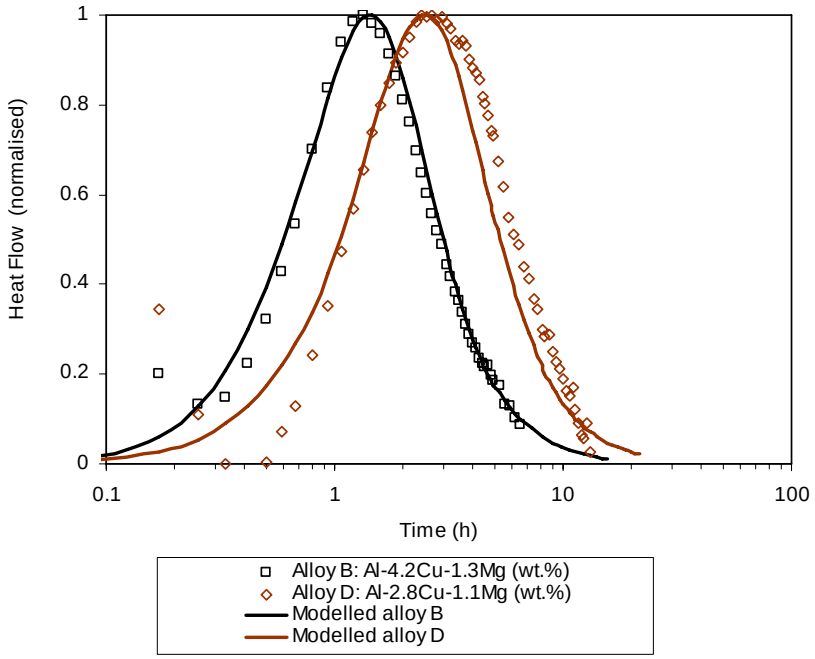

Fig. 6.1 Isothermal calorimetry data on the heat flow due to Cu-Mg co-cluster formation at 25ºC in the alloys B and D (dots) compared with predictions from the model outlined in Section 5.3.3 (n=2.5, η_i=0.6, γ = 0.07±0.01J/m^2) (lines).

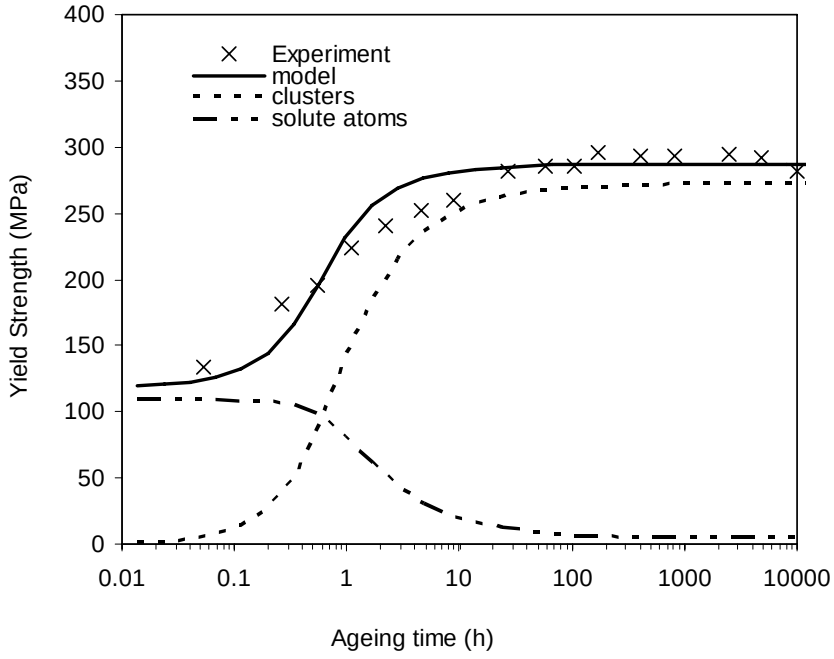

Fig. 6.2 Experimental yield strength from [7] and modelling results for an Al-4.0Cu-1.5Mg (wt.%) alloy aged at 25ºC. Predicted contributions from the solute atoms and from the clusters to the yield strength are also shown.

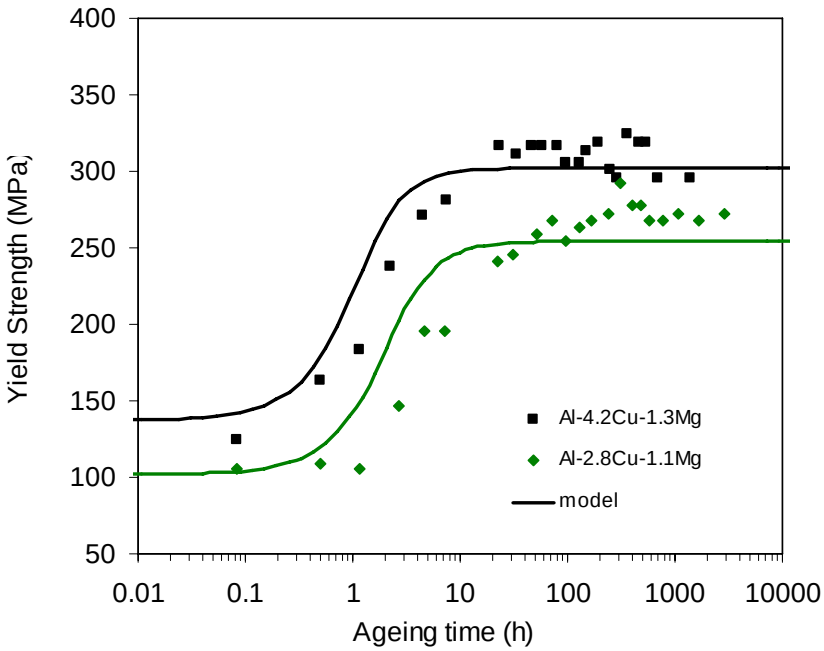

Fig. 6.3 Predicted and converted strength evolution for the Al-4.2Cu-1.3Mg (alloy B) and the Al-2.8Cu-1.1Mg alloy (alloy D) aged at 25ºC. The converted strengths were calculated from Vickers hardness using Eq.(4.2) with λ_1=1.35 and λ_2=2.3.

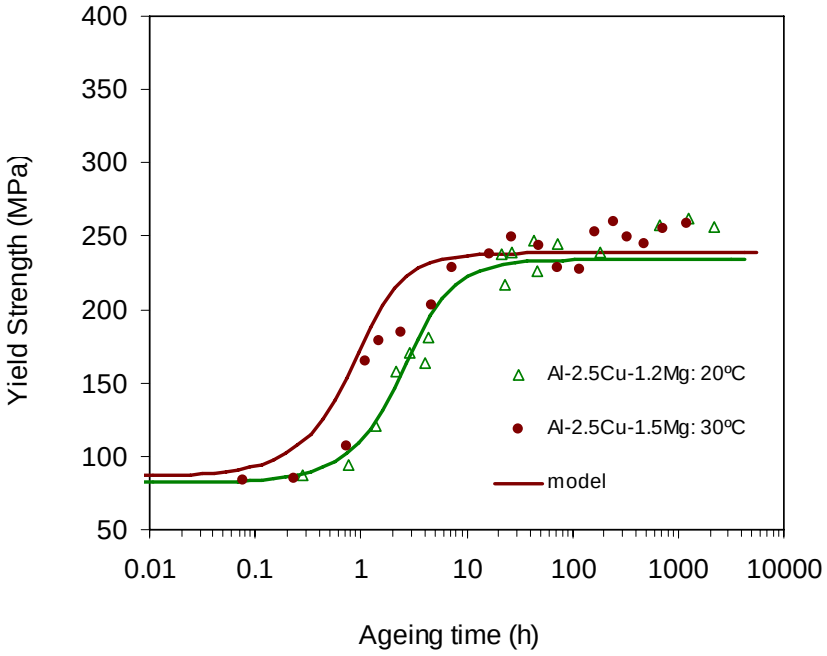

Fig. 6.4 Predicted and converted strength evolution for an Al-2.5Cu-1.5Mg alloy [10] and an Al-2.5Cu-1.2Mg alloy [9]. The converted strengths were calculated from Vickers hardness using Eq.(4.2) with λ_1=1.35 and λ_2=2.3.

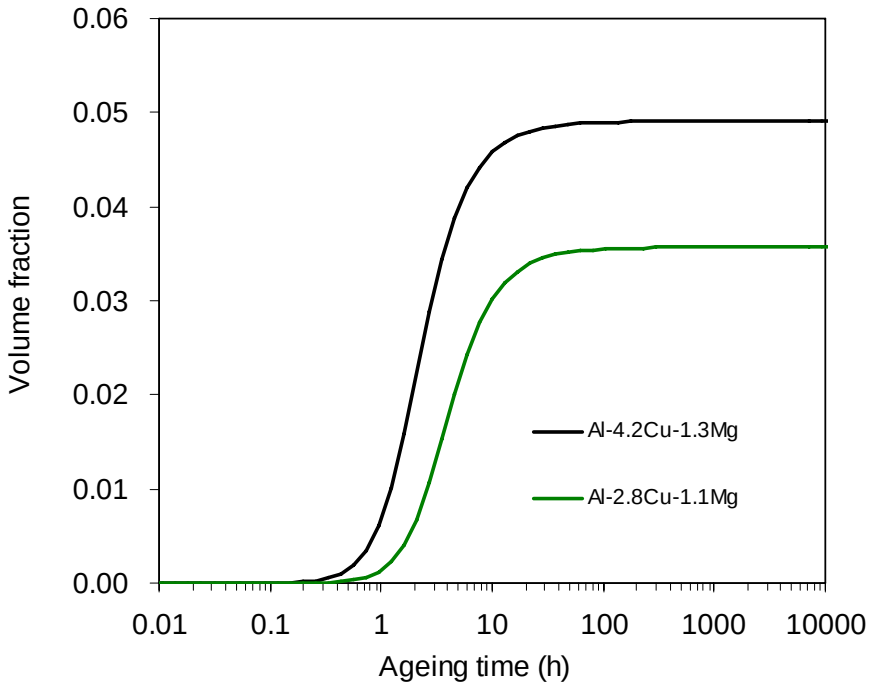

Fig. 6.5 Predicted evolution of the volume fraction of Cu-Mg co-clusters for the Al-4.2Cu-1.3Mg (alloy B) and the Al-2.8Cu-1.1Mg alloy (alloy D) aged at 25ºC.

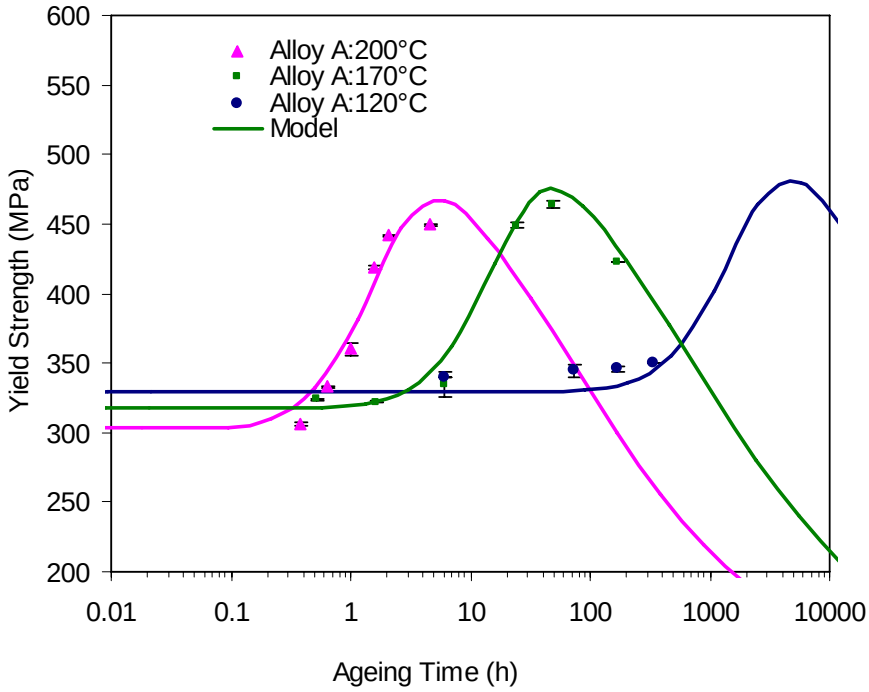

Fig. 6.6 Predicted and measured strength evolution for alloy A (2024-T351) aged at 120°C, 170°C and 200°C.

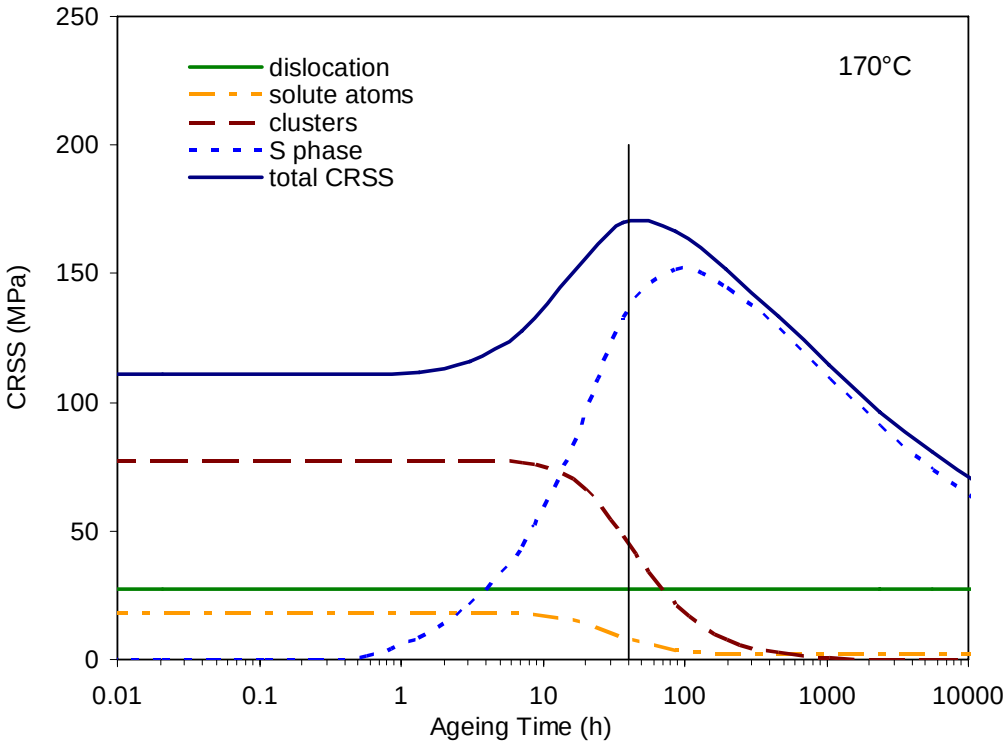

Fig. 6.7 Contributions to the critical resolved shear stress (CRSS) of grains of alloy A during ageing at 170°C.

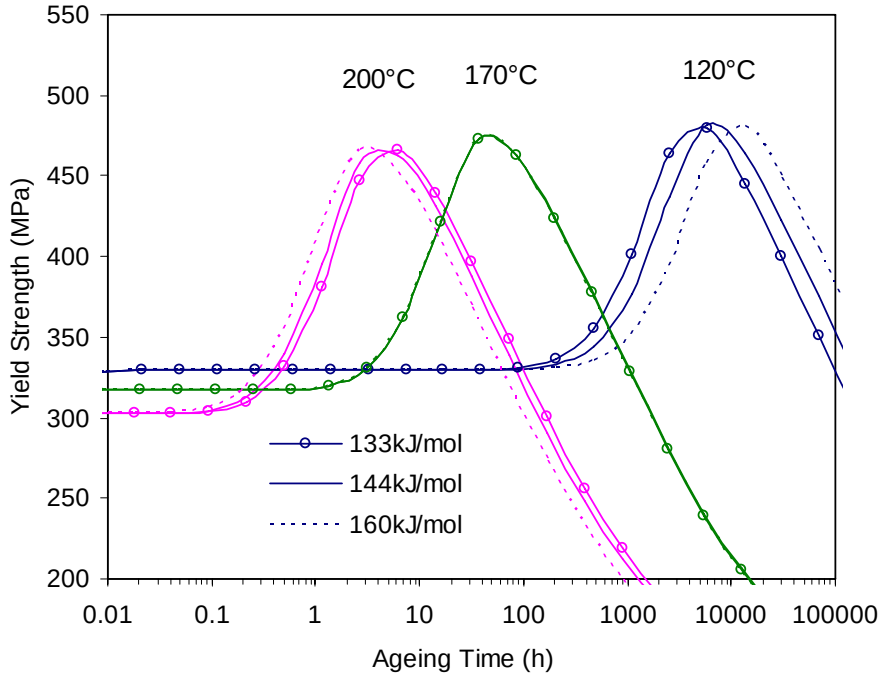

Fig. 6.8 Variation of yield strength with change in the activation energy of S phase for alloy A (2024-T351) aged at 120°C, 170°C and 200°C.

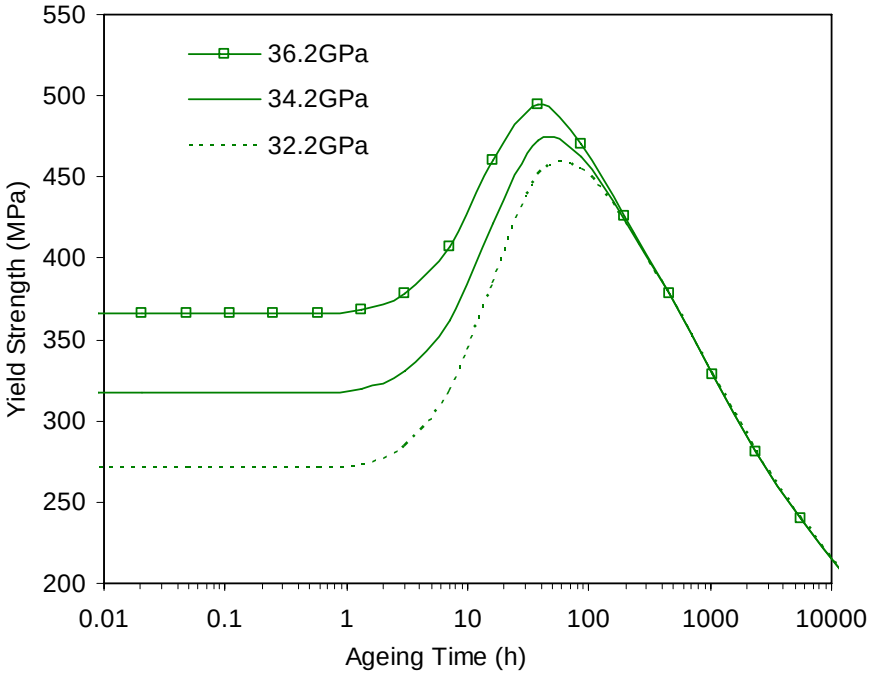

Fig. 6.9 Variation of yield strength with change in the shear modulus of the Cu-Mg co-clusters for alloy A (2024-T351) at 170°C.

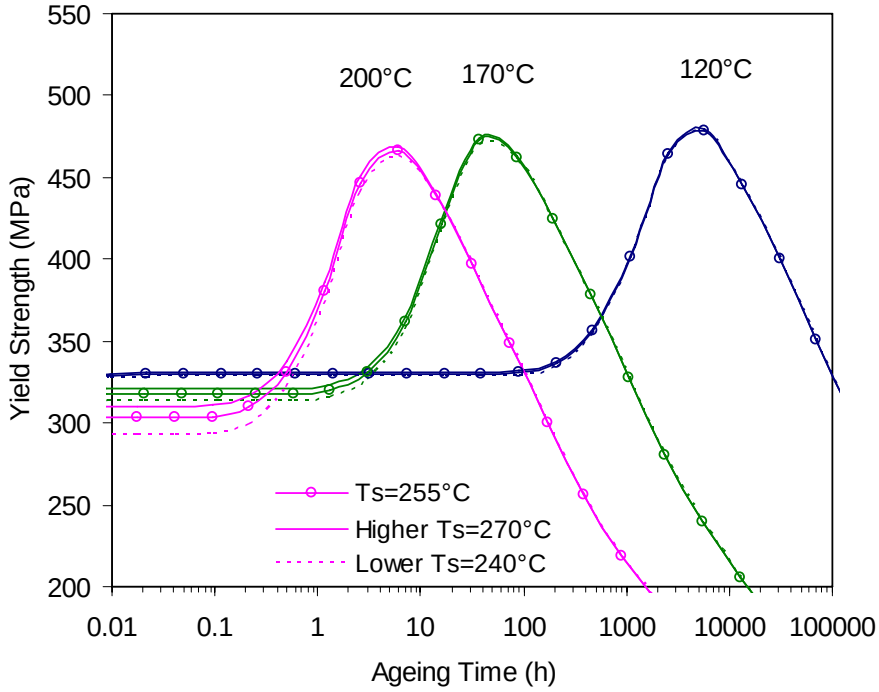

Fig. 6.10 Variation of yield strength with change in the solvus temperature of the Cu-Mg co-clusters for alloy A (2024-T351).

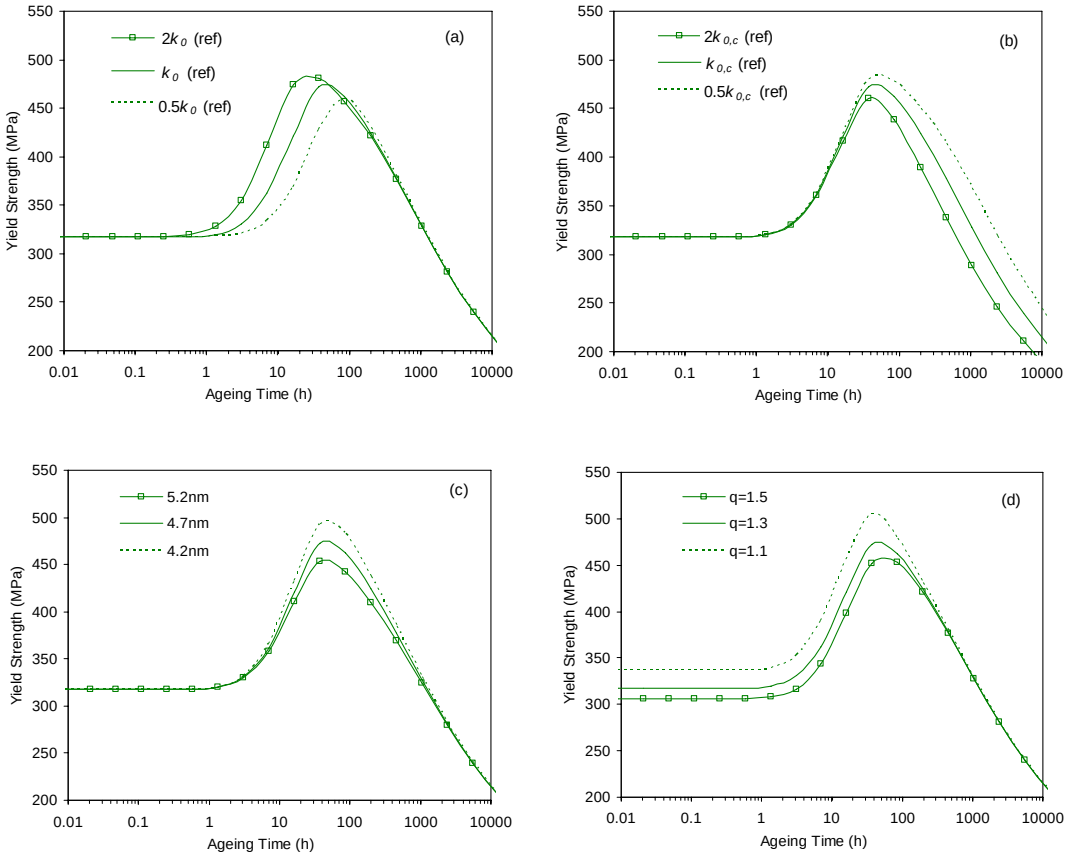

Fig. 6.11 Variations of yield strength with changes in (a) the pre-exponential factor for precipitation k_0, (b) the pre-exponential factor for coarsening $k_{0,c}$, (c) the average radius of S precipitates at the start of coarsening l_0 and (d) the superposition exponent q.

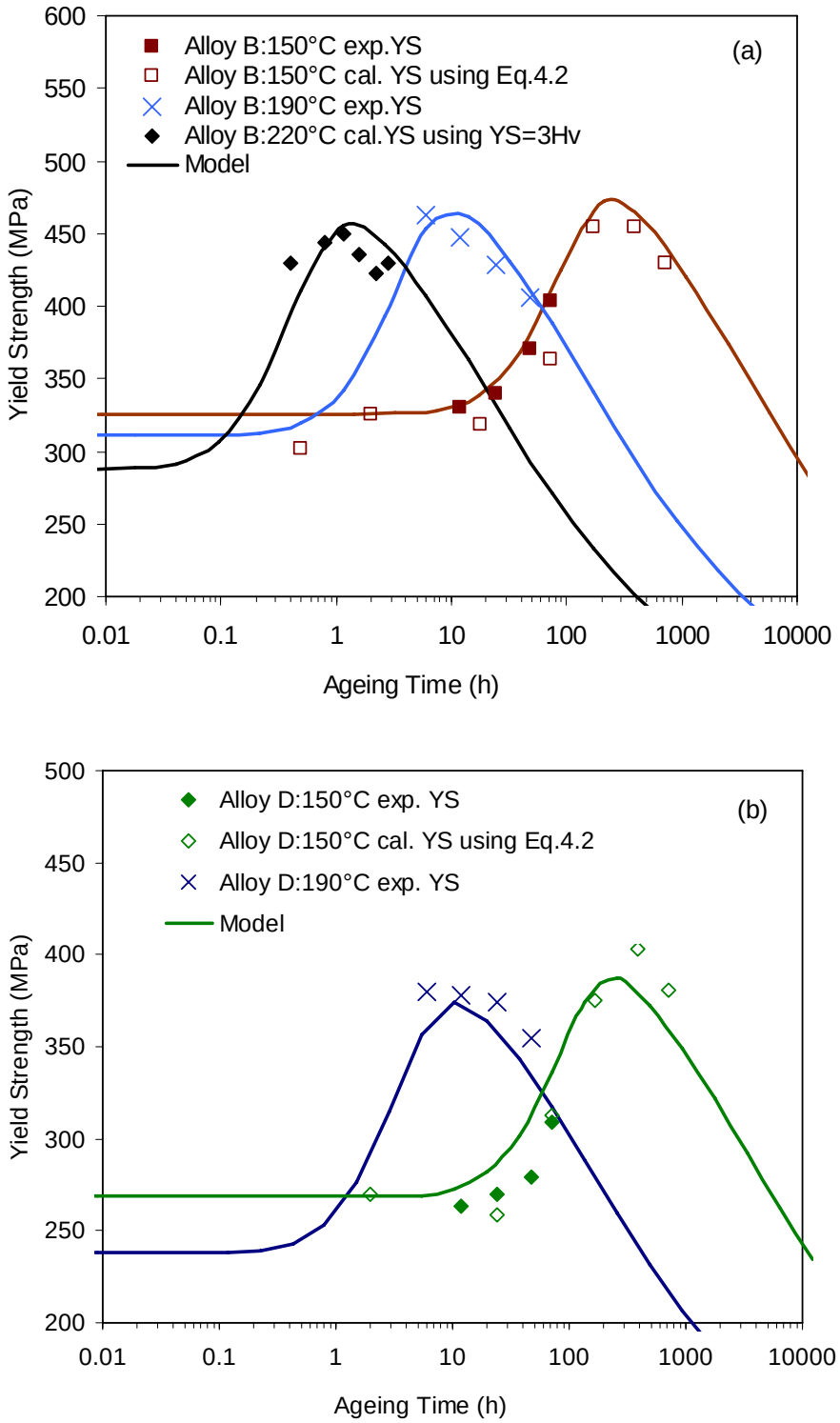

Fig. 6.12 Predicted and measured strength evolution for (a) alloy B and (b) alloy D. Experimental YS data of alloys B and D aged at 150°C and 190°C are from Table 3.2. Vickers hardness data of alloys B and D aged at 150°C and 220°C (see Fig.4.1) were converted to YS data as indicated in the figures.

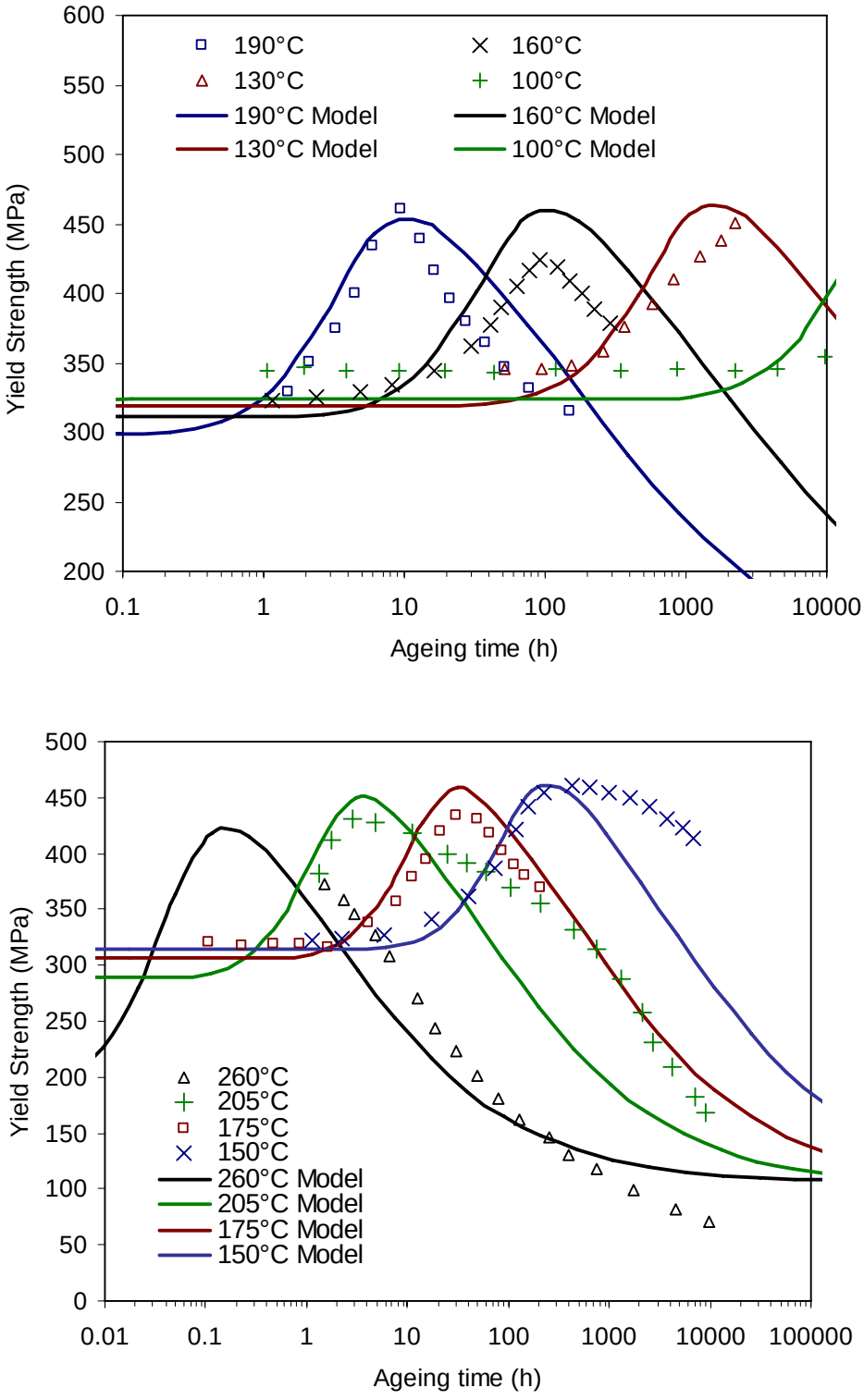

Fig. 6.13 Predicted and measured yield strength evolutions for 2024-T3 alloys. Experimental data were taken from [25] (see the text).

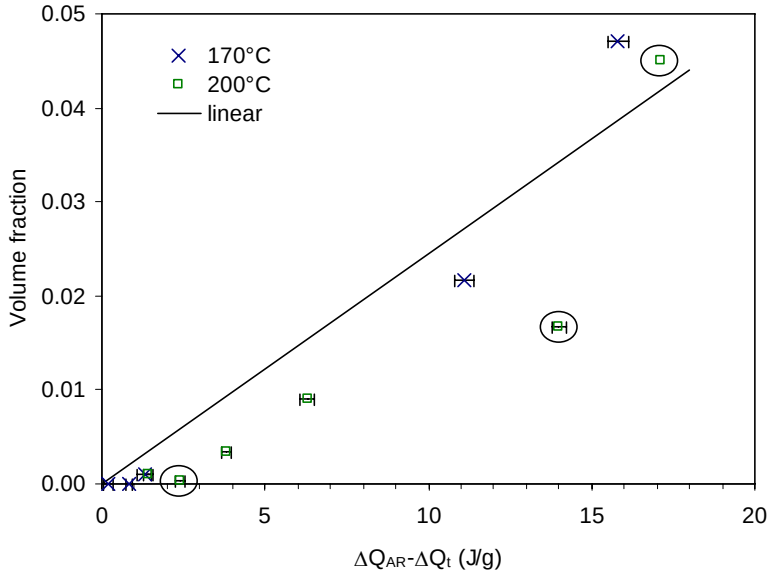

Fig. 6.14 Change in the heat evolved (ΔQ_{AR}- ΔQ_t) of the S formation effect versus the predicted volume fraction of S phase in alloy A. The standard deviation of (ΔQ_{AR}-ΔQ_t) is calculated by $\sqrt{(STD_{AR})^2 + (STD_t)^2}$.

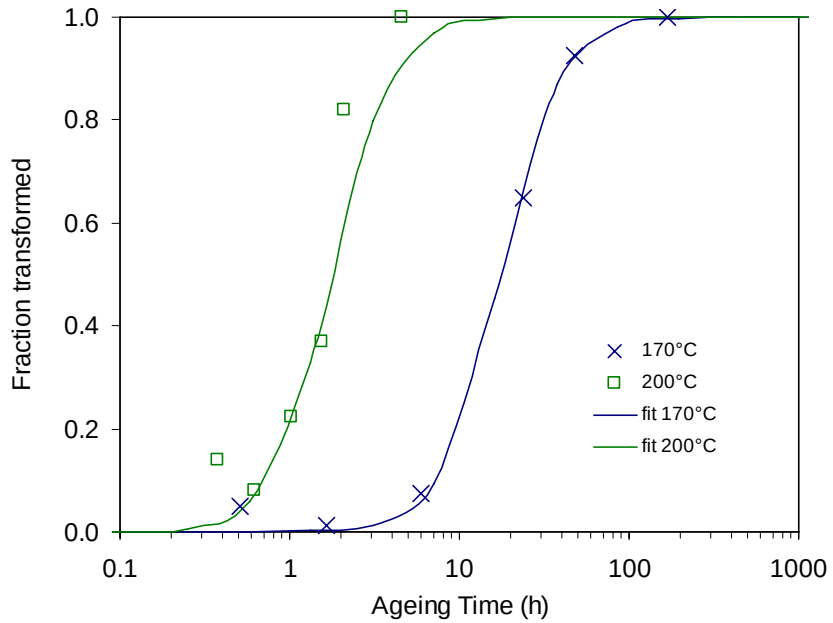

Fig. 6.15 The transformation curves for S precipitation in alloy A during ageing at 170°C and 200°C. The fraction transformed is either obtained from the change in the heats evolved of S formation effect (points) or from the fit based on Eq.(5.8) (curves).

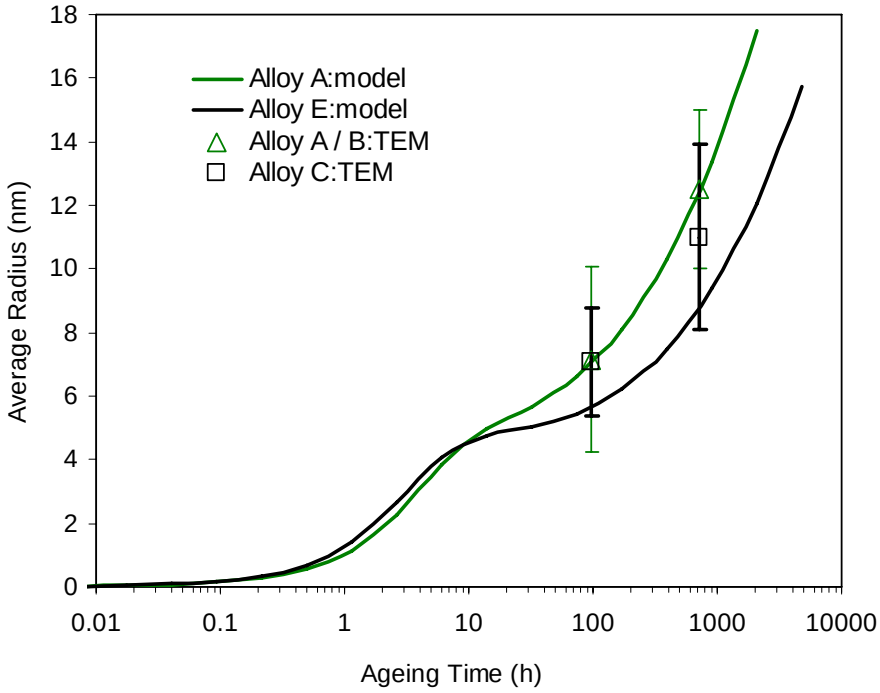

Fig. 6.16 Comparison between predicted and measured average radius of S rods in alloys A/B (Si content <0.06wt.%) and alloys C/E (Si content=0.12wt.% or 0.14wt.%) aged at 190°C.

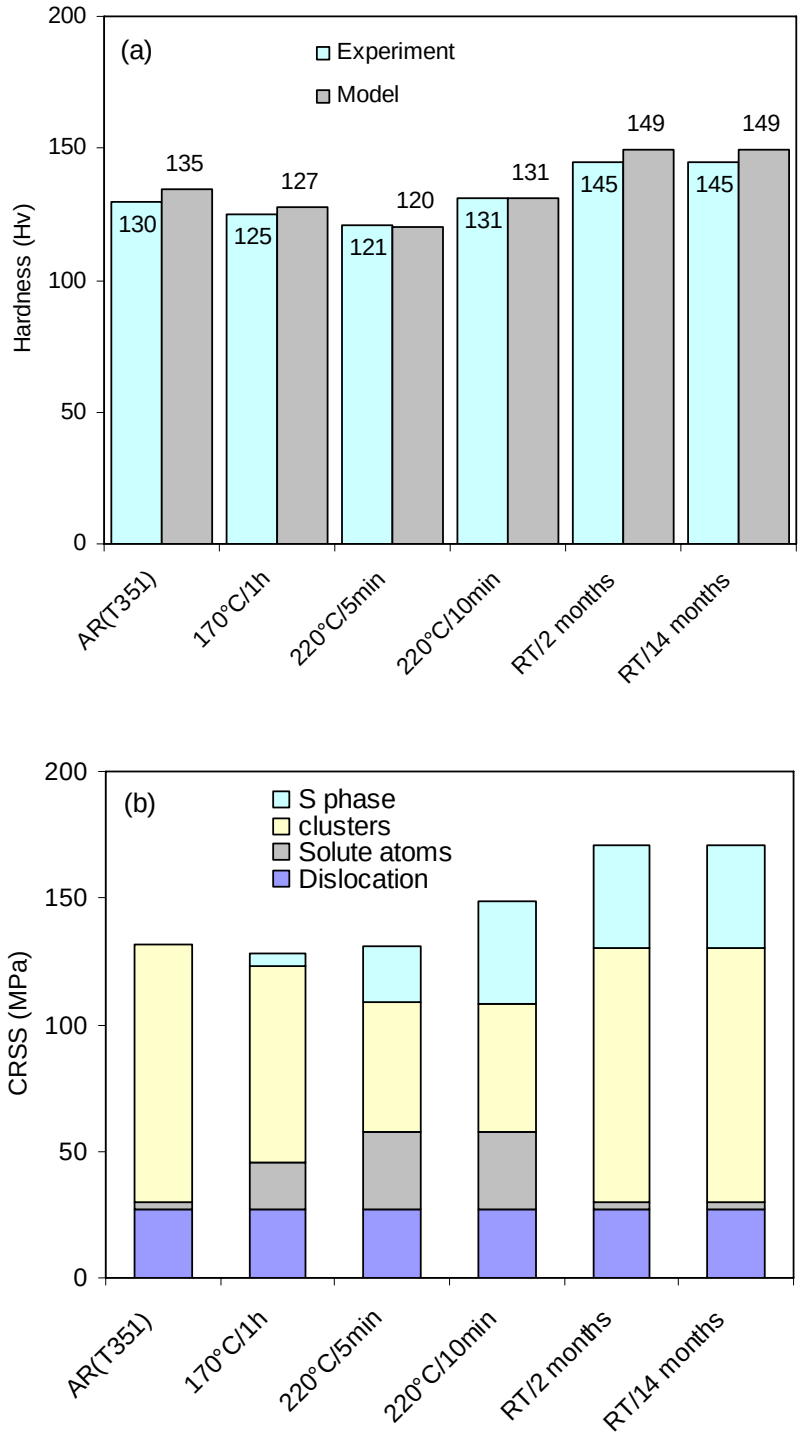

Fig. 6.17 Changes in hardness for alloy A during multi-stage heat treatment I (a) Comparison between the predicted and the experimental hardness. The predicted yield strength was converted to Vickers hardness number by Hv=YS/2.5. (b) Different contributions to the CRSS.

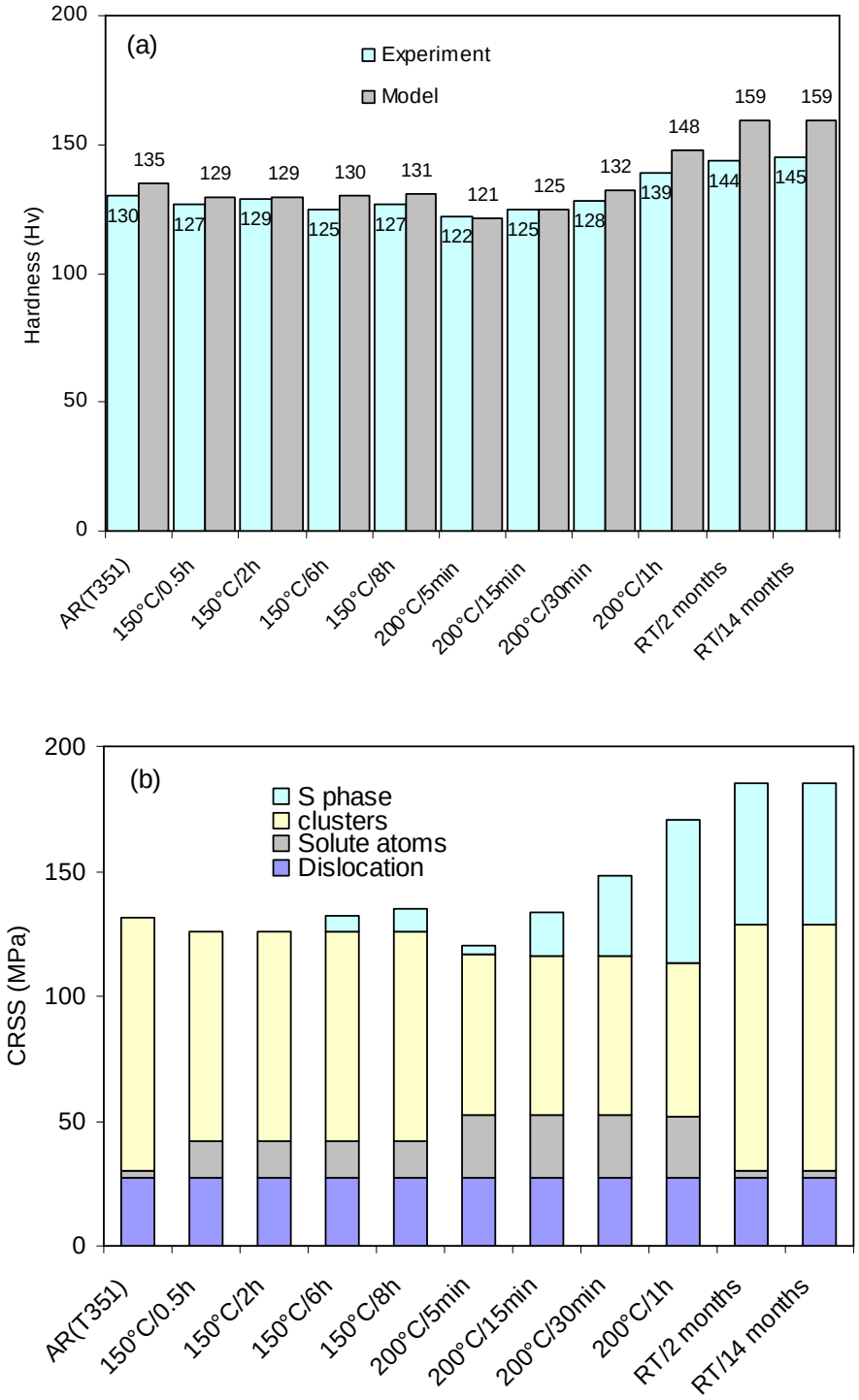

Fig. 6.18 Changes in hardness for alloy A during multi-stage heat treatment II (a) Comparison between the predicted and the experimental hardness. The predicted yield strength was converted to Vickers hardness number by Hv=YS/2.5. (b) Different contributions to the CRSS.

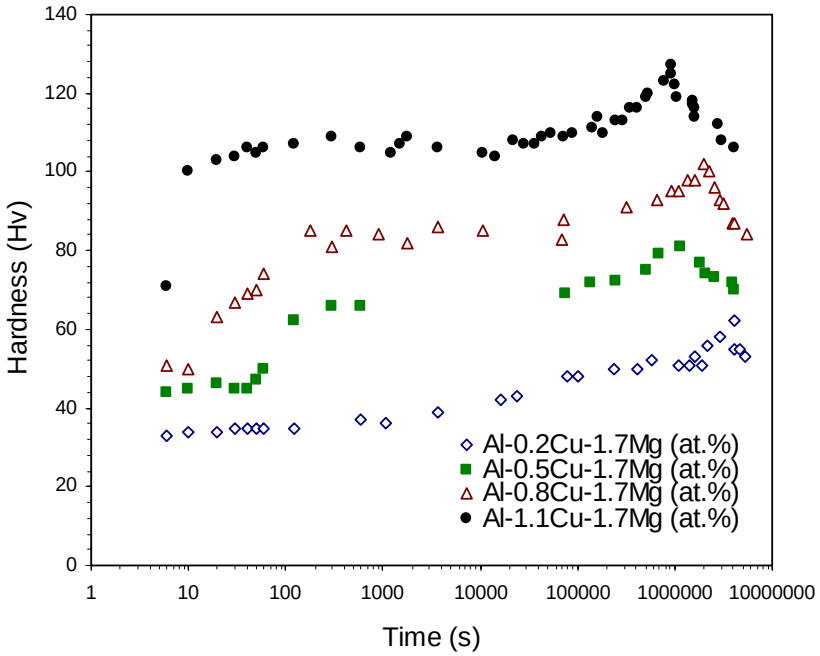

Fig. 6.19 Age hardening of the Al-xCu-1.7Mg alloys (x=0.2, 0.5, 0.8 and 1.1) (at.%) [33] (Courtesy of Dr. K. Raviprasad).

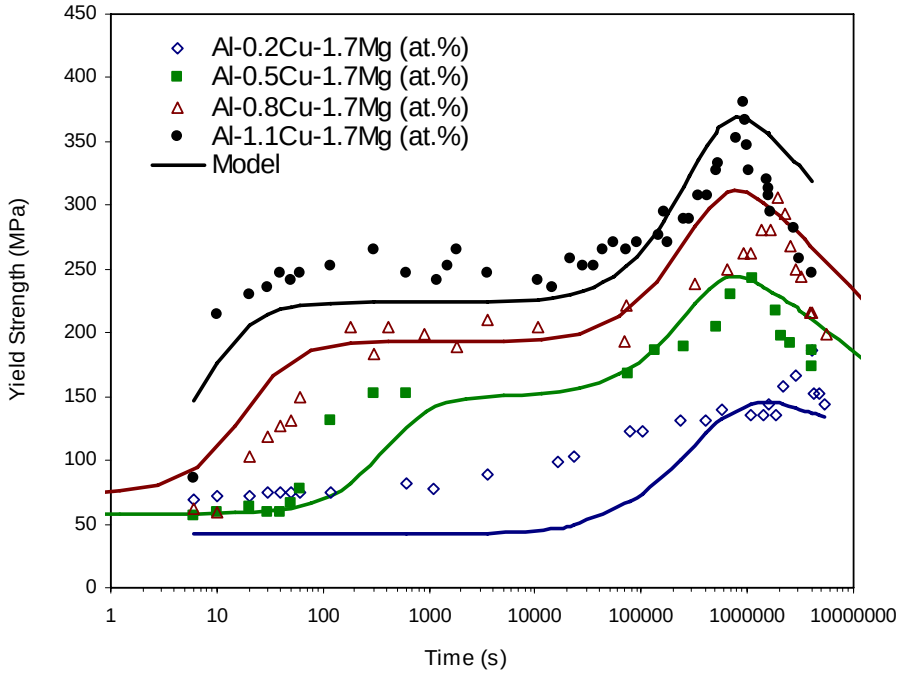

Fig. 6.20 Predicted and converted strength evolution for the Al-xCu-1.7Mg alloys (x=0.2, 0.5, 0.8 and 1.1) (at.%) aged at 150°C. The hardness in Fig. 6.19 was converted to the yield strength using Eq.(4.2) with λ_1=2.3 and λ_2=3.0.

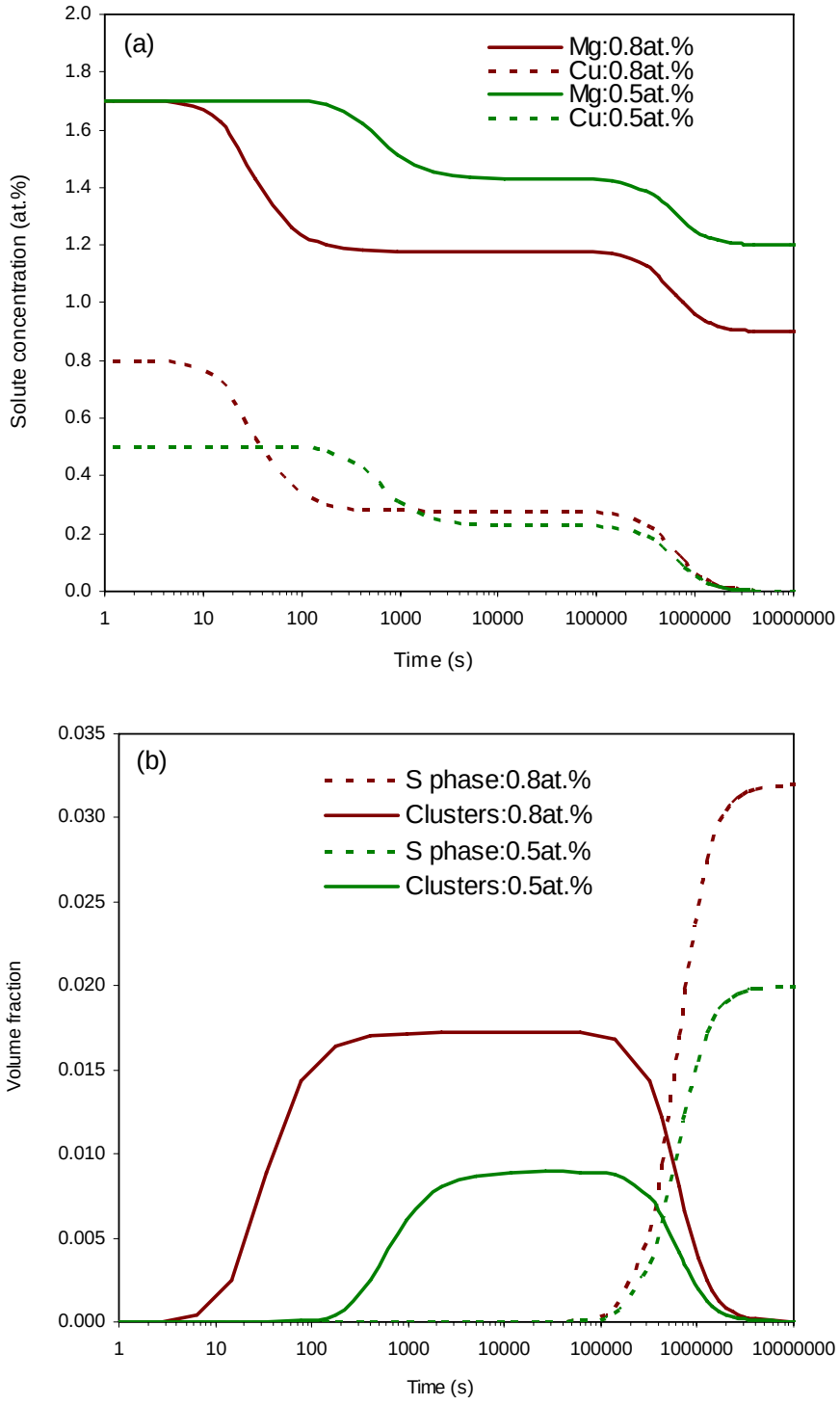

Fig. 6.21 Predicted evolution of microstructural parameters for the Al-xCu-1.7Mg alloys (x=0.5 and 0.8) (at.%) during ageing at 150°C (a) solute concentration of Cu and Mg (b) volume fractions of the Cu-Mg co-clusters and the S phase.

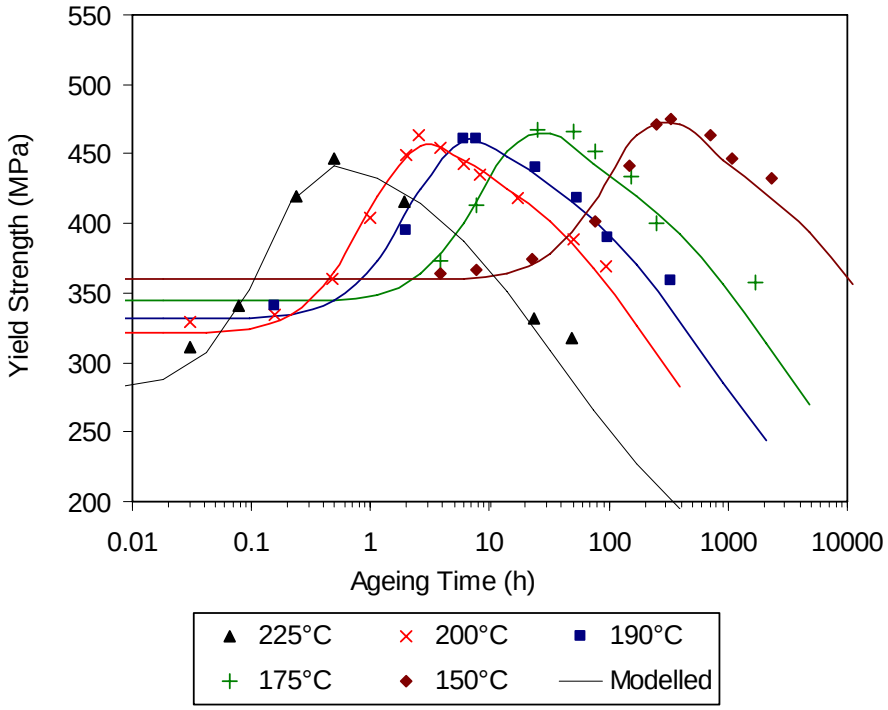

Fig. 6.22 Predicted and measured strength evolution for an Al-4.25Cu-1.68Mg-0.71Mn-0.14Si-0.24Fe (wt.%) alloy. Data were taken from [24].

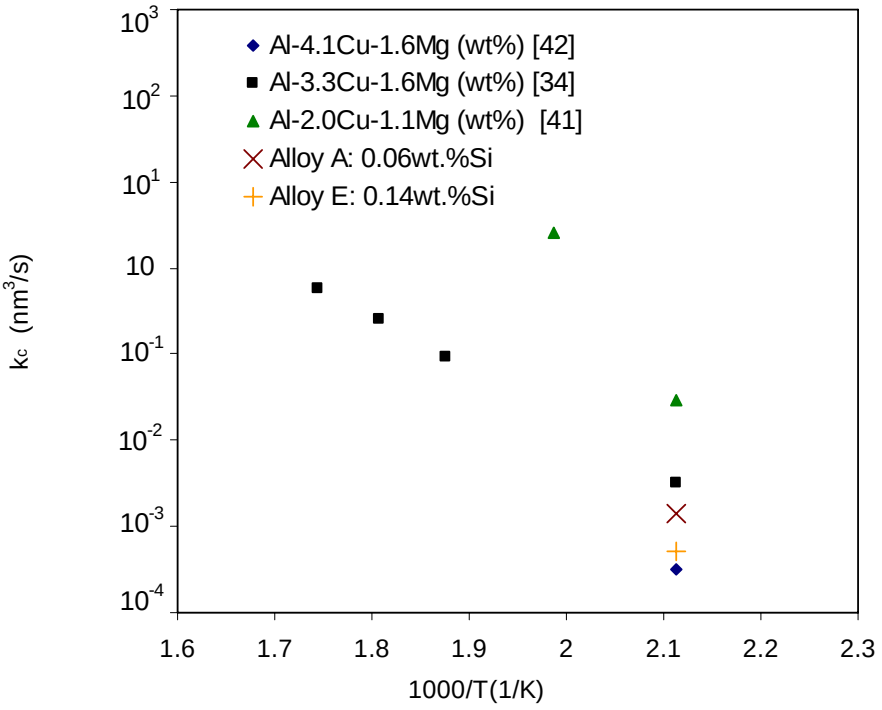

Fig. 6.23 Rate constant $k_c(T)$ (plotted logarithmically) versus *1/T* for the comparison of the coarsening rate of S precipitates in Al-Cu-Mg alloys.

References

[1] M. J. Starink, N. Gao, L. Davin, J. Yan, and A. Cerezo, 'Room temperature precipitation in quenched Al–Cu–Mg alloys: a model for the reaction kinetics and yield strength development', *Philos. Mag.*, 2005, **85**, 1395-1417.

[2] L. F. Davin, 'Ultra-fine Characterisation of Nanostructures in Al-(Li)-Cu-Mg-(Zr) alloys by Three-Dimensional Atom Probe', PhD thesis, Oxford University, 2004.

[3] B. Reppich, 'Particle Strengthening', in: R. W. Cahn, P. Haasen, and E. J. Kramer (Eds.), *Materials Science and Technology: A Comprehensive Treatment Plastic Deformation and Fracture of Materials*, Vol. **6**, p.311-357, 1992, Wiley-VCH, Weinheim.

[4] P. Gomiero, Y. Brechet, F. Louchet, A. Tourabi, and B. Wack, 'Microstructure and Mechanical-Properties of a 2091 Al-Li Alloy .2. Mechanical-Properties - Yield Stress and Work-Hardening', *Acta Metall. Mater.*, 1992, **40**, 857-861.

[5] C. J. Smithells, *Metals Reference Book*, 7th edn, Butterworths-Heinemann, London, 1992.

[6] X. Q. Guo, R. Podloucky, and A. J. Freeman, '1st Principles Calculation of the Elastic-Constants of Intermetallic Compounds - Metastable Al_3Li', *J. Mater. Res.*, 1991, **6**, 324-329.

[7] W. L. Fink, D. W. Smith, and L. A. Willey, 'Precipitation hardening of high purity binary and ternary aluminum-copper alloys', in: *Age hardening of metals*, p.31-55, 1940, ASM.

[8] R. D. Schueller, F. E. Wawner, and A. K. Sachdev, 'Strengthening Potential of the Cubic-Sigma Precipitate in Al- Cu-Mg-Si Alloys', *J. Mater. Sci.*, 1994, **29**, 239-249.

[9] R. N. Wilson, D. M. Moore, and P. J. E. Forsyth, 'Effect of 0.25% silicon on precipitation porcesses in an aluminium-2.5% copper-1.2% magnesium alloy', *J.Inst.Metals*, 1967, **95**, 177-183.

[10] I. J. Polmear, 'The effects of small additions of silver on the aging of some aluminum alloys', *Trans. Met. Soc. AIME*, 1964, **230**, 1331-1339.

[11] C. Genevois, A. Deschamps, A. Denquin, and B. Doisneau-cottignies, 'Quantitative investigation of precipitation and mechanical behaviour for AA2024 friction stir welds', *Acta Mater.*, 2005, **53**, 2447-2458.

[12] P. Gomiero, F. Livet, Y. Brechet, and F. Louchet, 'Microstructure and Mechanical-Properties of a 2091 AlLi Alloy .1. Microstructure Investigated by SAXS and TEM', *Acta Metall. Mater.*, 1992, **40**, 847-855.

[13] N. Unlu, B. M. Gable, G. J. Shiflet, and E. A. Starke, 'The effect of cold work on the precipitation of Omega and theta ' in a ternary Al-Cu-Mg alloy', *Metall. Mater. Trans. A*, 2003, **34A**, 2757-2769.

[14] S. P. Ringer, B. C. Muddle, and I. J. Polmear, 'Effects of Cold Work on Precipitation in Al-Cu-Mg-(Ag) and Al- Cu-Li-(Mg-Ag) Alloys', *Metall. Mater. Trans. A*, 1995, **26**, 1659-1671.

[15] H. C. Shih, N. J. Ho, and J. C. Huang, 'Precipitation behaviors in Al-Cu-Mg and 2024 aluminum alloys', *Metall. Mater. Trans. A*, 1996, **27**, 2479-2494.

[16] H. K. Hardy, 'The ageing characteristics of some ternary aluminium-copper-magnesium alloys with copper : magnesium weight ratios of 7:1 and 2.2:1', *J. Inst. Metals*, 1954-55, **83**, 17-34.

[17] S. P. Ringer, T. Sakurai, and I. J. Polmear, 'Origins of hardening in aged Al-Cu-Mg-(Ag) alloys', *Acta Mater.*, 1997, **45**, 3731-3744.

[18] M. J. Starink, P. Wang, I. Sinclair, and P. J. Gregson, 'Microstructure and strengthening of Al-Li-Cu-Mg alloys and MMCs: I. Analysis and modelling of microstructural changes', *Acta Mater.*, 1999, **47**, 3841-3853.

[19] M. J. Starink, C. Y. Zahra, and A. M. Zahra, 'Analysis of precipitation in Al-based alloys using a novel model for nucleation and growth reactions', *J. Therm. Anal.*, 1998, **51**, 933-942.

[20] J. M. Silcock, 'The structural ageing characteristics of Al-Cu-Mg alloys with copper:magnesium weight ratios of 7:1 and 2.2:1', *J. Inst. Metals*, 1960-61, **89**, 203-210.

[21] H. R. Shercliff and M. F. Ashby, 'A Process Model for Age Hardening of Aluminum-Alloys .1. The Model', *Acta Metall. Mater.*, 1990, **38**, 1789-1802.

[22] G. Liu, G. J. Zhang, X. D. Ding, J. Sun, and K. H. Chen, 'Modeling the strengthening response to aging process of heat- treatable aluminum alloys containing plate/disc- or rod/needle- shaped precipitates', *Mater. Sci. Eng.*, 2003, **344**, 113-124.

[23] M. J. Starink, P. Wang, I. Sinclair, and P. J. Gregson, 'Microstrucure and strengthening of Al-Li-Cu-Mg alloys and MMCs: II. Modelling of yield strength', *Acta Mater.*, 1999, **47**, 3855-3868.

[24] H. Martinod, C. Renon, and J. Calvet, 'Influence of deformation after quenching on mechanical characteristics and resistance to creep of aluminium alloys used in aeronautics', *Rev. Metall.*, 1966, **63**, 815-821.

[25] J. R. Davis (Ed.), *ASM Specialty Handbook: Aluminum and Aluminum Alloys*, Materials Park, OH: ASM International, 1993, p.312: Fig.23(b) of Chapter 'Fabrication and Finishing of Aluminum Alloys'.

[26] O. R. Myhr, O. Grong, and S. J. Andersen, 'Modelling of the age hardening behaviour of Al-Mg-Si alloys', *Acta Mater.*, 2001, **49**, 65-75.

[27] A. Deschamps and Y. Brechet, 'Influence of predeformation and ageing of an Al-Zn-Mg alloy - II. Modeling of precipitation kinetics and yield stress', *Acta Mater.*, 1999, **47**, 293-305.

[28] A. Dupasquier, R. Ferragut, P. Folegati, M. Massazza, G. Riontino, and A. Somoza, 'Secondary ageing in an Al-Cu-Mg alloy with high Cu/Mg ratio', *Mater. Sci. Forum*, 2002, **396-4**, 783-788.

[29] M. Massazza, G. Riontino, A. Dupasquier, P. Folegati, R. Ferragut, and A. Somoza, 'Secondary ageing in Al-Cu-Mg', *Philos. Mag. Lett.*, 2002, **82**, 495-502.

[30] F. Lefebvre, S. Ganguly, and I. Sinclair, 'Micromechanical aspects of fatigue in a MIG welded aluminium airframe alloy - Part 1. Microstructural characterization', *Mater. Sci. Eng. A*, 2005, **397**, 338-345.

[31] D. Booth and I. Sinclair, 'Fatigue of friction stir welded 2024-T351 aluminium alloy', *Mater. Sci. Forum*, 2002, **396-4**, 1671-1676.

[32] S. C. Wang, F. Lefebvre, J. L. Yan, I. Sinclair, and M. J. Starink, 'VPPA welds of Al-2024 alloys: analysis and modelling of local microstructure and strength', *submitted to Acta Mater.*, 2005.

[33] K. Raviprasad and S. Moutsos, 'Early stage hardening in Al-Cu-Mg alloys', in: J. F. Nie, A. J. Morton, and B. C. Muddle (Eds.), *Proc. 9th International Conference on Aluminium Alloys (ICAA9)*, brisbane, Australia, 2004, p.412-417.

[34] N. Sen and D. R. F. West, 'Some factors influencing S precipitation in Al-Cu-Mg and Al-Cu-Mg-Ag alloys', *J.Inst.Metals*, 1969, **97**, 87-92.

[35] S. P. Ringer, K. Hono, I. J. Polmear, and T. Sakurai, 'Precipitation processes during the early stages of ageing in Al-Cu-Mg alloys', *Appl. Surf. Sci.*, 1996, **94-95**, 253-260.

[36] J. T. Vietz and I. J. Polmear, 'The influence of small additions of silver on the ageing of aluminium alloys: observations on Al-Cu-Mg alloys', *J. Inst. Metals*, 1966, **94**, 410-419.

[37] C. R. Hutchinson and S. P. Ringer, 'Precipitation processes in Al-Cu-Mg alloys microalloyed with Si', *Metall. Mater. Trans. A*, 2000, **31**, 2721-2733.

[38] K. Raviprasad, C. R. Hutchinson, T. Sakurai, and S. P. Ringer, 'Precipitation processes in an Al-2.5Cu-1.5Mg (wt. %) alloy microalloyed with Ag and Si', *Acta Mater.*, 2003, **51**, 5037-5050.

[39] R. N. Wilson and P. G. Partridge, 'The nucleation and growth of S' precipitates in an aluminium-2.5% copper-1.2% magnesium alloy', *Acta Metall.*, 1965, **13**, 1321-1327.

[40] R. N. Wilson, 'The effect of 0.24% silicon upon the initial stages of ageing of an Aluminium-2.5%Copper-1.2% Magnesium alloy', *J.Inst.Metals*, 1969, **97**, 80-86.

[41] H. K. Cho, 'Ostwald ripening of S metastable phase in Al-2.0%Cu-1.1%Mg alloy', *J.Korean Inst.Metall.*, 1978, **16**, 160-165.

[42] L. M. Rylands, W. M. Rainforth, and H. Jones, 'Coarsening rates of S' precipitates in Al-4.1wt% Cu- 1.6wt% Mg alloy during extended treatment at 200°C', *Philos. Mag. Lett.*, 1997, **76**, 63-67.

[43] C. Wagner, 'Theorie der alterung von niederschlagen durch umlosen (Ostwald Reifung)', *Z. Elektrochem.*, 1961, **65**, 581-591.

[44] W. M. Rainforth and H. Jones, 'Coarsening of S'-Al_2CuMg in Al-Cu-Mg base alloys', *J. Mater. Sci. Lett.*, 1997, **16**, 420-421.

[45] L. M. Brown and R. K. Ham, in: A. Kelly and R. B. Nicholson (Eds.), *Strengthening Methods in Crystals*, p.9, 1971, Elsevier, London.

[46] I. Khan, *PhD work*, Southampton University, 2005.

Chapter 7 Summary and Conclusions

The strength of age-hardenable Al-Cu-Mg type alloys depends on the presence of precipitate particles which are obtained from the decomposition of a supersaturated solid solution. In this thesis, a physically based two-stage age hardening model for the yield strength of Al-Cu-Mg alloys with compositions in the (α+S) phase region is presented. The model considers a simplified precipitation sequence, which involves the formation and dissolution of a Cu-Mg containing pre-precipitate structure followed by the precipitation of the S phase. The pre-precipitate structure, which is aggregates of solute atoms (mainly Cu and Mg) in the Al matrix and is fully coherent with the matrix, is referred to as Cu-Mg co-clusters instead of GPB zones. This is based on 3DAP and TEM studies from collaborators and on a review of the literature concerning the nature of the Cu-Mg co-clusters and the GPB zones. The Cu:Mg atomic ratios of the Cu-Mg co-clusters are taken as 1:1. The competing reactions of the Cu-Mg co-clusters and S phase are described by assuming the S phase forms at the expense of the Cu-Mg co-clusters.

The model consists of three components: a thermodynamic model for the solvi of Cu-Mg co-clusters and S phase which are approximated by a regular solution model; a kinetic model for the evolution of precipitates (precipitate volume fraction and average precipitate size) and the remaining solute concentration in the matrix during the precipitation process, which are described by the Starink-Zahra kinetic model incorporated with a new, simple treatment for the evolution of the average precipitate size; and a strength model for the yield strength which is obtained by superposition of various strengthening contributions including precipitation strengthening, solution strengthening and dislocation strengthening. Strengthening by Cu-Mg co-clusters and

S phase is described by the modulus strengthening mechanism and the Orowan bypassing mechanism, respectively.

Experiments by means of hardness and tensile tests, DSC/isothermal calorimetry and TEM have been carried out on three 2024-T351 type alloys and an alloy with reduced Cu and Mg contents to provide the relevant information for the verification of the model. The model has been calibrated and validated by comparing the predictions with experimental data. The evolution of microstructure and the yield strength of Al-Cu-Mg alloys have been modelled as a function of composition (the Cu, Mg, Fe and Mn contents) and heat treatments, taking account of the composition dependency of precipitation rate for homogeneous precipitation of the Cu-Mg co-clusters and the amount of Cu and Mg present in undissolved intermetallic phases.

The main conclusions from the experiments and model applications are as follows:

- Analysis of the reaction exponent from DSC and isothermal calorimetry curves indicates that the Cu-Mg co-cluster formation is a nucleation and growth process with continuous nucleation. This is consistent with 3DAP observations from collaborators.

- A new method for conversion of Vickers hardness to yield strength has been derived. Using two proportionality constants which can be easily obtained from the yield strength to hardness ratios, the converted yield strengths show good agreement with the experimental yield strengths. The accuracy of this method is comparable to the one using the strain hardening exponent.

- It has been shown that to model the two-stage age hardening behaviour, i.e. a first rapid hardness rise followed by a constant hardness plateau until a second rise to the peak hardness, it is necessary to consider two types of strengthening precipitates.

- Based on TEM and 3DAP results from collaborators and from the literature, analysis of the present DSC and mechanical tests results shows that the

formation of the Cu-Mg co-clusters is responsible for the natural age hardening and the first stage of artificial age hardening while the precipitation of the S phase is responsible for the second stage of hardening. With the formation rate of the Cu-Mg co-clusters determined from room temperature isothermal calorimetry and the precipitation rate of the S precipitates fitted to the ageing curves and verified by DSC experiments, the predicted contributions to the critical resolved shear stress show that strengthening in the alloys is mainly due to the Cu-Mg co-clusters in the first stage of hardening and due to the S phase in the second stage of hardening. This is consistent with the analysis of the experiments.

- The evolution of the S phase formation effect in the DSC curves of samples aged for a range of ageing times has been analysed semi-quantitatively. The changes in the heat evolved, which are associated with the amount of the S precipitates formed, show good correspondence with the predicted volume fractions of the S precipitates. This suggests that DSC can be useful tool to obtain the relative volume fraction of the precipitates.

- The shear modulus of the Cu-Mg co-clusters is predicted to be 34.2GPa for Al-Cu-Mg alloys with Si content less than 0.1wt.%. This value was obtained under the assumption that the atomic concentration of Cu, Mg and Al in the Cu-Mg co-clusters is 30%, 30% and 40%, respectively based on 3DAP analysis.

- With a training root mean square error of 12MPa on a 2024 alloy aged at 120°C, 170°C and 200°C, the modelling accuracy on unseen yield strength data of two other alloys (one 2024 alloy and one alloy with reduced Cu and Mg contents) aged at 150°C and 190°C is 16MPa. The model has been applied to alloys with different compositions that underwent heat treatments of natural ageing, or artificial ageing or multi-stage ageing using a single set of parameters. It is shown that the model has good predictive capabilities for Al-Cu-Mg alloys with approximately fixed Si content.

- Multi-stage heat treatments were carried out on a 2024-T351 alloy. The samples were firstly aged at low temperature to reach the plateau hardness, then underaged at a higher temperature for a short time followed by air cooling and room temperature ageing. Addition hardening was observed in samples aged at room temperature after air cooling from short time elevated temperature ageing. Applications of the model to multi-stage heat treatment gave good agreements between the predictions and the experiments, indicating that the hardness changes can be well interpreted by considering the dissolution of the Cu-Mg co-clusters, precipitation of the S phase and re-formation of the Cu-Mg co-clusters. The model is therefore considered to be a potential predictive tool for predicting the strength of Al-Cu-Mg based welds.

- Application of the model to Al-xCu-1.7Mg alloys (x=0.2, 0.5, 0.8 and 1.1at.%) has shown that the composition dependence of the rates for the first stage of hardening are well captured by the model. This indicates that the model is able to describe not only the peak strength accurately but also the first rapid rise to plateau strength.

- Hardness-time ageing curves of two 2024-T351 alloys with different levels of impurities confirm the enhanced hardening in the alloy with higher Si content. Measurements on TEM images indicate a slower coarsening rate in alloys with higher Si content. In the present model, variation of Si content on the yield strength is not accounted for. By re-calibration of the shear modulus of the Cu-Mg co-clusters and the pre-exponential factor for S coarsening, the model is applicable to model the enhanced hardening in Al-Cu-Mg alloys with Si contents at levels of 0.1-0.2wt.%. Modelling results indicating increased shear modulus of the Cu-Mg co-clusters and decreased coarsening rate of the S precipitates for Si containing alloys are supported by experimental evidence in the literature.